Timing Young Pulsars: Challenges to Standard Pulsar Spin-Down Models

Margaret Anne Livingstone
Department of Physics
McGill University
Montréal, Québec
Canada

A Thesis submitted to the
Faculty of Graduate Studies and Research
in partial fulfillment of the requirements for the degree of
Doctor of Philosophy

Dedicated to Jack Livingstone, who would have really enjoyed this.

Abstract

Pulsars are rapidly rotating neutron stars which are often noted for their very regular rotation rates. Young pulsars, however, frequently exhibit two types of deviations from steady spin down, "glitches" – sudden jumps in spin frequency, which provide insight into pulsar interiors, and "timing noise," a smooth stochastic wander of the pulse phase over long time periods. The youngest pulsars also offer a window into the physics that govern pulsar spin down via the measurement of the "braking index" – a parameter that relates the observable spin frequency of the pulsar with the slowing down torque acting on the neutron star.

This thesis discusses long-term timing observations of two young pulsars. First, we present observations of PSR J0205+6449, acquired with the Green Bank Telescope, the Jodrell Bank Observatory and the *Rossi X-ray Timing Explorer*. We present phase-coherent timing analyses showing timing noise and two spin-up glitches. We also present an X-ray pulse profile analysis showing that the pulsar is detected up to $\sim$40 keV and does not vary appreciably over four years. We report the phase offset between the radio and X-ray pulse, showing that the radio pulse leads by $\phi = 0.10 \pm 0.01$ in phase. We compile measurements of phase offsets for this and other X-ray and γ-ray pulsars and show that there is no relationship between pulse period and phase offset.

Next, we present 10 years of monitoring of PSR J1846−0258 with the *Rossi X-ray Timing Explorer*. We report the first measurement of the braking index for this pulsar, $n = 2.65 \pm 0.01$, only the sixth such measurement ever made, and show that the pulsar experienced a small glitch in 2001.

In May 2006, PSR J1846−0258 was briefly transformed: it exhibited a series of X-ray bursts, a dramatic increase in the source flux, and significant softening of its X-ray spectrum – behaviours best explained in the context of the magnetar model. PSR J1846−0258 was thus identified as the first rotation-powered pulsar/magnetar transition object. We quantify the properties of a large glitch that occurred contemporaneously with the outburst, and show that it is unique among pulsar glitches in that it had an over-shoot recovery of $870 \pm 250\%$, resulting in a net decrease of the spin-frequency. We also report torque variations over a period of several hundred days during the period of glitch recovery, that are reminiscent of behaviour seen in some magnetars.

Finally, we report that the post-outburst braking index for PSR J1846−0258 is $n = 2.16 \pm 0.13$, corresponding to a decrease of $18 \pm 5\%$ relative to its pre-burst value, the first significant change measured in any braking index. We also show that four years after the outburst, the timing noise remains at a higher state than its pre-burst quiescent level.

Résumé

Les pulsars, des étoiles à neutrons tournant rapidement sur elles-mêmes, sont reconnus pour leur vitesse de rotation très régulière. Les jeunes pulsars, par contre, présentent fréquemment des comportements qui dévient du ralentissement uniforme de leur vitesse de rotation: des glitchs, variations brutales de la fréquence de révolution qui nous aident à comprendre l'intérieur des plusars, et le bruit chronométrique, une variation stochastique de la phase de rotation sur une longue échelle de temps. Les pulsars les plus jeunes nous offrent aussi un aperçu de la physique qui gouverne le ralentissement de la vitesse de rotation par l'indice de freinage, un paramètre qui relie la fréquence de rotation d'un pulsar au torque qui agit sur lui, et dont la valeur diminue graduellement.

Cette thèse discute du chronométrage à long terme de deux jeunes pulsars. Tout d'abord, nous présentons des observations de PSR J0205+6449 acquises avec l'Observatoire de Green Bank, l'Observatoire Jodrell Bank ainsi que le *Rossi X-ray Timing Explorer*. Nous présentons l'analyse du chronométrage à phase cohérente montrant du bruit chronométrique ainsi que deux glitchs. Nous présentons aussi une analyse du profil du pulse en rayons X montrant que le pulsar est détectable jusqu'à $\sim$40 keV et ne varie pas significativement sur quatre ans. Nous rapportons une mesure de la différence de phase entre le pulse radio et le pulse en rayons X, montrant que le pulse radio précède le pulse en rayons X par $\phi = 0.10 \pm 0.01$. Une compilation des différences de phase pour ce pulsar et d'autres qui émettent en rayons X et en rayons γ montre qu'il n'y a aucune relation entre la période de rotation et la différence de phase.

Ensuite, nous présentons 10 années de suivi de PSR J1846−0258 avec le *Rossi X-ray Timing Explorer*. Nous rapportons la première mesure de l'indice de freinage pour ce pulsar, $n = 2.65 \pm 0.01$, le sixième indice mesuré à ce jour, et montrons que ce pulsar a subit un petit glitch en 2001.

En mai 2006, ce pulsar a subit une brève transition: il a montré une série de bursts, une augmentation dramatique du flux d'émission ainsi qu'un adoucissement marqué de son spectre de rayons X: tous des comportements qui sont possibles à expliquer dans le cadre du modèle des magnétars. PSR J1846−0258 a donc été identifié comme le premier objet de transition pulsar/magnétar. Nous quantifions un glitch de grande amplitude qui s'est produit en même temps que la série de bursts. Ce glitch est

unique puisqu'il sur-récupère de $870 \pm 250\%$, ce qui résulte en une diminution nette de sa fréquence de rotation. Nous observons aussi des variations de torque sur une période de plusieurs centaines de jours suivant le glitch, ce qui n'est pas sans rapeller le comportement de certains magnétars.

Finalement, nous montrons que l'indice de freinage après les bursts, $n = 2.16 \pm 0.13$, est réduit de $18 \pm 5\%$ par rapport à sa valeur antérieure, ce qui représente le premier cas connu d'un changement significatif de l'indice de freinage. Nous montrons aussi que, quatre ans après ces événements, le bruit chronométrique se maintient à une valeur supérieure à celle de son état quiescent pré-bursts.

Contents

List of Figures

List of Tables

Acknowledgments

First and foremost I want to thank my supervisor Vicky Kaspi. Vicky has far surpassed the usual expected level of support to a graduate student in my case. Vicky took me on as an undergraduate summer student with no experience and blue hair. Eight years later, she has guided me through three degrees and the much more challenging journey of motherhood. I can never thank her enough for her mentorship as a scientist and a mother, not to mention the crates of clothing and other baby supplies.

Every astronomical observation comes as a result of a collaboration between the researcher and the people who have made those observations possible: the telescope designers, engineers, builders, and operators. Many thanks to all of the operators, schedulers, and people manning the *RXTE* help desk over the past 5 years, in particular, long-term P.I. Jean Swank, Divya Pereira, Evan Smith, Gail Rohrbach, Keith Jahoda and Craig Markwardt. I would also like to thank the operators and maintenance crews at the Lovell Telescope at Jodrell Bank and the Robert C. Byrd Green Bank Telescope.

Technical support is another too-often overlooked area of important help to any research. As such, I must offer my undying gratitude to Paul Mercure, who has really gone above and beyond the call of duty. Thanks also to Juan Gallego at McGill and Kenton Philips and Ed Morgan at MIT for additional support.

This research makes use of data obtained from the High Energy Astrophysics Science Archive Research Center Online Service (HEASARC), provided by the NASA-Goddard Space Flight Center, the pulsar database operated by The Australia Telescope National Facility (ATNF), the NASA Astrophysics Data System abstract service, and the magnetar catalogue maintained by the McGill Pulsar Group.

The National Radio Astronomy Observatory is a facility of the National Science Fundation operated under cooperative agreement by Associated Universities, Inc. The *Rossi X-ray Timing Explorer* is operated by the National Aeronautics and Space Administration (NASA). Funding for this work was provided by a Natural Science and Enginerring Research Council of Canada (NSERC) PGS-D fellowship. Additional funding was provided by a NSERC Discovery Grant Rgpin 228738, Fonds de Recherche de la Nature et des Technologies du Québec and the Canadian Institute for Advanced Research, and the Canadian Foundation for Innovation.

This thesis contains several manuscripts reviewed by anonymous referees, whose

efforts significantly improved the papers. In addition, many discussions with visitors to McGill over the years has helped both individual manuscripts and my development as a researcher. In particular I would like to thank Bennett Link, Anatoly Spitkovsky, Roger Blandford, Andrei Beloborodov, Andrew Melatos, Richard Manchester, and my "doctor grandfather," Joe Taylor.

Thanks are due to all the current and past members of the McGill Pulsar group. Firstly, to my many office mates over the years for putting up with my quirks, and especially Scott Ransom for sharing his coffee maker and post doc office with me in the early days. Cheers to Mallory, Fotis, Cindy, Rim, Marjorie, Rene, David, and Patrick and everyone else for making the department an engaging and fun place to come every day. Thanks also to everyone in the physics department who participated in the now-defunct Astro Tea, and everyone who provided such good discussion at the Neutron Star coffee.

Fotis Gavriil wrote "McGill Tools," scripts that are used in the analysis of X-ray data in this thesis; while Rim Dib wrote additional scripts. Both Fotis and Rim have been my *RXTE* partners in crime over the years and I have very much enjoyed working with them both.

This thesis may never have been finished without the encouragment and exasperation of my faithful readers, Patrick and Jens, who unfailingly told me what made sense and what was nonsense, and told me to get on with it already.

I couldn't have done this without my family or friends. I love you all. Especially to Jens and Norah, without whom I neither could have done this, nor would have wanted to.

Preface

Statement of Originality and Contribution of Authors

This thesis is a collection of papers published in the *Astrophysical Journal* (Chapters 4, 5, and 6) and submitted for publication in the *Astrophysical Journal* (Chapter 7). Each paper reports a new and original result concerning timing observations of a young pulsar. Here we summarize the main results of each paper and detail the contributions of the authors.

- **Chapter 4 – The Young, Energetic Pulsar in the Supernova Remnant 3C 58**

  The contents of this Chapter originally appeared as:

  Livingstone, Margaret A.; Ransom, Scott M.; Camilo, Fernando; Kaspi, Victoria M.; Lyne, Andrew G.; Kramer, Michael; Stairs, Ingrid H. *X-ray and Radio Timing of the Pulsar in 3C 58*. ApJ, 706:1163-1173 (2009)

  In this Chapter, we use a combination of radio and X-ray observations to perform long-term phase-coherent timing on PSR J0205+6449. We present two spin-up glitches, which are unusually large if the true age of the pulsar is 829 years, as has previously been suggested. We present an X-ray pulse profile analysis of four years of *Rossi X-ray Timing Explorer* data showing that the pulsar is detected up to ∼40 keV (the first reported detection of the pulsar in the X-ray band above 10 keV). We show that the pulse profile is steady over four years and does not evolve significantly over the energy range of 2 – 40 keV. We also present the first measurement of the phase offset between the radio and X-ray pulse for this source, showing that the radio pulse leads the X-ray pulse by $\phi = 0.10 \pm 0.01$ in phase. We compile all known measurements of the phase offsets between radio and high energy pulses for X-ray and γ-ray pulsars. We show that there is no relationship between pulse period and phase offset, supported by our measurement of the phase offset for PSR J0205+6449.

  The contributions of the co-authors for this paper are as follows. Drs. Andrew Lyne and Michael Kramer acquired the Jodrell Bank Observatory observations and performed the subsequent analysis to produce pulse times of arrival. Dr.

Ingrid Stairs performed the majority of the observations of the pulsar at the Green Bank Telescope, while additional observations were performed by Drs. Fernando Camilo and Scott Ransom. Drs. Fernando Camilo and Scott Ransom performed the reduction of GBT data to produce pulse times of arrival. Dr. Scott Ransom developed a new maximum likelihood method of finding X-ray pulsar times of arrival used in this Chapter and performed this analysis to produce barycentered pulse arrival times for *RXTE* data. This method was first described in Livingstone et al. (2009). Dr. Ransom also reduced a *Chandra X-ray Observatory* observation and created a corresponding pulse arrival time. Dr. Vicky Kaspi provided the code used fit the glitch using frequency measurements as well as provided substantial contributions to the text and interpretation of results. The proposals to acquire *RXTE* data for PSR J0205+6449 for Cycles 7 and 9 was written mainly by Dr. Scott Ransom, with help from Drs. Victoria Kaspi, Mallory Roberts, Bryan Gaensler, and Patrick Slane. The Cycle 10 *RXTE* proposal was written by myself and Drs. Ransom and Kaspi, with additional contributions from Drs. Mallory Roberts, Fotis Gavriil, Bryan Gaensler, and Patrick Slane. The proposal for the *RXTE* Cycle 6 data was part of a different observing program and was written by Dr. Eric Gotthelf. I performed the phase-coherent and partially-coherent timing analyses of both the radio and X-ray data, and the subsequent glitch fitting and analysis. I also performed the analysis to find the radio-to-X-ray phase offset and reduced the *RXTE* data for the pulse profile analysis.

- **Chapter 5 – Phase-coherent X-ray timing of the young pulsar PSR J1846−0258**

  The majority of the analysis and results presented in Chapter 5 originally appeared as:

  Livingstone, Margaret A.; Kaspi, Victoria M.; Gotthelf, E. V.; Kuiper, L. *A Braking Index for the Young, High Magnetic Field, Rotation-Powered Pulsar in Kesteven 75*. ApJ, Volume 647, Issue 2, pp. 1286-1292. (2006)

  Data continued to accrue on PSR J1846−0258 after the publication of the above manuscript. To improve the flow of this thesis, data taken between 2005 July 27 and 2006 May 24 were added to the analysis presented in this chapter. These data originally appeared in:

  Livingstone, Margaret A.; Kaspi, Victoria M.; Gavriil, Fotis. P. *Timing Behavior of the Magnetically Active Rotation-Powered Pulsar in the Supernova*

Remnant Kesteven 75. ApJ, Volume 710, Issue 2, pp. 1710-1717 (2010)

We present the first phase-coherent measurement of a braking index for the young, energetic rotation-powered pulsar PSR J1846−0258. Two independent phase-coherent timing solutions are derived which span 6.3 yr of data. A partially phase-coherent timing analysis confirms the fully phase-coherent result. The measured value of the braking index, $n = 2.65 \pm 0.01$, is significantly less than 3, the value expected from magnetic dipole radiation, implying another physical process must contribute to the pulsar's rotational evolution. Assuming the braking index has been constant since birth, we place an upper limit on the spin-down age of PSR J1846−0258 of 884 yr, the smallest timing age estimate of any rotation-powered pulsar. In addition, we detect and describe the first glitch observed from this pulsar and show that it is typical of glitches observed in young pulsars.

Dr. Eric Gotthelf and I performed parallel analyses of the *ASCA* data and obtained equivalent results. Some of the software used to analyze the *ASCA* data was written by Dr. Vicky Kaspi. Dr. Gotthelf also provided significant contributions to the text, in particular to the discussion section. I reduced the data as described in the text and produced barycentered pulse arrival times. I then performed the phase-coherent timing analysis, partially coherent analyses, and pulse profile analysis, as described in the text. Dr. Lucien Kuiper provided suggestions for the data analysis and contributed to the text. Dr. Vicky Kaspi provided guidance throughout the data analysis process as well as making contributions to the interpretation of results and the writing and editing of the text.

The proposals for the *RXTE* data for Cycles 4 through 9 were written by Drs. Eric Gotthelf and Victoria Kaspi, while proposals for Cycles 10 through 13 and onward were written by myself and Drs. Eric Gotthelf and Victoria Kaspi. The proposal was automatically renewed for observing Cycles 14 and 15.

- **Chapter 6 – Outburst Timing Behaviour of PSR J1846−0258**

The contents of this Chapter originally appeared in

Livingstone, Margaret A.; Kaspi, Victoria M.; Gavriil, Fotis. P. *Timing Behavior of the Magnetically Active Rotation-Powered Pulsar in the Supernova Remnant Kesteven 75* ApJ, Volume 710, Issue 2, pp. 1710-1717 (2010)

We report a large spin-up glitch in PSR J1846−0258 which coincided with the onset of magnetar-like behaviour on 2006 May 31. We show that the pulsar

experienced an unusually large glitch recovery, with a recovery fraction of $Q = 8.7 \pm 2.5$, resulting in a net decrease of the pulse frequency. Such a glitch recovery has never before been observed in a rotation-powered pulsar. We also report a large increase in the timing noise of the source.

I created the pulse arrival times and performed the timing analysis for all data in this Chapter. I fitted the glitch and performed the pulse profile analysis. I searched for bursts manually and using software written by Dr. Fotis Gavriil. Dr. Fotis Gavriil performed the pulsed flux analysis and contributed the text for the corresponding section of the manuscript. Dr. Vicky Kaspi provided a substantial contribution to the text as well as to the interpretation of the results.

- **Chapter 7 – Persistent Changes to the Timing Properties of PSR J1846−0258**

  The contents of this Chapter are based on a manuscript that has been submitted to the *Astrophysical Journal*, which will appear as:

  Livingstone, Margaret A., Ng, C.-Y., Kaspi, Victoria M., Gavriil, Fotis P., and Gotthelf, Eric, V. "Post-outburst Observations of the Magnetically active pulsar J1846−0258: a new braking index, increased timing noise, and radiative recovery" *Astrophysical Journal*

  This chapter presents X-ray timing observations of PSR J1846−0258 taken with the *Rossi X-ray Timing Explorer* over a 2.2-yr period after the X-ray outburst and accompanying glitch had recovered. We observe that the braking index of the pulsar, previously measured to be $n = 2.65 \pm 0.01$ is now $n = 2.16 \pm 0.13$, a decrease of $18 \pm 5\%$. We also quantify a persistent increase in the timing noise relative to the pre-outburst level.

  I performed all of the analysis of the *RXTE* data in this chapter, including the phase-coherent and partially coherent timing analyses, the pulse profile analysis, and the various quantifications of timing noise.

  Dr. C.-Y. Ng performed an analysis of a *Chandra X-ray Observatory* and provided the text to the corresponding section, as well as making significant contributions to the discussion section. The *Chandra* data and analysis do not appear in this thesis, but do appear in the accompanying paper. Dr. Eric Gotthelf contributed to the discussion and text. Drs. Vicky Kaspi and Fotis Gavriil made suggestions for further analyses, and provided significant contributions to the discussion of the results in this manuscripts.

1 Introduction

1.1 Neutron Stars

The existence of neutron stars – stars supported from gravitational collapse by neutron degeneracy pressure – was predicted by Baade & Zwicky in 1934, only 2 years after the discovery of the neutron (Chadwick, 1932). It was not thought that these objects would be observable, as the implied diameter was small (roughly 20 km) and the objects should be cold, so the concept was largely ignored for many years. Observational evidence of neutron stars would not arise until 1967. A Cambridge research group led by Professor Antony Hewish aimed to study scintillation of compact radio sources. Famously persistent graduate student Jocelyn Bell noticed an unusual signal in their data. The signal was a pulse of radio emission emitted with a regularity previously unseen from any cosmic source. This regularity nearly resulted in the signal being dismissed as man-made interference. After it was painstakingly established that the signals were in fact cosmic in origin, the new sources were denoted pulsars for PULSating stARS (Hewish et al., 1968). After several hypotheses were proposed and rejected for the origin of the periodic emission (including pulsing white dwarf stars, Black, 1969; and, briefly, an alien civilization, Bell-Burnell, 1977) they were identified as rapidly rotating neutron stars (e.g. Gold, 1968; Pacini, 1968) – confirming the theoretical prediction made 34 yr prior.

In the four decades since their serendipitous discovery, neutron stars have proven to be a fertile ground for the study of matter in extreme conditions. They are model observatories for the exploration of the physics of matter at supernuclear densities, the theory of general relativity, and the nature of super-strong magnetic fields – each of which can be studied from a unique perspective in pulsar astronomy. Pulsars have

also proven to be interesting objects in their own right. Although pulsars are much better understood today than in 1967, there remains a tantalizing array of unsolved problems in pulsar astronomy – a few of which are discussed in this thesis.

Neutron stars are born in spectacular and violent supernova explosions and thus have the same origins as the heavy elements that provide structure to the universe (Woosley & Weaver, 1986). In the stellar life cycle, neutron stars represent one of three possible end points. The least massive stars (for example, the Sun) end their lives as white dwarfs, supported from collapse by electron degeneracy pressure, while the most massive stars become black holes (e.g. van den Heuvel & Habets, 1984). Neutron stars are produced from stars with initial masses in the range of $8M_{\odot} < M < 25M_{\odot}$[1] (e.g. Carroll & Ostlie, 2007). Neutron stars are supported from total gravitational collapse by neutron degeneracy pressure. This pressure is supplied by neutrons (i.e. fermions) which are prevented from falling into a single low energy state by the Pauli exclusion principle (e.g. Sakurai, 1994).

Theoretical estimates of the mass, density, and radius of a neutron star depend on the precise "Equation Of State" (EOS) describing the relationship between the pressure supporting the star and its density (e.g. Page et al., 2006, and references therein). The EOS can be constrained with measurements of neutron star radii, masses, temperatures, and the fastest pulsar spin-periods (Pavlov et al., 2002; Hessels et al., 2006). Observationally, estimates of neutron star radii range from 9 to 16 km, though significant uncertainties remain (Rutledge et al., 2002; Güver et al., 2010a,b). For purposes of comparison and calculations, the neutron star radius is typically assumed to be $R = 10\,\mathrm{km}$. The physically allowable range for neutron star masses also depends on the precise EOS and is thus is not well determined. Theoretical estimates are roughly $1 - 3M_{\odot}$ (Lattimer & Prakash, 2004). The lower mass limit is based on the stability of the collapsing proto-neutron star (Haensel et al., 2002), while the maximum mass is estimated from causality arguments (that the speed of sound

[1]The precise mass relationship is a matter of long-standing debate and there is some evidence that progenitors with initial masses as high as $50M_{\odot}$ could produce neutron stars (e.g Muno, 2007).

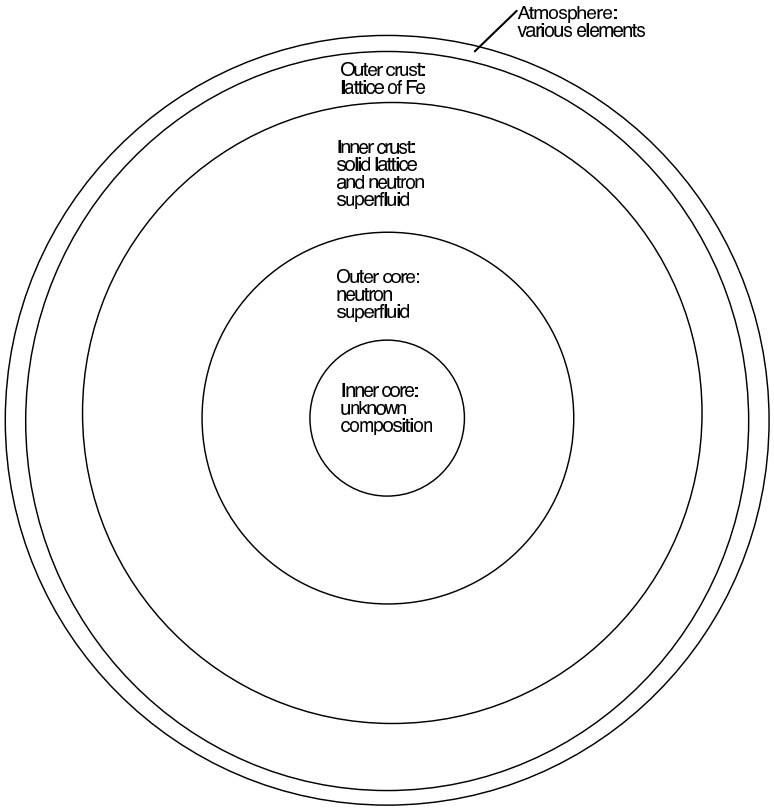

Figure 1.1: Cross section of the neutron star showing the different layers of material. Not to scale, as different equations of state predict different radii and layer thicknesses

must be less than the speed of light in dense matter, e.g. Bombaci, 1996). Estimates of neutron star masses are best constrained from observations of double-neutron star binary systems and lie in the $1.2 - 1.7 M_{\odot}$ range (Janssen et al., 2008; Kramer et al., 2006; Champion et al., 2008). The canonical neutron star mass, used in calculations, is the Chandrasekar mass of $1.4\,M_{\odot}$.

The structure of neutron stars can be separated into several distinct layers, as shown in Figure 1.1, and outlined below.

- Atmosphere:

  The atmosphere of a neutron star has a low density of $\rho \simeq 10^2\,\mathrm{g/cm^3}$ and is only a few centimetres thick (Fig. 1.1; Zavlin & Pavlov, 2002). The atmosphere has negligible mass and contribution to the EOS, but is important for thermal emission from the surface (Lattimer & Prakash, 2004). The composition is not well known, though atmosphere models with different compositions can be fitted

to observations (e.g. Ho & Heinke, 2009).

- Outer Crust:

  Approximately 0.1 – 1 km thick depending on the particular EOS, the outer crust is a solid lattice of heavy nuclei (probably in part ^{56}Fe) and a sea of degenerate electrons (very similar to the composition of white dwarfs; Page et al., 2006).

- Inner Crust:

  Approximately 0.5 – 3 km thick, the inner crust begins at the neutron drip density of $\sim 4 \times 10^{11}\,\mathrm{g/cm^3}$ – where neutrons "leak" out of nuclei because the energy required to remove a neutron from a nuclei is zero (Pethick & Ravenhall, 1991). The inner crust consists of a solid lattice and a Fermi gas of relativistic, degenerate neutrons that form a superfluid in the $^1S_0$ pairing state (Pines & Alpar, 1985). The crustal superfluid component of the inner crust rotates nearly independently from the remainder of the star, while the crustal lattice is strongly coupled to the core and outer crust (e.g. Anderson & Itoh, 1975).

- Core:

  The core comprises a large percentage of the mass of the neutron star (depending on the EOS, up to 99%), leading to densities large enough that all nuclei should be dissolved into their constituent nucleons (Lattimer & Prakash, 2004). The outer part of the core is mainly comprised of a neutron superfluid in the $^3P_2$ paired state (e.g. Lyne & Smith, 2005). The density of the inner core is several times larger than nuclear density, thus poorly understood but may consist of exotic matter such as quarks, hyperons or kaons (Lattimer & Prakash, 2004).

1.2 From Neutron Star to Pulsar

Pulsars are rapidly rotating neutron stars that emit a beam of emission that is swept through our line of sight, producing a "pulse" of light, much like a lighthouse (e.g. Gold, 1968). For this to be accomplished, a neutron star must have a relatively

rapid rotation rate and some method of producing beamed rather than isotropic emission. Pulsar spin periods are observed to slow down with time, which is an important clue for interpreting these objects. The conclusion reached soon after the 1967 discovery is that pulsars have very large magnetic fields and produce beams of emission along the magnetic axis, as shown in Figure 1.2 (Gunn & Ostriker, 1969). It then follows that pulsars spin down due to magnetic braking (see §1.3 for details). Measurements of spin-periods, P, and spin-down rates, $\dot{P}$, can be used to extract important information about pulsars, for example, estimates of the magnetic field ($B \propto \sqrt{P\dot{P}}$) and age ($\tau \propto P/\dot{P}$). The entire known pulsar population[1] is shown in Figure 1.3 in terms of P and $\dot{P}$. Lines of constant magnetic field and age are shown on the figure.

Classes of pulsars

The bulk of the pulsar population – the "island" of black dots in Figure 1.3 – have spin periods ranging from 16 ms – 8.5 s and $B \sim 10^{11} - 10^{13}$ G (Marshall et al., 2004; Manchester et al., 1996; Manchester et al., 2005). The large majority of these "normal" pulsars are seen only from their radio pulsations and are powered via the loss of rotational kinetic energy.

Fewer pulsars are seen with spin periods longer than several seconds. It is thought that the radio emission mechanism requires a significant amount of pair plasma, which cannot be produced for long spin-periods. This leads to a theoretical "death-line," as shown on the figure (Zhang et al., 2000). However, the radio-loud pulsars that are seen past this line highlight that uncertainties remain in this theory.

The bottom left hand corner of the figure shows those pulsars with the fastest rotation rates, the "millisecond pulsars," most of which are in binary systems (indicated in the figure by a circle around a point). These pulsars are thought to have different evolutionary tracks than the rest of the pulsar population: their periods are decreased during accretion from a binary companion, called "recycling." This can

[1]See ATNF pulsar database for a full list of all known pulsars. http://www.atnf.csiro.au/research/pulsar/psrcat/

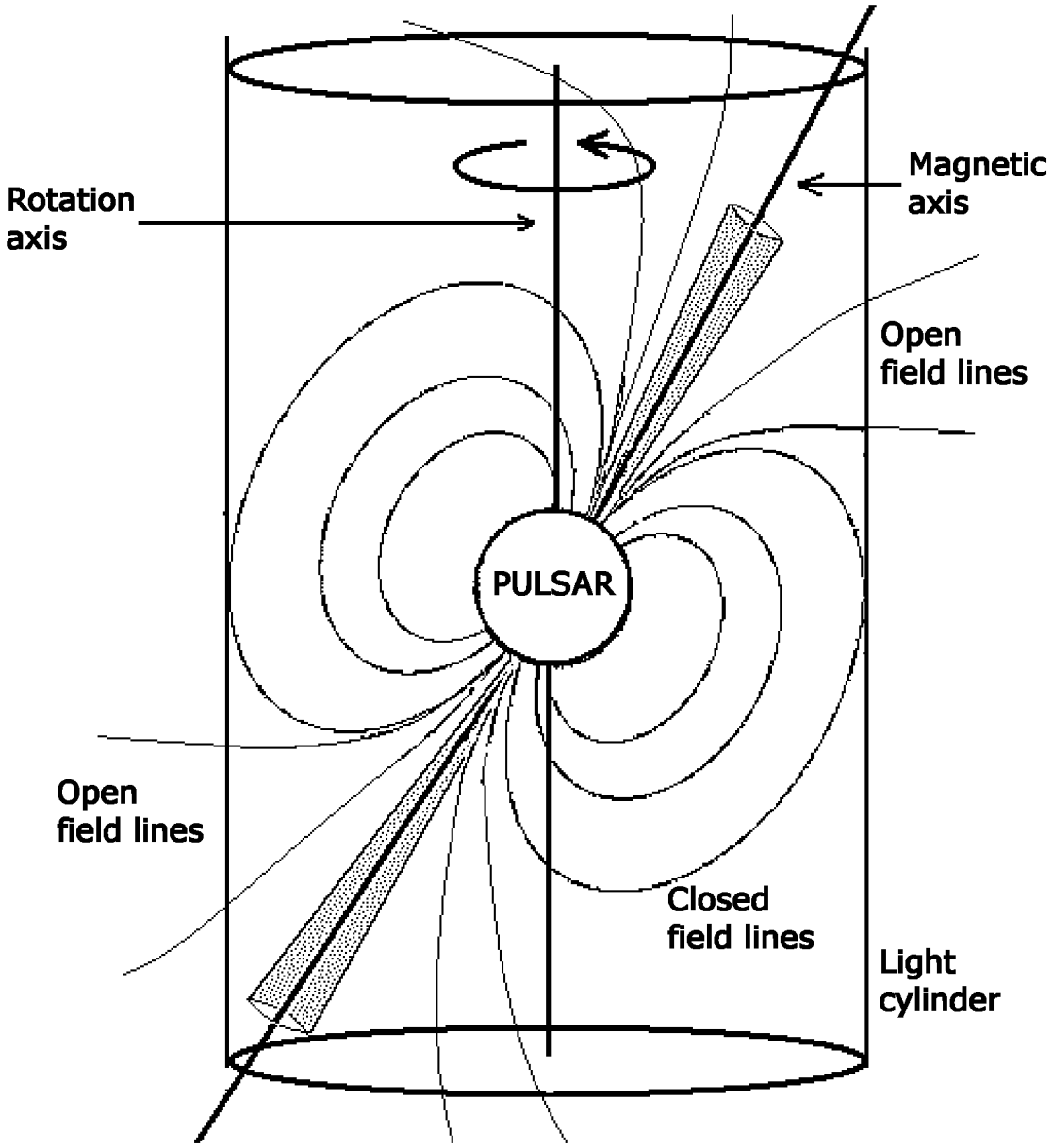

Figure 1.2: A diagram of a pulsar and its magnetosphere. The rotation axis is vertical, with the magnetic axis at an angle α to the rotation axis. The light cylinder radius, shown by the cylinder on the figure, is the largest radius at which the magnetosphere can co-rotate with the pulsar. The shaded region represents the beam of radio emission. Figure provided by Rim Dib.

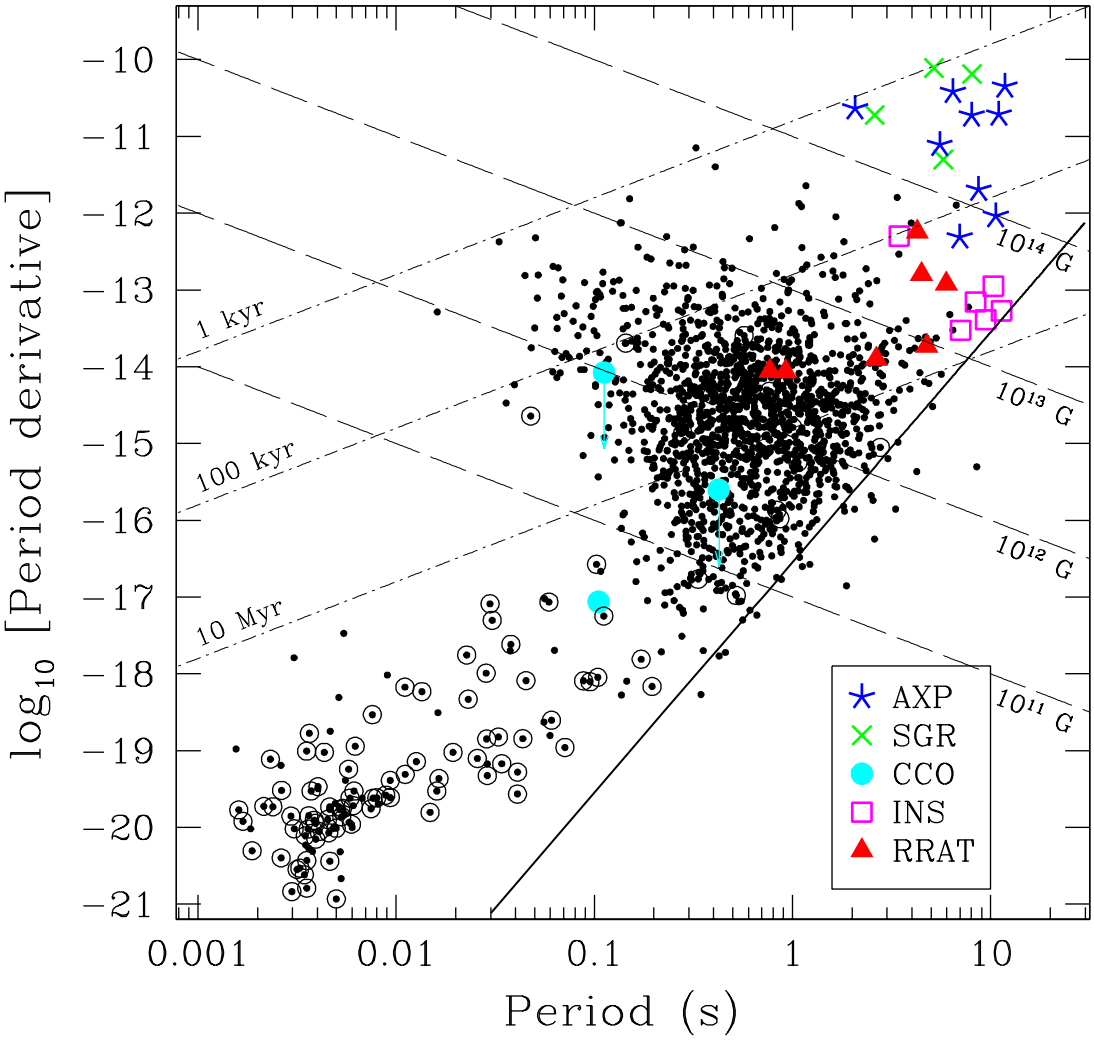

Figure 1.3: The period-period derivative diagram. Small black dots are rotation-powered pulsars (RPPs), while a circle surrounding a point indicates a binary system. Filled circles are central compact objects (CCOs). Stars are anomalous X-ray pulsars (AXPs), while crosses are soft-gamma ray repeaters (SGRs). Squares are the "Isolated Neutron Stars" (INSs), while triangles are rotating radio transients (RRATs). Lines of constant age (τ) and magnetic field (B) are shown, as is one theoretical "death-line," past which there should be no radio pulsations (Zhang et al., 2000). Figure provided by Victoria Kaspi.

produce very rapid rotation rates, the current record holder has $P = 1.39\,\mathrm{ms}$ (Hessels et al., 2006). Their B-fields are also the smallest among known pulsars, presumably "quenched" during accretion (Radhakrishnan & Srinivasan, 1982; Shibazaki et al., 1989). Despite their different evolutionary histories, these pulsars are also powered by the loss of rotational kinetic energy. As these pulsars are typically billions of years old, and this thesis discusses young neutron stars, we will not discuss this class of pulsars further.

The top right hand corner of Figure 1.3 shows pulsars with long spin periods and large B-fields - the magnetars (Anomalous X-ray Pulsars, AXPs, and Soft Gamma-ray Repeaters, SGRs, shown on the figure as stars and crosses, respectively) are believed to be powered by the decay of their extreme magnetic field instead of by rotation power. Most magnetars are radio quiet and are instead viewed primarily as pulsing X-ray sources (e.g. Kaspi, 2007).

Three further classes of pulsing neutron stars are known and appear in Figure 1.3. The "Isolated Neutron Stars" (INSs) have long spin periods, are radio-quiet and are typically millions of years old (as estimated from timing properties and/or from their surface temperatures; van Kerkwijk & Kaplan, 2008, and references therein). They are observed solely from their thermally cooling surfaces (e.g. Haberl, 2007). Similarly, the Central Compact Objects (CCOs) are radio quiet and observable from their hot surfaces. The CCOs, however, are located near the centres of supernova remnants and are therefore very young ($< 10\,\mathrm{kyr}$; Pavlov et al., 2004, see also §1.6.2).

The Rotating RAdio Transients (RRATs) are neutron stars that emit short, bright bursts of radio emission rather than a steady pulsed signal (McLaughlin et al., 2006). The properties of this recently discovered class of neutron stars are varied and the relationship between this and other classes of neutron stars is not currently well understood.

For historical reasons, pulsars powered by the loss of rotational kinetic energy were termed "radio pulsars." There are now several rotation-powered pulsars observed only as pulsed X-ray or γ-ray sources despite extensive searches for radio pulsations, thus,

we use instead the physically motivated term "Rotation-Powered Pulsars" (RPPs). This fits well with the physically motivated term "magnetar" for those neutron stars powered by the decay of ultra-large magnetic fields. For completeness, we also note a third power source for rotating neutron stars – accretion power. Pulsars powered via accretion from a surrounding disk of material onto their surfaces are bright X-ray sources and very noisy rotators, and are not discussed further here (Giaconni et al., 1971; Frank et al., 1992).

Birth properties of pulsars: spin-periods and magnetic fields

During the collapse of a massive star to a neutron star, angular momentum must be conserved. Thus, any rotation in the progenitor (e.g. ∼25 day period in the Sun; Snodgrass & Ulrich, 1990) will translate into rapid rotation in a 10 km neutron star. Birth spin periods are thought to range from $\sim 10 - 500$ ms (e.g. Faucher-Giguère & Kaspi, 2006).

In addition to rapid rotation, one of the most well-known properties of pulsars are their large magnetic fields ranging from $B \sim 10^8 - 10^{15}$ G. The simplest picture of how pulsar fields are created is that they are fossil fields; progenitor fields are amplified through magnetic flux conservation during collapse, analogous to angular momentum conservation. A magnetic field in a massive main sequence star can be ~ 100 G (Auriere et al., 2003). If such a star had a radius of $\sim 1 R_\odot$, and magnetic flux were strictly conserved, it would produce a final field strength of $B_2 = B_1(R_1/R_2)^2 = 10^{12}$ G (e.g. Lyne & Smith, 2005).

While the flux conservation picture is attractively simple, it has several problems that undermine its ability to explain the largest observed B-fields in neutron stars. In fact, owing to significant mass loss in the late stages of stellar evolution, it probably cannot even produce the standard 10^{12} G fields (Spruit, 2008). Furthermore, massive stars with large B-fields are relatively rare, while the fraction of pulsars with $B > 10^{12}$ G is comparitively large (Spruit, 2008).

A more realistic scenario is that pulsars gain their large B-fields with a dynamo (Thompson & Duncan, 1993). In short, B can be amplified via differential rotation

during the progenitor collapse, causing the field to become highly twisted and increasing its strength. Though the general picture is reasonable, many details remain uncertain. For example, the field must emerge from the neutron star on a timescale of seconds. If the field emerges too quickly, it will dissipate and result in a small dipole field. Conversely, if the field does not emerge quickly enough, it will remain trapped inside the star and will not affect the braking torque on the star (Spruit, 2008).

1.3 Pulsar Spin-Down: A Rotating Magnetic Dipole

The first theoretical model of neutron star spin-down was outlined by Pacini (1967, 1968); Gold (1968) and Gunn & Ostriker (1969) as a spinning magnetic dipole in a vacuum. In this picture, the neutron star is presented as a point particle with an ideal dipole B-field.

The energy available to an isolated pulsar is its rotational kinetic energy,

$$E = \frac{1}{2} I \Omega^2, \tag{1.1}$$

where Ω is the angular frequency[1], and I is the moment of inertia of the pulsar (e.g. Lyne & Smith, 2005). The true moment of inertia is unknown, but related to the EOS (e.g. Page et al., 2006). The common assumption is that the neutron star is a solid sphere of constant density and thus has a moment of inertia given by

$$I = \frac{2}{5} M R^2. \tag{1.2}$$

Given what is known about the interior of neutron stars (e.g. from observations of pulsar glitches, see §1.8.2), the assumption that neutron stars are solid and uniformly dense is certainly incorrect. However, as an order of magnitude estimate in the absence of a more physical and observationally verifiable model, it is considered

[1]Recall that $\Omega = 2\pi\nu = 2\pi/P$. Depending on the application, angular frequency Ω, spin frequency ν, and spin period P are used in pulsar astronomy, and this thesis. Pulsars are often identified by their spin-periods, while theorists typically use Ω for simplicity in derivations. Pulsar timing observations (see Chapter 3) are simplified by the use of ν as this is what is measured. We also define the spin-down rate as $d\nu/dt \equiv \dot{\nu} = -\dot{P}/P^2$.

sufficient (Manchester & Taylor, 1977). For the canonical values of mass and radius ($1.4M_\odot$ and 10 km, respectively see §1.1), $I = 10^{45}\,\mathrm{g\,cm^2}$.

From electrodynamics, it is known that a rotating magnetic dipole will radiate electromagnetic waves. The magnetic analog to the Larmor formula gives the energy radiated by a rotating magnetic dipole per unit time,

$$\frac{dE}{dt} = -\frac{2}{3c^3}\left(|\ddot{\overrightarrow{\mu}}|\right)^2, \tag{1.3}$$

where $\overrightarrow{\mu}$ is the magnetic moment of the dipole (e.g. Jackson, 1975). The magnetic moment of a magnetic dipole rotating with angular frequency, Ω, at an angle α to the spin axis (here taken to be the z-axis, as in Figure 1.2) is given by

$$\overrightarrow{\mu} = \mu_0[\sin\alpha\cos(\Omega t)\hat{i} + \sin\alpha\sin(\Omega t)\hat{j} + \cos\alpha\hat{k}] \tag{1.4}$$

where μ_0 is the magnitude of the magnetic moment (e.g. Jackson, 1975).

Substituting the second derivative of Equation 1.4 into Equation 1.3, we arrive at an equation for the energy radiated by a rotating magnetized neutron star:

$$\frac{dE}{dt} = -\frac{2{\mu_0}^2\sin^2\alpha}{3c^3}\Omega^4. \tag{1.5}$$

The kinetic energy lost by a pulsar is radiated away, so we can equate the time derivative of Equation 1.1 with Equation 1.5, and solve for $\dot{\Omega}$, relating the spin frequency and spin-down rate,

$$\dot{\Omega} = -\frac{2{\mu_0}^2\sin^2\alpha}{3Ic^3}\Omega^3. \tag{1.6}$$

The great strength of the above model is that although it is derived for the special case of a magnetic dipole in a vacuum, it can be generalized to encompass more complicated physical scenarios. We do so here and present the standard model of pulsar spin down. We substitute $2\pi\nu$ for Ω (as ν is what is observed) and make the assumption that α, I, and μ_0 are constant and combine them into a single constant, K. Finally, we generalize the exponent in the above equation from 3 to n, called the "braking index," to account for spin-down not entirely due to magnetic braking. We thus arrive at the familiar form of the pulsar spin-down law,

$$\dot{\nu} = -K\nu^n. \tag{1.7}$$

As both ν and $\dot{\nu}$ are observable via pulsar timing techniques (see Chapter 3), this model can be observationally tested and compared with Equation 1.6. Perhaps not surprisingly, this simple model, though powerful, does not describe a physically realizable model for pulsars, as we will discuss further in §1.5. But first, we will outline the ways in which this simple model is useful for understanding some general properties of pulsar spin evolution.

1.4 Basic Derived Pulsar Parameters

The great strength of pulsar timing is that a surprising amount of physics can be deduced from observations of the spin-frequency and its derivatives. This is rather convenient as many other factors (some of which are very difficult to observe) can be largely ignored in the study of the temporal evolution of a pulsar: the surface temperature, the pulsar wind nebula, the spectral properties, distance, mass, radius, as well as details of the emission mechanism. This section outlines the key parameters that can be derived from measurements of ν, and its derivatives.

1.4.1 Spin-down luminosity

The spin-down luminosity of a pulsar represents the power available from its rotational kinetic energy to power pulsations and a pulsar wind (e.g. Gold, 1968). The spin-down luminosity can be found by taking a single time derivative of Equation 1.1,

$$\dot{E} = -4\pi^2 I \nu \dot{\nu} \,. \tag{1.8}$$

$\dot{E}$ is a good predictor of whether a pulsar has an observable pulsar wind nebula (e.g. Gotthelf, 2003), and high energy (i.e. X-ray or γ-ray) pulsed emission (e.g. Abdo et al., 2010b).

1.4.2 The magnetic field

The magnetic moment of a point dipole is approximately

$$\mu_0 \simeq BR^3 \,, \tag{1.9}$$

as from, e.g. Meszaros (1992).

Substituting this estimate into Equation 1.6 and solving for B gives

$$B = \left(\frac{3Mc^3}{20\pi^2 R^4 \sin^2\alpha}\right)^{1/2} \left(\frac{-\dot{\nu}}{\nu^3}\right)^{1/2}, \tag{1.10}$$

which can be estimated as

$$B = 3.2 \times 10^{19}\,\mathrm{G} \left(\frac{-\dot{\nu}}{\nu^3}\right)^{1/2} \tag{1.11}$$

(Lyne & Smith, 2005).

1.4.3 The braking index

The braking index, n, is a fundamental parameter describing pulsar electrodynamics. It describes the relationship between the braking torque acting on a pulsar and its spin frequency and thus provides insight into the underlying physics dictating pulsar temporal evolution. The braking index can be calculated by taking one derivative of Equation 1.7 and rearranging to solve for n,

$$n = \frac{\ddot{\nu}\nu}{\dot{\nu}^2}\,. \tag{1.12}$$

Different values of n are representative of different torques exerted on the pulsar. A value of $n = 3$ will result from either magnetic dipole radiation (as described in §1.3) or from a charge-filled magnetosphere (see §1.5.1). Gravitational radiation or magnetic quadrupole radiation results in $n = 5$ (Ferrari & Ruffini, 1969). If all the angular momentum is removed from the system via mass loss, i.e. a "solar" wind, a value of $n = 1$ will result (Michel & Tucker, 1969).

Variations in the moment of inertia (I) or the strength or alignment of B, will also cause variations in n, as can be seen from the formulation of the spin-down law derived from the magnetic dipole in vacuo (Eq. 1.6). Since it is assumed that B and α are constant, variation in either parameter will cause changes in the spin down of a pulsar. Alignment of the magnetic field results in $n > 3$, while counteralignment gives $n < 3$, where the precise value measured depends on the timescale of change of

α and its current value (Macy, 1974; Link & Epstein, 1997). Likewise, growth of the magnitude of the magnetic field will be observed as $n < 3$, while magnetic field decay manifests as $n > 3$. Radial deformation of field lines from an outflow of plasma will result in $1 < n < 3$ (Manchester & Taylor, 1977).

A verification of the spin down model can be obtained in principle with the measurement of a third frequency derivative, $\dddot{\nu}$. An expression for $\dddot{\nu}$ can be obtained by taking an additional derivative of Equation 1.7:

$$\dddot{\nu} = \frac{n(2n-1)\dot{\nu}^3}{\nu^2}. \tag{1.13}$$

One can then define a second order analog to n, the "second" braking index, m as $m_0 \equiv n(2n-1)$. A measurement of m can then be obtained if $\dddot{\nu}$ can be measured,

$$m = \frac{\nu^2\ \dddot{\nu}}{\dot{\nu}^3}. \tag{1.14}$$

If the spin-down model is an accurate description of the spin evolution of the pulsar, then $m = m_0$. If, however, m is not equal to m_0, then a measurement of m provides clues about how the true spin-down differs from the model. This parameter has been measured only for two pulsars, the Crab pulsar and PSR B1509−58, and in both cases, m agrees with m_0 within uncertainties (Lyne et al., 1993; Livingstone et al., 2005b).

1.4.4 The characteristic age

An estimate of the age of a pulsar can be determined by integrating the spin-down model (Eq. 1.7):

$$t = -\frac{\nu}{(n-1)\dot{\nu}}\left(1 - \frac{\nu^{n-1}}{{\nu_i}^{n-1}}\right), \tag{1.15}$$

where ν_i is the spin-frequency of the pulsar at birth, and the relation is only valid if $n \neq 1$. If the pulsar was born spinning much faster than at present, i.e. $\nu_i \gg \nu$, and $n = 3$ for the lifetime of the pulsar, then the above equation is simplified to the "characteristic age,"

$$\tau_c = -\frac{1}{2}\frac{\nu}{\dot{\nu}}. \tag{1.16}$$

For pulsars where n is known, another estimate of the age is

$$\tau = -\frac{1}{n-1}\frac{\nu}{\dot{\nu}}. \tag{1.17}$$

If the true age of the pulsar is known from supernova expansion measurements or an historical supernova association, Equation 1.15 can be used to estimate the birth spin frequency of the pulsar, ν_i. For example, the Crab pulsar is known to have been born in the historical supernova event of 1054 CE, so its birth period can be estimated as $P_0 \sim$19 ms (e.g. Manchester & Taylor, 1977).

The quality of τ_c as an estimator of the true age varies from case to case, and is known to be inaccurate in some cases. The young pulsar PSR J1811−1925 is located at the centre of the supernova remnant G11.2−0.3 (Torii et al., 1997). The remnant has an estimated age from expansion measurements of $960 - 3400$ yr (Tam & Roberts, 2003) and is believed to be the remnant of the historical supernova that occurred in 386 CE, making the system only 1624 yr-old. The pulsar, however, has $\tau_c \simeq 24,000$ yr – a factor of ∼15 larger than its true age. The discrepancy can most easily be understood if the pulsar was born spinning relatively slowly, at $P \simeq 62$ ms, that is, close to its present value of ~ 65 ms (Kaspi et al., 2001b). This would then render the assumption that $\nu_i \gg \nu$ incorrect. Another possible explanation is that the pulsar was born spinning rapidly, but experienced an unusual evolution, with a large braking index of ~ 29, a scenario that is difficult to imagine physically.

1.5 The Pulsar Magnetosphere

The pulsar magnetosphere is a plasma-filled region extending from the star surface to the last closed field line, as shown in Figure 1.2. The limit between open and closed field lines is determined by the light cylinder radius, defined as the radius where the magnetosphere would be travelling faster than the speed of light if it co-rotated with the star,

$$R_{LC} = \frac{c}{2\pi\nu} \tag{1.18}$$

shown in Figure 1.2 (Lyne & Smith, 2005).

The pulsar magnetosphere is the source of pulsed radio, optical, X-ray, and γ-ray emission from pulsars (with the exception of thermal X-ray pulsations from the surface of a neutron star, see §1.5.3). As it turns out, the magnetosphere also plays a key role in the spin-down of pulsars, though this is not yet thoroughly quantified (e.g. Spitkovsky, 2006) and magnetospheric fluctuations may also be the physical origin of stochastic variations in the rotation rates of pulsars (see §1.8.1; Cheng, 1987; Kramer et al., 2006; Lyne et al., 2010).

1.5.1 The Goldreich-Julian model

Although the vacuum dipole model of pulsars presented in §1.3 is widely used and has been crucial to our understanding of the temporal evolution of pulsars, it has long been known that the most basic assumption of the model – that the pulsar rotates in a vacuum – cannot be true. Instead, the pulsar exists inside the plasma-filled magnetosphere. This was first shown in the famous 1969 paper of Goldreich & Julian for the special case of an aligned rotator (i.e. $\alpha = 0$) .

The large magnetic field of a pulsar induces a vacuum electric field:

$$\overrightarrow{E}_{induced} = \frac{(\overrightarrow{\Omega} \times \overrightarrow{r})}{c} \times \overrightarrow{B}, \tag{1.19}$$

where the component parallel to the magnetic field at the neutron star surface, $E_{||}$, is

$$E_{||} = \frac{\Omega R}{c} B \tag{1.20}$$

(Lorimer & Kramer, 2005). To balance this field, a charge will accumulate on the surface of the neutron star, which is unstable given the force applied by $E_{||}$ (Lyne & Smith, 2005). The force on a point charge at the surface due to the induced electric field is

$$F_e = \frac{e\Omega RB}{c}. \tag{1.21}$$

The electric force is factor of $\sim 10^{10} - 10^{12}$ larger than the gravitational force securing a point particle to the surface, $F_g = GMm/r^2$ (Lyne & Smith, 2005). Thus, charged

particles will be pulled from the surface and travel along magnetic field lines (Lorimer & Kramer, 2005).

Goldreich and Julian further calculated a critical density of charged particles, the "Goldreich-Julian density",

$$\rho_{GJ} = \frac{\nu \cdot B}{c} \tag{1.22}$$

If this charge density is reached everywhere in the magnetosphere, the charge distribution will produce an $\overrightarrow{E}$ that balances the induced $E_{||}$. In the limit of small plasma inertia and temperature, the force-free condition is satisfied outside the star (Spitkovsky, 2008)

$$\overrightarrow{E} + \frac{1}{c}(\overrightarrow{\Omega} \times \overrightarrow{r}) \times \overrightarrow{B} = 0. \tag{1.23}$$

Once this condition is obtained, the plasma feels no force parallel to the magnetic field, thus, the charges will corotate with the star, out to a maximum radius of the light cylinder radius, R_{LC} (Eq. 1.18; Lorimer & Kramer, 2005).

The existence of the magnetosphere has important implications for the spin-down of pulsars. At the light cylinder, magnetic field lines cannot corotate with the star (by definition), thus the field is swept back azimuthally. Open field lines are bent back and wrap around the star, such that the poloidal field becomes a toroidal field. This produces a torque on the star, resulting in spin down even for an aligned rotator (Goldreich & Julian, 1969). Making the approximation that the field lines are dipolar within the light cylinder, the torque is

$$N = I\dot{\nu} = -\frac{k\pi^3}{c^3}(BR^3)^2\nu^3, \tag{1.24}$$

where k is a constant of order unity depending on the exact field structure (Manchester & Taylor, 1977). Note that $\dot{\nu} \propto \nu^3$ as in the vacuum dipolar case, so once again $n = 3$ (Manchester & Taylor, 1977).

Several issues are known to exist with the Goldreich-Julian model of the magnetosphere. First, it only applies in the special case of an aligned rotator, which would not result in a pulsing source. Further, it is not a self-consistent description of currents within the magnetosphere. The problem is that the model requires the

flow of positive charge through regions of negative charge, and vice versa (Lorimer & Kramer, 2005). In addition, from the point of view of high energy pulsar emission, particles must be accelerated to extremely high energies, a situation only possible if $\rho >> \rho_{\rm GJ}$. Physical situations leading to areas within the magnetosphere with the possibility of such large plasma densities will be discussed in more detail in §1.5.3.

1.5.2 Recent models of pulsar electrodynamics

After many different approaches to solving the problems associated with the Goldreich-Julian magnetosphere were unsuccessful (e.g. Mestel et al., 1999, and references therein), it was eventually realized that the structure of the pulsar magnetosphere could not be solved in closed analytic form (Spitkovsky, 2004).

Recently, encouraging progress has been made with 3-dimensional simulations of the pulsar magnetosphere using the force-free approximation (Eq. 1.23; Contopoulos et al., 1999; Spitkovsky, 2004; Contopoulos & Spitkovsky, 2006; Contopoulos, 2005; Timokhin, 2006). Spitkovsky (2006) uses these methods to produce a modified estimate of the magnetic field,

$$B_0 = 2.6 \times 10^{19} \left(\frac{P\dot{P}}{1 + \sin^2\alpha} \right)^{1/2} \text{G}. \tag{1.25}$$

This is reassuringly close to Equation 1.11, and if the assumption of $\alpha = 90^\circ$ is made for both models, then $B_0 \simeq 0.87B$ (Spitkovsky, 2006). As work continues, these models are beginning to produce predictions for energy dependent pulse profiles (e.g. Bai & Spitkovsky, 2010) and braking indices (e.g. Spitkovsky, 2008).

1.5.3 Emission mechanisms

The pulsar magnetosphere is the source of the bulk of pulsar emission, both pulsed non-thermal emission and relativistic particles observed as pulsar wind nebulae. Some pulsars exhibit a mix of thermal emission from the surface and (non-thermal) magnetospheric emission components in their X-ray spectra (Kaspi et al., 2006).

It is interesting to note that pulsed radio emission, which has been so important historically and in the ongoing study of pulsar behaviour is energetically unimportant

for pulsar evolution, making up a mere $\sim 10^{-7} - 10^{-5}$ of the total energy budget of the pulsar (e.g Ghosh, 2007). By contrast, emission in the X-ray band makes up a much more significant portion of the energy budget, up to $\sim 1\%$ (Roberts et al., 2004), while pulsed gamma-ray emission can account for up to $\sim 10\%$ of the energy budget of a pulsar (Camilo et al., 2009b).

Of the nearly 2000 pulsars known (see the ATNF pulsar catalog[1] and references therein; Manchester et al., 2005), approximately 70 emit X-rays (Kaspi et al., 2006). Of these, most are seen as thermally cooling X-ray sources (e.g. Becker & Aschenbach, 2002), while ~ 30 have pulsed magnetospheric X-ray emission (Gotthelf & Halpern, 2008, 2009b; Halpern & Gotthelf, 2010b; Kaspi et al., 2006, and references therein). A further ~ 50 pulsars have been detected as gamma-ray pulsars, several of which have either no detected radio pulsations, no X-ray pulsations, or neither (Abdo et al., 2010b).

Magnetospheric emission

Detailed knowledge of the pulsar emission mechanism is one of the outstanding problems in pulsar physics. A successful model of pulsar emission must produce pulse profiles and spectra that are reasonably similar to those observed.

High-energy pulsar emission is believed to originate in vacuum "gaps" in the magnetosphere, where the force-free condition breaks down, and the induced electric field remains (Eq. 1.20; Lorimer & Kramer, 2005). This strong electric field in the vacuum region act to accelerate particles to high energy resulting in particle multiplication and emission via one of several mechanisms described below. The radio emission mechanism is very poorly understood. In general, radio pulsations are thought to arise from the inner magnetosphere, near the magnetic poles of the star. Radio emission appears to halt when the spin-period reaches a few seconds, presumably because insufficient plasma is produced. This can be translated into a death-line (shown in Figure 1.3; Zhang et al., 2000) though several pulsars have been found beyond this prediction,

[1] http://www.atnf.csiro.au/research/pulsar/psrcat

for example, the RPP J2144−3933 which has a period of 8.5 s (Manchester et al., 1996). Pulse profiles are generally narrower in phase for longer spin periods, implying a relationship between the beaming fraction and the period (Tauris & Manchester, 1998).

High-energy emission models fall into two broad categories: polar cap models and outer gap models, each named for the location of the emission region and summarized below.

The polar cap model posits an acceleration gap directly above the magnetic pole of the neutron star (Ruderman & Sutherland, 1975; Daugherty & Harding, 1982). The polar cap region is defined as the area inside the last open field line on the surface. Electrons flow freely from the surface to populate the magnetosphere (Daugherty & Harding, 1996) and a vacuum gap will form in the polar region because of the curvature of the magnetic field and inertial frame dragging (Harding et al., 2002a). Particles are accelerated in the gap and emit Inverse Compton radiation, inducing either curvature radiation or pair cascades (Zhang & Harding, 2000). Polar cap models produce spectra with a super-exponential break at high-energies and a break energy that is inversely proportional to B (Baring, 2004). The produced high-energy beam is somewhat larger than the radio beam, leading to restrictions on the allowable inclination angle α that can produce the observed double-peaked γ-ray profiles (Abdo et al., 2009f).

The polar cap model has received a recent challenge owing to the nearly 50 γ-ray pulsars discovered with the *Fermi* Gamma-Ray Telescope (Abdo et al., 2010b). Most high energy spectra have an exponential rather than super-exponential break (e.g. Abdo et al., 2009f, 2010a). In addition, current results suggest that there is not a strong correlation between B and the break energy (Abdo et al., 2008), in contradiction to the polar cap model prediction (Harding, 2009).

The outer gap model posits particle acceleration in vacuum gaps that form in the outer magnetosphere between the open and closed field lines, as shown in Figure 1.2 (Cheng et al., 1986a). Emission occurs along the last open field line above the null

charge surface (where the charge changes sign; Cheng et al., 1986a). A gap forms in this location because charges escape along field lines beyond the light cylinder. When charges escape above the null charge surface, they cannot be replenished (Romani, 1996). The high-energy spectrum is a combination of synchrotron and curvature radiation from pairs flowing into and out of the gap, as well as Inverse Compton scattering of synchrotron photons by pairs.

The spectra produced by this model have exponential cutoffs at high energies as observed in most γ-ray pulsars (rather than super-exponential cutoffs as predicted for the polar cap model; Cheng et al., 2000). Profiles predicted from the outer gap model produce a wide fan beam of emission leading to narrow two-peaked profiles for a wide range of inclination angles (Cheng et al., 2000). However, problems arise in reproducing leading and trailing emission, like that observed in the Vela pulse profiles at high energies (Abdo et al., 2009f). The outer gap model predicts many more radio-quiet, high-energy-loud pulsars than the polar cap model because the high-energy beam is typically much larger than the radio beam. The large beam leads to a wide range of visible inclination angles (Romani & Yadigaroglu, 1995).

Information recently gleaned from new γ-ray pulsars points to high energy emission from the outer magnetosphere. The significant number of radio-quiet pulsars recently discovered, the correlation between the break energy and the magnetic field strength at the light cylinder and two-peaked profiles delayed from a radio pulse, are all predictions from the outer gap model recently confirmed by *Fermi* observations (Abdo et al., 2010b).

Thermal emission

Many neutron stars observed as X-ray sources have no detected magnetospheric emission, and are instead observed from their cooling surfaces (Kaspi et al., 2006, and references therein). The surfaces of neutron stars are hot from their formation in supernovae explosions and the processes by which they cool is an active field of research (e.g. Page et al., 2006, and references therein). Observations of the surface temperature and estimates of the neutron star age are compared with theories of

cooling mechanisms and atmospheric models (Pavlov et al., 2002).

1.6 Young Neutron Stars

Young neutron stars offer several perspectives on neutron star science not available from the bulk of the pulsar population. Studying young neutron stars allows for a connection to be made between the compact object and its progenitor via its supernova remnant, and the number of associations has implications for birthrate statistics (Manchester, 2004). Young neutron stars often emit high-energy radiation and their study can be illuminating for both radio and high-energy emission mechanisms (Abdo et al., 2010a). Moreover, young pulsars are the only ones that allow a detailed study of the spin-down of pulsars with the measurement of braking indices (e.g. Lyne et al., 1993).

In a discussion of the billion-year old recycled millisecond pulsars, a typical million-year old pulsar can be considered young. In the context of this discussion, however, we will consider pulsars with ages $< 100\,\mathrm{kyr}$ to be young, and most of our discussion focuses on those with ages less than $\sim 10\,\mathrm{kyr}$.

Neutron stars are born in violent supernova explosions and typically reside inside their remnants for tens of thousands of years, until their remnants have faded from view, or a large kick velocity imparted at birth allows the pulsar to escape its remnant (Frail et al., 1994). Because of the excellent astronomical records kept by several ancient cultures (notably, Chinese astronomers) a few supernova remnants – and their compact objects – have been identified with historical supernovae events. The most famous example is the Crab pulsar and nebula, whose birth was observed as a bright supernova event in 1054 CE (see Clark & Stephenson, 1977, for a detailed account of records of the event).

Many young neutron stars are associated with supernova remnants, but beyond this connecting factor, there is an impressively wide variety of observed properties in the three identified classes of young neutron stars. The three identified classes are: energetic rotation-powered pulsars, central compact objects, and magnetars, each

described in the following sections. The diversity of observed behaviour should be explainable via different birth conditions, however, these are currently poorly understood. Table 1.1 presents some key parameters for all neutron stars with detected pulsations that have either τ_c or estimated supernova remnant ages ($T_{\rm SNR}$) less than $\sim 12\,$kyr (arranged by increasing τ_c).

1.6.1 Energetic rotation-powered pulsars

Young rotation-powered pulsars typically have $\dot{E} > 10^{36}\,{\rm erg\,s^{-1}}$ and power Pulsar Wind Nebulae (PWN). PWN are bright, centrally condensed, diffuse nebulae with broadband non-thermal spectra (Chevalier, 1998). PWN often have complex structures including toroidal arcs, axial jets, and wisps, on arcsecond scales (e.g. Hester et al., 2002).

These pulsars are thought to be the progenitors of the bulk of the pulsar population (e.g. the island of Fig. 1.3). Many of these pulsars and their nebulae are observed across the electromagnetic spectrum (e.g. Kaspi et al., 2006). Like older pulsars, most young pulsars are observed from their radio pulsations. However, many young pulsars are also visible in the X-ray and γ-ray energy bands (e.g. Becker & Aschenbach, 2002; Abdo et al., 2010b). Less typical are optical pulsations, visible in only a few cases (e.g. Nather et al., 1969; Manchester & Peterson, 1989; Mignani, 2009, for a review). The youngest RPPs tend not to have detectable thermal emission, despite their presumably hot surface temperatures. This is likely due to contamination from their luminous magnetospheric X-ray emission, though for PSR J0205+6449 ($\tau_c \sim 5\,$kyr), a strict upper limit on thermal emission from the surface has been set (Slane et al., 2002).

From the perspective of pulsar timing, young RPPs offer several opportunities to explore the physics underlying much of pulsar behaviour. Young pulsars are spinning down rapidly (i.e. they have large values of $\dot{\nu}$) and present the most promising avenue for the measurement of braking indices on human timescales, as well as higher order frequency derivatives that can, in principle, distinguish models of pulsar spin down (Livingstone et al., 2005b). Young pulsars are also observed to experience

Table 1.1: Neutron stars with age estimates less than 12 kyr

Name	$\boldsymbol{P}$	$\boldsymbol{\tau_c/T_{SNR}}$	$\boldsymbol{B}$	$\boldsymbol{\dot{E}}$	**Type**[a]	**Glitch**[b]	**Ref**
			$\boldsymbol{(10^{12})}$	$\boldsymbol{(10^{36})}$			
	(s)	**(kyr)**	**(G)**	$\boldsymbol{(erg\,s^{-1})}$			
SGR 1806−20	7.56	0.218/–	2060	0.05	MGT,RQ	?	1
J1846−0258	0.326	0.728/1	48.6	8.1	RPP,RQ	Y	2
SGR 1900+14	5.17	1.05/–	642	0.022	MGT,RQ	?	3
B0531+21	0.033	1.24/0.9	3.78	4600	RPP	Y	4
1E 1547−5408	2.07	1.41/–	222	0.10	MGT,RL	?	5
B1509−58	0.151	1.55/2	15.4	18	RPP	N	6
J1119−6127	0.408	1.61/–	41	2.3	RPP	Y	7
B0540−69	0.051	1.67/0.8	4.98	150	RPP	Y	8
SGR 0526−66	8.047	1.96/–	732	0.0049	MGT,RQ	N	9
1E 1048−5937	6.45	2.68/–	502	0.0056	MGT,RQ	Y	10
J1124−5916	0.135	2.87/1.7	10.2	12	RPP	N	11
J1930+1852	0.137	2.89/–	10.3	12	RPP	N	12
1E 1841−045	11.8	4.18/1	734	0.0011	MGT,RQ	Y	13
J1813−1749	0.045	4.6/0.3-3	2.65	68	RPP,RQ	N	14
J1833−1034	0.062	4.85/1	3.58	34	RPP	N	15
J0537−6910	0.016	4.93/5	0.925	490	RPP	Y	16
J1747−2809	0.052	5.31/1-7	2.88	43	RPP	N	17
J0205+6449	0.066	5.37/0.8[c]	3.61	27	RPP	Y	18
J0100−7211	8.02	6.76/–	393	0.0014	MGT,RQ	N	19
J1357−6429	0.166	7.31/–	7.83	3.1	RPP	Y	20
B1610−50	0.232	7.42/5	10.8	1.6	RPP	Y	21
J1734−3333	1.169	8.13/–	52.2	0.056	RPP	N	22
J1617−5055	0.069	8.13/–	3.1	16	RPP	Y	23
J1708−4009	11.0	9.01/–	467	0.00057	MGT,RQ	Y	24
J1418−6058	0.111	10.3/ –	4.38	5.0	RPP,RQ	N	25

Table 1.1 continued

Name	P (s)	τ_c/T_{SNR} (kyr)	B (10^{12}) (G)	$\dot{E}$ (10^{36}) (erg s^{-1})	**Type**[a]	**Glitch**[b]	**Ref**
J2229+6114	0.052	10.5/–	2.03	22	RPP	N	26
J1301−6305	0.185	11.0/–	7.1	1.7	RPP	N	27
J1810−197	5.54	11.3/–	210	0.0018	MGT,RL	N	28
B0833−45	0.089	11.3/18	3.38	6.9	RPP	Y	29
J1811−1925	0.065	23.3/1.6	1.71	6.4	RPP,RQ	N	30
B1853+01	0.267	20.3/10	7.55	0.43	RPP	N	31
J0822−4430	0.112	>220/3.7	<0.98	<0.23	CCO,RQ	N	32
1E 1207−52	0.424	>24000/7	<0.35	<0.00015	CCO,RQ	N	33
J1852+0400	0.105	192000/6	0.031	0.0053	CCO,RQ	N	34

[a] - Type of neutron star: RPP - rotation-powered pulsar, MGT=magnetar, CCO=central compact object, RQ = radio quiet, RL=radio loud, only noted for magnetars where the majority of the class is radio quiet.

[b] - Glitches detected in a pulsar (Yes/No/?) ? - Candidates glitches have not been confirmed

[c] This SNR age is from an association with the historical supernova of 1181, which has come under serious scrutiny in recent years.

References: 1. Kouveliotou et al. (1998); Mereghetti et al. (2005) 2. Gotthelf et al. (2000); Livingstone et al. (2006); Blanton & Helfand (1996) 3. Kouveliotou et al. (1999); Woods et al. (2002) 4. Staelin & Reifenstein (1968); Lyne et al. (1993) 5. Camilo et al. (2007b) 6. Seward & Harnden Jr. (1982); Kaspi et al. (1994); Gaensler et al. (2002) 7. Manchester et al. (2001) 8. Seward et al. (1984); Kirshner et al. (1989); Livingstone et al. (2005a) 9. Cline et al. (1980); Kulkarni et al. (2003) 10. Seward et al. (1986); Kaspi et al. (2001a) 11. Camilo et al. (2002b) 12. Camilo et al. (2002a) 13. Vasisht & Gotthelf (1997); Kuiper et al. (2006); Tian & Leahy (2008) 14. Gotthelf & Halpern (2009b); Brogan et al. (2005) 15. Gupta et al. (2005); Camilo et al. (2006b); Bietenholz & Bartel (2008) 16. Marshall et al. (1998); Marshall et al. (2004) 17. Camilo et al. (2009a); Helfand & Becker (1987) 18. Murray et al. (2002); Camilo et al. (2002c) 19. Lamb et al. (2002); McGarry et al. (2005) 20. Lorimer et al. (2006) 21. Johnston et al. (1992); Wang et al. (2000) 22. Morris et al. (2002) 23. Kaspi et al. (1998) 24. Sugizaki et al. (1997); Kuiper et al. (2006) 25. Abdo et al. (2009a) 26. Halpern et al. (2001) 27. Manchester et al. (2001) 28. Ibrahim et al. (2004); Camilo et al. (2007a) 29. Large et al. (1968); Dodson et al. (2002) 30. Torii et al. (1997, 1999) 31. Wolszczan et al. (1991) 32. Gotthelf & Halpern (2008); Winkler et al. (1988) 33. Gotthelf & Halpern (2007); Roger et al. (1988) 34. Halpern & Gotthelf (2010a); Sun et al. (2004)

glitches – sudden increases in spin frequency, which provide a window into neutron star interiors (see §1.8.2 and Lyne et al., 1995), and they also often have a stochastic torque component, observed as a long-term wandering of the pulse phase, deemed "timing noise" (see §1.8.1). An unfortunate result of glitches and timing noise is that an accurate measurement of n can be impossible, even in pulsars spinning down very rapidly (e.g. Ransom et al., 2004). Thus a careful analysis of timing data for young pulsars is necessary in order to best separate the secular and stochastic components of its rotational evolution.

1.6.2 Central compact objects

Central Compact Objects, or CCOs, are hot, X-ray point sources located very near the centre of supernova remnants (e.g. de Luca, 2008). There are 6 – 8 members of the class, all of which have remnant ages less than $\sim 10\,\mathrm{kyr}$ (Pavlov et al., 2004). They are bright thermal X-ray sources and lack optical counterparts, as expected from compact objects (Pavlov et al., 2004). No radio pulsations have been been detected from any of the CCOs, nor do they power visible pulsar wind nebulae. That is, there is no evidence for any magnetospheric emission from these objects (de Luca, 2008). The most likely conclusion from their locations in remnants and their spectra is that they are young neutron stars (e.g. Pavlov et al., 2004).

The best known example of the class is the bright compact object at the centre of the very young ($\sim 330\,\mathrm{yr}$) supernova remnant Casseopeia A (e.g. Chakrabarty et al., 2001). Extensive searches for pulsations in both radio (McLaughlin et al., 2001) and X-ray energy bands have found no significant pulsations (Halpern & Gotthelf, 2010a, and references therein). It was recently suggested that this neutron star has a carbon atmosphere emitting isotropically, explaining the lack of pulsations (Ho & Heinke, 2009).

Thermal X-ray pulsations have been detected from three CCOs, the objects at the centre of the SNRs PKS 1209−51/52 (1E 1207.4−5209, P=424 ms, Zavlin et al., 2000; Pavlov et al., 2002; Gotthelf & Halpern, 2007), Kes 79 (PSR J1852+0040, P=105 ms; Halpern et al., 2007; Gotthelf et al., 2005; Halpern & Gotthelf, 2010a), and Puppis

A (RX J0822−44300, $P = 112\,\mathrm{ms}$; Gotthelf & Halpern, 2009a). Unlike other young neutron stars, these CCOs are spinning down very slowly. PSR J1852+0040 has a measured spin-down rate of $\dot{\nu} = -7.87 \times 10^{-16}\,\mathrm{s}^{-2}$ (Halpern & Gotthelf, 2010a; the other two currently only have upper limits on $\dot{\nu}$; Gotthelf & Halpern, 2007, 2009a). This small spin-down rate implies a very small magnetic field of $B = 3.1 \times 10^{10}\,\mathrm{G}$ (with potential implications for the intrinsic magnetic field distribution of neutron stars), and small $\dot{E}$ (explaining the lack of detected PWN or any other magnetospheric emission in these sources). The combination of relatively long ν and small $\dot{\nu}$ also implies that τ_c is many orders of magnitude larger than their SNR ages. For PSR J1852+0040, $\tau_c = 192\,\mathrm{Myr}$, while the SNR age is only 5.4 – 7.5 kyr (Sun et al., 2004). The easiest explanation for this discrepancy is that the pulsars were born spinning very close to their current spin frequencies and have not spun down significantly.

The mystery of why these three pulsars are radio-quiet is a matter of current debate (e.g. de Luca, 2008; Halpern & Gotthelf, 2010a, and references therein). None of the sources are past the empirical or theoretical "death-line" for radio emission (Zhang et al., 2000). One possibility is that their radio pulsations are not beamed towards Earth, though it would be unusual for all of the 6 known CCOs to be beamed away from Earth. Another possibility is that they are experiencing low-level accretion e.g., from a fallback disk formed during the supernova explosion, interrupting the radio emission mechanism (Gotthelf & Halpern, 2009a). However, the size of the magnetic field in the Kes 79 source, though small, is still of sufficient magnitude that such low-level accretion should be prevented (Halpern & Gotthelf, 2010a). Additionally, if the radio emission mechanism were currently being quieted by material in the magnetosphere, radio emission should become visible when accretion eventually stops. This implies that many radio-loud pulsars with similarly small B-field strengths should appear in Figure 1.3. In fact, few low B-field pulsars have been discovered, and those that are known are thought to be unrelated to CCOs: these are "recycled" during longer periods of significant accretion from binary companions (e.g. Radhakrishnan

& Srinivasan, 1982).

A connection has been postulated between the long birth spin periods and the low magnetic fields in the CCOs. The dynamo mechanism that can create large pulsar magnetic fields (as in the magnetars, §1.6.3) requires very rapid rotation to create large B-fields. Thus slow birth spin periods for the CCOs may be a natural explanation for their small fields (Thompson & Duncan, 1993; Halpern & Gotthelf, 2010a).

Another unique feature in the pulsed CCO 1E 1207−5209 is absorption lines at ~ 0.7 and 1.4 keV (Sanwal et al., 2002), and perhaps also at 2.1 and 2.8 keV (De Luca et al., 2004). One interpretation of these spectral features is that they are electron cyclotron lines, implying $B = 8 \times 10^{10}$ G (smaller than the current upper limit; Sanwal et al., 2002). An alternative explanation is that the absorption features represent atomic transition in the neutron star atmosphere. Mori & Hailey (2006) propose that an oxygen or neon atmosphere is the only self-consistent model that can described the lines. A definitive measurement of the dipole field via timing measurements could offer significant insight into the physics of this pulsar.

1.6.3 Magnetars

Magnetars are rotating neutron stars whose emission is derived from the decay of ultra-strong magnetic fields rather than rotation power. Magnetars have estimated dipole magnetic fields in the range of $B \simeq 6 \times 10^{13} - 10^{15}$ G[1] several orders of magnitude larger than the average RPP field of $B \sim 10^{12}$ G, and larger than the so-called quantum-critical limit, where the cyclotron energy is equal to the electron rest-mass energy (Daugherty & Harding, 1982),

$$B_{QED} = \frac{2\pi m^2{}_e c^3}{eh} \sim 4.4 \times 10^{13}\,\mathrm{G}\,. \tag{1.26}$$

Magnetars exhibit a wide range of radiative and timing behaviour not seen in RPPs, interpreted to arise as a direct result of their super-critical magnetic fields: bursts of

[1] A recently discovered magnetar has an upper limit on the magnetic field strength of $B < 3 \times 10^{13}$ G (Esposito et al., 2010).

X-rays and soft γ-rays (e.g. Gavriil et al., 2002), long-term flux variability (e.g. Dib et al., 2009), large flares (e.g. Mazets et al., 1979), and large pulse profile variations (e.g. Mazets et al., 1999). Compared to RPPs, magnetar spin-periods are long, falling in the range of $\sim$2 – 12 s. The two known varieties of magnetars, Soft Gamma-ray Repeaters (SGRs; Mazets et al., 1979) and Anomalous X-ray Pulsars (AXPs; Fahlman & Gregory, 1981) have only been definitively linked in the last decade (e.g. Gavriil et al., 2002). The SGRs were identified (and named) by repetitive bursts of soft γ-rays (Mazets et al., 1979). By contrast, the AXPs, were identified from their persistent pulsed X-ray emission (Fahlman & Gregory, 1981). The AXPs were classified as "anomalous" because their X-ray luminosities, L_X, are larger than their spin-down luminosities, $\dot{E}$, meaning that rotation cannot power their persistent emission. This lead to the hypothesis – now disproven – that AXPs were powered by accretion either from a binary companion (Fahlman & Gregory, 1981) or a supernova fallback disk (e.g. Alpar, 2001).

Soft γ-ray repeaters

SGRs are typified by repetitive emission of bright bursts of low-energy gamma-rays, typically lasting ~ 0.1 s with peak luminosities of $\sim 10^{41}\,\mathrm{erg\,s^{-1}}$. SGR bursts are often clustered in active phases, though the bursts are randomly distributed within an active phase, as are the active phases themselves (Woods & Thompson, 2006). Some SGRs have persistent X-ray pulsations (e.g. Rothschild et al., 1994; Sonobe et al., 1994) and Kouveliotou et al. (1998) measured both P and $\dot{P}$ for the SGR 1806−20 allowing for an estimate of $B \simeq 10^{15}\,\mathrm{G}$ (from Eq. 1.11).

In addition to bursts, SGRs occasionally show extremely bright flares of gamma-rays whose luminosities can reach $10^6\,L_{\mathrm{Edd}}$ for a $1.4\,M_\odot$ neutron star. Only three such events have been observed (SGR 0526−66: Mazets et al., 1979; SGR 1900+14: Hurley et al., 1999a, Feroci et al., 1999, Mazets et al., 1999a, Feroci et al., 2001; SGR 1806−20: Hurley et al., 2005, Mereghetti et al., 2005a, Palmer et al., 2005). No object has shown a second large event, implying an event rate per object of less

than one per 15 – 55 years (Woods & Thompson, 2006). The second observed SGR flare occurred in the object SGR 1900+14 on August 27, 1998 (Hurley et al., 1999). The event began with a bright spike of emission for $\sim 0.35\,\mathrm{s}$ with a peak luminosity greater than $3 \times 10^{44}\,\mathrm{erg\,s^{-1}}$. The flare persisted for 400 s following the initial spike, and the emission was observed to be modulated at the pulse period of 5.16 s (Hurley et al., 1999). Pulse profile changes were observed throughout the event (Göğüş et al., 2002) and significant timing variations occurred around the time of the giant flare (Woods et al., 1999).

Anomalous X-ray pulsars

AXPs are observed to spin down similarly to RPPs (e.g. Koyama et al., 1987). Their quiescent X-ray luminosities lie in the range of $10^{35-36}\,\mathrm{erg\,s^{-1}}$, significantly larger than their spin-down luminosities of $\sim 10^{33}\,\mathrm{erg\,s^{-1}}$. AXPs have soft X-ray spectra, typically well described with a blackbody and steep power-law component, however, a hard component above $\sim 20\,\mathrm{keV}$ has recently been detected in several sources (e.g. Kuiper et al., 2006). Observations of AXP spectra show that their surface temperatures, $kT = 0.3 - 0.68\,\mathrm{keV}$[1] and systematically higher than those of RPPs with similar characteristic ages where $kT \sim 0.05 - 0.18\,\mathrm{keV}$ are observed (Kaspi et al., 2006).

Because AXPs have persistent, though variable, X-ray emission, several of the objects can be timed coherently in the same manner as RPPs (e.g. Kaspi et al., 1999). Timing observations of AXPs have shown that their dipole field strengths lie in the range of $B = (0.6 - 7.1) \times 10^{14}\,\mathrm{G}$, systematically smaller than those of SGRs but systematically larger than those of typical RPPs (Gavriil & Kaspi, 2002; Gotthelf et al., 2002a).

A connection between AXPs and SGRs was long suspected but not confirmed until SGR-like X-ray bursts were discovered from two AXPs, 1E 1048.1−5937 (Gavriil et al., 2002) and 1E 2259+586 (Kaspi et al., 2003). X-ray bursts have since been

[1] Data are compiled for all known magnetars at http://www.physics.mcgill.ca/∼pulsar/magnetar/main.html

discovered from 6 of the 9 confirmed AXPs, though no giant SGR-like flares have been observed (Kaspi, 2007). In addition to X-ray bursts, AXPs show a variety of other radiative changes, often occurring concurrently with bursts, such as pulsed and total flux variability (e.g. Gavriil & Kaspi, 2004; Mereghetti et al., 2004), pulse profile changes, and spectral variations (e.g. Woods et al., 2004).

Transient magnetars

Three AXPs and one SGR have entered long-term, quiescent, low-luminosity states where their X-ray luminosities fall below $L_X < 10^{33}\,\mathrm{erg\,s^{-1}}$ (e.g. Israel et al., 2004). When they emerge from the quiescent state, their X-ray luminosity increases suddenly by a factor of $\sim 50-100$, with or without accompanying X-ray bursts (Woods, 2008). Interestingly, pulsed radio emission has been detected from two of the transient AXPs, XTE 1810−197 and 1E 1547−5408, while in their active states (Camilo et al., 2006a, 2007b).

The magnetar model

In the magnetar model proposed by Duncan & Thompson (1992), magnetars are fundamentally different from RPPs because of their larger B-fields, which become wound up in the stellar interior and are manifested observationally as very large dipole fields (Thompson & Duncan, 2001).

Both persistent and burst emission from magnetars are powered by the decay of their large magnetic fields (Thompson & Duncan, 1995). A magnetic field of $B > 10^{15}\,\mathrm{G}$ should decay on a timescale of 10 kyr, raising the temperature of the interior of the neutron star in the process (Thompson & Duncan, 1996). A large interior temperature combined with a large magnetic field induces stresses in the crust that will eventually cause crustal cracking. This will be associated with energy release, perhaps being the cause of magnetar bursts and the giant SGR flares, which are likely associated with global changes in the field structure (Thompson & Duncan, 1995; Woods et al., 2001). The persistent emission observed from AXPs and SGRs is

thought to arise from some combination of thermal emission from their heated surfaces (Özel et al., 2001), and magnetospheric currents driven by twists in the magnetic field (Thompson & Duncan, 1996).

1.7 High-Magnetic Field Rotation-Powered Pulsars

While most rotation-powered pulsars have modest magnetic fields of $\sim 10^{12}$ G, and most magnetars have field strengths in excess of 10^{14} G, there is a region of overlap between the two populations, visible in Figure 1.3. In fact, some RPPs have larger estimated dipole fields than those of *bona-fide* magnetars, but show no anomalous X-ray emission (Kaspi & McLaughlin, 2005; Zhu et al., 2009). For example, PSR J1718−3718 has $B = 7.4 \times 10^{13}$ G (Kaspi & McLaughlin, 2005), while the AXP 1E 2259+586 has $B = 5.9 \times 10^{13}$ G (Gavriil & Kaspi, 2002). This is somewhat puzzling since magnetic field strength is thought to be the basis of all the observational differences between RPPs and magnetars (Duncan & Thompson, 1992). A list of all rotation-powered pulsars with fields above 2×10^{13} G is given in Table 1.2.

One possible explanation is that the dipole field estimated from Eq. 1.11 is inaccurate. This is not unreasonable because of the large number of assumptions leading to this estimate of B. For example, α, the angle between the spin and magnetic axis, is assumed to be 90° in all cases. This leads to an under-estimate of B when $\alpha < 90°$. Nevertheless, it is curious that there are so many otherwise-normal rotation-powered pulsars with such large fields, and suggests a possible connection between these sources and the magnetars.

In particular, a connection could exist between the high-B field RPPs, most of which are radio loud, and the transient AXPs, two of which are the only confirmed magnetars with detected radio pulsations (Israel et al., 2004; Camilo et al., 2007b). Before the discovery of radio pulsations from neutron stars with dipole fields above the quantum-critical limit, it was predicted that the radio emission mechanism should be suppressed in any source with such a large magnetic field, because processes like photon-splitting should inhibit pair cascades (Baring & Harding, 1998).

Table 1.2: High-magnetic field rotation-powered pulsars

Name	$\boldsymbol{B}$ $(\mathbf{10^{13}\,G})$	$\boldsymbol{P}$ **(s)**	$\boldsymbol{\tau_c}$ **(kyr)**	$\boldsymbol{\dot{E}}$ $(\mathbf{10^{33}\,erg\,s^{-1}})$	**Type**	**Ref**
J1847−0130	9.36	6.707	83.3	0.17	RPP	1
J1718−3718	7.44	3.378	33.5	1.6	RPP	2
J1814−1744	5.51	3.976	84.6	0.47	RPP	3
J1734−3333	5.22	1.169	8.13	56	RPP	4
J1819−1458	5.01	4.263	117	0.29	RRAT	5
J1846−0258	4.86	0.326	0.728	8100	RPP,RQ	6
J0420−5022	4.20	3.453	109	0.48	INS,RQ	7
J1119−6127	4.10	0.408	1.61	2300	RPP	8
J1821−1419	3.89	1.656	29.3	7.8	RPP	9
J1746−2850	3.85	1.077	12.7	42	RPP	10
J1726−3530	3.72	1.110	14.5	35	RPP	11
J1308+2127	3.44	10.312	1460	0.0040	INS	12
J0726−2612	3.21	3.442	186	0.28	RPP	13
J0534−6703	2.81	1.818	67.8	2.8	RPP	14
J1846−0257	2.71	4.477	442	0.071	RRAT	15
J0847−4316	2.71	5.977	790	0.022	RRAT	15

Rotation powered pulsars with estimated dipole fields larger than $B > 2.5 \times 10^{13}$ G. References: 1. McLaughlin et al. (2003); Hobbs et al. (2004) 2. Hobbs et al. (2004) 3. Camilo et al. (2000); Janssen & Stappers (2006) 4. Morris et al. (2002) 5. McLaughlin et al. (2006); Lyne et al. (2009) 6. Gotthelf et al. (2000); Livingstone et al. (2006) 7. Haberl et al. (2004) 8. Manchester et al. (2001) 9. Hobbs et al. (2004) 10. Deneva et al. (2009) 11. Manchester et al. (2001) 12. Hambaryan et al. (2002); Kaplan & van Kerkwijk (2005) 13. Burgay et al. (2006) 14. Manchester et al. (2006) 15. McLaughlin et al. (2006, 2009)

1.8 Deviations From Normal Pulsar Spin-Down

In addition to the deterministic slow-down of pulsars, two types of irregularities are observed. Timing noise, a smooth wandering of the pulse phase superposed on regular spin-down, and glitches – a sudden increase in spin-frequency. Both are especially common in young pulsars and are discussed in the following sections.

1.8.1 Timing noise

Superposed on the deterministic spin-down of pulsars is a stochastic wandering of the pulse phase called timing noise. It is observed as structure remaining in timing residuals after the removal deterministic parameters, and as a result often seriously contaminates their measurement (Lyne et al., 1995). Instead of individual steps in phase, the combined effect of many unresolved events is observed (Cordes & Greenstein, 1981). That is, timing residuals reveal the statistical fluctutations in the underlying mechanism, making the physical origins of timing noise difficult to uncover (Lyne et al., 1995). Timing noise is thought to be present at some level in all pulsars, though there is tremendous variation in the amount of timing noise in different objects (e.g. Lyne & Smith, 2005). Timing noise is often characterized with the measurement of the second frequency derivative, $\ddot{\nu}$, which, for the large majority of pulsars, is dominated by noise processes. Because we discuss deterministic measurements of $\ddot{\nu}$, we define here $\ddot{\nu}_{noise}$ as a measurement dominated by a noise process (see §1.4.3 for a discussion of deterministic measurements of $\ddot{\nu}$ and corresponding measurements of n). Measured $\ddot{\nu}_{noise}$ can be up to $\sim 10^6$ times larger than what would be expected from magnetic braking, and is often of the wrong sign (D'Alessandro et al., 1995).

One common characterization of timing noise is the Δ_8 parameter, which measures the contribution of $\ddot{\nu}_{noise}$ to the pulse phase (Arzoumanian et al., 1994). The parameter is defined as

$$\Delta_8 = \log\left(\frac{1}{6\nu}|\ddot{\nu}_{noise}|(10^8\mathrm{s})^3\right). \tag{1.27}$$

Hobbs et al. (2010) calculated Δ_8 for 366 pulsars and found an empirical correlation between $\dot{P}$ and Δ_8 of $\Delta_8 = 5.1 + 0.5\log\dot{P}$.

The correlation between Δ_8 and $\dot{P}$ is often interpreted as a correlation between timing noise and pulsar age (because the common method to estimate age is with the characteristic age, i.e. $\tau_c \propto 1/\dot{P}$; Arzoumanian et al., 1994; Cordes & Downs, 1985; Urama et al., 2006; Hobbs et al., 2010). However, the recent discovery of extremely steady rotation in the very young CCOs, which have anomalously large τ_c, (Halpern & Gotthelf, 2010a) present a challenge to this interpretation. That is, while the correlation between small $\dot{P}$ and timing noise holds for the CCOs, in this case, the low-noise pulsars are, in fact, very young.

A weakness of the Δ_8 parameter is that it gives the amplitude of noise for a single time span ($\sim$3 yr), whereas timing noise is observed on a hierarchy of timescales. In fact, timing noise is typically a low-frequency process, commonly known as "red noise" (Boynton et al., 1972). This type of spectra can be characterized by

$$S \propto f^{-\alpha}, \tag{1.28}$$

(e.g. Cordes & Greenstein, 1981; Cordes & Downs, 1985; Deeter, 1984). A random walk in phase, spin frequency, or spin frequency derivative corresponds to a spectral index of $\alpha = 2, 4, 6$ respectively. Gaussian (or white) noise, by contrast, has a spectral index of $\alpha = 0$ (Deeter, 1984; Groth, 1975). Measurements of timing noise spectra range from $\alpha \sim 2 - 6$, but are often not consistent with being integers, so do not correspond to a pure random walk. Figure 1.4 shows the power spectrum for the young pulsar PSR B1509−58, with the best-fit spectral index of $\alpha = -4.6 \pm 1.0$. A spectral break at higher frequencies is also often observed, as visible in the figure (Livingstone et al., 2005b; Scott et al., 2003). Some noise spectra indicate quasi-periodicities (Scott et al., 2003), while others are consistent with white noise (Hobbs et al., 2010).

The physical origins of timing noise

Fluctuations from timing noise are "real" in the sense that they do not arise from measurement uncertainties (D'Alessandro et al., 1995). Timing noise is not correlated with location in the Galaxy or radio luminosity (Cordes & Greenstein, 1981). It has been shown that variability in the ISM or a surrounding supernova remnant is not a

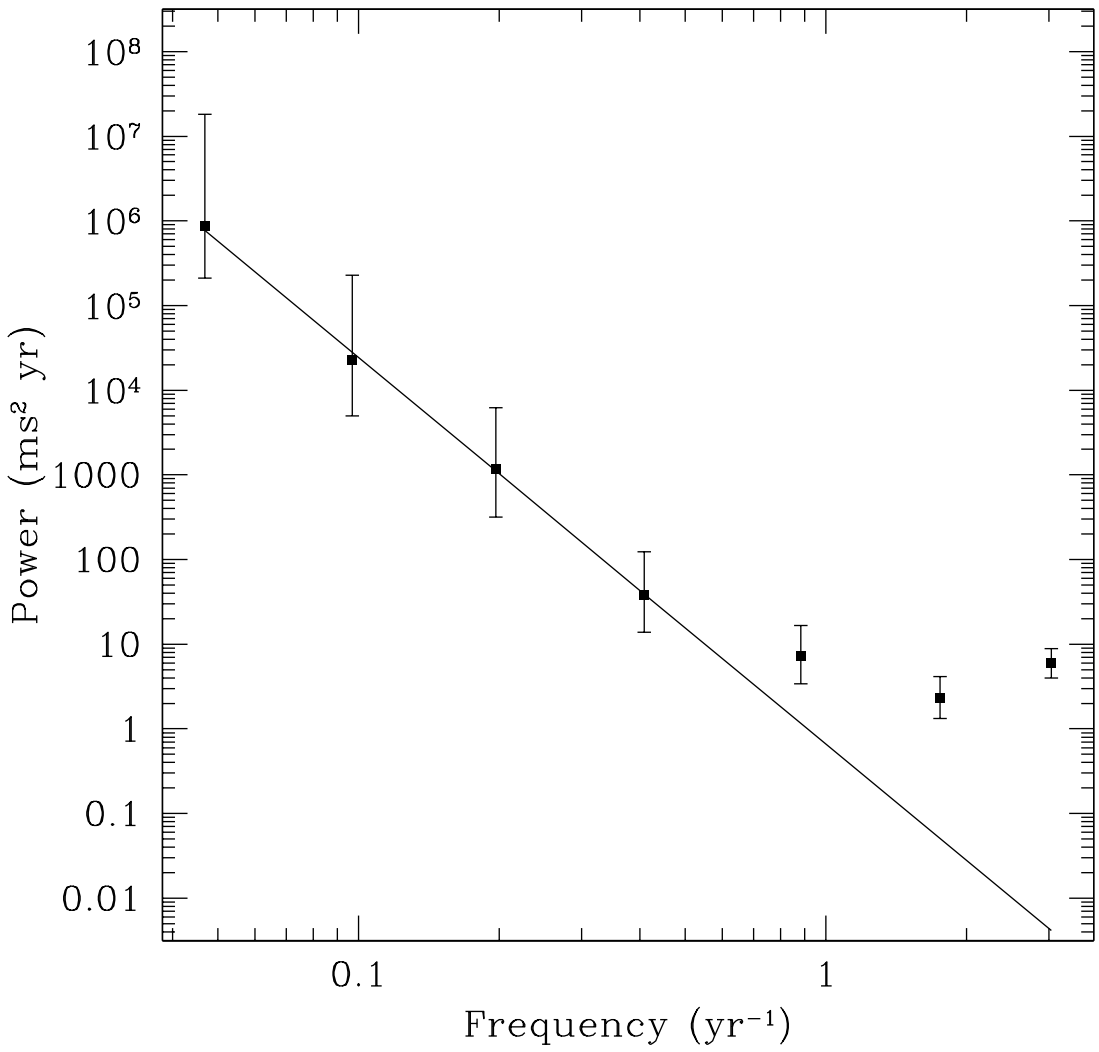

Figure 1.4: An example of a timing noise spectrum, shown here for the young pulsar PSR B1509−58.

major cause of timing noise, though, in the case of radio observations, it can add an additional noise component owing to unmodeled variations in the dispersion measure (see §3.6 for a discussion of dispersion and its importance to radio pulsar timing; Backer et al., 1993; Hamilton et al., 1977).

Another possibility is that some observed timing noise is, in fact, unresolved glitches, particularly in pulsars with $\tau_c < 100\,\mathrm{kyr}$ (Hobbs et al., 2010). Contamination could arise from either small glitches in the data that have not been resolved (e.g. Janssen & Stappers, 2006) or glitches occurring prior to the start of observations, where glitch recovery from a previous unseen glitch affects the measured spin parameters (Shemar & Lyne, 1996; Hobbs et al., 2010).

Most physical explanations for timing noise are understood as the response of the neutron star to a noisy component of torque, that is, noise in the pulsar "clock" (e.g. D'Alessandro et al., 1995). Suggestions for the origins of such a torque include random pinning and unpinning of vortex lines in the neutron star superfluid (Alpar et al., 1986), the response of the neutron star to heat pulses (Greenstein, 1979), or fluctuations in magnetospheric outer gaps (Cheng, 1987). Other explanations include the existence of planets or "planetessimals" around the star (Scott et al., 2003). Planets would eventually be detectable as periodicities in timing residuals, as has been detected in two sources (Wolszczan & Frail, 1992; Sigurdsson et al., 2003).

More recently, a new possible explanation for timing noise has come to light, via long-term timing observations of PSR B1931+24. Radio pulsations in this source are observed to turn on and off in a quasi-periodic manner with a cycle of 5 – 10 days "on" followed by 25 – 30 days "off" (Kramer et al., 2006). Intriguingly, the pulsar spins-down 1.5 times faster while emitting radio waves than while not, implying a correlation between the radio emission mechanism and the spin-down torque acting on the pulsar. It is likely that the correlation arises from the plasma density in the magnetosphere or magnetospheric outer gaps (Cheng, 1987), implying that the noise torque is affected by the pulsar's local environment rathen than its interior. Recently, a similar effect has been shown to be active in several other pulsars, where changes

in $\dot{\nu}$ are correlated with radio pulse profile variations (Lyne et al., 2010).

Timing noise in magnetars

In general, AXPs and SGRs are noisier rotators than RPPs of similar characteristic age, though, like RPPs, a correlation between $\dot{\nu}$ and timing noise is observed (Gavriil & Kaspi, 2002; Woods et al., 2002). SGRs are sufficiently noisy that efforts to time them phase-coherently in the manner of RPPs have failed (although this is also in part due to their low luminosity in quiescence, e.g. Kouveliotou et al., 2003). Several AXPs can be timed coherently in the same manner as the RPPs and show a range of timing noise behaviour, from the relatively steady rotator 1E 2259+586, to the extremely noisy 1E 1048−5937 (Gavriil & Kaspi, 2002; Dib et al., 2009).

One dramatic instance of timing variability in a magnetar was in SGR 1900+14 in the months before the giant flare in 1998. Over an 80-day window where no timing observations were obtained, the pulse frequency decreased by $\Delta\nu/\nu \sim 10^{-4}$, corresponding to an increase in the average $\dot{\nu}$ by a factor of ~ 2 (Woods et al., 1999). The amplitude of the observed change in ν is consistent with an enhanced magnetic torque due to a relativistic flow of particles for a magnetic field of $B \simeq 10^{15}$ (Thompson & Blaes, 1998). Torque variability has also been observed in the SGR 1806−20 where the long-term spin-down rate varies by an order of magnitude (Woods et al., 2002, 2007).

Thompson & Blaes (1998) proposed that SGR fields should be highly variable, implying that the torque on the neutron star should also vary. A magnetic field changing on short time scales could be responsible for the large amount of timing noise observed in both AXPs and SGRs, via a flux of particles away from the star which is a possible explanation for the dramatic change in ν in SGR 1900+14 near its giant flare (Harding et al., 1999; Thompson et al., 2000). In the same vein, matter injected into the magnetosphere could cause variations in the amount of open field lines, and thus co-rotation radius, affecting the spin-down torque (Ibrahim et al., 2001).

In some cases, there is a time lag between radiative behaviour and torque variations

(e.g. in 1E 1048−5937, though there may not be a causal correlation between these two behaviours; Dib et al., 2009). These behaviours, if connected, could be explained as the result of large-scale static currents travelling along closed field lines, which could also explain observed variability in pulse profiles (Thompson et al., 2002).

1.8.2 Glitches

A pulsar "glitch" is a sudden, usually unresolved, increase in spin-frequency, ν. Glitches are often accompanied by an increase in the magnitude of $\dot{\nu}$, and are sometimes followed by an exponential decay on time scale τ_d, where some of the initial jump in ν is recovered. Figure 1.5 shows the two most common realizations of pulsar glitches, with and without an exponential recovery. The first glitch was observed in the Vela pulsar only a year after the discovery of pulsars (Radhakrishnan & Manchester, 1969), which has sinced been observed to glitch 16 times (Buchner & Flanagan, 2006).

In general, a glitch at time t_g can be modeled as:

$$\nu(t) = \nu_0(t - t_g) + \Delta\nu_p + \Delta\nu_d e^{-(t-t_g)/\tau_d} + \Delta\dot{\nu}(t - t_g), \tag{1.29}$$

where $\nu_0(t)$ is the frequency of the pulsar prior to the glitch and $\Delta\nu$ is the initial frequency jump, which can be decomposed into the part of the glitch that is permanent, $\Delta\nu_p$, and that which decays, $\Delta\nu_d$. The recovery fraction is defined as $Q \equiv \Delta\nu_d/\Delta\nu$. The magnitude of a glitch is typically quantified by the fractional change in ν, that is, $\Delta\nu/\nu$[1]. A permanent change in $\dot{\nu}$ is also sometimes observed at a glitch, given by $\Delta\dot{\nu}$.

Glitches are excellent probes of neutron star interiors. The conclusion that glitches are phenomena of the interior rather than the magnetosphere can be reached from the observation that changes in the pulse structure are not observed in glitches in radio-loud pulsars (Cordes & Greenstein, 1981). The radio pulse is created away from the

[1]One can argue that since $\Delta\nu$ is proportional to the change in angular momentum at a glitch, $\Delta L = 2\pi I\Delta\nu$, $\Delta\nu$ is a more physical measure of glitch magnitude. Regardless, it is common throughout the field to report the fractional frequency increase, thus we follow this convention here.

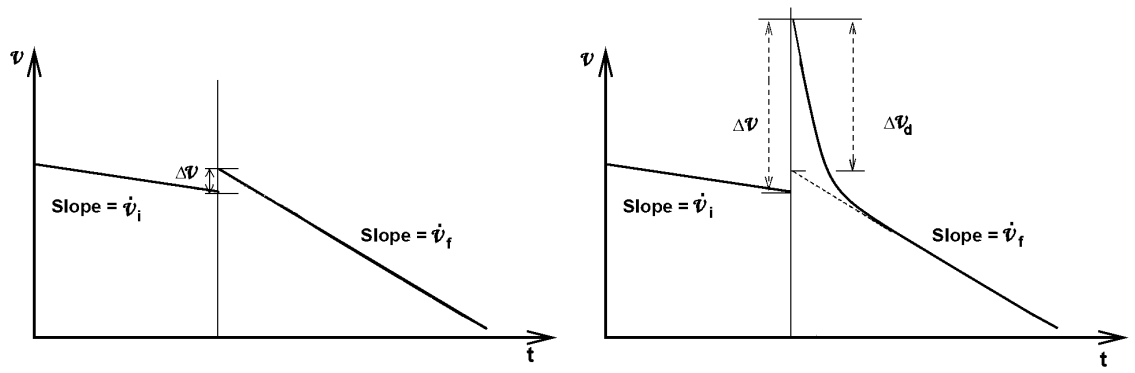

Figure 1.5: The two most common realizations of a pulsar glitch. Left: A glitch showing an increase in ν and dominated by an increase in magnitude of $\dot{\nu}$, as typical of many young pulsars. Right: A glitch showing an increase in ν, followed by an exponential recovery with time scale, τ_d, accompanied by an increase in magnitude of $\dot{\nu}$. Figure adapted from Lorimer & Kramer (2005), provided by Rim Dib.

neutron star surface in the magnetosphere. If the magnetosphere were involved in glitches, one would expect changes in pulse shape and/or intensity during the glitch and its recovery, which are not observed in radio pulses (during glitches or otherwise). An exception to this rule can be found in the glitches observed in magnetars, which are sometimes accompanied by radiative changes (e.g. Kaspi et al., 2003), implying that these events may not have the same origins as in RPPs.

Approximately 300 glitches have been observed in $\sim$ 100 pulsars (Yuan et al., 2010; Peralta, 2006, and references therein). The fractional sizes of detected glitches span six orders of magnitude, with $\Delta\nu/\nu \sim 10^{-11} - 10^{-5}$ (Cognard & Backer, 2004; Janssen & Stappers, 2006; Hobbs et al., 2002), while in a single source, B1737−30 there is a span of 4 orders of magnitude in detected glitch sizes (Janssen & Stappers, 2006; Zou et al., 2008). Glitches are common in pulsars with $\tau_c < 100\,\mathrm{kyr}$ and the nature of glitches appears to change with a pulsar's characteristic age.

Glitches in the youngest pulsars ($\tau_c \simeq 0.5-2\,\mathrm{kyr}$) are typically small in magnitude, on the order of $\Delta\nu/\nu \sim 10^{-9}-10^{-8}$ (Lyne et al., 1993; Camilo et al., 2000; Livingstone et al., 2005a), and tend to be dominated by an increase in the magnitude of $\dot{\nu}$ (e.g. Lyne & Smith, 2005). Among these very young pulsars, the Crab pulsar is the only one where glitch recovery, Q, has been observed, and, is typically on the order of,

but less than, unity (Wong et al., 2001). However, for some glitches, a recovery may have occurred but not been observed, due to a sparsity of observations. Whereas the Crab pulsar is observed daily (Wong et al., 2001), most pulsars are observed much less frequently (e.g. monthly; Morris et al., 2002). Thus the size of the glitch and amount of recovery may be underestimated in some cases, particularly where infrequent observations are paired with a short recovery time scale.

By contrast, glitches in Vela-aged pulsar ($\tau_c \simeq 5 - 10\,\mathrm{kyr}$) tend to be larger, with typical magnitudes of $\Delta\nu/\nu \sim 10^{-7} - 10^{-6}$, and recover a small percentage of the original frequency increase, if any recovery is detected (Lyne et al., 2000). As pulsars age, the fractional size of the glitches they experience decreases (Lyne et al., 2000).

The oldest pulsars are very rarely seen to glitch. A single "micro" glitch has been observed in a recycled millisecond pulsar, PSR B1821−24 with $\tau_c = 30\,\mathrm{Myr}$ with magnitude $\Delta\nu/\nu = 9.5 \times 10^{-12}$ (Cognard & Backer, 2004). Similarly, non-recycled pulsars with ages 1 – 10 Myr are rarely observed to glitch although smaller glitches may have been missed or confused with timing noise (e.g. Janssen & Stappers, 2006).

One intriguing object is the young pulsar PSR B1509−58, with an age of $\sim 1700\,\mathrm{yr}$, which has not glitched in over 21 years of continuous timing observations (Livingstone et al., 2005b). This pulsar has similar spin properties to the Crab pulsar, PSR J1119−6127, and PSR B0540−69, which have all been observed to glitch on much shorter timescales (Lyne et al., 1993; Camilo et al., 2000; Livingstone et al., 2005a).

One way to characterize glitches is by the total change in fractional spin frequency over the total observation time, A_G, the "glitch activity" parameter (McKenna & Lyne, 1990),

$$A_G = \frac{1}{\Delta t}\Sigma\left(\frac{\Delta\nu}{\nu}\right). \tag{1.30}$$

The Crab pulsar has frequent, but typically small glitches, and has a resulting glitch activity parameter of $A_g \sim 0.1 \times 10^{-7}\,\mathrm{yr}^{-1}$ (Shemar & Lyne, 1996), while the frequent large glitcher, the Vela pulsar has $A_g \sim 8 \times 10^{-7}\,\mathrm{yr}^{-1}$ (Urama & Okeke, 1999).

McKenna & Lyne (1990) showed that there is an inverse-linear relationship between pulsar age and glitch activity, for pulsars older than ∼5 kyr. Pulsars younger

than $\sim 5\,\mathrm{kyr}$ glitch less than this correlation predicts, which they interpreted as a relationship between glitch activity and neutron star temperature. The youngest pulsars, which should have the highest temperatures, would glitch the least because the vortex creep rate is highly temperature dependent (Link & Epstein, 1996, and see discussion in following section). Thus angular momentum in the hottest pulsars could be transferred from the superfluid to the crust in a smooth manner. However, large glitches have been observed in anomalous X-ray pulsars which have large inferred surface temperatures, calling this theory into question (Kaspi et al., 2000; Kaspi & Gavriil, 2003; Dall'Osso et al., 2003).

Glitches in magnetars

It is now well established that glitches are ubiquitous in magnetars as well as rotation-powered pulsars (Kaspi et al., 2000; Kaspi & Gavriil, 2003; Dall'Osso et al., 2003; Dib et al., 2008a; Gavriil et al., 2009). What is not currently known is whether glitches in magnetars have the same physical origins as in RPPs or if the super-critical magnetic fields of magnetars are responsible for different glitch origins and evolutions. On one hand, some magnetar glitches are indistinguishable from those in RPPs (e.g. AXP 1E 1841−45; Dib et al., 2008a). However other magnetar glitches differ significantly from those in RPPs. Some magnetar glitches are accompanied by radiative changes such as X-ray bursts, flux enhancements, and spectral or pulse-profile variations (e.g. Kaspi et al., 2003).

Physical models of glitches

Starquake model

The initial model put forward to explain the glitch phenomenon was one of starquakes that decrease the moment of inertia, I, of the pulsar, resulting in an increase in ν in order to conserve angular momentum (Ruderman, 1969). A newly formed, rapidly rotating neutron star is oblate rather than spherical. As the star slows down, the now-solid crust of the neutron star cannot plastically rearrange into a more energetically favourable state. Stresses build until the crust cracks and rearranges,

resulting in a lower I. The amount by which the spin-frequency increases can be related to I by

$$\frac{\Delta\nu}{\nu} = -\frac{\Delta I}{I}. \tag{1.31}$$

Assuming $I \propto MR^2$, one can calculate the radial change necessary in order to achieve the observed change in ν,

$$\frac{\Delta R}{R} = \frac{\Delta I}{2I} \tag{1.32}$$

For a glitch of magnitude $\Delta\nu/\nu \sim 10^{-8}$, a radial decrease of 10^{-4} cm is required, whereas for a glitch of magnitude $\Delta\nu/\nu \sim 10^{-6}$, a change of 1 cm is required (D'Alessandro et al., 1995). This model can account for small Crab-like glitches, but fails when applied to the large, frequent glitches observed in the Vela pulsar. The large glitches observed in the Vela pulsar should have a recurrence rate of ∼1 per century to allow sufficient stress to build in the crust, rather than once every ~ 3 years as is observed (Baym & Pines, 1971). Thus a model that could explain both small and large pulsar glitches was required.

The two-component model of pulsar glitches and superfluid vortices

The two-component model of pulsar glitches supposes that the inner crust of the neutron star is composed of a solid lattice of heavy nuclei and a neutron superfluid (Baym et al., 1969). Though neutrons are fermions (i.e. spin 1/2 particles), pairs of neutrons can act as bosons (i.e. integer spin particles), similar to ^4He atoms (Baym et al., 1969). Superfluids are friction-free fluids, that is, they have no viscosity (Shapiro & Teukolsky, 1983). This leads to several unusual behaviours compared to normal fluids.

Observationally, the argument that neutron stars contain some superfluid are from observations of relaxation times after glitches, which are much longer (days to weeks) than those expected from a normal fluid or solid ($\sim 10^{-17}$ s; Baym et al., 1969). Theoretically, the existence of a superfluid component of the neutron star interior was posited based on their density and internal temperature. The latent heat is the amount of energy required to cause a phase transition of neutrons from the paired to

unpaired state (Landau & Lifshitz, 1987). For neutron star densities, the latent heat of the neutron fluid is $\simeq 1 - 2\,\mathrm{MeV}$, while the internal temperature is only $\sim$keV, implying that the interior is highly degenerate, that is, essentially all of the neutrons in the crust should be in the paired state, and there should exist a crustal superfluid.

A result of the lack of viscosity in superfluids is that angular momentum is quantized in vortices, as shown in Figure 1.6, instead of bulk rotation as in a normal fluid. The angular momentum of a superfluid is determined by the area density of vortices, given by (Anderson & Itoh, 1975)

$$n_v \simeq 4\nu m_n/\hbar. \tag{1.33}$$

In a lab situation, as the fluid slows down, vortices will be lost and the remaining vortices will rearrange into a new configuration corresponding to a smaller angular momentum, as indicated in Figure 1.6. In a neutron star, however, some of the vortices become "pinned" at lattice nuclei sites, i.e. it is energetically favourable for the vortex line to pass through the lattice site (though the pinning force remains poorly understood; Anderson & Itoh, 1975). As long as vortices are pinned, the angular momentum of the superfluid cannot change. Thus, while the solid crust and core spin down via the external braking torque, the superfluid component of the crust has roughly constant angular momentum. This gives rise to a differential rotation of the solid crust (Ω_C) and superfluid (Ω_{SF}), or a frequency lag given by $\Omega_{lag} = \Omega_{SF} - \Omega_C$.

As the star spins down and the differential rotation increases, a force acts on the pinned vortices. At some critical value, a catastrophic unpinning of vortices occurs (e.g. Pines & Alpar, 1985). Vortices can then rearrange and transfer angular momentum to the lattice (and all coupled components of the neutron star), whereupon an increase in rotation rate is observed (Baym et al., 1969; Pines & Alpar, 1985).

In the aftermath of a glitch, the spun-up crust will have an increased rate of spin-down as the crust relaxes exponentially back to the original frequency. In the two-component model, the frequency should recover completely, i.e. $Q = 1$ and τ_d should remain the same for each pulsar (Shapiro & Teukolsky, 1983). While an exponential

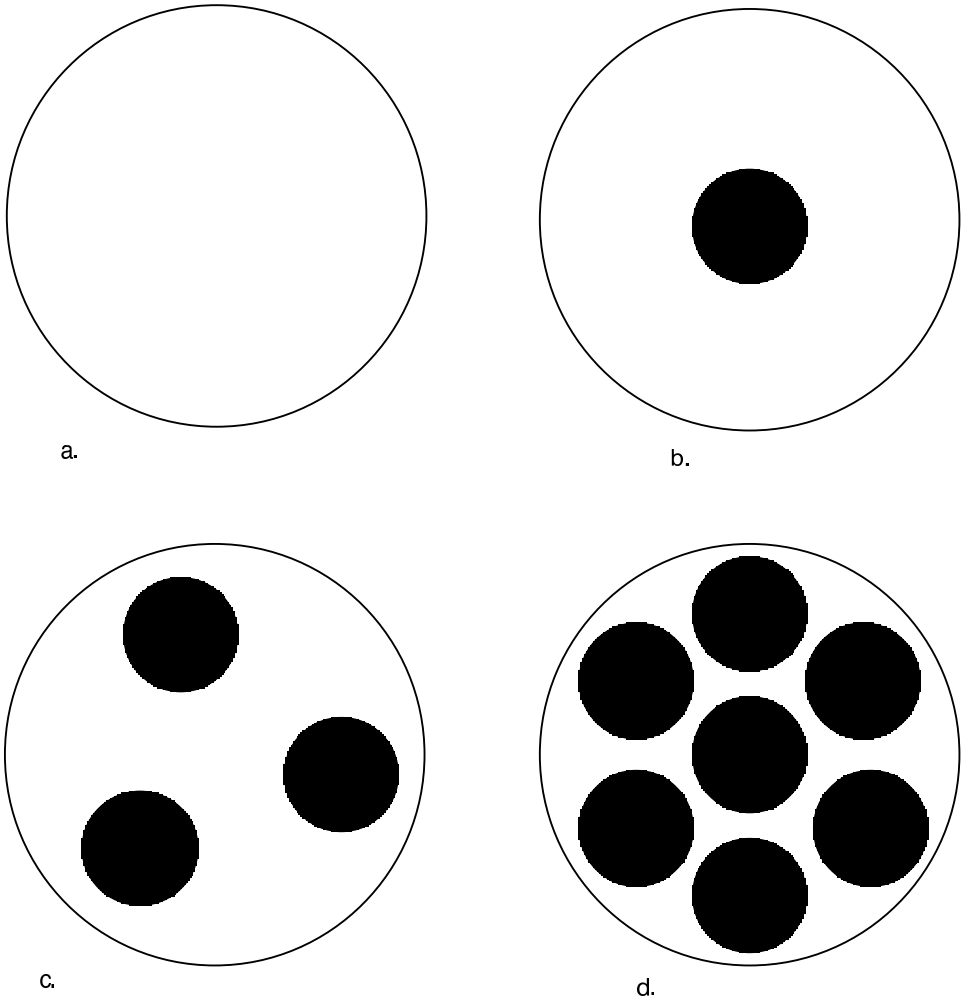

Figure 1.6: A schematic view of superfluid vortices. The angular momentum of the fluid increases from the top left to bottom right. Panel a. shows the fluid with no rotation. Vortices increase in density as the angular frequency increases in panels b, c, and d.

recovery is often observed after a glitch, the recovery is very rarely complete, and several values of τ_d have been observed in a single pulsar (e.g. Wong et al., 2001). Furthermore, some glitches have more than one exponential recovery timescale (e.g. Lyne et al., 1992).

Additionally, the two-component model offers no explanation for the permanent change in $\dot{\nu}$ observed in many glitches (Wong et al., 2001). The observed increase in the magnitude of $\dot{\nu}$ implies a permanent change in effective torque at the time of the glitch. This could be attributed to a decrease in effective moment of inertia, i.e. by increasing the fraction of pinned I_{SF}, or by a decrease in the oblateness of the star (Alpar et al., 1994). Another proposed explanation for an increased torque could be that the magnetic field is rearranged and effectively increased at the time of the glitch (Link & Epstein, 1996).

While the two-component model provides a good framework for understanding glitches of variable magnitude and a general picture for glitch recovery, it fails to reproduce the details of glitch recovery and provides no explanation for a permanent increase in the spin-down rate that we observe in many cases.

The vortex creep model

Alpar et al. (1981) proposed an alternative to the two-component model (in which vortices are perfectly pinned at lattice sites except during a glitch). They propose instead that vortices are able to unpin, migrate outwards radially, and re-pin at a new lattice site. While the majority of vortices remain firmly pinned at lattice sites, there is a constant pinning and unpinning due to thermal excitation or quantum tunneling, termed "vortex creep" (Link et al., 1993). Thus a slow, but nearly continuous, rearrangement of vortices allows the superfluid to spin down.

Vortex creep amounts to a weak frictional force between the superfluid and the crustal lattice (Link & Epstein, 1991). While the superfluid rotates faster than the solid part of the crust, it rotates at the equilibrium frequency lag, and, crucially, both the superfluid and solid components spin down at the same rate (Alpar et al.,

1989). Fluctuations in the vortex creep rate have been suggested as a source of observed timing noise in pulsars, causing brief variations in the spin-down rate as the superfluid deviates from and returns to the equilibrium lag frequency (Alpar et al., 1986).

In this picture, an external impulse may be required to trigger small Crab-like glitches. Link et al. (1992) suggest that because the vortex creep rate is highly temperature dependent, heat deposition in the crust (e.g. from crustal cracking or a rearrangement of the B-field) would cause a sudden, dramatic increase in the vortex creep rate, thus acting as a trigger for a glitch. A starquake could also provide the necessary trigger to release pinned vortices.

Alpar et al. (1996) suggest that while small Crab-like glitches require an external trigger, larger Vela-like glitches result naturally from inhomogeneities in the vortex distribution. Significant inhomogeneities prevent the normal action of vortex creep and a large force is allowed to build until it overcomes the pinning forces and a catastrophic unpinning event is triggered, similar to the perfect pinning model (Alpar et al., 1993).

A coherent picture emerges from the idea that the small glitches typically observed in very young pulsars build up regions of inhomogeneities in the vortex distribution. These inhomogeneities then lead to the larger glitches observed in older pulsars, as described below. In the smaller, externally triggered glitches (especially in the case of star-quake triggered glitches) imperfections will be created in the crustal lattice, causing areas with very large pinning energies to be created (Alpar et al., 1994). The end result is a clumpy vortex distribution, with areas of high vortex density surrounded by areas of very low density. The areas of low vortex density, or "depletion regions", cannot support a vortex current, thus do not contribute to the vortex creep rate (Alpar & Pines, 1993). These areas of low vortex density are uncoupled from spin down, effectively lowering I_{SF}, and allowing a net increase in $\dot{\nu}$, as observed in many glitches (Alpar et al., 1989). Depletion regions still contribute to the spin-up at glitches, since the catastrophic unpinning of vortices at glitches does not involve vortex

creep (Alpar et al., 1996). Thus the vortex creep model suggests that the youngest pulsars are building areas of vortex "capacitance", evidenced by a permanent increase in $\dot{\nu}$ at the glitch, while Vela-aged pulsars have already built regions of clumpy vortex density, leading to a large increase in ν at the glitch and no permanent $\dot{\nu}$ increase.

The concept of vortex creep also provides an explanation for glitch relaxation. At the moment that momentum is transferred from the superfluid to the solid crust, the superfluid and crust are decoupled (i.e. because most of the vortices are unpinned, there is essentially no vortex creep to couple the two components). The crustal solid initially spins down more rapidly, and slows as vortices pin at new lattice sites. The superfluid is very senstive to the equilibrium frequency lag and any change from this rate will result in a sudden change in the spin-down rate. The theory allows for different values of Q and τ_d for different pulsars, corresponding to the coupling between the two components. However, since the coupling should be related to internal temperature, both Q and τ_d should remain roughly the same from glitch to glitch. However, this is not the case in observed glitches, though Q or τ_d are nearly the same in most Crab and Vela glitches (Wong et al., 2001; Buchner & Flanagan, 2008).

Much about neutron star glitches is still poorly understood. The variety of behaviours seen in glitches has proven difficult to explain with a single theory. The range of glitch sizes in a single pulsar, the permanent change in $\dot{\nu}$, and different values of Q and τ_d observed in the same pulsars are all difficult to explain with any current theory. None of the theories can easily explain a glitch followed by no relaxation, i.e. $Q = 0$, though this has been observed for many glitches. Recent work suggests that turbulence in the superfluid could have a major effect on observed glitches (Melatos & Peralta, 2007; Peralta et al., 2006).

1.9 Outline of Thesis

The remainder of the thesis is organized as follows:

Chapter 2 – Observatories and Instrumentation

This Chapter describes the four telescopes used to collect data analyzed in this thesis.

Chapter 3 – Pulsar Timing

This Chapter presents an overview of the techniques of pulsar timing and the preliminary analysis necessary to perform phase-coherent pulsar timing.

Chapter 4 – Radio and X-ray timing of the young pulsar at the centre of the supernova remnant 3C 58

This Chapter describes 6.4 years of radio and X-ray timing data for the young pulsar PSR J0205+6449. We discuss two large glitches and timing noise observed in these data. We also present an analysis of the X-ray pulse profile from 2 – 40 keV and present the first measurement of the phase offset between the radio and X-ray pulse for this pulsar.

Chapter 5 – A Braking Index for the Young Pulsar J1846−0258

In this Chapter we present long-term timing observations of the very young pulsar PSR J1846−0258 at the centre of the supernova remnant Kes 75. We present the first measurement of a braking index for this pulsar, which is of particular interest because of its extreme youth and large magnetic field. In addition, we present an analysis of the first detected glitch from this pulsar.

Chapter 6 – Outburst Timing Behaviour of PSR J1846−0258

Continued observations of PSR J1846−0258 revealed a dramatic episode of magnetar-like activity in 2006 (Gavriil et al., 2008). In this Chapter, we present a timing analysis of a large and very unusual glitch that occurred contemporaneously with the magnetar-like outburst. This is the first rotation-powered pulsar to exhibit a magnetar-like outburst and the accompanying glitch is unlike any seen before from a rotation-powered pulsar. We also report a large increase in the timing noise of the pulsar and discuss the implications of the dramatic change in the timing behaviour of the first magnetically active rotation-powered pulsar.

Chapter 7 – Persistent Changes to the Timing Properties of PSR J1846−0258

This Chapter discusses the persistent changes in the timing behaviour observed in PSR J1846−0258 after the magnetar-like outburst. We report a post-outburst mea-

surement of the braking index smaller than that previously reported in Chapter 5. We also identify and quantify an increase in the timing noise that has persisted for four years after the magnetar-like activity in the pulsar.

Chapter 8 – Conclusions

In this Chapter we summarize our results on the two young pulsars studied in this work and draw some general conclusions. We also discuss further avenues of research suggested by this work.

2
Observatories and Instrumentation

The data analyzed in this thesis were acquired with X-ray and radio telescopes. These are the two energy regimes in which the most pulsars are observable, yet the observation techniques are vastly different. This difference stems primarily from the wave-particle duality of light. In the X-ray regime, light can be treated as particles, so X-ray detectors are essentially photon counters. Accordingly, the techniques of particle physics have been heavily mined in the development of X-ray astronomy. Photons are neutral particles which have interaction cross-sections that vary as a function of energy. In the X-ray regime, photons interact with matter via photo-electric absorption. At the other end of the electromagnetic spectrum – in the radio regime, light is better understood as a wave, thus we speak of "radio waves," and radio telescopes convert electromagnetic waves into electronic signals.

Another significant difference between X-ray and radio astronomy is the effect of the atmosphere on different wavelengths of light. X-ray photons are absorbed by elements in the atmosphere, thus do not reach the ground. As a result, X-ray detectors are located above the atmosphere, typically aboard a satellite. On the other hand, the atmosphere is transparent to radio waves, thus the large collecting areas necessary to detect notoriously weak radio-wave signals can be conveniently located on the ground. A complication of placing a radio telescope on the ground, however, is the tendency to be contaminated by man-made interference. In this Chapter, I will give a brief introduction to the X-ray and radio telescopes used gather the data that appears in the subsequent Chapters.

2.1 The Rossi X-ray Timing Explorer

The majority of the data analyzed in this thesis were taken with the Rossi X-ray

Timing Explorer. Observations of PSR J0205+6449 were obtained between 2002 and 2006 and are presented in Chapter 4. Observations of PSR J1846−0258 were taken between 1999 and 2010 and are presented in Chapters 5, 6, and 7.

The *Rossi X-ray Timing Explorer* (hereafter, *RXTE*), was launched from a Delta-II rocket on December 30, 1995 from Cape Canaveral into a circular low-Earth orbit with an altitude of 580 km and 23° inclination. The spacecraft completes an orbit every 96 minutes and is regularly powered-down for ∼15 – 30 minutes of each orbit as it passes through the South Atlantic Anomaly and/or experiences an Earth occultation[1].

RXTE has excellent time resolution along with moderate energy resolution allowing for the study of variable X-ray sources over millisecond-to-year time scales in the 2 – 250 keV energy range. Initially designed for a 2-year mission, with a goal of 5 years, it has far exceeded this goal, currently operating in its fourteenth year – making it the longest surviving X-ray telescope to date. One of the great advantages of *RXTE* is its flexibility. The X-ray sky is highly variable, so the ability to observe sources while they are active, requiring rapid slewing times and a flexible observing schedule, is paramount.

RXTE holds three scientific experiments: the All Sky Monitor (ASM), the High Energy X-ray Timing Experiment (HEXTE), and the Proportional Counter Array (PCA). The ASM consists of three wide field rotating cameras that scan 80% of the sky during each orbit in order to identify transient phenomena. The ASM is sensitive to photons in the 1.5 – 12 keV energy range and has modest spatial resolution of $3' \times 15'$ (Levine et al., 1996). HEXTE consists of two clusters of four sodium iodide/cesium iodide scintillators, sensitive from 15 – 250 keV. It has a 1° field-of-view and a total collecting area of 1600 cm^2 (Rothschild et al., 1998). The final instrument, the PCA, is the sole instrument used in this thesis and is described in detail below.

2.1.1 The spacecraft

The three instruments aboard *RXTE* are integrated into a single spacecraft unit, shown in Figure 2.1. The spacecraft was designed to be highly maneuverable and

[1] https://heasarc.gsfc.nasa.gov/docs/xte/xte2.html

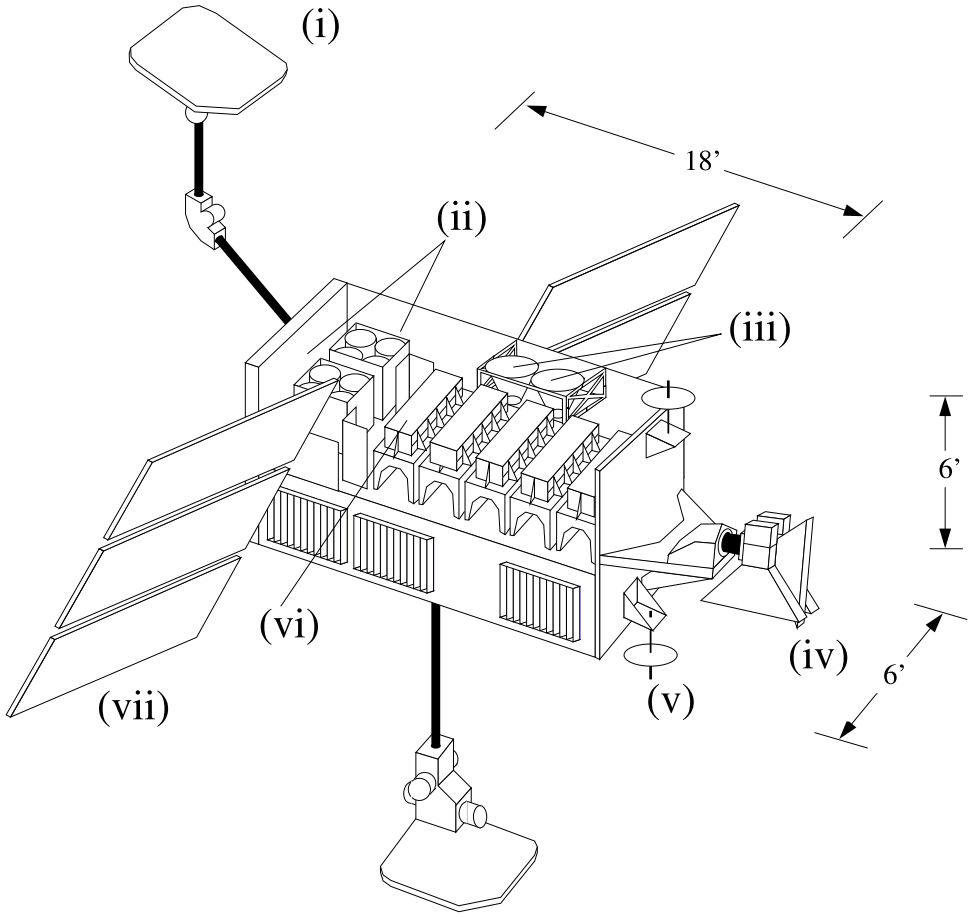

Figure 2.1: *The Rossi X-ray Timing Explorer*.
(i) High-gain antenna; (ii) High-Energy X-ray Timing Experiment; (iii) Star trackers; (iv) All-Sky Monitor; (v) Low-gain antenna; (vi) One of five Proportional Counter Units; (vii) Solar-power array. Image courtesy Fotis Gavriil, adapted from a Figure in Bradt et al. (1993).

able to slew at a rate of 6°/minute. The PCA and HEXTE are co-aligned and can be pointed to within 30° of the Sun, allowing for long viewing windows for most sources. The pointing accuracy of the spacecraft is $\sim 2 - 10''$ (Jahoda et al., 2006).

2.1.2 The proportional counter array

The PCA consists of five proportional counter units (PCUs), each with an effective area of $\sim$1300 cm^2, resulting in a combined total effective area of 6500 cm^2. A diagram of the PCA is shown in Figure 2.2. The PCA is sensitive to incoming photons in the 2 – 60 keV energy range and has an effective energy resolution of 18% at 6 keV (Bradt et al., 1993), although the instrument sensitivity varies significantly over this energy

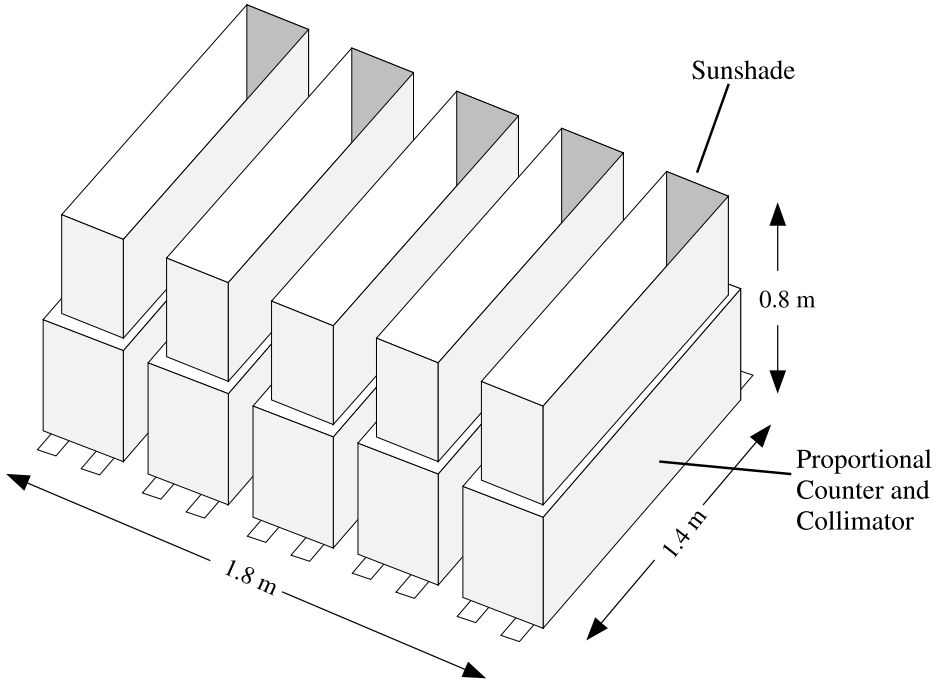

Figure 2.2: The Proportional Counter Array, comprised of 5 Proportional Counter Units. Image courtesy Fotis Gavriil, as adapted from Bradt et al. (1993).

range (Jahoda et al., 2006).

A "proportional counter" is a type of photon detector long used in Earth-based particle physics applications. A chamber is filled with a neutral gas, separated with wire electrodes, and a voltage is applied. Photons enter the chamber and interact with gas particles via photoelectric absorption, producing electrons and ions. Charged particles then drift to the appropriate electrode. Because of their small mass, electrons gain significant kinetic energy during collisions with gas atoms. The kinetic energy of some of the electrons will exceed the ionization energy of the gas, leading to new electron-ion pairs. These newly created electrons will also be accelerated, creating more electron-ion pairs, resulting in a shower of charged particles. If the applied voltage is within a restricted range (where the specific value depends on the type of gas used), the amount of collected charge will be proportional to the energy of the incoming photon. This allows the instrument to record the energy as well as the arrival time of the photon.

Each of the five PCUs that together make up the PCA consists of several detection

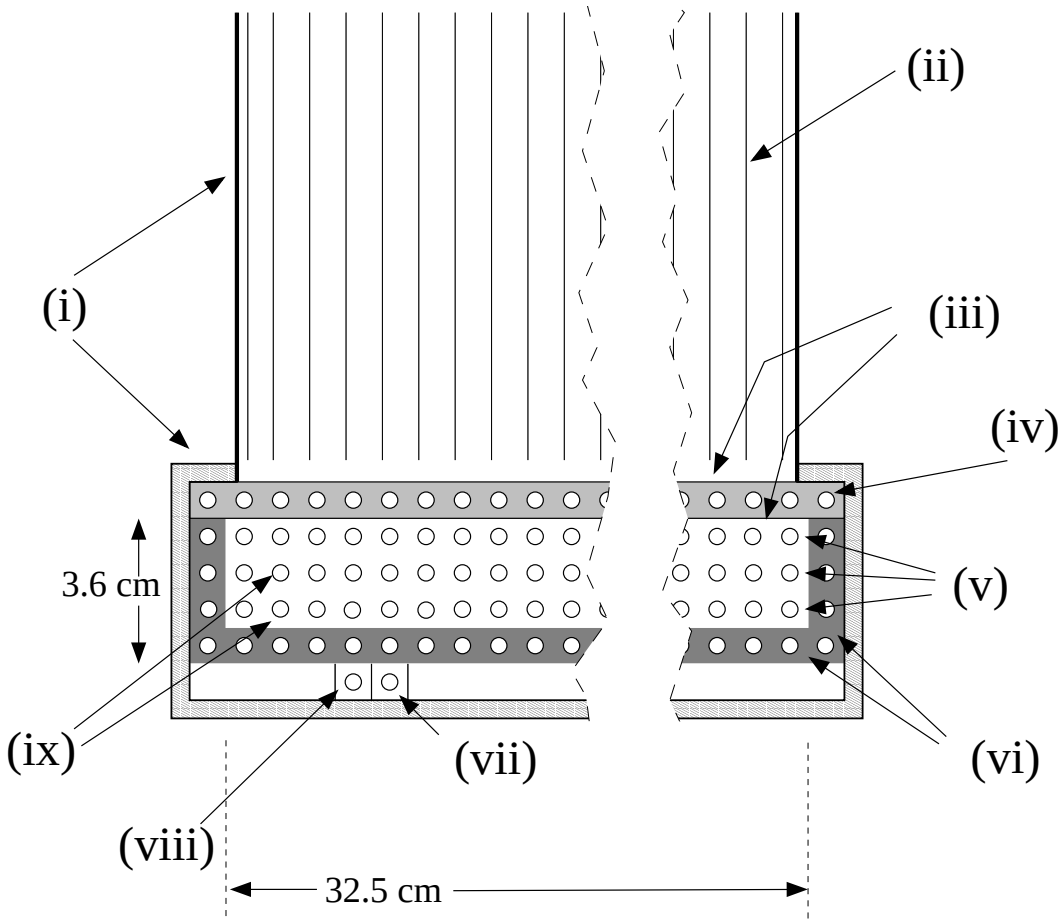

Figure 2.3: A Proportional Counter Unit. (i) X-ray shielding; (ii) Hexagonal collimator; (iii) Mylar windows; (iv) Propane anticoincidence layer; (v) Three xenon/methane signal layers; (vi) Xenon/methane anticoincidence layers; (vii) Americium source; (viii) Alpha detector; (ix) Anodes. Image courtesy Fotis Gavriil, adapted from a Figure in Bradt et al. (1993).

layers and anticoincidence layers, shown in Figure 2.3. Three layers of xenon gas are the primary photon detection layers of the instrument, with a total thickness of 3.6 cm. The layers are separated by wire anodes, creating three separate chambers.

Anticoincidence detection is the identification of incoming particles as charged particles rather than photons. Incoming charged particles of sufficient energy will also ionize gas atoms, resulting in an erroneous identification as X-ray photons. This can be avoided if particles are identified as charged, and the signals can be removed in data processing. The main method of identifying a particle as charged is that the shower resulting from a charged particle will typically be detected in more than one

layer and/or in adjacent cells. Thus any event satisfying these conditions is excluded (though this does result in some accidental vetoing of X-rays, but is a small effect for all photons except those above ∼35 keV; Glasser et al., 1994). Anticoincidence detection is provided in the viewing direction of each PCU with a 1.3 cm thick propane layer, separated from the xenon detection layers by a 25 μm thick aluminum-coated mylar window[1]. Anticoincidence is provided on the non-viewing sides of each PCU by an admixture of xenon and methane.

The gas layers of the telescope are covered in the viewing direction with a hexagonal beryllium copper collimator, which limits the field of view to one degree (see Fig. 2.3). A 25μm thick mylar layer between the collimator and the gas layers acts as the front window to the instrument. The entire PCA, except for a 32.5 cm^2 open area, is covered with X-ray shielding made of tin and tantalum. An americium source is used to continuously monitor the voltage for each PCU – it emits alpha particles at a known energy allowing the gain to be calibrated. Each PCU has an analogue-to-digital converter that provides 256 energy channel resolution.

While the PCA has no imaging capabilities and modest energy resolution, it has a high time resolution of 1μs for a single photon. The absolute timing capabilities of the instrument are also excellent, calculated to be $\sim 5 - 8\mu$s (Rots et al., 1998). The *RXTE* Mission Operations Center performs roughly 10 calibration observations per day, achieved with a round trip signal, tagged by the spacecraft clock time stamp, thus determining the spacecraft offset from the ground station clock at White Sands (Rots et al., 1998).

Instrument evolution

In March 1996, PCUs 3 and 4 began to exhibit failure events, while PCU 1 began to show such events in March 1999. The failures are typified by a sudden, dramatic increase in count rate. An afflicted PCU is turned off within one minute when this occurs. Failures of this type are minimized in several ways. First, PCUs are cycled on and off to lengthen the lifetime of each unit. The voltage across all units was

[1]The propane layer can also be used as a photon detection layer for 1.8 – 3.5 keV photons

decreased by $\sim 35\%$ to $\sim$2000 V, since it was found that this lessened the incidence of breakdowns. The operation temperature for the units was increased to $\sim 0.5°$C, also decreasing the incidence of unit failures (Jahoda et al., 2006).

In early 2000, the propane layer of PCU0 was lost, likely as a result of a collision with a micro-meteor (Jahoda et al., 2006). The charged particle background of this PCU increased dramatically, and is therefore often excluded in flux analyses. However, timing information is not seriously affected.

Today, fourteen years into the mission, the average number of active PCUs in any observation has fallen from $\sim$4 to $\sim$2, and the instance of instrumental flares has risen despite the measures implemented to minimize them. However, for an admittedly aged telescope, the PCA remains an efficient detector of X-rays and has continued to produce new and interesting results well into its twilight years.

2.1.3 The experimental data system

The Experimental Data System (EDS) is a micro-processor driven data system used for the on-board processing of PCA and ASM data. The EDS consists of eight independent processors, called "Event Analyzers" (EAs). Six EAs are dedicated to the PCA data stream, while two are reserved for ASM data processing.

Every event is passed from the PCA to the EDS. The EDS provides a time stamp with $\sim 1\mu$s resolution to each incoming PCA event (Bradt et al., 1993). All background rejection and time stamping is performed by the EDS. Data compression is also performed at this stage for the various data modes, discussed below.

Data modes

There are two main classes of data modes that are processed by the EDS: event mode and binned mode. Event mode records each photon as a separate event, while binned mode data records histograms to telemeter to the ground (where either time, energy, or both can be binned).

Two EAs are reserved for `Standard` data modes, which are taken for every observation in order to produce a uniform database for archival purposes. `Standard1` records data with 0.125 s time resolution and no spectral resolution, while `Standard2`

records 129 energy channels for each PCU layer with a time resolution of 16 s.

For sources with count rates <420 counts s^{-1}, one of the uncompressed data-modes such as `GoodXenon` or `GoodXenonWithPropane` can be used. Uncompressed data modes require two EAs, one each for spectral and temporal information. Both `GoodXenon` modes record the arrival time (with 1-μs resolution) and energy (256 channel resolution) of every unrejected event. Pulsar observations are typically performed in one of the two `GoodXenon` modes, since the relatively low count rates allow for the maximum use of the instrument, with all information being retained. All of the *RXTE* data analyzed in this thesis were taken in `GoodXenon` mode.

2.1.4 Preliminary analysis of RXTE pulsar timing data

The *RXTE* data analyzed in this thesis were downloaded from the archive service operated by the High Energy Astrophysics Science Archive Research Center (HEASARC)[1] in Flexible Image Transport System (FITS) format[2]. All PSR J1846−0258 and PSR J0205+6449 data were obtained with the PCA in `GoodXenon` mode. The full listing of observations is given in Tables 2.1 and 2.2.

Several data selection criteria must be applied to each observation (see Table 2.4). An appropriate energy range (or equivalently, channel range) and the number of xenon detection layers (1, 2, or 3) from which to accept photons must be selected. The energy spectrum of the source dictates how these selections are made. However, these selections are determined empirically for each source. Most of the lower-energy counts (<10 keV) are absorbed by the first xenon layer, thus only sources with relatively hard X-ray spectra have counts from the second and third detection layers included. Data from all active PCUs are merged using the `Ftools`[3] (Blackburn, 1995) "`seextrct`" and "`fselect`," unless data from an active PCU are contaminated by an instrumental flare, or data from PCU0 are excluded due to the propane layer loss.

As discussed in detail in Chapter 3, photons need to be corrected to the time

[1] http://heasarc.gsfc.nasa.gov/docs/archive.html
[2] http://heasarc.gsfc.nasa.gov/docs/heasarc/fits.html
[3] http://heasarc.gsfc.nasa.gov/docs/software/ftools

Table 2.1: *RXTE* observations of PSR J1846−0258

Proposal Number	Epoch (Year)	Target	Offset (′)	Number of Obs	Exposure (ks)
40140	1999	AX J1845−0258	23.54	13	78.8
40141	2000	Kes 75	0.062	13	39.4
50075	2000	AX J1845−0258	23.02	18	89.4
60064	2001	AX J1845−0258	23.02	22	149.7
60129	2001	G29.7−0.3	0.062	24	129.5
70073	2002	AX J1845−0258	23.02	13	74.8
70085	2002	J1846−0258	2.00	27	195.2
80095	2003	J1846−0258	0.005	23	196.2
90071	2004	J1846−0258	0.016,23.5[a]	29	225.3
91071	2005	J1846−0258	0.016,23.5[a]	44	224.0
92012	2006	J1846−0258	0.016	40	159.7
93010	2007-08	J1846−0258	0.002	83	358.6
94010	2009	J1846−0258	0.002	51	203.5
95010	2010	J1846−0258	0.002	9	39.4

[a] - Several of the observations in this observing program were erroneously pointed at the Candidate AXP AX J1845−0258 rather than PSR J1846−0258. PSR J1846−0258 remained in the field of view, thus the only effect was a lower signal-to-noise ratio for these observations.

Table 2.2: *RXTE* observations of PSR J0205+6449

Proposal Number	Epoch (Year)	Target	Offset (′)	Number of Obs	Exposure (ks)
60130	2001	G130.7+3.1	0.333	5	65.4
70089	2002	J0205+6449	0.042	34	319.7
90080	2003	J0205+6449	0.027	59	282.7
91063	2004	J0205+6449	0.003	48	383.7

Table 2.3: J2000 source positions

Source	**Right Ascension**	**Declination**	**Ref.**
PSR J1846−0258	$18^{\rm h}46^{\rm m}24\overset{\rm s}{.}94 \pm 0\overset{\rm s}{.}01$	$-02°58'30.1'' \pm 0.2''$	1
PSR J0205+6449	$02^{\rm h}\ 05^{\rm m}\ 37\overset{\rm s}{.}92 \pm 0\overset{\rm s}{.}02$	$64°\ 49'\ 42.8'' \pm 0.72''$	2

References: 1. Helfand et al. (2003); 2. Slane et al. (2002).

they would have arrived at the barycentre, the centre of mass of the solar system. Each selected event is converted to barycentric dynamical time (TDB) using the J2000 source position, listed in Table 2.3, and the JPL DE200 solar system ephemeris (Standish, 1982). Barycentering is performed with the `Ftool` "`faxbary`," which takes the orbit of the satellite as well as the motion of the Earth into account, while also performing the other corrections discussed in Chapter 3.

Finally, a time series is created from the selected events, where the time resolution can be as high as 1μs for PCA data. For both pulsars analyzed here, a time resolution of $t_r = 2^{-10}\text{s} = 1/1024\,\text{s}$ is used. Data are converted into a format created at the Massachusetts Institute of Technology (MIT) for handling raw spacecraft telemetry data, deemed "`DS`" format, which is useful for analyzing *RXTE* data because of the large number of instrument-specific tools created at MIT[1]. Further tools for handling pulsar timing data for *RXTE* were developed at McGill by Drs. Fotis Gavriil and Rim Dib.

2.2 Advanced Satellite for Cosmology and Astrophysics

Two observations of the supernova remnant Kes 75 were taken with the Advanced Satellite for Cosmology and Astrophysics in 1993 and 1999, and are presented in Chapter 5.

[1]Data can also be obtained from MIT directly in `DS` format more rapidly than from the HEASARC archive in FITS format. Data are typically available 2 days rather than 2 weeks after an observation. This is achieved using a temporary satellite ephemeris file. This allows for a quick look at the data to check for transient behaviour that might require a Target of Opportunity observation to be triggered, such as X-ray bursts or a glitch. However, we report only on data obtained in FITS format from HEASARC in this thesis.

Table 2.4: *RXTE* Analysis Parameters for PSR J1846−0258 and PSR J0205+6449

Parameter	**PSR J1846−0258**	**PSR J0205+6449**
Data Mode	GoodXenon	GoodXenon
Time Binning (s)	1/1024	1/1024
Profile bins	16	64[a]
Energy Range (keV)	2 – 20	2 – 18; 2 – 60[b]
Layers used	1	1; 3[a]

[a] – The number of bins across the profile listed here only refers to the pulse profile analysis performed for PSR J0205+6449. The timing analysis for this pulsar was performed using a maximum likelihood method which does not employ phase bins. This method was developed by Dr. S. Ransom and is described in detail in Chapter 4.

[b] – The pulse profile analysis was performed using two sets of analysis parameters to provide superior signal-to-noise ratios for different energy ranges of *RXTE* data. Lower energy counts are preferentially absorbed by the first layer of the PCA, while higher energy counts are often absorbed by the second or third xenon detection layer.

The fourth Japanese X-ray mission, the *Advanced Satellite for Cosmology and Astrophysics*, or *ASCA*, was launched February 20, 1993. During a geomagnetic storm on July 14, 2000, control of the spacecraft was lost, ending scientific observations[1].

ASCA consisted of four large-area X-Ray Telescopes (XRTs), each with an X-ray detector located at the focus. The 4 XRTs had a combined effective area of 1300 cm^2 at 1 keV and 600 cm^2 at 7 keV. The XRTs consisted of conical surfaces (in approximation to a Wolter Type I design) built from 120 nested thin aluminum/gold foils. The XRTs were able to focus photons in the 0.5 – 12 keV energy range and had a 24′ field of view (at 1 keV). The half power diameter angular resolution was 2.9′ (Serlemitsos et al., 1995).

Two detectors were "Gas Imaging Spectrometers" (GISs) and two were "Solid-state Imaging Spectrometer" (SISs). The SISs were charge coupled device cameras, while the GISs were gas imaging scintillation proportional counters (Tanaka et al., 1994). The GISs were sensitive to photons in the energy range of 0.7 – 10 keV with

[1] http://heasarc.gsfc.nasa.gov/docs/asca/asca_nra06/appendix_e/appendix_e.html

an energy resolution of 8% at 6 keV. They had a circular field of view of 50′. Each GIS consisted of a xenon/helium gas cell and a phototube. The photo-multiplier tube had ten stage dynodes with a 7.5 cm thick quartz window. The maximum time resolution was 61μs, enabling pulsar timing observations, as well as imaging observations (Ohashi et al., 1996).

2.3 Detecting Radio Pulsations

In this thesis, we analyze pulsar timing data from single antenna, or dish, radio telescopes. Radio waves are reflected by the dish to the focus of the telescope, where a waveguide feed samples the signal with two channels for orthogonal polarizations. The signal is then amplified by a low-noise amplifier with frequency response centered at $f_{\rm RF}$. The signal is then sent through a bandpass filter to remove noise from non-astrophysical out-of-band signals. In order to improve transmission efficiency as well as for software compatibility reasons, the frequency is down-converted to an intermediate frequency, $f_{\rm IF}$, with a mixer. The signal, $f_{\rm RF}$, is mixed with a local oscillator of frequency $f_{\rm LO}$, such that $f_{\rm IF} = f_{\rm RF} - f_{\rm LO}$. The intermediate frequency is then corrected for the "dispersion" of the pulse. Dispersion is the frequency dependent delay of a radio signal which arises from interaction with interstellar plasma. This has important implications for pulsar timing and is described in detail in Chapter 3. The dispersion of the signal can be corrected at the telescope, that is, dedispersed, with the use of a filterbank spectrometer, or other dedispersion technique (though filterbanks are used in this work). In the case of a filterbank spectrometer the signal is passed through narrow-band filters and split into many adjacent frequency channels. A time delay is then added to each frequency channel to correct for the dispersion of the pulse. After online dedispersion, the signal is digitized and recorded to disk for further off-line analysis.

2.4 The 76-m Lovell Telescope at the Jodrell Bank Observatory

Observations of PSR J0205+6449 were obtained with the Jodrell Bank Observatory between 2005 and 2008. The analysis of these data appears in Chapter 4.

The 76-m Lovell telescope at the Jodrell Bank Observatory, Cheshire, England, is the world's third largest fully steerable radio telescope. Construction of the telescope began in 1951 and observations of celestial sources began in 1957. An image of the telescope is shown in Figure 2.4. The dish is a prime focus paraboloid which is altitude-azimuth mounted and has a collecting area of 5270 m^2.

Radio waves are reflected by the paraboloid dish to the focus box on top of a central tower, where a dual-channel receiver is located. For higher-frequency observations ($>$ 800 MHz), the receiver is kept cooled to 10–15 degrees above absolute zero to minimize receiver noise. Several receivers have been used which are sensitive to radio frequencies up to 5 GHz.

Several upgrades have been performed on the telescope since its inception. In particular, major structural upgrades were performed between 1969 and 1971 and the surface was upgraded in 1971 and 2001. The 2001 surface upgrade increased the bandwidth by a factor of four (by allowing higher frequency radio waves to be focused by the dish) and resulted in an increase in the telescope sensitivity.

2.4.1 Pulsar timing observations at Jodrell Bank

After down-conversion to an intermediate frequency as described in §2.3, the signal is split into 64 channels (for each polarization channel, that is 2×32 channels) by a filter-bank spectrometer and 1-bit digitized. Data are dedispersed in hardware and folded on-line with the predetermined spin-period and dispersion measure (Hobbs et al., 2004). Orthogonal polarizations are combined and radio-frequency interference that dominates sub-integrations is removed (Hobbs, 2002). Remaining subintegrations are folded to produce a pulse profile, sampled with high time resolution.

Further information specific to observations of PSR J0205+6449 is given in Chap-

Figure 2.4: The 76-m Lovell Telescope. Photograph by Mike Peel (www.mikepeel.net) Creative commons copyright (CC-BY-SA-2.5.).

ter 4.

2.5 The 100-m Robert C. Byrd Green Bank Telescope

Observations of PSR J0205+6449 were obtained with the Green Bank Telescope in 2002 and 2003, and the analysis of these data appears in Chapter 4.

The 100-m Robert C. Byrd Green Bank Telescope (GBT), shown in Figure 2.5 is the world's largest fully steerable radio telescope. It is located outside the town of Green Bank, West Virginia and is operated by the National Radio Astronomy Observatory[1].

The dish is a 100-m by 110-m elliptical section of a 208-m paraboloid, which changes the focal length from that of a 100-m paraboloid, allowing for an off-axis feed arm, visible in the figure. This orientation keeps the aperture free from obstruction, in contrast to the more typical design where the receiver is supported by a central arm which lessens the overall senstivity and complicates the response pattern to radiation (Jewell & Prestage, 2004).

The telescope has a wheel and track design, and can view all angles above 5°

[1]www.gb.nrao.edu/

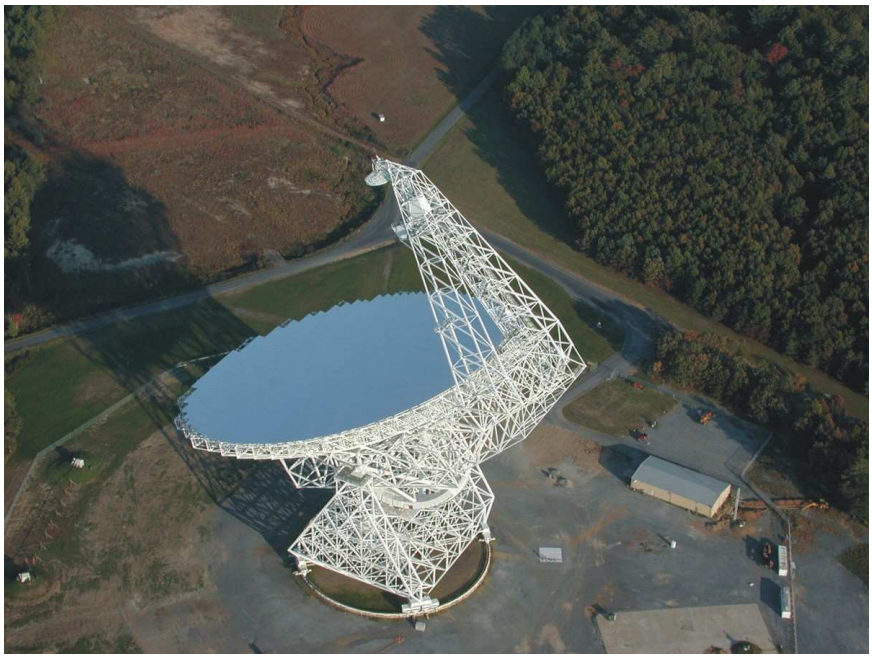

Figure 2.5: The Robert C. Byrd Green Bank Telescope. Image credit: NRAO/AUI/NSF.

elevation. The track upon which the dish is moved is extremely precise in order to provide very accurate pointing (4″ blind) of the 7856 metric ton structure.

The GBT was specifically designed to be sensitive to very high frequency radio waves, and can observe frequencies between 100 MHz and 115 GHz (Prestage et al., 2009). The surface has 2,004 adjustable panels, which are used to create the active surface necessary to observe high radio frequencies. For observations above 1.2 GHz, a secondary reflector is placed at the prime focus of the telescope and used to focus radio waves to a receiver cabin located on the feed arm. This helps to minimize noise from the ground, which becomes increasingly problematic at higher radio frequencies.

Further information concerning the observations of PSR J0205+6449 is given in Chapter 4.

2.5.1 *Berkeley-Caltech Pulsar Machine*

Early pulsar observations at the GBT (such as those of PSR J0205+6449) were taken with the Berkeley-Caltech Pulsar Machine (BCPM; Backer et al., 1997), an analog/digital filterbank which samples 2×96 channels.

A digital filterbank, unlike an analog filterbank, offers flexibility in total bandwidth, channel bandwith, and channel spacing. The maximum bandwidth for the BCPM is 172 MHz and the finest time resolution is 2.4 μs (Foster et al., 1996).

Two intermediate frequency signals (one for each polarization channel) are sent to an array of 2×6 mixer/filter modules, which perform low-pass filtering and baseband mixing. These modules provide variable width filters, resulting the flexibility of this type of filterbank. The signals are then passed to 2×6 digital filter boards. The bandwidth is set by the requirements for the current observations. Each filter board splits the signal into 16 frequency channels, resulting in a total of 2×96 channels (Camilo et al., 2002c). Combiner boards down-sample power vectors and sum polarization pairs. The data mean is removed and the signal is 4-bit digitized. Data are sent to a workstation and recorded onto disk for offline processing[1].

[1] http://www.gb.nrao.edu/∼dbacker/

3
Pulsar Timing

3.1 Introduction

Finding a precise description of the rotation of a pulsar over an extended period of time has many applications. This is best achieved with phase-coherent pulsar timing, that is, fully accounting for each rotation of the pulsar, such that the phase of the pulse can be unambiguously determined at any time (e.g. Boynton et al., 1969). Phase-coherent timing provides sufficiently accurate spin-parameters to allow for the measurement of braking indices for some pulsars, as well as the accuracy required to distinguish between small glitches and timing noise. The same techniques are used to find orbital parameters of binary pulsars, leading to tests of the theory of General Relativity, among many other applications.

In this Chapter, we review the basic techniques of pulsar timing and the preliminary analysis performed on pulsar data in order to establish a phase-coherent timing solution and find pulsar rotational parameters.

3.2 The Time Series

Pulsar data are collected by a telescope either as a continuous signal (for radio data) or as individual events (for X-ray and γ-ray data). Radio data are sampled with high time resolution to create a time series. Although much of the subsequent analysis can be performed from either events or a time series, for timing purposes, X-ray data are often converted into a time series (as described for *RXTE* data in §2.1.4). An example of a time series for the young pulsar PSR B1509−58 made with *RXTE* data

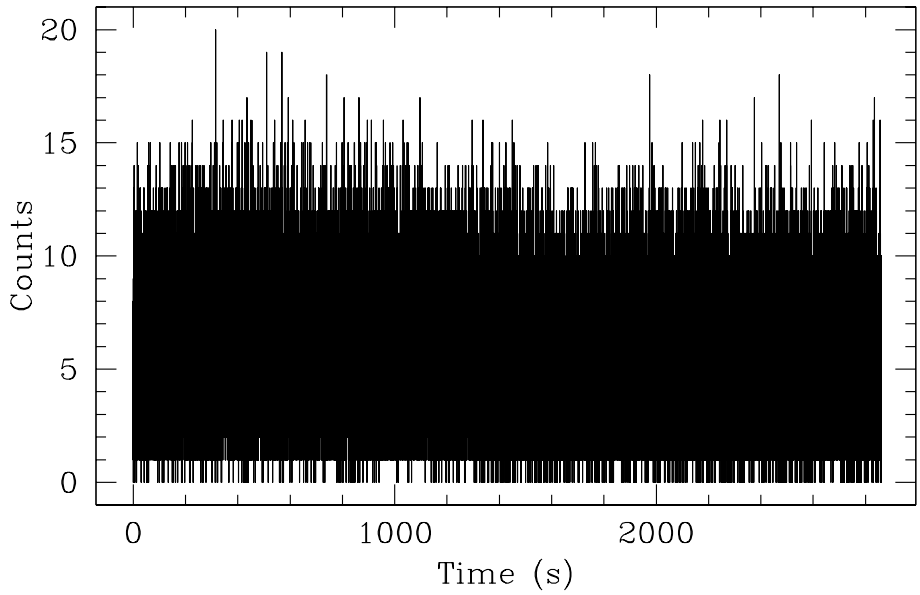

Figure 3.1: A time series for PSR B1509−58 (P=151 ms) made from *RXTE* data. 5.1×10^5 counts were detected in the 2860 s observation containing counts from all three xenon layers of *RXTE* in the energy range 2 – 60 keV.

is shown in Figure 3.1[1].

3.3 The Pulse Profile

Each pulsar has a unique emission profile in phase, essentially a cross-section through the emission beam, called a "pulse profile" (Manchester & Taylor, 1977). However, most known pulsars are much too dim for a single pulse to be observable. This can be seen in Figure 3.1, in which the time series has no visible modulation at the 151 ms pulse period of the pulsar contained within. In order to observe pulsed emission many

[1]PSR J0205+6449 data are reduced in a different manner for several stages of the process described in this Chapter. Details of the analysis for PSR J0205+6449 are described in Chapter 4.

(typically hundreds to thousands) pulses are summed together in order to increase the signal-to-noise ratio. This is achieved by dividing the time series at the pulse period and summing the data subsets together, a process called "folding." Background noise will largely cancel, while the signal will not, thus increasing the signal-to-noise ratio of the pulse and making it visible (Lorimer & Kramer, 2005). In practice this is achieved by using the known ephemeris to calculate the pulse phase of each bin of the time series (or for each individual event), and assign each to a phase bin, as shown for the pulsar PSR B1509−58 with 64 phase bins in Figure 3.2. The optimal number of phase bins across the pulse profile to be used in a given analysis is determined by the pulse period of the source, the signal-to-noise ratio of individual pulses and the duty cycle of the pulse.

3.4 Finding the Pulse Period

In some cases, the pulsar ephemeris is not known with sufficient precision to obtain a pulse profile. This arises in cases in which there is no previous phase-coherent timing solution, after a large glitch where the spin-frequency changed significantly, or after a gap between subsequent timing observations (because many young pulsars spin-down rapidly, their spin frequencies vary on short time scales).

In such cases, a "periodogram" or epoch folding can be performed (Leahy et al., 1983). Data are folded many times in succession with slightly different spin-frequencies over a relatively narrow frequency range. Then for each profile, the χ^2 statistic is calculated for each resulting profile, given by,

$$\chi^2 = \sum_{i=1}^{j} \frac{(p_i - < p >)^2}{{\sigma_i}^2}, \tag{3.1}$$

where j is the number of phase bins across the profile, p_i is the number of counts in each phase bin, and $< p >= 1/N \sum_{j=0}^{N-1} p_j$ is the average number of counts in each phase bin, with N being the total number of counts in the profile. Because photon arrival times are governed by Poissonian statistics, $\sigma_i = \sqrt{p_i}$.

The χ^2 for each folded profile is considered against the null hypothesis that the count rate is constant. The maximum χ^2 corresponds to the profile the most different

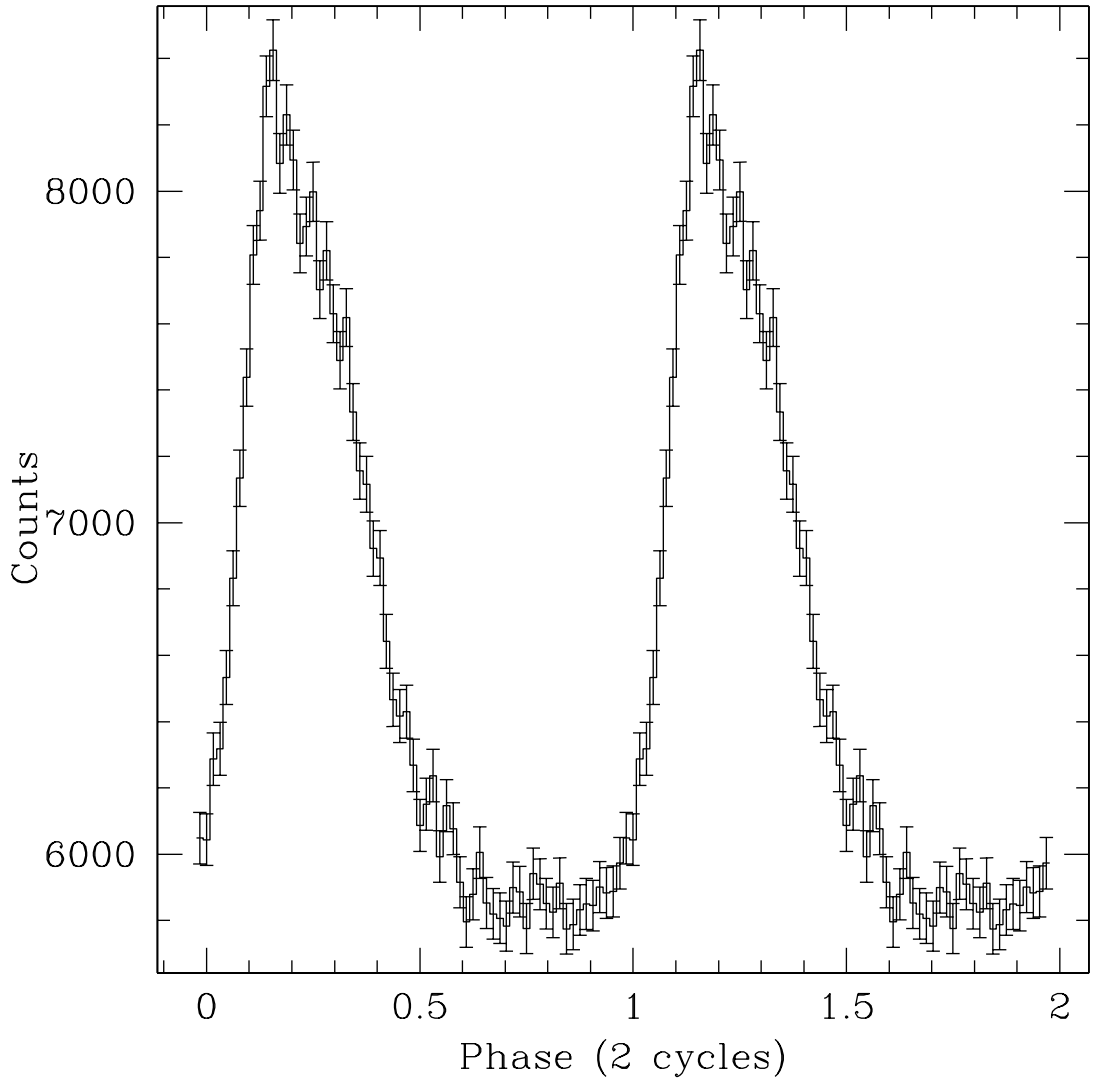

Figure 3.2: A 2 – 60 keV X-ray pulse profile for PSR B1509−58. This profile was produced by folding the time series shown in Figure 3.1. The pulse period of the pulsar is $P = 151$ ms and the profile has 64 phase bins. Two cycles are shown for clarity.

from a constant, which, in turn, will correspond to the best spin-frequency of the pulsar in case of a detection, as shown in Figure 3.3.

In some cases, a pulsar is suspected to be present in data but no pulsations have yet been found, thus no pulse period information is known (e.g. a point source at the centre of a supernova remnant). In such cases, a periodogram is too computationally expensive, so a Fourier transform is performed instead. A peak in the power spectrum may be associated with a pulsar spin period. However, searches for pulsed signals can be significantly more complex than a simple Fourier transform. For example, pulsars in binary systems are accelerated as they travel around their orbits, resulting in a smearing of a peak in a power spectrum. To find such sources, changes in spin period due to acceleration must also be searched. Another unknown is the dispersion measure, DM, of the pulsar, discussed in detail in §3.6 below. The DM is the integral of the density of free electrons along the line of sight to the pulsar, which impart a frequency-dependent delay to the radio pulse. The net effect is a broadening of the pulse, which can prevent a detection in many cases. Thus, a wide range of DMs must be searched. For this thesis, an estimate of the pulse period is always known beforehand, thus these latter types of searches are not discussed further. For a good review of search techniques see Ransom (2001).

Once a good estimate of the spin-period has been found, the data can be folded as described above in §3.3.

3.5 Finding the Pulse Time of Arrival

The goal of the analysis thus far is to produce pulse arrival times that can then be related in a phase-coherent manner. If the ephemeris used to fold the pulse profile perfectly described the rotation of the pulsar, the peak of each profile would arrive at the same phase. In that case, the peak phase of each profile could simply be converted to a time of arrival.

However, such an accurate ephemeris is rarely known. Phase jitter, measurement uncertainities, or innaccurate spin parameters result in phase-offsets between an in-

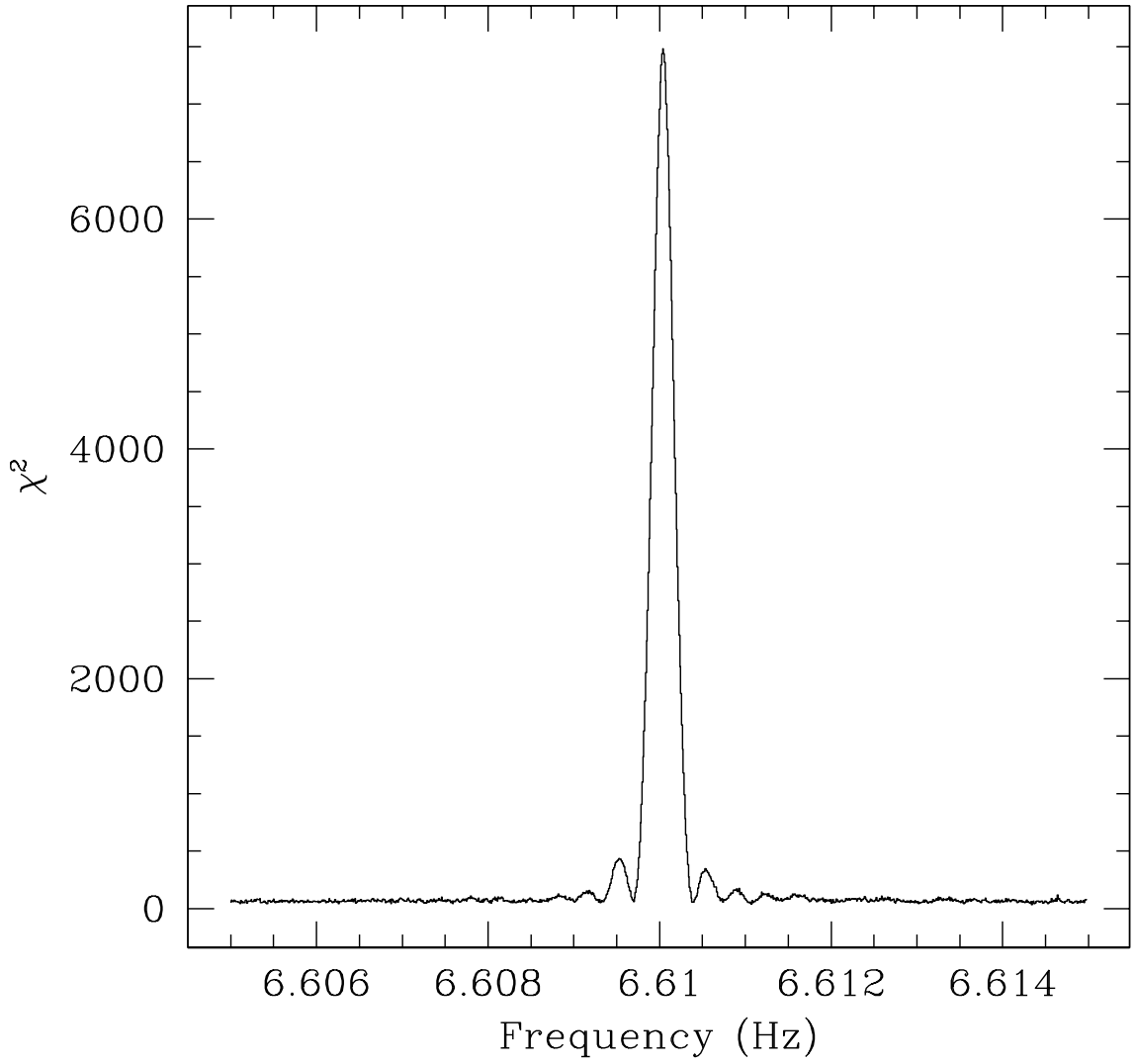

Figure 3.3: An example of a periodogram χ^2 output for PSR B1509−58. The visible side lobes arise as a result of a finite data train, that is, the output of the periodogram is the convolution of the periodic pulsar signal and a rectangular window.

dividual profile and a high signal-to-noise average profile. These offsets must be accounted for in order to maintain the correct phase relationship between subsequent observations.

Pulse profiles are typically stable on long time scales, so for a single observation, the profile, $p(t)$ can be compared to a high signal-to-noise template profile, $s(t)$, built by aligning and summing many individual observations (Taylor, 1992). Each individual profile is assumed to be a lower signal-to-noise version of the template, shifted by an arbitrary amount, τ,

$$p(t) = As(t - \tau) + N(t), \tag{3.2}$$

where A is a scale factor, and $N(t)$ is background noise. The time, τ, or phase, $\delta\phi = \tau/P$, offset is calculated by the cross-correlation of the individual profile with the template (e.g. Boynton et al., 1969). An example of an individual profile with a phase offset from a high signal-to-noise template is given in Figure 3.4.

Pulsar spin parameters are obtained by measuring the time between successive pulses. To find the correct relationship between pulses, a single point on the pulse profile, typically the highest peak, is chosen as the fiducial point to be compared with all other measured profiles of the source. The fiducial point for each profile is cross-correlated (see below) with the template and assigned an absolute time stamp and called the pulse "Time Of Arrival" (TOA). The elapsed time between TOAs is compared to extract values of ν and $\dot{\nu}$, as discussed further in §3.7.

3.5.1 Cross-correlation

Cross-correlation is closely related to convolution and is given by

$$(s \star p)(\delta\phi) \equiv \int_{-\infty}^{\infty} s^*(\phi)p(\phi + \delta\phi)d\phi, \tag{3.3}$$

where $s^*(\phi)$ is the complex conjugate of the template and $p(\phi)$ is the individual profile. The value of $\delta\phi$ which maximizes $s \star p$ is the optimal phase offset. Using the convolution theorem, we can write Equation 3.3 as

$$\mathcal{F}(s \star p) = \mathcal{F}^*(s) \cdot \mathcal{F}(p) \tag{3.4}$$

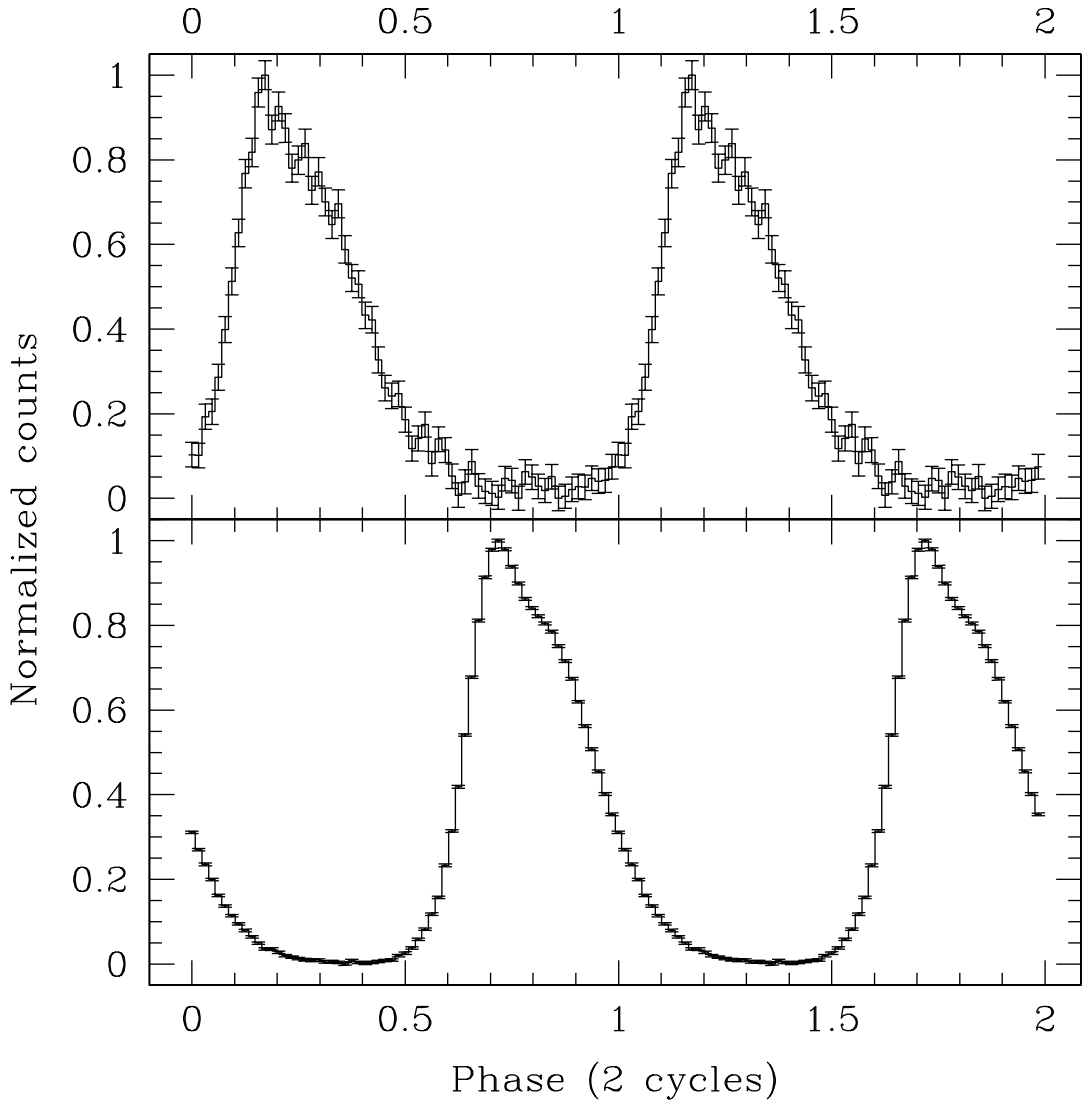

Figure 3.4: An individual profile (as from Fig. 3.2) and high significance template for PSR B1509−58 each with 64 phase bins. The template was created by phase-aligning hundreds of individual profiles, all with photons from three xenon layers and in the energy range 2 – 60 keV. Two cycles are shown for clarity.

where $\mathcal{F}$ indicates a Fourier transform. The advantage of performing the cross-correlation procedure in the frequency domain rather than the time domain is that it allows the user to filter out higher order harmonics if desired. This can be useful for many X-ray pulsars which tend to have nearly sinusoidal profiles.

The TOA is then given by

$$TOA = t_0 + \delta\phi/\nu(t_0), \tag{3.5}$$

where t_0 is the reference epoch used to fold the data.

The uncertainty on each TOA is determined by a Monte Carlo simulation where 10,000 simulated profiles are created with Poissonian noise added to each. Simulated noisy profiles are cross-correlated with the template in the same manner as the original profile and the phase offset is measured for each. The standard deviation from the resulting 10,000 offsets is taken to be the TOA uncertainty.

3.6 Corrections to Pulse Times of Arrival

A simplistic view of phase-coherent timing relies on the spin-down of the pulsar being the only factor affecting the time of a pulse's arrival at the observatory. In practice, this is not the case. As the pulse travels from the neutron star to the observatory, it is smeared by electrons in the interstellar medium, and the gravitational wells of the Sun and other bodies in the solar system as well as other relativisitic effects affect the arrival time of the pulse. In addition, the observatories used to acquire the data are moving due to the motion of the Earth, and in the case of X-ray observations, the motion of the satellite. Thus the time between successive pulses is affected by many factors. These must be properly accounted for before accurate spin parameters can be extracted from the data.

This work discusses both X-ray and radio pulsar timing, for which there are several differences in data collection and analysis, largely related to the differences between counting photons (as in X-ray astronomy) and recording a continuous signal (as in radio astronomy), though the rapidly moving satellite in the case of X-ray observations

adds a complicating factor. For X-ray observations, the corrections are applied to individual photons before data are folded and a TOA is extracted (e.g. Nagase et al., 1990), while corrections are applied to the already-built TOA for radio timing data.

Because of the motion of the Earth and/or motion of a satellite, pulsar observations are taken from a moving observatory. To correct for this, pulse arrival times must be adjusted to the solar system barycentre (the centre of mass of the solar system). Thus, a good model of solar system dynamics is required. An inherent advantage for radio observations is that this information about the motion of the Earth is contained within the TOAs, allowing for the pulsar position and proper motion to be fit from the data, since this information is not removed before folding a pulse profile.

A corrected TOA, t, (or a corrected single photon arrival time) is given by:

$$t = t_{obs} + \Delta_c + \Delta_R(\alpha, \delta, \mu_\alpha, \mu_\delta) + \Delta_{E_\odot} - \Delta_{S_\odot}(\alpha, \delta) - \frac{D}{f^2}\,, \tag{3.6}$$

where t_{obs} is the measured time of arrival at the observatory and Δ_c is a clock correction between the standard time and the observatory clock time. The Roemer propagation delay, Δ_R, is the light travel time across the Earth's orbit, where the pulsar position is given in right ascension (α) and declination (δ), and the proper motion is μ_α and μ_δ, respectively (Taylor, 1992). The correction for the Roemer delay includes the correction to the solar system barycenter, $\overrightarrow{r_{\rm ob}} \cdot \hat{s}/c$, where $\overrightarrow{r_{\rm ob}}$ is the vector from the observatory to the barycentre, and $\hat{s}$ is the unit vector in the direction of the source (Taylor, 1992).

The Einstein delay, $\Delta_{E_\odot}$, corrects for the relativistic effects of time dilation and gravitational redshift due to the motion of the Earth and other bodies in the solar system (Taylor, 1992), while the Shapiro delay, $\Delta_{S_\odot}(\alpha, \delta)$ corrects for the delay of the pulse signal due to its travel through the gravitation potential well of the Sun (Manchester & Taylor, 1977).

Finally, D, is the dispersion constant, which at an observing frequency f imparts a time delay of $-D/f^2$ to a radio pulse. Dispersion is the cumulative effect of all the charged particles along the line of sight to the pulsar, both in the interstellar medium and from material in the immediate environment of the pulsar, e.g. from progenitor

stellar winds or a supernova remnant (Backer et al., 1993). The result of dispersion is that lower frequency radio waves arrive at the telescope later than higher frequency waves. Because signals from radio pulsars are broadband in nature, and radio telescope receivers are sensitive to some finite frequency bandwidth (preferably large in order to maximize sensitivity to weak pulsar signals), the resulting pulsed is smeared compared to the true pulse, in some cases preventing its detection (Manchester & Taylor, 1977). The dispersion constant, D, is defined as:

$$D \equiv \frac{t_2 - t_1}{f_2 - f_1} = \frac{e^2}{2\pi mc} DM. \tag{3.7}$$

Where, DM, the dispersion measure (in units of $\mathrm{pc\,cm^{-3}}$) is the integral of the free electron density, n_e, to the pulsar at a distance d, that is (e.g. Lyne & Smith, 2005)

$$DM = \int_0^d n_e(x) dx. \tag{3.8}$$

The resulting time delay between a single pulse observed at two frequencies f_{low} and f_{high} is then given by:

$$\Delta t = \frac{DM}{2.410 \times 10^{-4}} \left(\frac{1}{f^2{}_{low}} - \frac{1}{f^2{}_{high}} \right) \mathrm{s}. \tag{3.9}$$

Because DM is related to the distance to the source, in principle, the distance to radio-loud pulsars can be estimated from the measured DM (Cordes & Lazio, 2002). However, a good knowledge of the distribution of free electrons in the galaxy is required for an accurate estimate of pulsar distances and can be biased by an excess near a remnant or an HII region. Current models, such as that given in Cordes & Lazio (2002), are known to have inaccuracies resulting in large uncertainties in some distances estimated in this way. The frequency dependence of dispersion means that the dispersion for an X-ray photon is negligible and this term can be safely neglected in the high-energy regime.

3.7 Phase-coherent Pulsar Timing

If we assume that the pulsar phase varies smoothly (e.g. from magnetic dipole spin down), corrected TOAs can be fitted with a Taylor expansion in pulse phase, ϕ. Pulse

phase at time t can be expressed as

$$\phi(t) = \phi(t_0) + \nu_0(t - t_0) + \frac{1}{2}\dot{\nu}_0(t - t_0)^2 + \frac{1}{6}\ddot{\nu}_0(t - t_0)^3 + \frac{1}{24}\dddot{\nu}_0(t - t_0)^4 \ldots, \quad (3.10)$$

where the subscript "0" denotes a parameter evaluated at the reference epoch (Manchester & Taylor, 1977). TOAs are fitted with an intial model using the software package `TEMPO`[1]. The software was written primarily by J.H. Taylor and R.N. Manchester and the major scripts used are outlined in Taylor (1992). `TEMPO` takes as input spin parameters, position, and DM. If the spin parameters are known with sufficient accuracy, the phase will be close to an integer number of rotations. Phase residuals are defined as

$$R = \phi - n_i \,, \quad (3.11)$$

where n_i is the closest integer to $\phi(t)$ (as calculated from the initial model), corresponding to the i^{th} TOA. `TEMPO` then performs a χ^2 minimization of the weighted sum of squared residuals,

$$\chi^2 = \sum_{i=1}^{N} \left(\frac{\phi(t) - n_i}{\sigma_i / P} \right)^2 \,, \quad (3.12)$$

and gives as output refined parameters and phase residuals resulting from these fitted parameters, an example of which is shown in Figure 3.5[2].

Residuals can be used to diagnose an incorrect spin parameter value, a position error, a proper motion, a glitch or timing noise. An incorrect ν will be seen as a linear trend in the residuals, while an incorrect value of $\dot{\nu}$ will produce a parabola. A position error (or an error in the solar system ephemeris) will produce a sinusoid with a 1-yr period in the timing residuals, an example of which is shown in the top panel of Figure 3.5, while proper motion will produce a 1-yr sinusoid with increasing amplitude (Manchester & Taylor, 1977). Timing noise is visible as a long-term wander of the pulse phase, while a glitch (a sudden increase in ν) is visible as a linear decrease in timing residuals.

[1] Software can be found at http://www.atnf.csiro.au/research/pulsar/tempo/

[2] `TEMPO` performs barycentering and the other corrections given in Equation 3.6 for Earth-based timing observations. These corrections are performed separately for space-based observations. For *RXTE* data, barycentering is done with the `FTOOL` "faxbary."

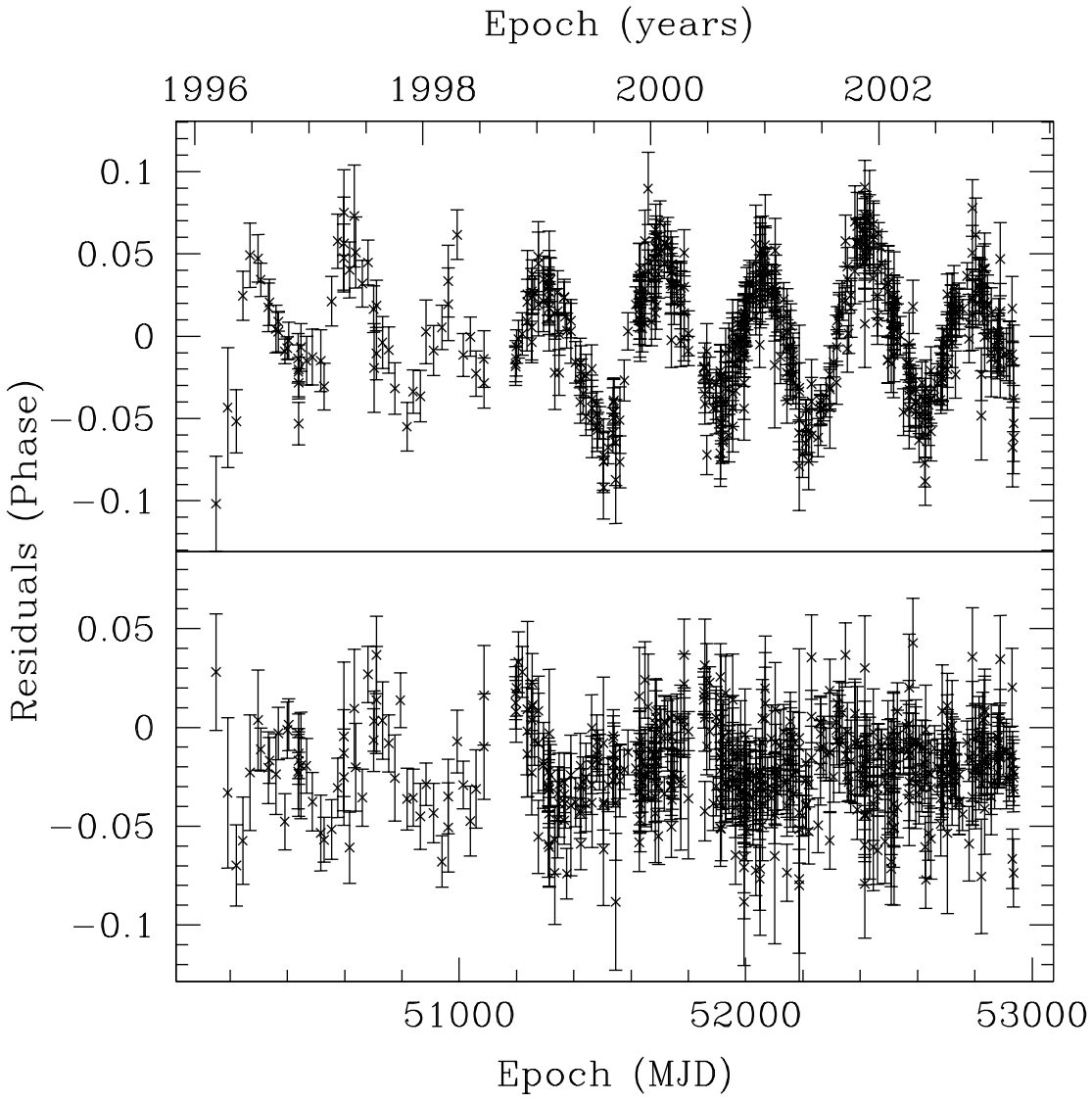

Figure 3.5: An example of timing residuals for the pulsar PSR B0540−69. The top panel shows phase residuals with the position determined from 2001 *Chandra X-ray Observatory* observations of the source. The bottom panel shows phase residuals with a position fitted from timing residuals, 1.3″ from the *Chandra* position (Livingstone et al., 2005a).

To establish a phase-coherent timing solution, it is necessary to acquire closely spaced observations so that ν and other parameters have not changed significantly between subsequent arrival times. In the case where input parameters are insufficiently precise or the gap between subsequent observations is too long, the result is a phase ambiguity between two pulse arrival times. That is, the pulse phase may have advanced by either $> +0.5$ or < -0.5, resulting in the loss of phase coherence.

We are now armed with the tools and techniques of pulsar timing, which can be used for a wide array of applications. In the following Chapters, we apply the above techniques to two young pulsars in order to explore their spin evolution.

4
The Young, Energetic Pulsar in the Supernova Remnant 3C 58

The contents of this Chapter first appeared in the article "X-ray and Radio Timing of the Pulsar in 3C 58," published in the *Astrophysical Journal* (Livingstone et al., 2009).

4.1 Introduction

PSR J0205+6449 is a 65-ms rotation-powered pulsar at the centre of the Crab-like supernova remnant 3C 58. The pulsar was discovered in a 2002 *Chandra X-ray Observatory* (*Chandra*) observation of the nebula, which had long been suspected of harbouring a pulsar, because a constant power source is required to produce the bright, non-thermal nebular emission (Murray et al., 2002). The pulsar was subsequently detected as a very low luminosity radio pulsar ($\sim$0.5 mJy kpc^2 at 1400 MHz; Camilo et al., 2002c). Despite its low radio luminosity, it is one of the most energetic pulsars in the Galaxy, with a spin-down luminosity of $\dot{E} \sim 2.7 \times 10^{37}$erg s^{-1}, a factor of $\sim$15 less than the Crab pulsar. The pulsar wind nebula is much less bright than the Crab nebula, particularly in X-rays ($\sim$2000 times dimmer; Green & Gull, 1982), while the pulsed X-ray luminosity of PSR J0205+6449 is $\sim$6000 times dimmer than that of the Crab pulsar (Murray et al., 2002).

The possible association between the 3C 58 pulsar/pulsar wind nebula complex and the historical supernova SN 1181 has long been a matter of debate. 3C 58 is the only known source positionally coincident and energetically compatible with the historical supernova, strongly suggesting an association (Stephenson & Green, 2002). However, in recent years, evidence has been mounting that the association may be

spurious and that the true age of the pulsar may be closer to its characteristic age, $\tau_c = 5.4\,\mathrm{kyr}$ rather than the implied historic age of 829 yr. If the source is 829-yr old, the size of the remnant implies a large expansion velocity ($\sim$4600 km s^{-1}; Stephenson, 1971) that is hard to reconcile with the measured velocities of the optical filaments (0.02–0.07″ yr^{-1} instead of $\sim$0.2″ yr^{-1}; Fesen, 1983; Fesen et al., 2008) and the expansion speed of the synchrotron bubble (0.014%/yr; Bietenholz et al., 2001; Bietenholz, 2006). The characteristic age estimate assumes that the pulsar was born spinning rapidly ($\nu_i \gg \nu$) and that the temporal spin evolution of the pulsar has proceeded according to the simple magnetic dipole spin-down model (as in §1.3). These assumptions are known to fail in some cases, such as for PSR J1811−1925 in the supernova remnant G11.2−0.3, for which the pulsar's characteristic age appears to be a factor of $\sim$15 greater than that of the remnant, as discussed in Chapter 1 (e.g. Torii et al., 1999; Kaspi et al., 2001b; Tam & Roberts, 2003). Likewise, the pulsar J0538+2817 has a characteristic age of 620 kyr, but a well established kinematic age of $\sim$40 kyr, implying a long initial spin period of $\sim$138 ms (Kramer et al., 2003; Ng et al., 2007). Similarly, if PSR J0205+6449 was born spinning with a period of $\sim$60 ms, the estimated timing age of the pulsar could be reconciled with the historical supernova age (Murray et al., 2002). An alternate explanation for the apparent timing age disparity for PSR J0205+6449 is that the pulsar was born with a short spin period but evolved more rapidly than is typically assumed for magnetic dipole braking, i.e. with $n \simeq 14$. However, while such scenarios can readily solve the discrepancy between the historical supernova age and the timing age of the pulsar, the kinematic remnant age of 2500–7000 kyr (Fesen et al., 2008, and references therein) remains inconsistent with the historical age, suggesting that the association between the pulsar/PWN complex and the 1181 event may be spurious.

In this chapter, we present three phase-coherent timing solutions for PSR J0205+6449 spanning 6.4 yr with data obtained from the Green Bank Telescope (GBT), the Jodrell Bank Observatory (JBO) and the *Rossi X-ray Timing Explorer* (*RXTE*). We discuss two large glitches and timing noise found in these data. We also

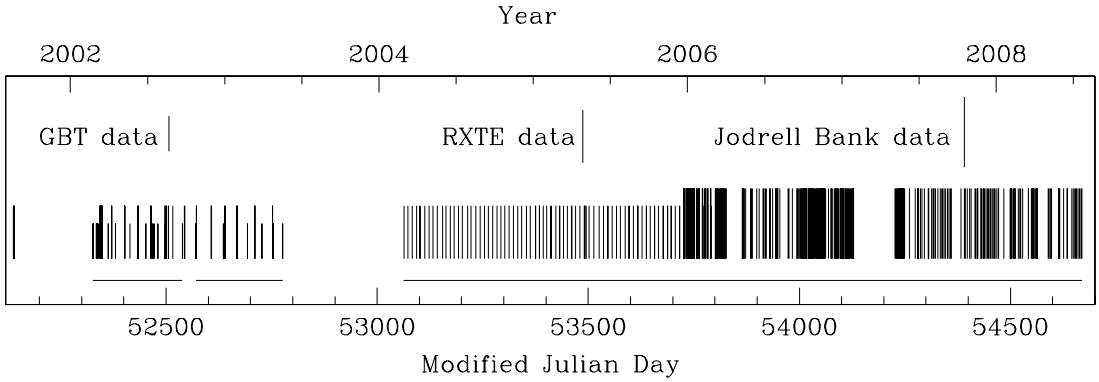

Figure 4.1: Distribution of observations of PSR J0205+6449 from *RXTE*, GBT, and JBO over 6.9 yr. GBT data are indicated with short lines, *RXTE* data with medium length lines, and JBO data with long lines. The three coherent timing solutions, spanning a total of 6.4 yr, are indicated with horizontal lines along the bottom of the plot.

present an analysis of the high energy emission of the pulsar from the *RXTE* data by examining the X-ray pulse profile from 2 – 40 keV and the phase offset between the radio and X-ray pulses.

4.2 Observations and Analysis

X-ray observations were taken with *RXTE*; radio observations were taken with the GBT and JBO, each detailed in Chapter 2. The data were unevenly spaced throughout 6.9 yr, as shown in Figure 4.1, and include a 202-day gap (between observations taken in *RXTE* Cycle 6 and Cycle 7) and a 287-day gap (corresponding to Cycle 8). GBT data are shown with short lines, *RXTE* data are shown with medium-length lines, and JBO data are shown with long lines. The first set of observations from *RXTE* Cycle 6 are only considered for the pulse profile analysis (§4.4) and are not included in the 6.4 yr of data used for the timing analysis (§4.3).

4.2.1 RXTE observations

X-ray data were obtained during *RXTE* observing Cycles 7, 9, and 10, spanning a period of 4 yr from 2002 February 22 to 2006 March 19 (MJD[1] 52327 to 53813), with

[1]MJD is a time unit called Modified Julian Day. Julian Day (or JD) is the number of days since Greenwich Mean Time on January 1, 4713 B.C.E at noon. MJD is given by JD−2400000.5 days,

a long gap (from MJD 52752 to 53036) corresponding to *RXTE* observing Cycle 8. In addition, four observations were taken in observing Cycle 6 (17.1 hr exposure over MJD 52138 – 52141). Because of the long data gap between the Cycle 6 data and the subsequent observations in Cycle 7 (202 days), they could not be unambiguously phase connected (i.e. there could be an additional phase turn or one less phase turn during the gap), rendering these observations of limited interest for our timing analysis. They were considered for a pulse profile analysis discussed in §4.4. The frequency for each Cycle 6 observation was determined by a periodogram analysis, which was then used for folding the data. Typically, 3 PCUs were operational during a single observation. For our timing analysis, we used only the first layer of each operational PCU in the energy range 2 – 18 keV, (*RXTE* channels 4 – 44) as this maximizes the signal-to-noise ratio of individual observations for this source.

We noted that two observations directly following the leap second occurring on 2006 January 1 had incorrect clock corrections, confirmed by the *RXTE* team (C. Markwardt, private communication). This was fixed by adding a 1 s time jump to each pulse time-of-arrival obtained from these observations.

The X-ray pulse profile as measured in each observing session by *RXTE* has two narrow components separated by approximately one-half of a rotation of the pulsar, as shown in Figure 4.2. Such sharp pulse features are usually very helpful for timing analyses, however, the "signal-to-noise" ratio (here defined as the ratio of pulsed source counts to all other counts) for the *RXTE* observations was very low, with typical values near 6×10^{-3}. These levels are so low that for some observations the pulses were not easily visible in the binned pulse profile plots. Therefore, in order to determine the TOAs from the X-ray data, we used a different technique than that described in Chapter 3. Instead, a maximum-likelihood technique for finding TOAs was developed and implemented for these data by Dr. S.M. Ransom as first described in Livingstone et al. (2009), and summarized here.

The maximum-likelihood method avoids the information loss inherent in binning

and is used throughout the field and this work.

event-based (i.e. photon) pulse profiles. The inputs to the method are an accurate model pulse profile $I(\Phi)$ of intensity as a function of rotational phase Φ (where $0 \leq \Phi < 1$), and the computed rotational phases ϕ_i of the N events (where $1 \leq i \leq N$) from the observation according to the best timing model of the pulsar. $I(\Phi)$ is normalized so that it has unit area and can be treated as a probability density function for the individual event arrival times.

For the X-ray timing of PSR J0205+6449, we used a two-Gaussian template, which was fitted along with a DC component to a high signal-to-noise ratio pulse profile from four months of *RXTE* data from early 2004 (Cycle 9). The timing model used for the profile included several frequency derivatives such that no timing noise was apparent in the timing residuals. The Gaussian template with 1000 phase bins is shown in Figure 4.2.

For each *RXTE* observation, we folded the X-ray data using the best predicted spin period for that day with the software package `PRESTO` (Ransom, 2001), but we allowed the software to search in a narrow range for the best pulsation period. We then used the refined spin period to determine pulse phases ϕ_i for each of the X-rays. Typical uncertainties were between 450 – 750 μs for each TOA. The phase offset, as determined by the median of the resulting likelihood distribution, was multiplied by the current pulse period and added to the reference epoch for each observation, in our case the first X-ray recorded, to make a TOA. For each *RXTE* observation, we typically determined 2 – 3 TOAs.

4.2.2 Green Bank Telescope observations

Observations with the GBT were made at either 820 or 1400 MHz from MJD 52327 – 52776 using the Berkeley-Caltech Pulsar Machine (BCPM; Backer et al., 1997). We recorded data using two different receivers, each sampling two orthogonal polarizations. First, using a receiver located at the Gregorian focus of the telescope, we made observations centered at 1400 MHz with 134 MHz of bandwidth and 50 μs samples. For 820 MHz observations, a receiver was placed at the prime focus of the telescope, observations were made with 48 MHz of bandwidth and 72 μs samples.

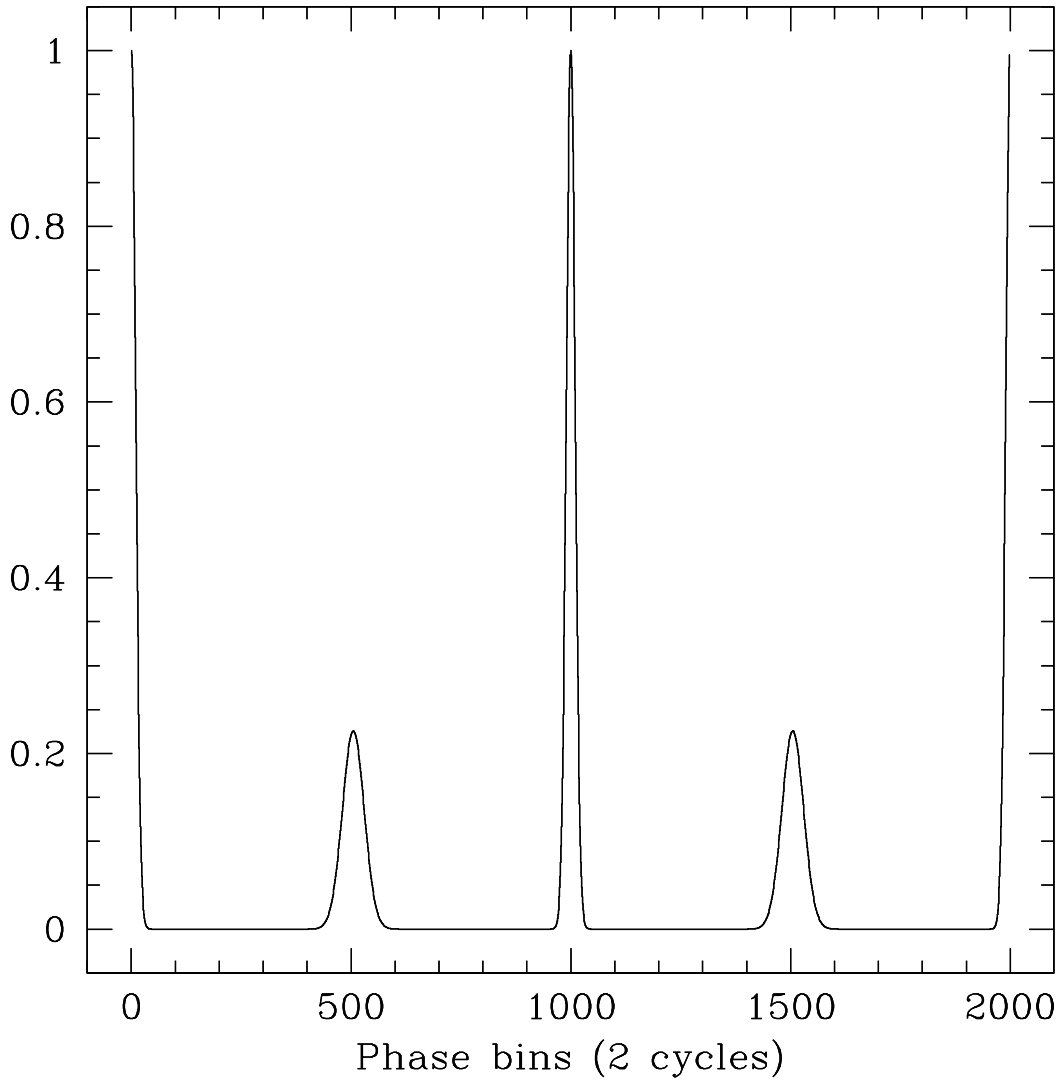

Figure 4.2: Best-fit two-Gaussian curve with 1000 phase bins from maximum-likelihood method of determining pulse times of arrival for 2 – 18 keV.

Typical integrations times lasted between 3 – 5 hrs. We dedispersed at the known DM of 140.7±0.3 pc cm^{-3} (Camilo et al., 2002c) and folded all of the data using `PRESTO` (Ransom, 2001), and then extracted 2 – 3 TOAs per observation by correlating in the frequency domain the folded 64-bin pulse profile with a Gaussian of fractional width 0.04 in phase. The typical precision of the TOAs was 200 – 400 μs. TOAs were corrected to the UTC timescale using data from Global Positioning System (GPS) satellites.

4.2.3 Jodrell Bank observations

Observations were made at JBO every 3 – 5 days between MJD 53725 and 54666 using the 76-m Lovell telescope of the University of Manchester at a frequency of 1400 MHz with 32 MHz of bandwidth. Each observation typically lasted 3 hr, divided into 1-minute sub-integrations. The data were de-dispersed using a 64-channel filterbank recorder at the known DM and folded on-line. The resulting profiles, sampled in intervals of 164.3 μs, were added in polarization pairs and then combined to provide a single total-intensity profile. This was then convolved with a template derived from a single high signal-to-noise-ratio 400-bin profile at the same frequency to yield a TOA. TOAs were corrected to UTC using information from the GPS. Further details can be found in Hobbs et al. (2004). The typical precision of the TOAs was 200 – 700 μs.

4.3 Timing Analysis

A single phase-coherent timing solution spanning all 6.4 yr of data proved impossible owing to the 287-day gap in timing observations as well as two large glitches. Phase-coherence will be lost when the pulse arrival time is different than the prediction by 0.5 in phase, resulting in a phase ambiguity. Thus, we present three phase-coherent timing solutions, summarized in Table 4.1. We verified that changing the assumed pulsar position by 3σ did not significantly change the fitted parameters, thus, the pulsar position was held fixed at that determined by Slane et al. (2002) from *Chandra* data (see Table 2.3). While in some cases long-term phase-coherent timing can pro-

duce accurate positions, this is typically not the case for young pulsars where timing noise and glitches prevent such a measurement. In comparison, position uncertainties available from *Chandra* of $\sim 0.6''$, are far superior to those from pulsar timing for a pulsar experiencing significant timing noise.

GBT and *RXTE* Cycle 7 data were fitted together, resulting in a timing solution spanning six months (MJD 52327 – 52538), with GBT (dots) and *RXTE* (crosses) as shown in Figure 4.3. Timing residuals are shown in the Figure, with the top panel showing residuals with ν, $\dot{\nu}$, and $\ddot{\nu}$ fitted. Significant timing noise remains in the data and can be fitted with six frequency derivatives, shown in the bottom panel of Figure 4.3.

Phase coherence was lost after MJD 52538, as the result of a glitch (see §4.3.1). A second coherent timing solution using GBT and *RXTE* data spans seven months (MJD 52571 – 52776). Timing residuals are shown in Figure 4.4, with ν, $\dot{\nu}$, and $\ddot{\nu}$ fitted in the top panel. As with the previous timing solution, significant timing noise remains in the residuals, which is fitted with 5 frequency derivatives, shown in the bottom panel of Figure 4.4.

Figure 4.5 shows residuals for the third timing solution spanning ∼4.4 yr (MJD 53063–54669). In addition to two years of X-ray timing observations (spanning MJD 53063 – 53813), on MJD 52725 (2005 December 21), radio timing observations began using JBO. X-ray and radio observations were concurrent for 88 days, after which no additional X-ray observations were obtained.

The top panel of Figure 4.5 shows residuals with ν, $\dot{\nu}$, and $\ddot{\nu}$ removed; the bottom panel shows residuals with 12 frequency derivatives fitted. The timing noise in this 4.4-yr period is so large that it cannot be fully described by a 12 degree polynomial (the largest allowed with current machine precision). In addition, some of the timing noise seen in these data is likely attributable to unmodeled glitch recovery (Lyne, 1996). In fact, the measured value of ν is significantly different from that predicted from the previous timing solution. The difference between the predicted and measured ν is $\sim 6\times10^{-5}$ Hz over 287 days. This corresponds to approximately 1500 phase turns,

Table 4.1: Phase-coherent timing parameters for PSR J0205+6449.

First phase-coherent solution	
Dates (Modified Julian Day)	52327 – 52538
Dates	2002 Feb 22 – 2002 Sep 21
Number of TOAs	78
Epoch (Modified Julian Day)	52345.0
ν (Hz)	15.2238557657(5)
$\dot{\nu}$ (10^{-11} s^{-2})	−4.49522(2)
$\ddot{\nu}$ (10^{-21} s^{-3})	2.00(3)
RMS residuals with $\ddot{\nu}$ removed (ms)	1.56
Derivatives needed to "whiten"	6
Second phase-coherent solution	
Dates (Modified Julian Day)	52571 – 52776
Dates	2002 Oct 24 – 2003 May 17
Number of TOAs	33
Epoch (Modified Julian Day)	52345.0
ν (Hz)	15.22386798(2)
$\dot{\nu}$ (10^{-11} s^{-2})	−4.5415(1)
$\ddot{\nu}$ (10^{-21} s^{-3})	12.33(4)
RMS residuals with $\ddot{\nu}$ removed (ms)	1.13
Derivatives needed to "whiten"	5
Third phase-coherent solution	
Dates (Modified Julian Day)	53063 – 54669
Dates	2004 Feb 28 – 2008 Jul 22
Number of TOAs	379
Epoch (Modified Julian Day)	54114.46
ν (Hz)	15.21701089718(2)
$\dot{\nu}$ (10^{-11} s^{-2})	−4.48652358(9)
$\ddot{\nu}$ (10^{-21} s^{-3})	5.85153(5)
RMS residuals with $\ddot{\nu}$ removed (ms)	965
Derivatives needed to "whiten"	>12

Figures in parentheses are uncertainties in the last digits quoted and are the formal 1σ uncertainties reported by `TEMPO`.

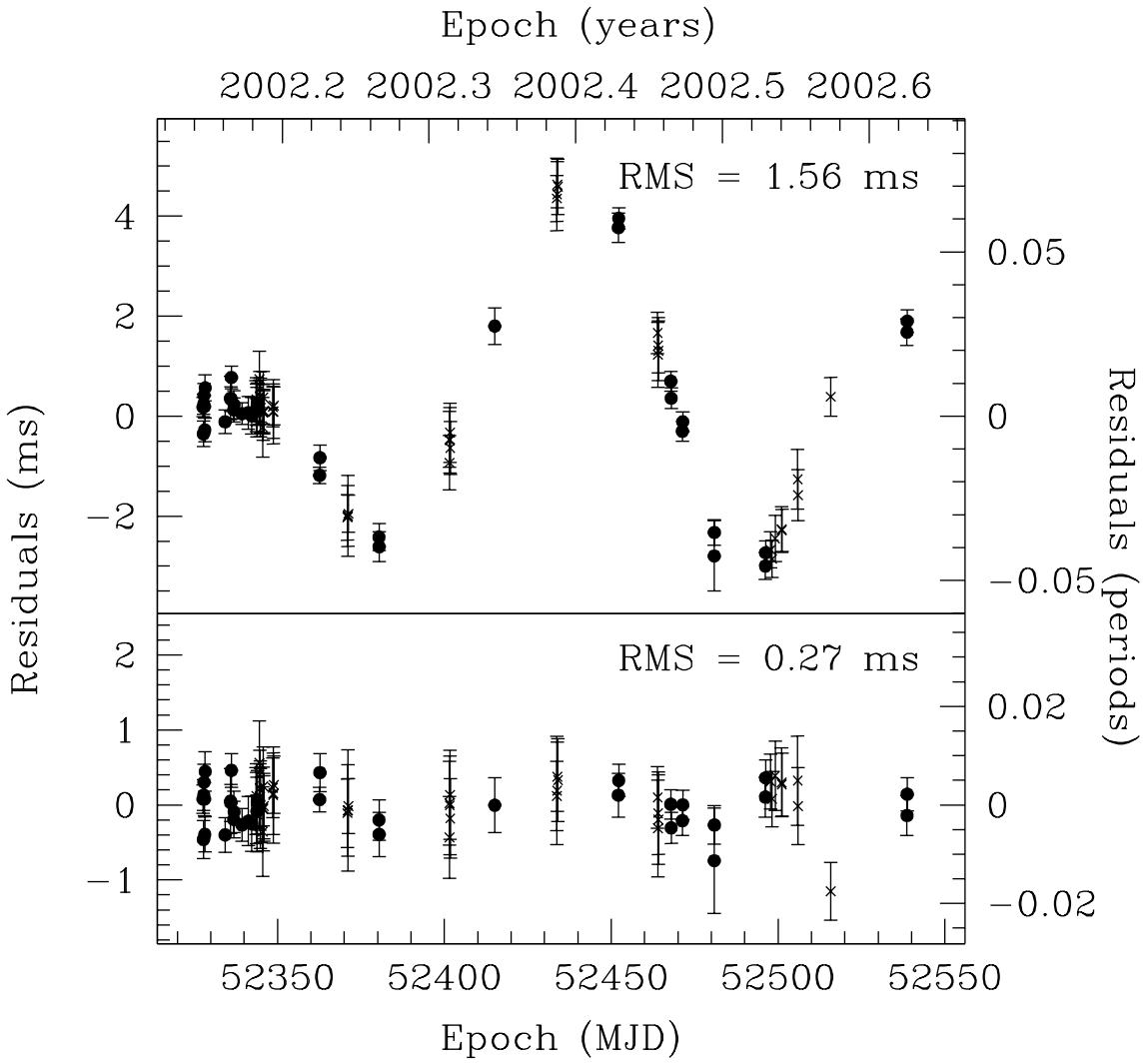

Figure 4.3: Timing residuals for *RXTE* observing Cycle 7 (crosses) and GBT data (dots) spanning MJDs 52327 – 52538. The top panel shows residuals with ν, $\dot{\nu}$, and $\ddot{\nu}$ fitted. The bottom panel shows residuals with an additional four frequency derivatives removed.

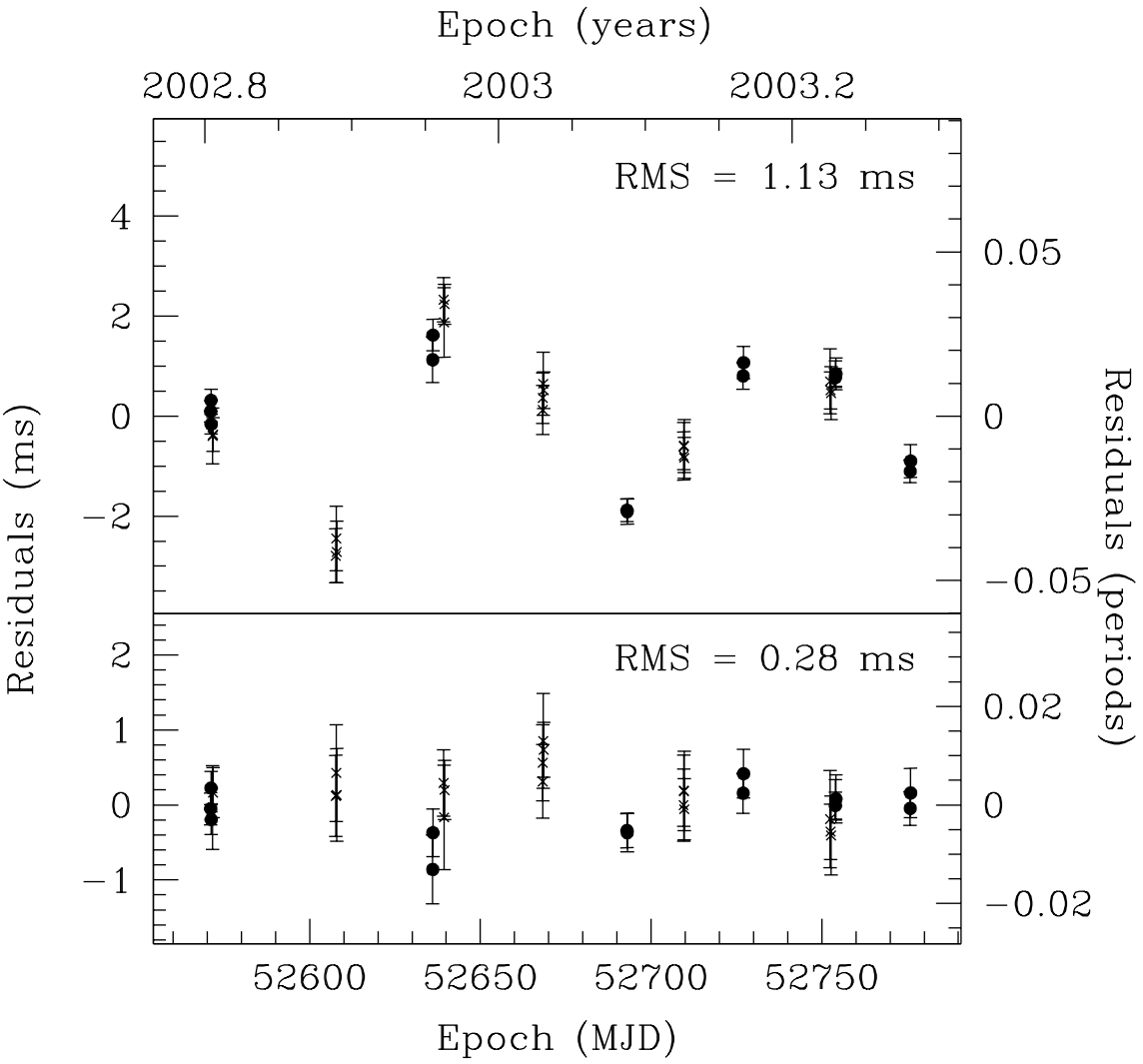

Figure 4.4: Timing residuals for *RXTE* observing Cycle 7 (crosses) and GBT data (dots) spanning MJDs 52571 – 52776. The top panel shows residuals with ν, $\dot{\nu}$, and $\ddot{\nu}$ fitted. The bottom panel shows residuals with an additional three frequency derivatives removed.

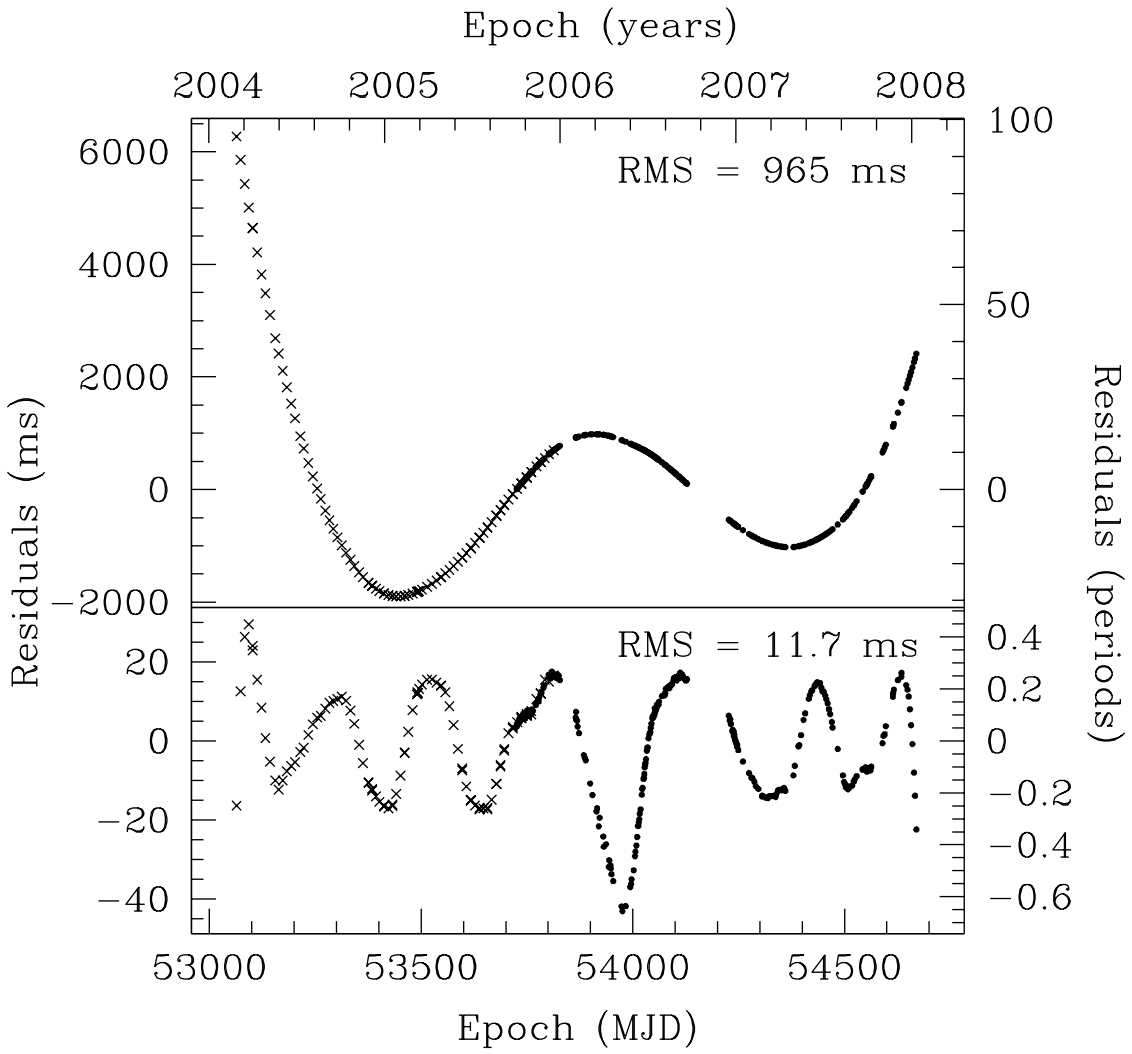

Figure 4.5: Timing residuals for *RXTE* observing Cycles 9 and 10 (crosses), and Jodrell Bank data (small dots), after the glitch occurring between MJD 52777 and 53062. The top panel shows residuals with only ν, $\dot{\nu}$, and $\ddot{\nu}$ fitted. The bottom panel shows residuals with ν and 12 frequency derivatives fitted (the maximum allowed with current machine precision).

which is much more than expected from typical timing noise during such a time period, indicating that a glitch probably occurred during the gap in the data.

4.3.1 Glitches

In order to analyze the two glitches inferred from our coherent timing analysis, we performed a partially coherent timing analysis over short time intervals (on average ∼40 days), fitting only for ν and $\dot{\nu}$ and choosing the length of each data subset such that the phase residuals are Gaussian-distributed (i.e. "white"). The results, with the average $\dot{\nu}$ from the inter-glitch period removed, are shown plotted in the top panel of Figure 4.6. Two glitches (a sudden increase in ν) as well as timing noise (long term wander in ν) are clearly present. We also show measurements of $\dot{\nu}$ for the same intervals in the bottom panel of Figure 4.6. Again, the two glitches are apparent, as is the significant timing noise in the data.

To measure accurately the size of each glitch while minimizing the contaminating effect of long-term timing noise, we took ν measurements spanning only ∼200 days before and after each glitch to measure the fractional increase in spin frequency. Figures 4.7 and 4.8 show pre- and post-glitch ν measurements with the post-glitch slope subtracted.

We observed a frequency increase between MJDs 52538 and 52571 (Fig. 4.7), corresponding to the loss of phase coherence discussed in §4.3. This ν increase corresponds to a glitch of fractional magnitude $\Delta\nu/\nu = (3.4 \pm 1.1) \times 10^{-7}$ (see also Ransom et al. 2004). The change in $\dot{\nu}$ over the glitch is not statistically significant when measured from the slope of frequency measurements, as shown in the Figure. However, the fractional change in $\dot{\nu}$ from the individual $\dot{\nu}$ measurements before and after the glitch is significant, with $\Delta\dot{\nu}/\dot{\nu} \sim 0.005 \pm 0.001$, i.e. seen in the bottom panel of Figure 4.6. No short-term post-glitch relaxation is detected; however, because of the sparse sampling (roughly a single observation every two weeks), it cannot be precluded. Neither can a long-term post-glitch relaxation be distinguished from a simple change in $\dot{\nu}$ because a decay, if present, was interrupted by a second glitch.

We observed a second frequency increase between MJDs 52776 and 53063 as shown

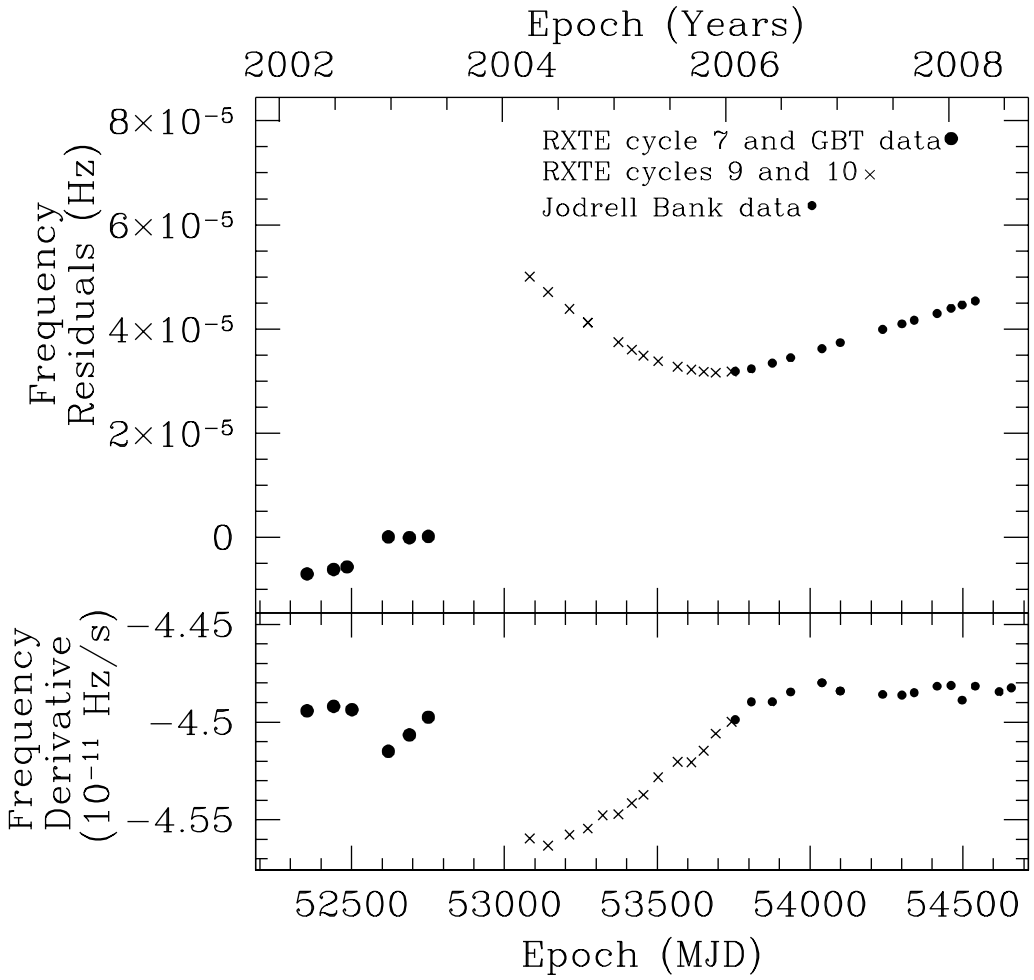

Figure 4.6: Frequency and frequency derivative evolution of PSR J0205+6449 over 6.4 yr. The top panel shows frequency measurements from short, phase-coherent timing solutions with the overall trend in the inter-glitch interval subtracted. The bottom panel shows measurements of the frequency derivative. Uncertainties are smaller than the plotted points.

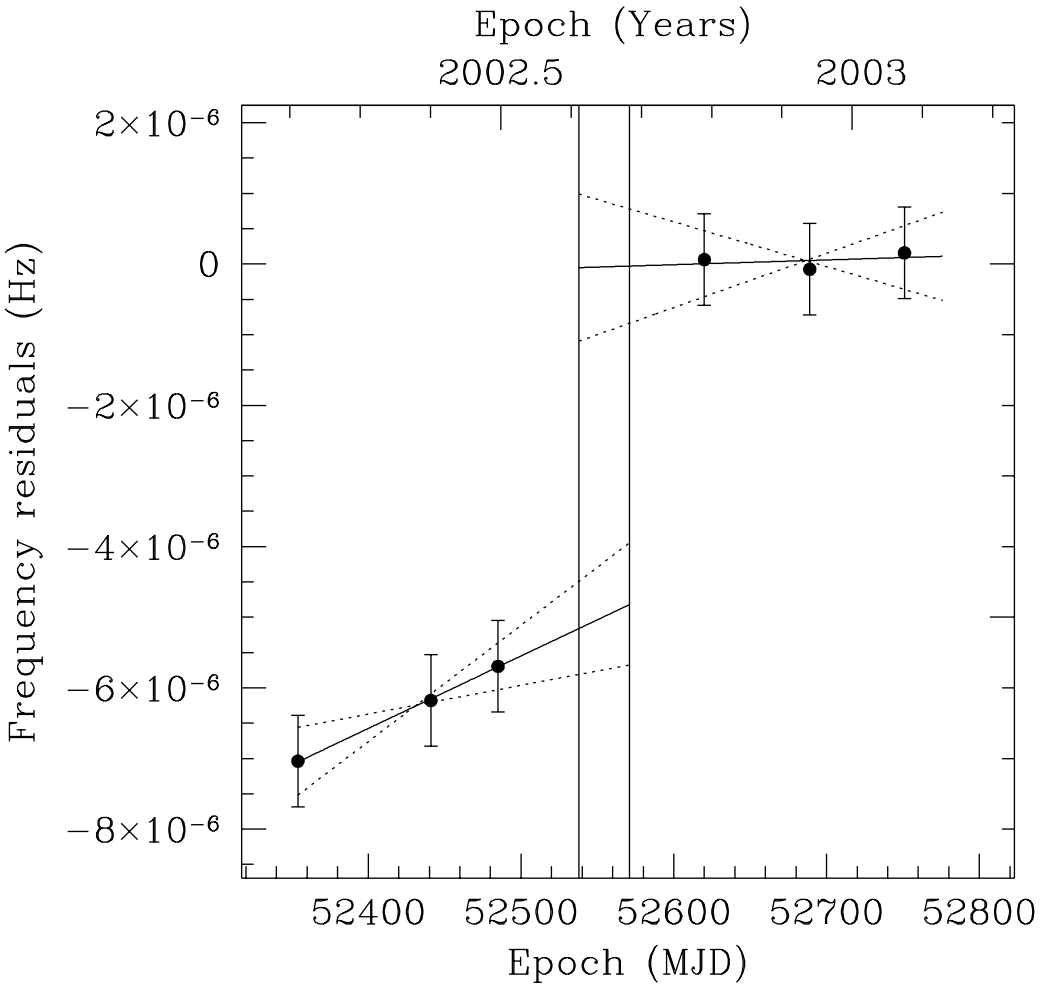

Figure 4.7: Frequency measurements with the post-glitch trend subtracted, showing the first observed glitch occurring between MJDs 52538 and 52571 (indicated by vertical lines) with fractional magnitude of $\Delta\nu/\nu = (3.4 \pm 1.1) \times 10^{-7}$. 1σ uncertainties in the pre- and post-glitch slopes are shown with hatched lines. The change in $\dot{\nu}$ as measured from the difference in the slope before and after the glitch is not statistically significant.

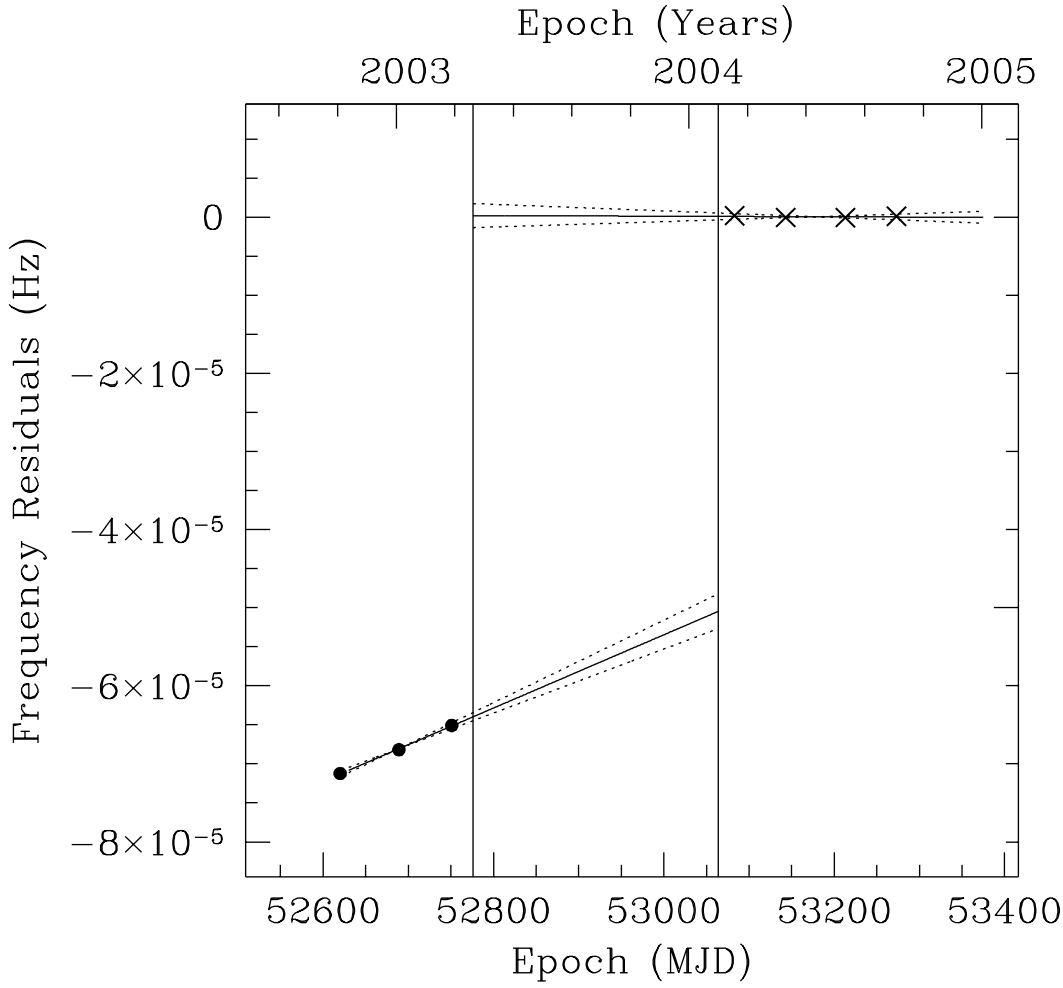

Figure 4.8: Frequency measurements with the post-glitch trend subtracted, showing the frequency increase occurring between MJDs 52777 and 53062 (indicated by vertical lines). This could be the result of two or more separate glitches occurring during 287-day gap in the data, however, we interpret the frequency jump as the likely result of a single glitch of fractional magnitude $\Delta\nu/\nu = (3.8 \pm 0.4) \times 10^{-6}$. 1σ uncertainties on pre- and post-glitch slopes are shown with hatched lines and are indicative of a change in $\Delta\dot{\nu}/\dot{\nu} = 0.012 \pm 0.001$.

in Figure 4.8. Because no timing data were taken during the 287-day period where the frequency jump occurred, it is not possible to differentiate between a single glitch and two (or more) smaller glitches. However, because there is no clear evidence of more than one glitch, we interpret the frequency increase as a single glitch of fractional magnitude $\Delta\nu/\nu = (3.8 \pm 0.4) \times 10^{-6}$. The frequency derivative, as measured from the change in slope over the glitch (see Fig. 4.8) also changed significantly, with a fractional magnitude of $\Delta\dot{\nu}/\dot{\nu} = 0.012 \pm 0.001$.

Another possible description of this glitch is a large increase in ν followed by an exponential recovery. The behaviour of $\dot{\nu}$ after the spin-up is suggestive of an exponential recovery, i.e. that the change in $\dot{\nu}$ was not permanent. Fitting a glitch model including an exponential decay to all the frequency measurements before and after the glitch, we found models which span a wide range of possible glitch parameters, with a reduced χ^2 of $\sim 3.6 - 3.9$ for 25 degrees of freedom. We found fits of roughly equal probability for all possible glitch epochs between the two bounding coherent timing solutions, thus we present a range of glitch parameters corresponding to the date limits of MJD 52777 and MJD 53062. A typical fit and residuals are shown in Figure 4.9. The fractional magnitude of the glitch from these models ranges from $\Delta\nu/\nu \sim (3.6 - 7.2) \times 10^{-6}$, while the recovery fraction spans $Q \sim 0.66 - 0.88$ and $\tau_d \sim 280 - 295$. The long-term change in frequency derivative, $\Delta\dot{\nu}/\dot{\nu}$, is always negative, i.e. in the opposite direction from that expected from a typical glitch, and is approximately equal to ~ -0.0046 for all fitted models. This could be attributed to unusual glitch recovery, timing noise, or a combination thereof. However, this effect is possibly an artifact of the fitting procedure, where it is assumed that the pre-glitch ν is not itself recovering from the previous glitch.

Because of the unusual long-term behaviour of $\Delta\dot{\nu}$ after the glitch, and the possibility that this behaviour is not a direct result of the glitch, we performed a third fit to the frequency data, this time excluding frequency measurements after MJD 53700 (after which the unusual $\Delta\dot{\nu}$ dominates, see Fig. 4.6), and fixing the change in $\dot{\nu}$ to be zero. Fitting an exponential glitch recovery model to this subset of data provides

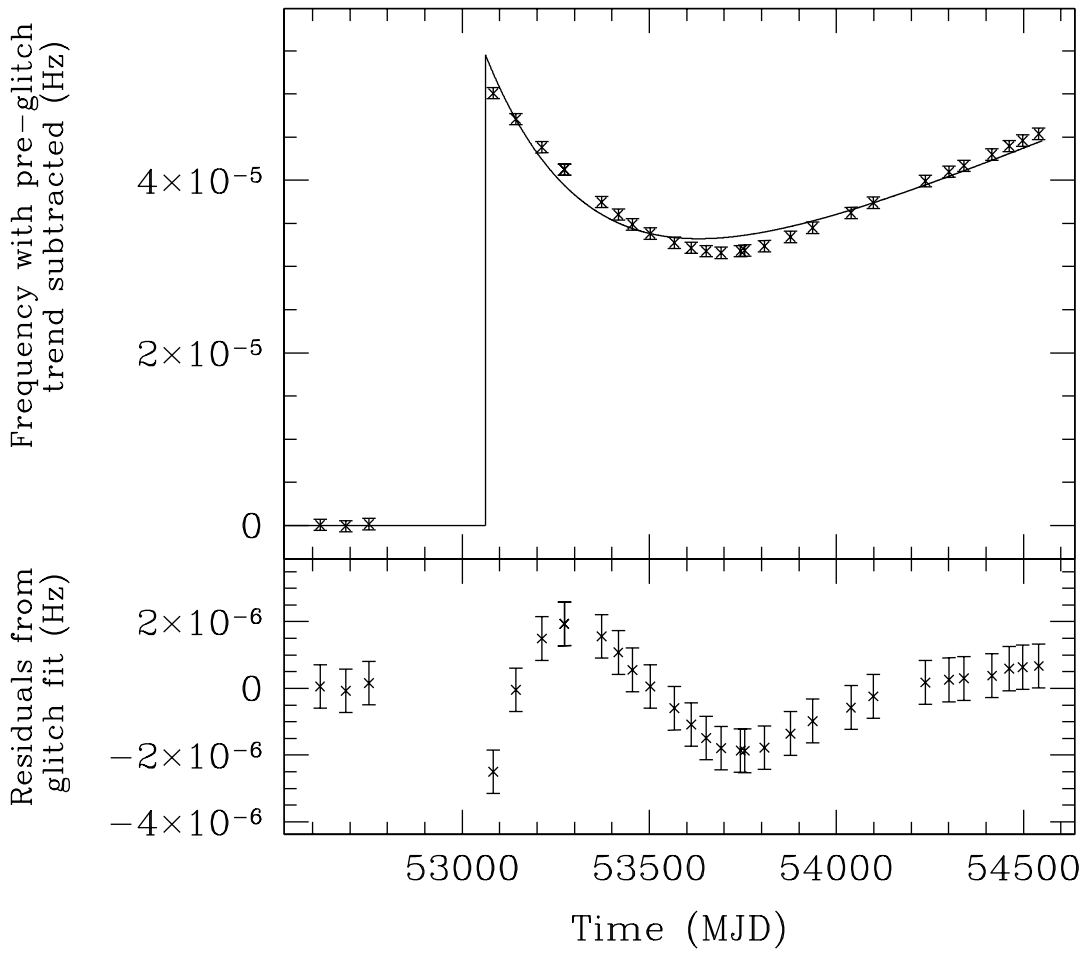

Figure 4.9: Pulse frequency measurements and fitted glitch model for the large glitch occurring between MJDs 52777 and 53062 for PSR J0205+6449. The top panel shows frequency measurements with pre-glitch trend removed, with the fitted model for a typical glitch epoch over-plotted, while the bottom panel shows the residuals. The uncertainties on each point are dominated by the uncertainty in the pre-glitch trend subtracted from the data and therefore are of roughly uniform size and are correlated. For this fit to the data, the glitch epoch is MJD 53062, with $\Delta\nu/\nu \sim 3.6\times10^{-6}$, $Q \sim 0.66$, $\tau_d \sim 280$ and $\Delta\dot{\nu}/\dot{\nu} \sim -0.00453$, resulting in ${\chi^2}_\nu = 3.9$ for 25 degrees of freedom.

a much better fit, as shown for a sample glitch epoch in Figure 4.10. Again, the glitch may have occurred at any time between MJD 52777 and 53062. For this fit, the range of possible fractional increases in frequency is $\Delta\nu/\nu = (3.4 - 5.3) \times 10^{-6}$, while the recovery fraction is $Q = 0.5 - 0.67$ and the recovery time scale is $\tau_d = 379 - 383$ days.

4.4 X-ray Profile Analysis

For each *RXTE* observation in observing Cycles 7, 9, and 10, we created a phase-resolved spectrum with 64 phase bins across the profile, using the `FTOOL` "fasebin"[1] and the partially coherent timing ephemerides described above (§4.3.1). We also created phase-resolved spectra as described above for the four observations taken during *RXTE* Cycle 6. These observations could not be unambiguously phase-connected with the later data because of a 202-day gap between these and the subsequent Cycle 7 observations. Instead, we folded the observations at a frequency determined by a periodogram analysis, $\nu = 15.22466(2)$ Hz with a frequency derivative of $\dot{\nu} = -4.49(1) \times 10^{-11}\,\mathrm{s}^{-2}$ evaluated at the reference epoch MJD 52139.5.

Because of the hard spectrum of the source (Ransom et al., 2004), we selected photons from all three layers of the xenon detectors, and from all operational PCUs and included all photons within the energy range 2 – 60 keV. In addition, we repeated the entire process using the first xenon layer for the energy range 2 – 18 keV, where the majority of the softer source counts reside. We also created phase-averaged spectra which were used to build response matrices for each PCU. We then used XSPEC[2] to create a pulse profile in count rate for each PCU for each observation. We then combined data from all PCUs for each observation, dividing by a factor to account for the amount of time each PCU was on, resulting in a pulse profile in units of count rate per PCU.

We aligned the 2 – 18 keV profile for each observation by cross-correlating with the two-Gaussian template (Fig. 4.2) and summed profiles from each *RXTE* cycle

[1] http://heasarc.gsfc.nasa.gov/lheasoft/ftools/fhelp/fasebin.txt

[2] See http://xspec.gsfc.nasa.gov, ver. 11.3.1.

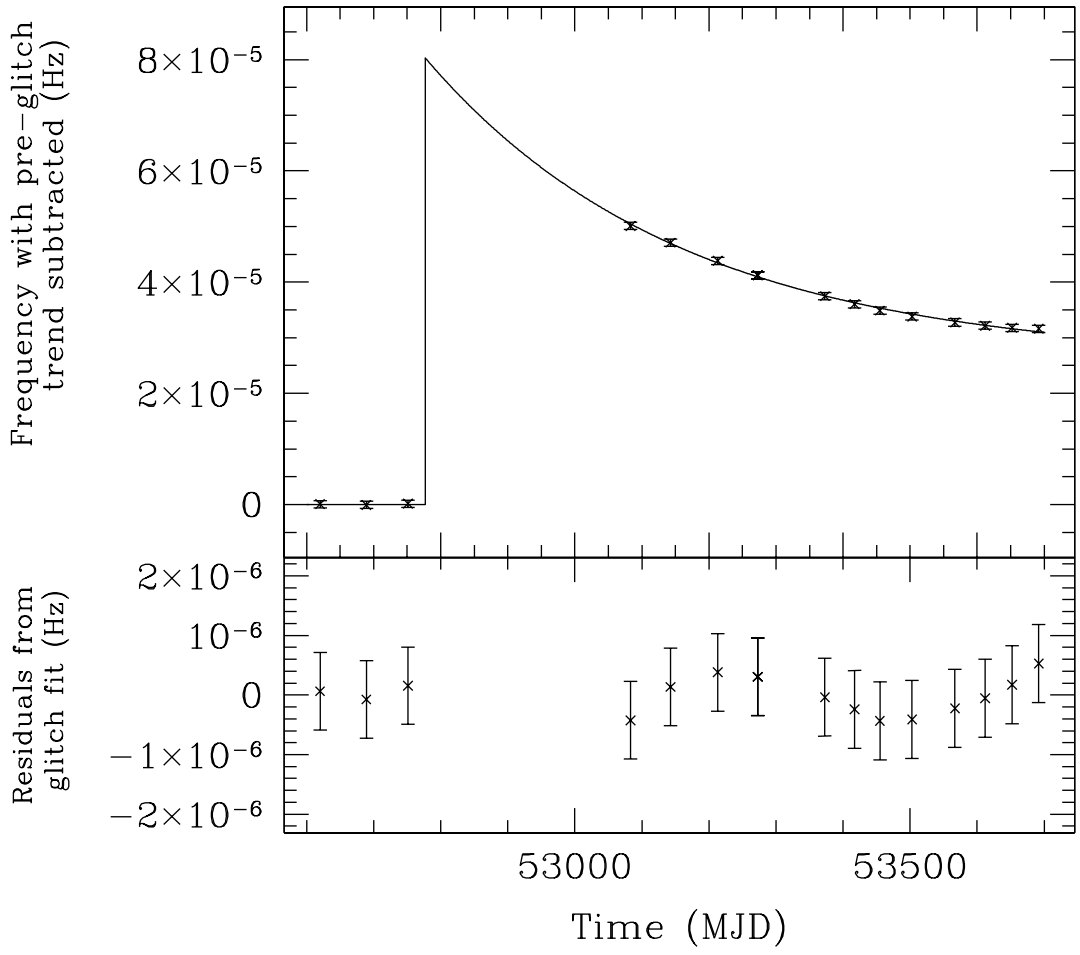

Figure 4.10: Pulse frequency measurements and fitted glitch model for a typical glitch epoch for PSR J0205+6449, considering only the period of glitch recovery and ignoring the long-term post-glitch change in $\dot{\nu}$. The top panel shows frequency measurements with the pre-glitch trend removed, with the fitted model over-plotted, while the bottom panel shows the residuals from the fit. The uncertainties on each point are dominated by the uncertainty in the pre-glitch trend subtracted from the data and therefore are of roughly uniform size. Shown here is the best fit model for a glitch occurring on MJD 52777 with $\Delta\nu/\nu \sim 5.3 \times 10^{-6}$, $\tau_d \sim 383$, and $Q = 0.67$. The reduced χ^2 for the fit is 0.262 for 12 degrees of freedom.

together, as shown in Figure 4.11. There is no evidence for evolution in the profile over $\sim$4 yr.

We also created profiles for different energy bands: 2 – 10 keV, 10 – 18 keV, and 18 – 40 keV and summed profiles from *RXTE* Cycles 7, 9, and 10 (i.e. where phase-coherent timing solutions exist) into a single profile for each energy band, shown in Figure 4.12. In addition, we produced a profile for the energy band 40 – 60 keV, in the same manner described above, but did not detect the pulsar. We used the phase offset determined from cross correlating the 2 – 18 keV profile to align the profiles from all the energy ranges. This ensures that the correct phase offset is applied to the 18 – 40 keV profiles, where the signal-to-noise ratio of individual profiles is very poor, and a noise spike can be mistaken by the cross correlation algorithm for the sharp peak of the profile. We note that using the phase offset determined for a different energy range profile could be problematic in building added profiles if there is signifcant energy evolution across the energy range of interest. This does not appear to be the case for this pulsar for the relevant energy range. The pulsar is visible up to $\sim$ 40 keV and the pulse shape does not vary significantly with increasing energy.

There is some possible unusual structure in the off-pulse region of the profiles, particularly for the energy range 18 – 40 keV (as in Fig 4.12). We examined this putative structure by performing several additional analyses. First, we produced summed profiles using a different method than described above. We extracted events and created a time series for each energy range, for each individual observation. We folded each time series with the local ephemeris and aligned and summed the profiles several times using different template profiles. This analysis produced pulse profiles that are not significantly different from those shown in Figure 4.12.

We further analyzed the off-pulse region of the profiles by applying a χ^2 test, a Z^2 test (Buccheri et al., 1983), and an H test (de Jager et al., 1989). The reduced χ^2 values for the 10 – 18 keV and 18 – 40 keV are less than 1, while the χ^2 for the off-pulse region of the 2 – 10 keV profile is 55 for 48 degrees of freedom (where the probability of this χ^2 or higer occurring by chance is 21%). The Z^2 test for 1, 2, 4,

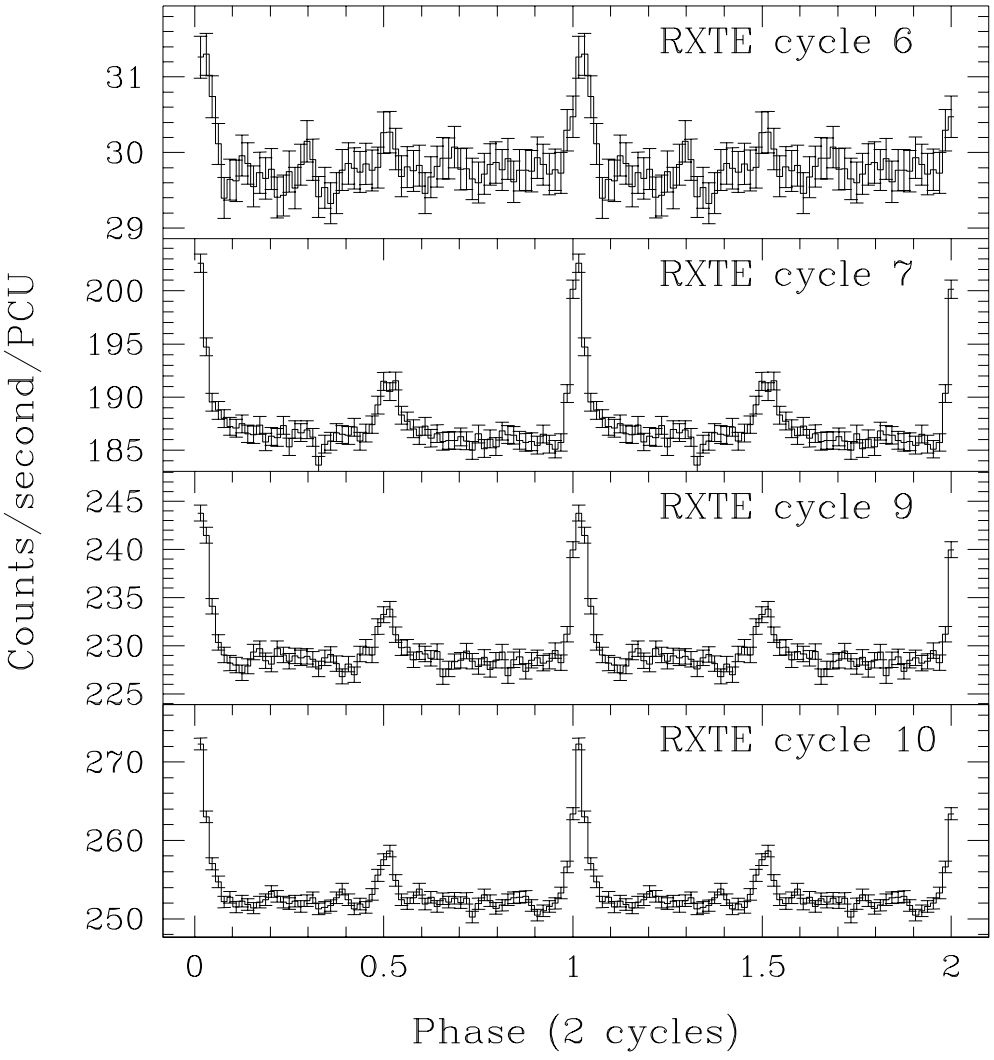

Figure 4.11: Pulse profiles of PSR J0205+6449 for *RXTE* Cycles 6, 7, 9 and 10 for the energy range 2 – 18 keV. Note that *RXTE* Cycle 6 comprised significantly less observing time, resulting in larger uncertainties. The interpulse is not clearly visible in the Cycle 6 data, but a χ^2 test shows that the profile is not significantly different from the Cycle 7, 9, or 10 pulse profiles.

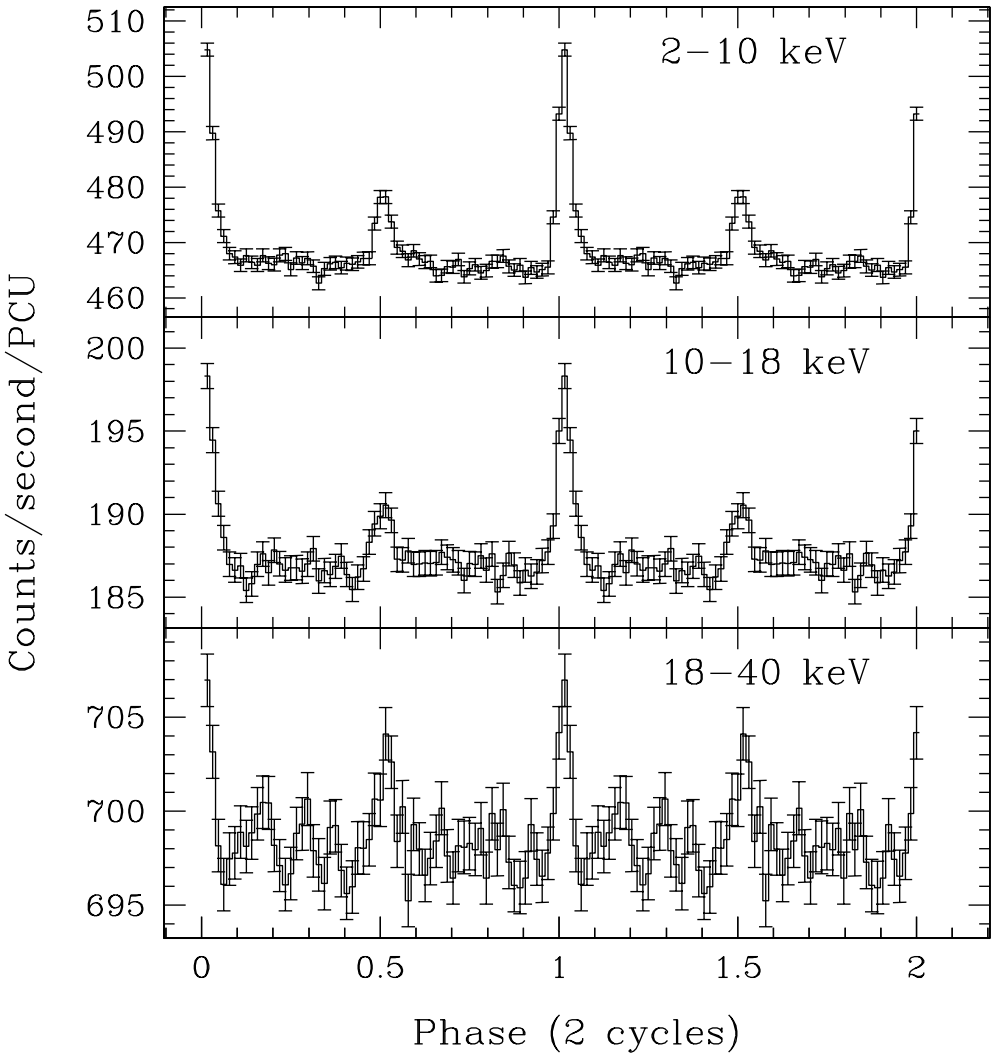

Figure 4.12: Pulse profile of PSR J0205+6449 shown in energy bands 2 – 10 keV, 10 – 18 keV, and 18 – 40 keV. Each pulse profile is created by aligning and summing individual profiles from *RXTE* Cycles 7, 9, and 10. Visible structure in the off-pulse region of the 18 – 40 keV profile is not statistically significant as shown by a χ^2 test, a Z^2 test, and a H test.

and 8 harmonics, and the H test applied to the off-pulse region of all three profiles resulted in the null hypothesis. Therefore, the off-pulse regions of the profiles are not statistically different from a DC offset.

4.5 Phase Offset Between the Radio and X-ray Pulses

Precise measurement of the phase lag between the radio and X-ray pulses is important for understanding the pulse emission mechanism. Emission from rotation-powered pulsars is thought to arise from either a polar cap (e.g. Daugherty & Harding, 1982), or in magnetospheric outer gaps (e.g. Cheng et al., 1986b; Romani, 1996, see § 1.5.3). Absolute timing for several different energy regimes can place constraints on the shape of the outer gap and the height in the magnetosphere where radiation is generated (Romani & Yadigaroglu, 1995). The radio pulse profile of PSR J0205+6449 is single peaked with a width of $\sim 0.05P$ (Camilo et al., 2002c); the X-ray profile is double peaked, with a peak-to-peak separation of ~ 0.5. We made two independent measurements of the phase offset between the radio pulse and the main X-ray pulse for PSR J0205+6449, by finding the offset between the GBT and *RXTE* data, and the JBO and *RXTE* data.

We used the first timing solution (GBT and *RXTE* data prior to glitch 1) spanning MJDs 52327 to 52538 to make three independent measurements of the phase offset. We split our timing solution into three subsets, fitting only for ν and $\dot{\nu}$. Radio TOAs were shifted to infinite frequency using the nominal DM (Camilo et al., 2002c). The data subsets were chosen such that there was good overlap between the sparsely sampled X-ray and radio data, and that each solution had Gaussian-distributed residuals. The weighted average value of these three measurements is 6.72 ± 0.66 ms, or 0.102 ± 0.010 in phase (radio leading). This analysis could not be repeated for the post-glitch GBT/*RXTE* timing solution because of the even more sparsely sampled data, which consist of significant lags between most radio and X-ray observations, leading to poorly constrained values of the phase offset for short sections of the data.

We obtained a second measurement of the phase offset by simultaneously fit-

ting overlapping timing observations from *RXTE* and JBO, spanning 88 days from MJDs 53725 to 53813. We first obtained a phase-coherent timing solution from the well sampled radio data, and then added the overlapping, more sparsely sampled X-ray TOAs. Again, radio TOAs were shifted to infinite frequency using the nominal DM value. We split the data into three subsets, fitting only for ν and $\dot{\nu}$ and ensuring that each subset had Gaussian residuals. The JBO TOAs were created using a different fiducial point than the GBT and *RXTE* profiles, so each TOA was shifted by a constant to adjust for the difference between the two fiducial points used. The weighted average of these offset measurements is 5.55 ± 0.66 ms, corresponding to a phase offset of 0.085 ± 0.010. The difference between this measurement and that made with *RXTE* and GBT data is 1.17 ± 0.94 ms, i.e., in agreement within 1.25σ.

We further verified the phase offset by extracting a single TOA from an archival *Chandra* observation from February 2002 (Observation ID 2756). The offset measured from the *Chandra* TOA to the GBT radio TOAs agrees with our GBT/*RXTE* offset within $1.2\,\sigma$.

The uncertainty in the phase offset is dominated by the uncertainty in the DM. The DM was measured to be $140.7 \pm 0.3\,\mathrm{pc\,cm^{-3}}$ using 800 and 1375 MHz GBT data in 2002, as reported in Camilo et al. (2002c). Thus the JBO determination of the phase lag, made $\sim$3.5 yr after the measurement of DM, could be affected by short or long-term changes in DM. We therefore report the first measurement of the phase offset made with GBT and *RXTE*, of $\phi = 0.102 \pm 0.010$.

4.6 Discussion

4.6.1 Timing noise, glitches, and the age of PSR J0205+6449

We show evidence for two large glitches in PSR J0205+6449 over a 6.4 yr period. The fractional magnitudes of these glitches ($\Delta\nu/\nu \sim 10^{-7} - 10^{-6}$) are typical of pulsars with characteristic ages of 5−10 kyr, such as the frequent large glitcher PSR J0537−6910 ($\tau_c = 4.9$ kyr) and the Vela pulsar ($\tau_c = 11$ kyr). The youngest pulsars such as the Crab pulsar (955 yr), PSR B0540−69 ($\tau_c = 1.7$ kyr) and PSR J1119−6127

($\tau_c = 1.6\,\mathrm{kyr}$) typically have glitches with smaller fractional magnitudes ranging from $\Delta\nu/\nu \sim 10^{-9} - 10^{-8}$. Perhaps this indicates that the pulsar age is closer to its characteristic age of $\tau_c \sim 5.4\,\mathrm{kyr}$, rather than the historical supernova age of 829 yr.

If the pulsar was born in the historical supernova event 829 yr ago, these glitches are unusually large. Glitches may be related to pulsar age via neutron star temperature (McKenna & Lyne, 1990). If this is the case, the large glitches observed here could be related to the very low measured temperature of PSR J0205+6449 (Slane et al., 2004), rather than its chronological age. The reason for the exceptionally cool surface temperature of this neutron star is still a mystery, though may be explained with a large neutron star mass (Yakovlev et al., 2002). On the other hand, large glitches have been observed in the hot surface temperature AXPs (Kaspi et al., 2000; Dib et al., 2007). If the mechanism behind rotation-powered pulsar and magnetar glitches is similar, the neutron star surface temperature may not be the primary factor in determining the size of glitches.

Young pulsars emit large amounts of energy as they spin down, providing for easy measurement of $\dot{\nu}$, and occasionally higher order frequency derivatives ($\ddot{\nu}$, $\dddot{\nu}$, Lyne et al. 1993, Livingstone et al. 2005). Generally, only the youngest pulsars, with $\tau_c < 2\,\mathrm{kyr}$, have measurable braking indices. The exception is the 11 kyr-old Vela pulsar, where frequent large glitches prevent a phase-coherent measurement of the braking index, but measuring $\dot{\nu}$ in the aftermath of glitches has allowed a measurement of $n = 1.4 \pm 0.2$ over $\sim$25 yrs of data (Lyne et al., 1996). A combination of timing noise and glitches prevents a measurement of n in all other young pulsars.

The initial goal of timing PSR J0205+6449 was to measure its braking index. However, the measured value of n varies significantly among the three phase-coherent timing solutions obtained for this source, ranging from $n \simeq 15 - 90$. A partially coherent timing analysis (Fig. 4.6) shows that $\dot{\nu}$ does not evolve linearly implying that a deterministic value of $\ddot{\nu}$ and thus n cannot be measured from these data. However, excluding data in the immediate aftermath of the glitches and looking at the overall trend in $\dot{\nu}$ from the first three and last 10 measurements of $\dot{\nu}$ from Figure 4.6 (bottom

panel), the implied value is $n \sim 4$. Though this value is contaminated by timing noise and glitch recovery, it is suggestive that the true, underlying value of n may eventually be measurable with long-term timing.

The long-term change in frequency derivative after the second glitch, $\Delta\dot{\nu}/\dot{\nu} \simeq -0.0046$ is in the opposite direction from that seen from other glitches. While a permanent change in $\dot{\nu}$ is not observed in all glitches, when it does occur, the magnitude of $\dot{\nu}$ increases in every case, except for the second PSR J0205+6449 glitch reported here and a recent glitch observed from the RRAT J1819−1458, where a significant decrease in the magnitude of $\Delta\dot{\nu}/\dot{\nu} = -0.025 \pm 0.001$(Lyne et al., 2009). This is neither predicted nor explained by any current glitch models, and would either imply a decrease in effective torque acting on the pulsar.

Often observed at a glitch is $\Delta\dot{\nu}/\dot{\nu} > 0$, which can be explained in the vortex creep model by some of the superfluid becoming uncoupled from spin down and causing an effective decrease in I_{SF}. Thus if instead a decrease of the magnitude of $\dot{\nu}$ is observed, perhaps this can be explained by areas of vortices re-coupling with the majority of the star and contributing to the observed spin-down. Why this would be such a rare occurrence is mysterious. The interpretation suggested by Lyne et al. (2009) is that the RRAT is a former magnetar whose B-field decays via glitches. In this picture, the decrease in magnitude of $\dot{\nu}$ corresponds to a decrease in B, and thus a decrease in the external torque acting on the neutron star. Because this RRAT is older ($\tau_c = 120\,\mathrm{kyr}$) than PSR J0205+6449 and has a large magnetic field of $B \simeq 5 \times 10^{13}\,\mathrm{G}$, a field decay interpretation is more reasonable than for the very young and small field PSR J0205+6449.

4.6.2 Absolute timing and the pulse emission mechanism

The observed phase difference between radio and high-energy pulses, as well as the pulse shape and peak-to-peak separation, in principle provide important information about the pulsar emission mechanism by constraining the pulse emission region. Polar cap models predict that the bulk of the high energy emission originates near the neutron star surface, resulting in a γ-ray pulsar that is nearly aligned with the ra-

dio pulse (Daugherty & Harding, 1996). By contrast, the outer gap model predicts emission in narrow gaps high in the outer magnetosphere, leading to wide beams not aligned with the radio pulse (e.g. Romani & Yadigaroglu, 1995). Table 4.2 shows the offsets between the radio and X-ray pulses and the radio and γ-ray pulses for 28 pulsars, while Figure 4.13 shows the same offsets plotted versus spin-period. These compiled data show that there is a large scatter in the measured offsets and no correlation between pulse period and phase offset, in contrast to the suggestion that more rapidly rotating pulsars should have aligned pulses (e.g. Dyks & Rudak, 2003).

In addition, we note that many more phase offsets for magnetospheric X-ray and γ-ray emission are measured to be in the 0.0 – 0.5 range (20 pulsars) than in the -0.5 – 0.0 range (4 pulsars), though this could be largely a result of observational bias when measuring the phase offset, particularly in situations of more complicated pulse profiles. If the asymmetry in measured pulse profiles is real, it may provide interesting constraints for models of high-energy pulsed emission.

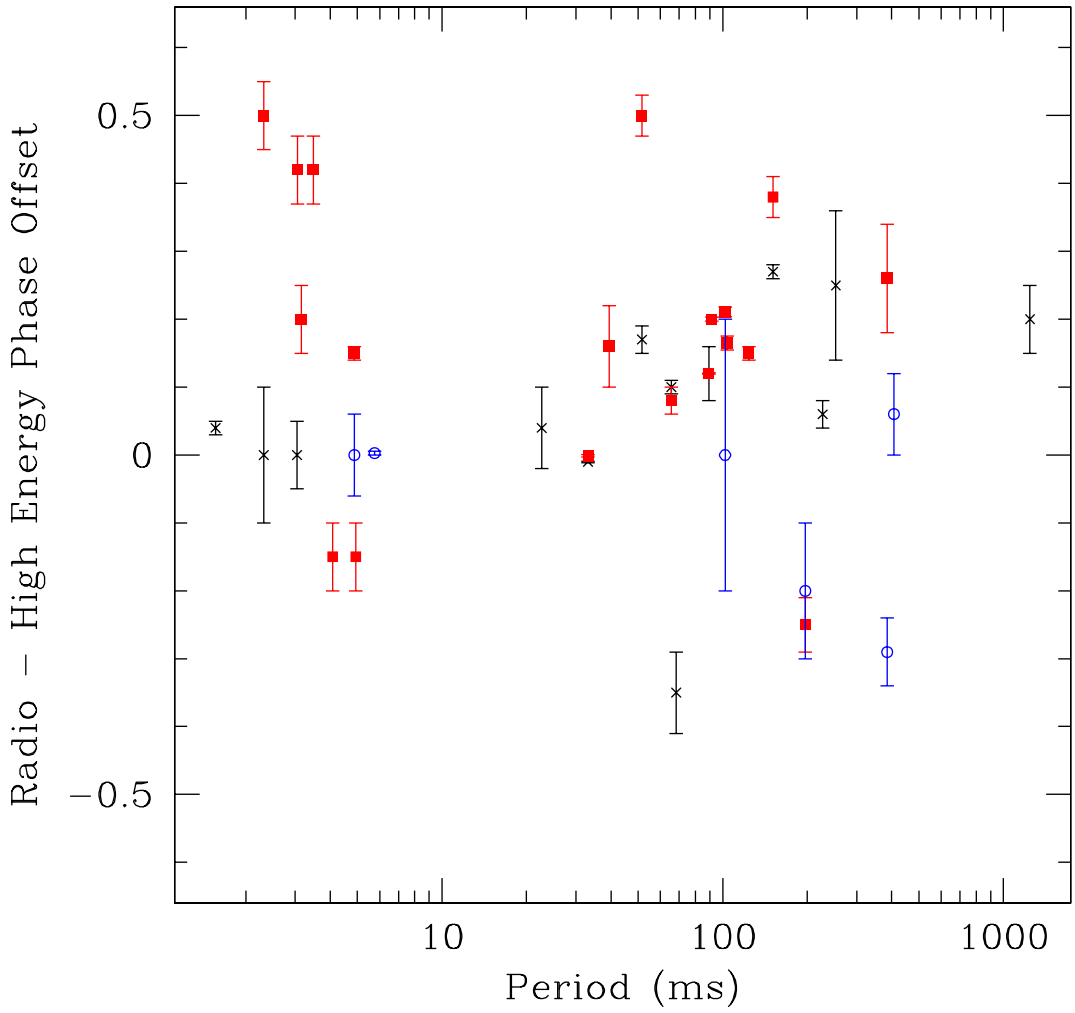

Figure 4.13: Phase delay between radio and high-energy pulses for 28 pulsars. Blue open circles are the offset between the radio and thermal X-ray pulse, the red squares represent the phase offset between the radio and γ-ray pulse, while the black crosses are the phase offset between the radio pulse and the non-thermal X-ray pulse.

Table 4.2: Phase offset between radio and high-energy pulse for 28 pulsars.

Pulsar	**Period (ms)**	**Radio/X-ray offset**[b]	**Radio/Gamma-ray offset**	**References**
B1937+21	1.56	0.04(1)	–	1
J0218+4232	2.32	0.0(1)	0.50(5)	2, 3
B1821−24	3.05	0.00(2),−0.341(3)	0.00(5)	4, 5, 6
J0613−0200	3.06	–	0.42(5)	3
J1614−2230	3.15	–	0.20(5)	3
J0751+1807	3.48	–	0.42(5)	3
J1744−1134	4.08	–	−0.15(5)	3
J0030+0451	4.87	0.00(6)[c]	0.15(1)	7, 3
J2124−3358	4.93	–	−0.15(5)	3
J0437−4715	5.76	0.003(3)[c]	0.45(5)	8, 3
J0737−3039A	22.7	0.04(6)	–	9
Crab	33.1	−0.0102(12)[d]	−0.001(2)	10, 11
B1951+32	39.5	–	0.16(6)	12
J2229+6114	51.6	0.17(2)	0.50(3),0.51(2)	6,13
J0205+6449	65.7	0.10(1)	0.08(2)	This work, 14
J1420−6048	68.2	−0.35(6)	–	15
Vela	89.3	0.12(1)	0.1339(7), 0.130(1)	16, 11, 17
J1028−5819	91.4	–	0.200(3)	18
B1706−44	102	0.0(2)	0.211(7)	19, 11
J2021+3651	104	–	0.165(10), 0.162(14)	20, 21
J1048−5832	124	–	0.15(1)	13
B1509−58	151	0.27(1)	0.38(3),0.30(5)	4, 22, 6

Table 4.2, cont.

Pulsar	**Period (ms)**	**Radio/X-ray offset**[b]	**Radio/Gamma-ray offset**	**References**
B1055−52	197	−0.20(5)[c]	−0.25(4)	23, 24
B1929+10	227	0.06(2)	–	25
B0950+08	253	0.25(11)	–	26
B0656+14	385	−0.25(5)[c]	0.26(8)	23, 27
J1119−6127	408	0.006(6)[c]	–	28
B0628−28	1244	0.20(5)	–	29

Radio - High energy phase offset for "main" pulse.

[a] The phase offset is presented from −0.5 to 0.5 in phase, where a positive value of the phase offset indicates that the radio pulse leads the high-energy pulse in phase. Where uncertainties are not specified in the original publication, an estimate is given.

[b] X-ray pulse represents magnetospheric emission except where otherwise noted.

[c] Thermal X-ray pulsations.

[d] The phase lag for the Crab pulsar is calculated from the phase of the main peak of the radio profile. However, the Crab pulsar also has a precursor to the main radio pulse seen only at low radio frequencies (Moffett, D. A. and Hankins, T. H., 1996). If the precursor pulse is the true radio pulse, the phase offset between radio and the higher energy pulses is ∼0.05 in phase (see e.g. Romani & Yadigaroglu, 1995).

1. Cusumano et al. (2004), 2. Kuiper et al. (2004), 3. Abdo et al. (2009a), 4. Rots et al. (1998), 5. Rutledge et al. (2004), 6. Pellizzoni & et al. (2009), 7. Abdo et al. (2009g) 8. Zavlin et al. (2002), 9. Chatterjee et al. (2007), 10. Rots et al. (2004), 11. Pellizzoni et al. (2009), 12. Ramanamurthy et al. (1995), 13. Abdo et al. (2009c), 14. Abdo et al. (2009b), 15. Roberts et al. (2001), 16. Harding et al. (2002b), 17. Abdo et al. (2009f), 18. Abdo et al. (2009e), 19. Gotthelf et al. (2002b), 20. Halpern et al. (2008), 21. Abdo et al. (2009d), 22. Kuiper et al. (1999), 23. De Luca et al. (2005), 24. Thompson et al. (1999), 25. Becker et al. (2006), 26. Zavlin & Pavlov (2004), 27. Hermsen et al. (1997), 28. Gonzalez et al. (2005), 29. Becker et al. (2005),

The measured offset for PSR J0205+6449 of $\phi = 0.10 \pm 0.01$ supports the lack of correlation between phase offset and pulse period. In particular, PSR J0205+6449 has a very similar pulse period (65.7 ms) to the pulsar PSR J1420−6048 (68.2 ms), while the phase offset of PSR J1420−6048 is $\phi = -0.35(6)$ (Roberts et al., 2001). It is likely that the geometry and viewing angle of each system will affect the measured phase offset and may ultimately explain the range of observed offsets.

The radio-to-X-ray phase offset for PSR J0205+6449 is consistent with the radio-to-γ-ray offset of $\phi = 0.08 \pm 0.02$ (Abdo et al., 2009b). The X-ray and γ-ray phase offsets are likewise aligned for the Crab (Pellizzoni et al., 2009) and Vela pulsars (e.g. Abdo et al., 2009f), while this is not the case for the young pulsar PSR B1509−58 (Kuiper et al., 1999), nor the millisecond pulsar PSR J0218+4232 (Abdo et al., 2009a).

The outer gap model of Romani & Yadigaroglu (1995) predicts that the magnetospheric X-ray pulse should lag the radio pulse by 0.35−0.5 in phase and should appear as a single broad pulse. Neither prediction is supported by the X-ray profile of PSR J0205+6449. In addition, a thermal X-ray pulse arriving in phase with the radio pulse is predicted, while no thermal pulsations have been detected from PSR J0205+6449 (Murray et al., 2002).

PSR J0205+6449 is detected up to 40 keV with the PCA on board *RXTE*. It is one of an increasing number of young pulsars detected in the hard X-ray energy range and has also recently been detected up to ~ 3 GeV with the *Fermi Space Telescope* (Abdo et al., 2009b). Comparing the emission of the Crab pulsar and nebula to the 3C 58 pulsar and nebula at higher energies may offer insight into the physical reasons behind the intriguing differences between these two seemingly similar objects.

4.7 Conclusions

Multi-wavelength timing observations offer an excellent probe of both the temporal and emission characteristics of young pulsars. We observed two large glitches that are not characteristic of the proposed young age of PSR J0205+6449. This is not conclusive however, and the timing data are consistent with an age of 829 yr if the

pulsar was born spinning slowly with $P_0 \sim 60\,\mathrm{ms}$, or an age of $\tau_c \sim 5.4\,\mathrm{kyr}$ if the pulsar was born spinning rapidly. Furthermore, the age of the pulsar is consistent with $\tau > \tau_c = 5.4\,\mathrm{kyr}$ if its true braking index $n < 3$, as is the case for all measured values of n, though there is currently no evidence for $n < 3$ for PSR J0205+6449. Long-term timing may eventually allow for the measurement of n by using the incoherent method performed on the Vela pulsar (Lyne et al., 1996). Alternatively, if the source experiences a long period without glitches, n might be constrained using a partially phase-coherent method used for PSR B0540−69 (Livingstone et al., 2005a).

We have presented the first measurement of the phase offset between the radio and X-ray pulses of PSR J0205+6449 to be 0.10 ± 0.01, which is consistent with the recently reported γ-ray phase offset of $\phi = 0.08 \pm 0.02$ (Abdo et al., 2009b). PSR J0205+6449 is rare in that it has both the magnetospheric X-ray and γ-ray phase offset precisely measured. Among the pulsars with measured phase offsets, with periods ranging from 1.56 ms to 1250 ms, there is no correlation between pulse period and phase offset, as shown in Table 4.2 and Figure 4.13. Phase offset measurements are important for constraining the pulse emission region and significant progress is occurring at present in the measurement of radio-to-γ-ray phase offsets with the ongoing detection of many radio pulsars as γ-ray pulsars with *Fermi* (Abdo et al., 2010b).

5
Long-term X-ray Timing of the Young Pulsar PSR J1846−0258

The contents of this Chapter are reported in the paper "A Braking Index for the Young, High-Magnetic Field Pulsar PSR J1846−0258 in the Supernova Remnant Kesteven 75," published in the *Astrophysical Journal* (Livingstone et al., 2006). After the publication of the paper, timing data continued to accumulate and the pulsar spun-down without incident for a further 301 days. We included these data in our analysis, and present the updated results here. The addition of these data does not significantly change the results or the conclusions of the paper.

Since the publication of this paper, a significantly improved distance measurement was reported, changing the derived X-ray luminosity for the pulsar (though not significantly changing the main result of the paper). Calculations using the updated distance are included in this Chapter.

5.1 Introduction

The very young and energetic pulsar PSR J1846−0258 was discovered in 1999 in an archival *RXTE* observation (Gotthelf et al., 2000). With a characteristic age of only $\tau_c = 728\,\mathrm{yr}$, PSR J1846−0258 is possibly the youngest of all known rotation-powered pulsars. It is situated at the centre of the composite supernova remnant Kesteven 75 (commonly called Kes 75, and also known as G29.7−0.3), which is observed as a half-shell of $3.5'$ diameter, with a central nebula powered by the pulsar (Helfand et al., 2003). The pulsar's X-ray spectrum is typical of rotation-powered pulsars, exhibiting non-thermal power-law emission with a relatively hard spectral index of $\Gamma = 1.1$ (Ng et al., 2008). However, its large inferred magnetic field of $B = 4.9 \times 10^{13}\,\mathrm{G}$ places it

in an emerging class of rotation-powered pulsars with magnetar-strength fields (e.g. Kaspi & McLaughlin, 2005). Unlike the majority of rotation-powered pulsars, radio pulsations have never been detected from this source (Kaspi et al., 1996; Archibald et al., 2008).

The distance to the pulsar has been a matter of debate. Neutral hydrogen absorption measurements indicate that the pulsar resides well across the Galaxy, roughly at a distance of 19 kpc (Becker & Helfand, 1984). This distance, however, was difficult to reconcile with the large implied diameter of the remnant of 9.7 pc, which, in turn implied either a supernova explosion energy of 10^{53} erg or a much larger system age (Helfand et al., 2003). More recently, Leahy & Tian (2008) suggested a distance of ∼6 kpc based on measurements of HI and ^{13}CO spectra, while Su et al. (2009) suggest a kinematic distance to the supernova remnant of ∼ 10 kpc based on measurements of the velocity structure within the molecular cloud thought to be interacting with the remnant.

Radiation from this pulsar is detected exclusively in the X-ray band, with a 0.5 – 10 keV luminosity of $L_X = 2.6 \times 10^{34} (d/6\,\mathrm{kpc})^2\,\mathrm{erg\,s^{-1}}$ (Ng et al., 2008). This corresponds to an X-ray efficiency of converting spin-down energy into X-ray luminosity of ∼ 0.32%, similar to the Crab pulsar X-ray efficiency of ∼ 0.16% (Saito, 1998). If the real distance to the pulsar is closer to 10 kpc as suggested by Su et al. (2009), its X-ray efficiency is ∼ 0.89%.

The measurement of pulsar braking indices (n) is crucial to the understanding of the physics underlying pulsar spin down, as described in Chapter 1. The simple spin-down model presumes that a pulsar slows as a simple magnetic dipole in a vacuum and thus $n = 3$. Of the five unambiguous measurements of pulsar braking indices obtained so far, all yield a value of $n < 3$ (Lyne et al., 1993, 1996; Camilo et al., 2000; Livingstone et al., 2005a,b).

There are few pulsars that are potential candidates for a significant measurement of n; 4 of the 5 measured values are from sources with characteristic ages less than 2000 yr. The first requirement for a significant measurement of n is that the pulsar

spins down sufficiently quickly for a measurement of $\ddot{\nu}$. The second requirement is that the position of the pulsar is accurately known at the $\sim$1 arcsecond level. The third requirement is that the spin-down must not be seriously affected by glitches or timing noise. Since both glitches and significant timing noise are common in young pulsars (particularly for $\tau_c > 5\,\mathrm{kyr}$; McKenna & Lyne, 1990; Marshall et al., 2004), many of the pulsars that spin down fast enough for a measurement of n are irretrievably contaminated. Thus a new pulsar younger than 2 kyr such as PSR J1846−0258 provides an excellent opportunity to measure a new braking index and test different models of pulsar spin down (e.g. Melatos, 1997).

In this Chapter, we present the first phase-coherent timing solution for the Kes 75 pulsar based on 6.3 yr of X-ray timing data from a long-term monitoring campaign with the *Rossi X-ray Timing Explorer* (*RXTE*).

5.2 Observations and Analysis

The data analyzed in this Chapter span 7.1 yr from 1999 April 18 – 2006 May 24 (MJD 51286 – 52879). Typically, 3 PCUs were operational during any single observation. We used the first layer of each operational PCU and extracted events in the 2 – 20 keV range (*RXTE* channels 4 – 48) as this maximizes the signal-to-noise ratio of individual profiles of this source. We analyzed 196 observations, resulting in 182 detections of the pulse for a total integration time of 342 hr. The data were unevenly spaced throughout the 7.1 yr of observations, as shown in Figure 5.1. Because PSR J1846−0258 was occasionally not the primary target of *RXTE* (see Chapter 2, Table 2.1), integration times ranged from $\sim$1.5 to >25 ks, resulting in a variety of signal-to-noise ratios for individual pulse profiles.

Relatively accurate input spin parameters are required to "bootstrap" a phase-coherent ephemeris. We determined an initial ephemeris by merging observations taken on a single day and performing a periodogram analysis on each combined observation, resulting in a set of 134 frequency measurements spanning the 7.1-yr monitoring interval. From these measurements, we derived an initial frequency derivative,

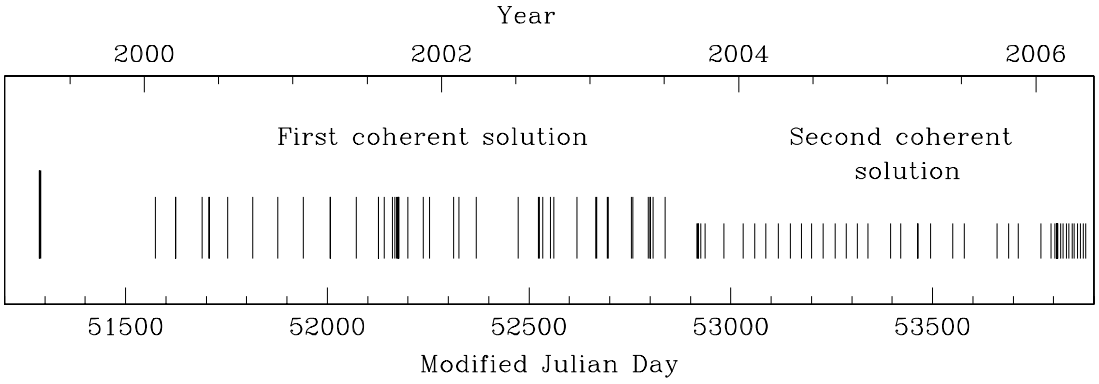

Figure 5.1: Distribution of *RXTE* observations of PSR J1846−0258 over the 7.1-yr interval analyzed in this Chapter. Each bar represents all observations occurring on a single day; 96 merged observations are shown in total. The mid-length bars represent data included in the first phase-connected solution, while the short bars represent data included in the second phase-connected solution. The initial three *RXTE* observations (tallest bars) of the source occur significantly before the monitoring observations and cannot be unambiguously phase connected with the later data.

$\dot{\nu}$. This ephemeris was then used to fold each time series with 16 phase bins. This number of bins was chosen because of the lack of features in the roughly sinusoidal profile and the resulting reasonable signal-to-noise ratio for individual profiles, particularly those made from short integrations. Resulting profiles were cross-correlated in the Fourier domain with a high signal-to-noise ratio template, shown in Figure 5.2. The cross-correlation process assumes that the pulse profile is stable; indeed, we found no evidence for variability (as discussed further in Chapters 6 and 7). We implemented a Fourier domain filter by using only the first six harmonics in the cross-correlation. For each observation, the cross-correlation yielded the time of arrival of phase-zero of the average pulse profile at the fold epoch. The TOAs were fitted to a timing model (see §5.3 and §5.3.1) using the pulsar timing software package `TEMPO` (as described in §3.7). After phase-connecting the data, we merged observations occurring on a single day and used the ephemeris to re-fold the data in order to obtain more accurate TOAs. This process produced 96 TOAs with a typical uncertainty of ∼8 ms (∼2.5% of the pulse period), improved from a typical TOA uncertainty of ∼10 ms.

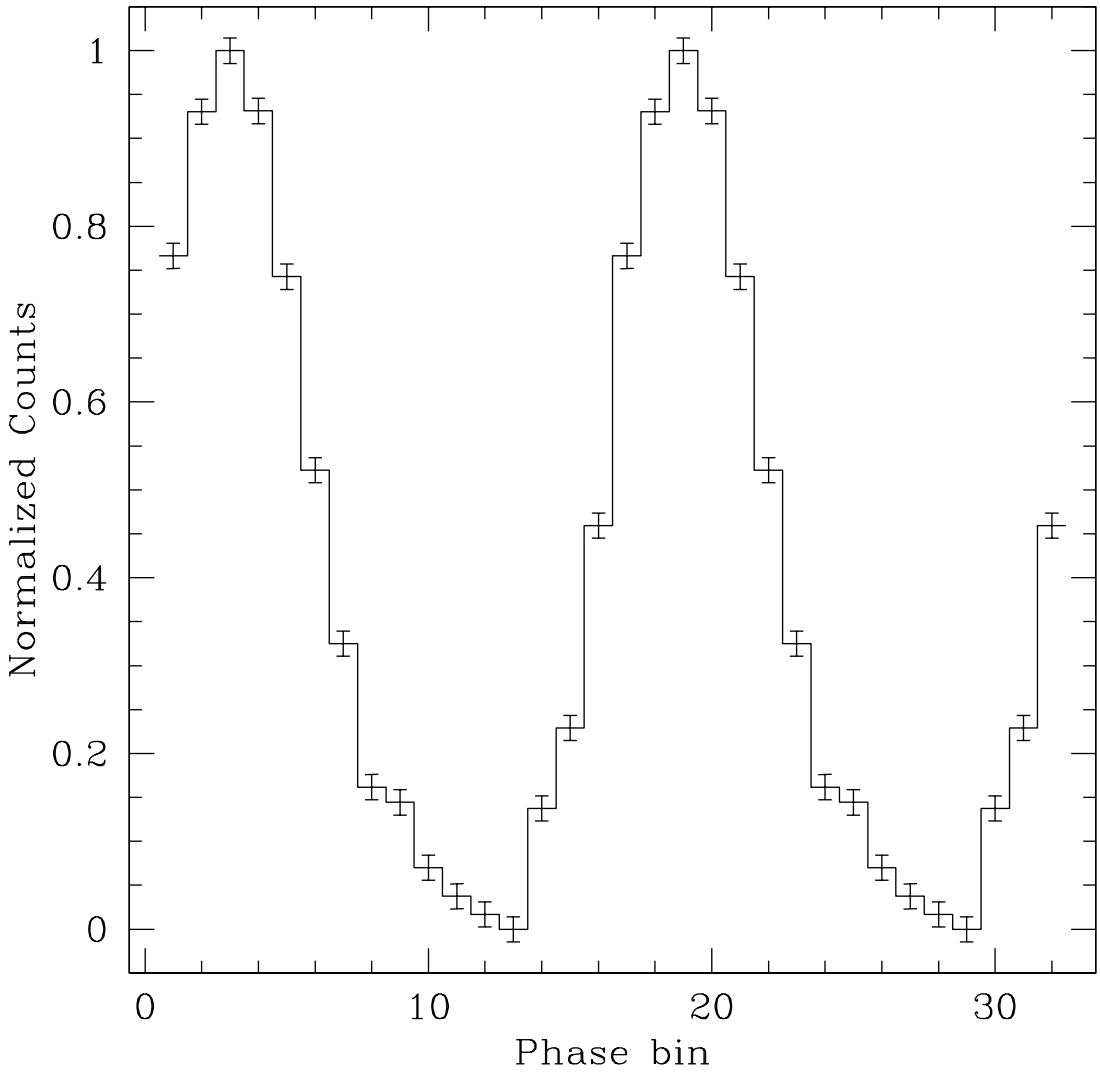

Figure 5.2: Integrated 2 – 20 keV pulse profile of 342 hr of data over 7.1-yr of *RXTE* observations of PSR J1846−0258, with 16 phase bins. Two full pulse cycles are shown for clarity.

5.3 Phase-Coherent Timing Analysis

To determine spin parameters for PSR J1846−0258, we obtained phase-connected timing solutions for 6.3 yr of X-ray timing data spanning 2000 January 31 to 2006 May 24, including 93 TOAs[1]. The sampling of the observations over 7.1 yr includes several large gaps, which precludes a single phase-coherent timing solution for the entire interval. The first *RXTE* observations of the pulsar (which resulted in its discovery) occurred $\sim$ 9 months prior to the commencement of regular monitoring observations, and so were not useful in our phase-coherent analysis. The first coherent solution is valid over the range MJD 51574 – 52837 (3.5 yr), while the second coherent solution is valid over the range MJD 52915 – 53879 (2.6 yr), as indicated in Fig. 5.1.

We used our initial incoherent ephemeris (as described in § 5.2) to bootstrap a phase-coherent solution over the 3.5 yr interval from MJD 51574 – 52837. This solution includes ν, $\dot{\nu}$, and $\ddot{\nu}$, whose values are given in Table 5.1. In the process of phase connection, it became clear that a small glitch occurred at MJD 52210 ± 10. The measured glitch parameters are $\Delta\nu/\nu = 2.5(2) \times 10^{-9}$ and $\Delta\dot{\nu}/\dot{\nu} \sim 9.3(1) \times 10^{-4}$, as determined with the glitch fitting facility in `TEMPO`. The effect of the glitch on the spin frequency of the pulsar is shown in Figure 5.3, where the pre-glitch ephemeris has been removed from all measurements of ν for clarity. The increase in the magnitude of $\dot{\nu}$ clearly dominates the event. On this scale, the very small increase in ν is not visible, though clearly indicated by the coherent fit to the data.

The relatively wide spacing of data near the glitch epoch prevents the detection of any glitch recovery, if any occurred. In fact, it is possible that the initial frequency jump was larger and recovered significantly before the following observation was taken. Timing residuals after subtraction of our best-fit timing model, including the glitch, are shown in the top panel of Figure 5.4. Note that systematic trends remaining in the residuals are likely the result of timing noise, common among young

[1]Three additional observations that occurred significantly earlier than monitoring observations could not be unambiguously phase-connected with these later data and thus were not included in the phase-coherent analysis.

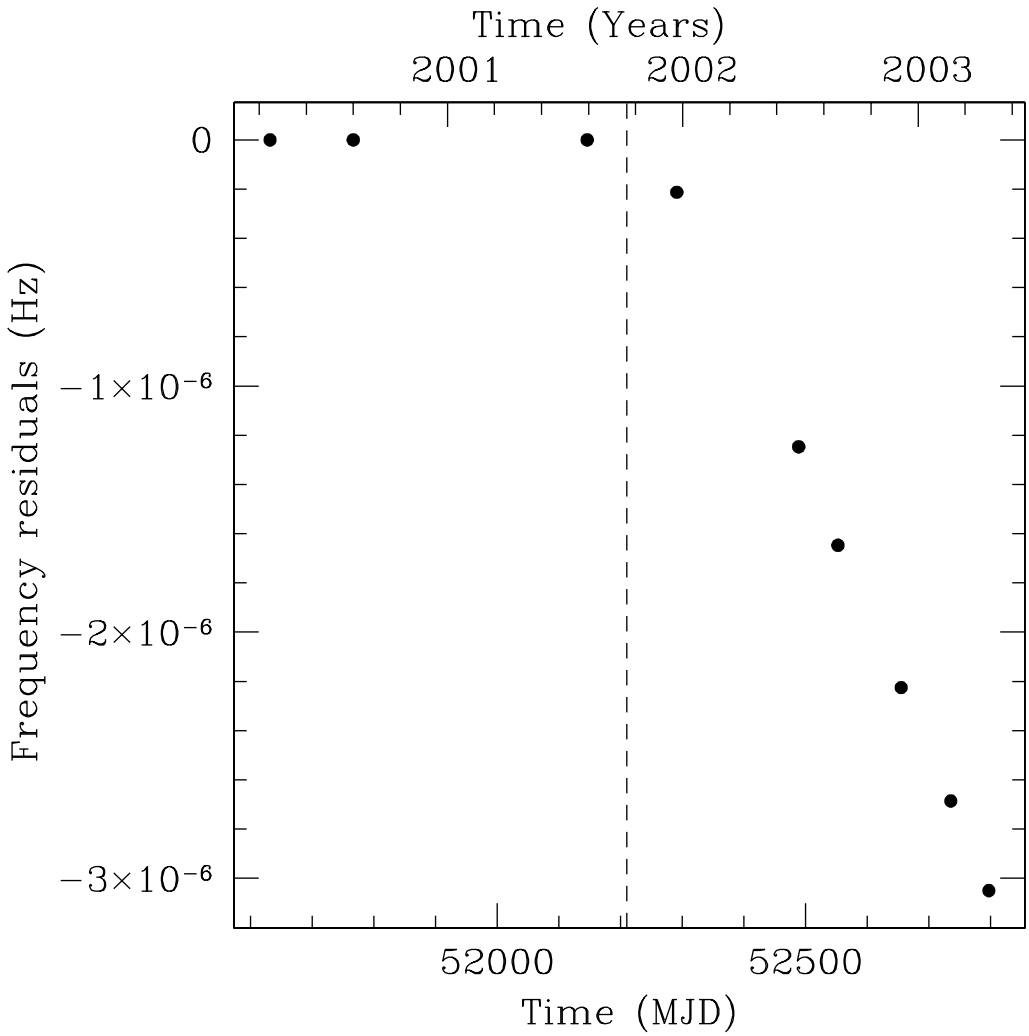

Figure 5.3: Measurements of ν with the pre-glitch trend removed. The dotted line marks the glitch epoch MJD 52210. Uncertainties are smaller than the points. Because the magnitude of the spin-up is so much smaller than the effect of the increase in magnitude of $\dot{\nu}$, the initial increase in ν is not visible on the figure.

pulsars, though unmodelled glitch recovery may also contribute to the observed residuals. Timing noise processes are known to contaminate measured spin parameters hence it is typically advisable to remove the systematics from the residuals by fitting additional frequency derivatives until the residuals are consistent with Gaussian noise (e.g. Kaspi et al., 1994). For this data span, a total of eight frequency derivatives were required to obtain Gaussian distributed residuals. Timing residuals with all eight derivatives removed are shown in the bottom panel of Figure 5.4. Fitting these additional frequency derivatives improves the χ^2 from 2933 for 43 degrees of freedom to 77 for 37 degrees of freedom. This χ^2 value indicates that the fit does not completely describe the data, however, this is not uncommon when fitting timing noise, which is not necessarily well described by a polynomial. The braking index, resulting from this "whitened" timing solution is $n = 2.64 \pm 0.01$. Deterministic spin-down parameters (i.e. not the higher order derivatives that correspond to timing noise) as well as glitch parameteres for this timing solution are given in Table 5.1.

Phase coherence was lost over a 78-day gap in the data beginning at MJD 52837, made clear by the fact that a timing solution attempting to connect over this gap fails to predict the pulse frequency at other epochs. This loss of phase could be due either to timing noise or another glitch. However, the estimated change in frequency over the gap calculated from phase-coherent solutions on either side of the data gap is negative, i.e. in the opposite direction from a conventional glitch, implying that a simple $\Delta\nu$ glitch alone cannot account for the loss in phase. However, a glitch with significant $\Delta\dot{\nu}/\dot{\nu} > 0$ could produce such an effect (see, however, §5.3.1).

A second phase-coherent timing solution was obtained for the 2.6-yr interval from MJD 52915 – 53879, with ν, $\dot{\nu}$, and $\ddot{\nu}$ fitted. The residuals after subtraction of the best-fit parameters are shown in the top panel of Figure 5.5. As systematic trends, again interpreted as timing noise or possibly unmodelled glitch recovery, remained in the residuals, three higher-order frequency derivatives were fitted. The resulting residuals are shown in the bottom panel of Figure 5.5. The measured braking index resulting from the "whitened" timing solution is $n = 2.68 \pm 0.02$, 1.7σ from that

Table 5.1: Phase-coherent timing parameters for PSR J1846−0258.

First phase-coherent solution	
Dates (Modified Julian Day)	51574.2 – 52837.4
Dates (Years)	2000 Jan 31 – 2003 Jul 17
Number of TOAs	47
Epoch (Modified Julian Day)	52064.0
ν (Hz)	3.0782148166(9)
$\dot{\nu}$ (10^{-11} s^{-2})	−6.71563(1)
$\ddot{\nu}$ (10^{-21} s^{-3})	3.87(2)
Braking Index, n	2.64(1)
Number of derivatives fitted	8
RMS residuals (ms)	7.65
Glitch epoch (Modified Julian Day)	52210(10)
$\Delta\nu/\nu$	$2.5(2) \times 10^{-9}$
$\Delta\dot{\nu}/\dot{\nu}$	$9.3(1) \times 10^{-4}$
Second phase-coherent solution	
Dates (Modified Julian Day)	52915.8 – 53879.5
Dates (Years)	2003 Oct 3 – 2006 May 24
Number of TOAs	46
Epoch (Modified Julian Day)	53404.0
ν (Hz)	3.070458589(1)
$\dot{\nu}$ (10^{-11} s^{-2})	−6.67801(1)
$\ddot{\nu}$ (10^{-21} s^{-3})	3.899(28)
Braking Index, n	2.68(2)
Number of derivatives fitted	6
RMS residuals (ms)	7.32

[a] - Quoted uncertainties are formal 1σ uncertainties as reported by `TEMPO`.

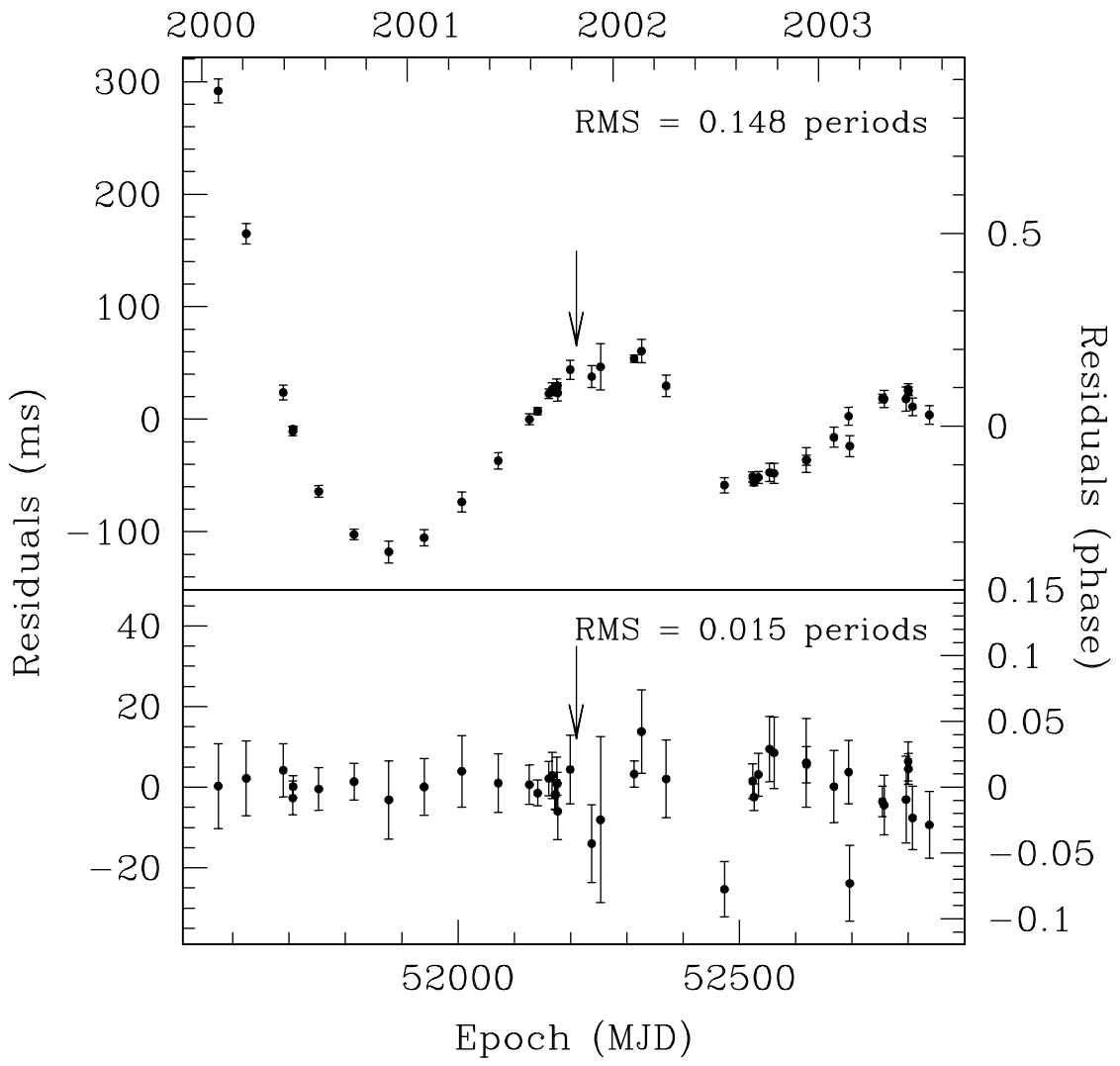

Figure 5.4: Phase-coherent X-ray timing analysis of the young pulsar PSR J1846−0258 spanning a 3.5-yr interval from MJD 51574 – 52837. Top panel: Residuals with ν, $\dot{\nu}$, $\ddot{\nu}$, as well as glitch parameters $\Delta\nu$ and $\Delta\dot{\nu}$ fitted. The glitch epoch MJD 52210 is indicated by the arrow. Bottom panel: Residuals with glitch parameters and eight frequency derivatives in total fitted to render the residuals consistent with Gaussian noise. Fitting the additional parameters improves the χ^2 from 2933 for 43 degrees of freedom to 77 for 37 degrees of freedom. Although these parameters do not completely describe the data, the χ^2 is not improved significantly by fitting additional frequency derivatives, which is not uncommon when timing noise is present.

measured from the first segment of timing data. Deterministic parameters for the second timing solution are given in Table 5.1.

5.3.1 Partially phase-coherent timing analysis

In order to mitigate the effects of timing noise, we also performed a partially phase coherent analysis. We obtained measurements of ν spanning 7.1 years of data as well as $\dot{\nu}$ and $\ddot{\nu}$ over 6.3 years of data. This method is useful to detect small glitches, as well as to obtain more accurate measurements of n in some cases (e.g. Livingstone et al., 2005a). Using the overall phase-coherent ephemeris as a starting point, closely spaced (within ~ 2 days) observations were phase-connected to obtain a local measurement of ν. In this way we obtained a total of 22 measurements of ν. A two degree polynomial was fitted to these ν measurements to get another measurement of n, however, in this case the glitch near MJD 52210 and the possible glitch between MJD 52837 – 52915 restricted the available time baseline and rendered this analysis of limited value. The most contraining measurement is $n = 2.83 \pm 0.39$, from 13 values of ν spanning MJD 51286 – 52199, in agreement with our phase-coherent value.

We repeated this process, measuring eight independent values of $\dot{\nu}$, spanning on average 115 days, shown in the top panel of Figure 5.6. Note that the first $\dot{\nu}$ measurement was prior the glitch near MJD 52210 and the glitch can clearly be seen in the Figure, as a sudden increase in the magnitude of $\dot{\nu}$. The bottom panel of Figure 5.6 shows the post-glitch slope removed from the data, highlighting the change in $\dot{\nu}$ at the time of the glitch, $\Delta\dot{\nu}/\dot{\nu} = (9.5 \pm 0.3) \times 10^{-4}$, in agreement with the value obtained from the phase-coherent fit.

Note that at the 78-day data gap between MJD 52837 and 52915, there is not a significant permanent change in $\dot{\nu}$ in Figure 5.6. This indicates that if a glitch did occur during this period, it consisted of primarily a change in ν. The only glitch consistent with the data would have had to have occurred near MJD 52910 with magnitude $\Delta\nu/\nu < 5 \times 10^{-8}$. A glitch with no change in $\dot{\nu}$ is typical of pulsars with larger characteristic ages (> 5 kyr), but cannot be ruled out in this case. A glitch with a short timescale recovery is also a possible description of the data.

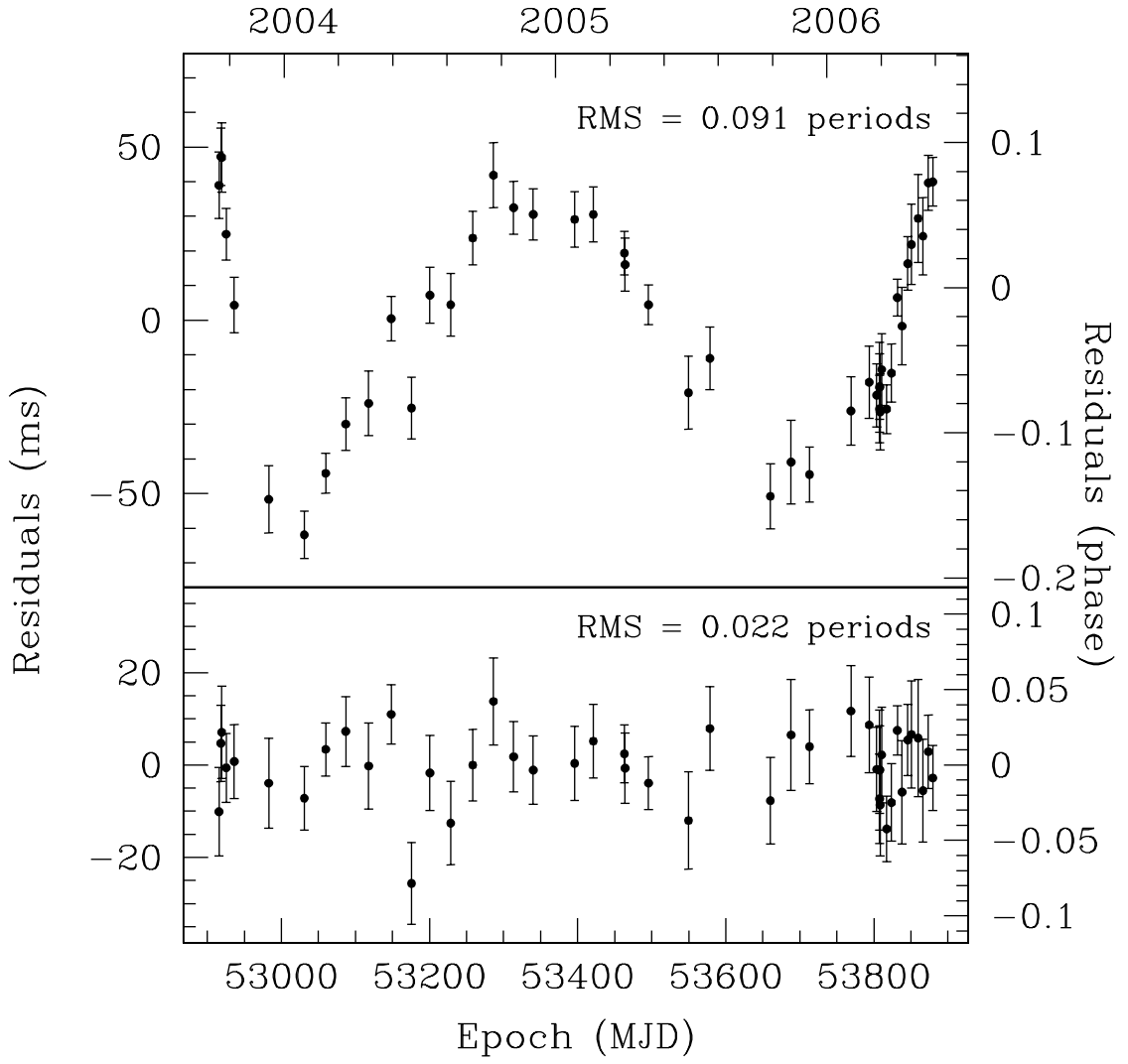

Figure 5.5: Phase-coherent X-ray timing analysis of PSR J1846−0258 spanning a 2.6-yr interval from MJD 52915 – 53879. Top panel: Residuals with ν, $\dot{\nu}$, and $\ddot{\nu}$ fitted. Bottom panel: Residuals with six frequency derivatives total fitted to render the residuals consistent with Gaussian noise. Fitting the additional parameters improves the χ^2 from 597.4 for 42 degrees of freedom to 36.3 for 38 degrees of freedom.

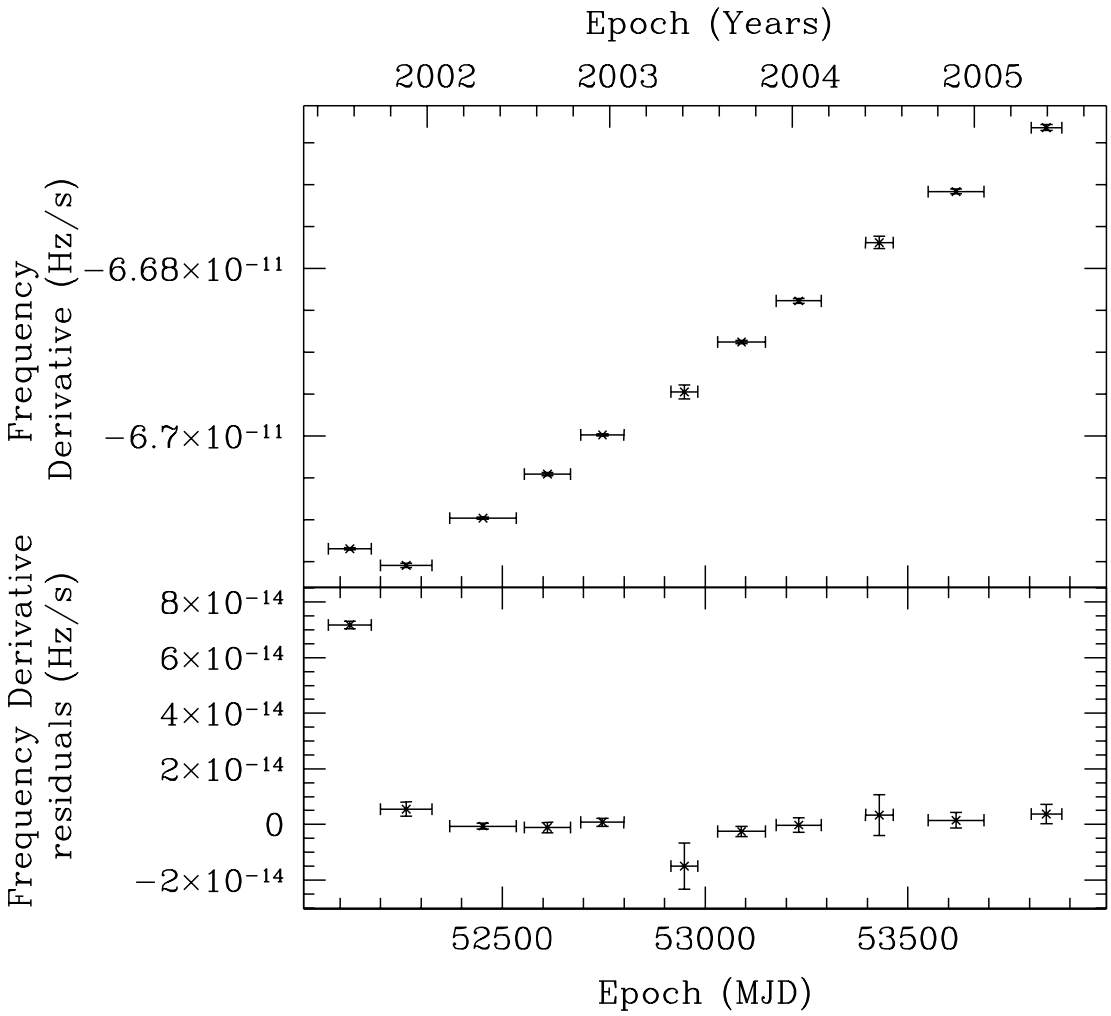

Figure 5.6: Eleven phase-coherent $\dot{\nu}$ measurements spanning 6.3 yr of *RXTE* monitoring observations of PSR J1846−0258. Top panel: Measurements of $\dot{\nu}$. There is a clear discontinuity after the first measurement of $\dot{\nu}$, which we interpret as a glitch. Bottom panel: $\dot{\nu}$ measurements with the post-glitch slope fitted to highlight the discontinuity, which is quantified as $\Delta\dot{\nu}/\dot{\nu} = (9.5 \pm 0.3) \times 10^{-4}$. The uncertainties in the x-direction represent the range of validity for each ephemeris.

We also performed two linear weighted least squares fit to the $\dot{\nu}$ measurements, both before and after the gap at MJD 52837 – 52915, to obtain measurements of $\ddot{\nu}$ and thus n. The first segment resulted in $n = 2.60 \pm 1.26$, while the second resulted in $n = 2.72 \pm 0.06$, in agreement with each other given the poor constraint on n available from the first set of $\dot{\nu}$ values. Uncertainties were obtained from a bootstrap analysis, since we suspected that the formal uncertainty may underestimate the true uncertainty because of the presence of timing noise. The bootstrap is a robust method of determining uncertainties when a small number of sample points is available, as in this case (Efron, 1979). The first measurement is in agreement with our phase-coherent average value of $n = 2.65 \pm 0.01$, while the second measurement is 1.7σ from the coherent value.

Finally, we obtained four independent measurements of $\ddot{\nu}$ by phase-connecting as much data as possible with just ν, $\dot{\nu}$, and $\ddot{\nu}$ fitted, such that there was no noticeable contamination by timing noise appearing in the resulting residuals. The resulting n measurements are shown in Figure 5.7. Note that there is some indication that n may be growing with time, at a rate of $\Delta n/\Delta t \simeq 0.02 \pm 0.01\,\mathrm{yr}^{-1}$, resulting in a change of n of $\sim 5\%$ over 6.3 yr. However, this effect is only significant at the 2σ level. A similar analysis of 21 years of data from the young pulsar PSR B1509−58 showed long-term variations of $\sim 1.5\%$ in n, though these were shown to fluctuate about an average value of n (Livingstone et al., 2005b).

5.4 ASCA and BeppoSAX Observations

In order to verify the validity of our *RXTE* timing analysis, we re-analyzed the timing signal in two archival observations of the pulsar obtained with the *Advanced Satellite for Cosmology and Astrophysics* (*ASCA*) observatory (Tanaka et al., 1994). Details of the first observation (1993 October) can be found in Blanton & Helfand (1996) and Gotthelf et al. (2000), while details of the second observation (1999 March) are described in Vasisht et al. (2000). Using the prescription in the *ASCA* Data Reduc-

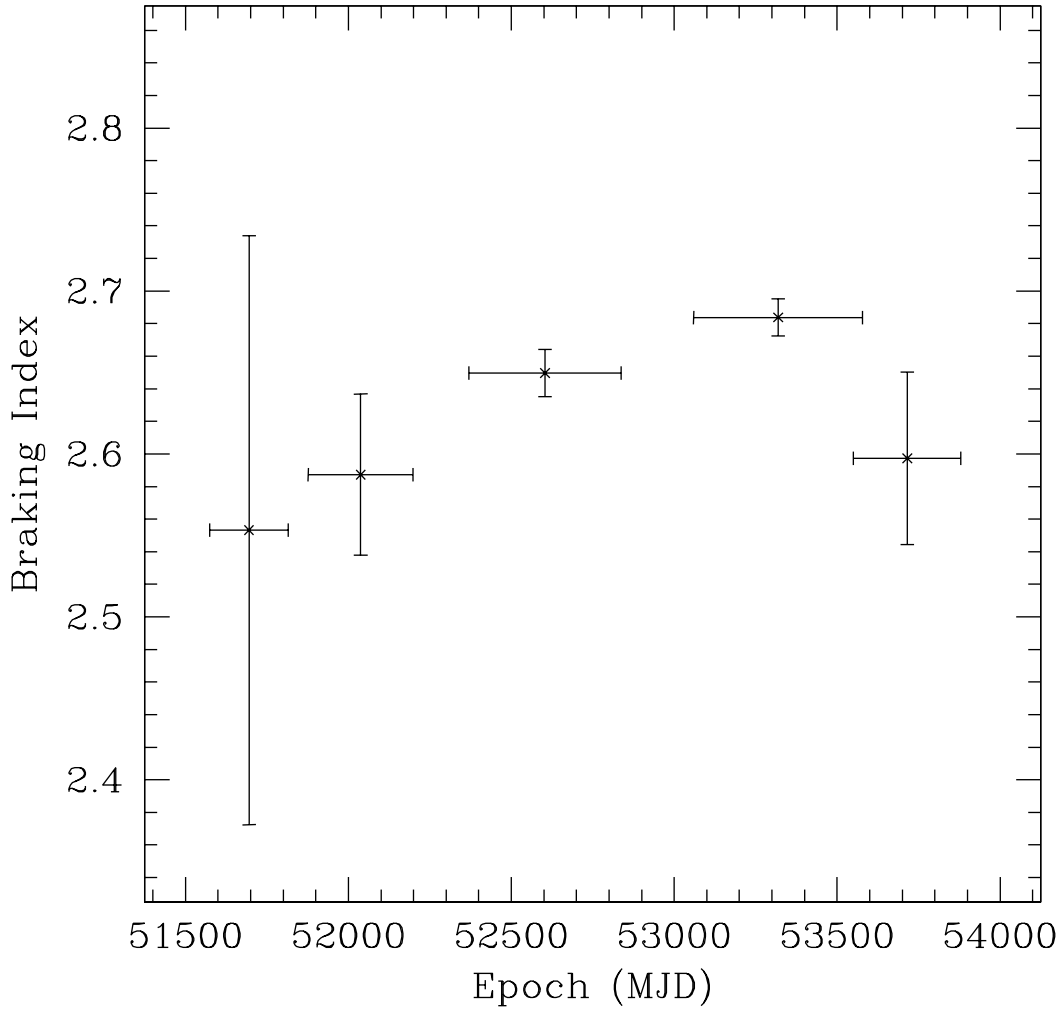

Figure 5.7: Phase-coherent measurements of the braking index, n of PSR J1846−0258, omitting $\sim$ 150 days of data after the glitch near MJD 52210 and the candidate glitch near MJD 52910 in order to avoid possible contamination from unmodelled glitch recovery. Each phase-connected solution has only ν, $\dot{\nu}$ and $\ddot{\nu}$ fitted and has Gaussian residuals. The braking index is consistent with being constant, since the slight increasing trend of $\Delta n/\Delta t \simeq 0.02 \pm 0.01\,\mathrm{yr}^{-1}$ is only significant of the 2σ level.

tion Guide[1] and standard `Ftools`, we extracted photons from the two gas-imaging spectrometers (GISs) in the 3 – 8 keV range from a $4'$ radius aperture surrounding the source. We chose this energy range in order to preferentially select the harder energy photons which come mainly from the pulsar rather than the softer energy events having a high probability coming from the supernova remnant (Gotthelf et al., 2000). We adjusted photon arrival times to the solar system barycentre using the *Chandra* position (Helfand et al., 2003) and then performed a periodogram analysis on the event data centered on the pulse frequency predicted by our *RXTE* ephemeris. We folded the data with 10 phase bins and detected a weak pulse in each observation. We generated a χ^2 periodogram in frequency space and identified the peak ν. To determine the uncertainty in the measured frequencies, we performed a Monte Carlo simulation that created fake data sets containing a periodic signal (at the same ν and amplitude determined from the periodogram) and Poisson noise. A periodogram was then performed on each noisy fake data set and the best ν was recorded. We performed 500 iterations for each observation and took the standard deviation as the 1σ uncertainty on our ν measurement. Using this method, we determined that for the 1993 October observation, $\nu = 3.094516(2)$ Hz and for the 1999 March observation, $\nu = 3.082859(3)$ Hz.

To verify our *RXTE* results, we compared the above *ASCA*-measured frequencies, as well as two 1999 *BeppoSAX* timing observations reported by (Mereghetti et al., 2002), with the *RXTE* ephemeris prediction. Both *BeppoSAX* ν measurements agree with our ephemeris within uncertainties, as do the two *ASCA* frequencies. That the 1993 *ASCA* measurement of ν agrees with our prediction is somewhat surprising, since the ephemeris used to predict ν covers a date range beginning seven years later. This does not necessarily exclude the possibility of glitches having occurred in the interim however, since glitches in this and other young pulsars have been measured that sometimes have amplitudes ~ 3 orders of magnitude smaller than we could detect given the uncertainties here (Livingstone et al., 2005a).

[1] http://heasarc.gsfc.nasa.gov/docs/asca/abc/abc.html

If no glitches occurred during the 6-yr gap from 1993 to 1999, then it is possible to fit all frequency measurements prior to the MJD 52210 glitch with a second order polynomial in order to mesure the braking index. Performing this analysis, the resulting braking index is $n = 2.44 \pm 0.09$, 2.2σ from our phase coherent result.

5.5 Discussion and Conclusions

Establishing the true ages of pulsars is important for several aspects of neutron-star studies including neutron star cooling, population synthesis, spatial velocity estimates, and to consider their associations with supernova remnants. Based on spin-down properties alone, a pulsar's true age is impossible to determine. However, we can estimate the age based on the standard spin-down model given our measurement of n. Assuming that the initial spin-frequency was much larger than the current value, $\nu_i >> \nu$, the age estimate for PSR J1846−0258 becomes,

$$\tau \leq -\frac{1}{n-1}\frac{\nu}{\dot{\nu}} \leq 884\text{yr}. \tag{5.1}$$

Since the initial spin frequency is unknown, the above estimate provides an upper limit on the pulsar age. Therefore, assuming that n and K (as from Eq. 1.7) have remained constant over the lifetime of the pulsar, the upper limit on the age of PSR J1846−0258 is $\sim$ 884 yr. This value is larger than the characteristic age of 728 yr, but still smaller than the unambiguously known age of the next youngest pulsar, that in the Crab Nebula.

Mereghetti et al. (2002) did an analysis of frequency measurements of the *ASCA* and *BeppoSAX* data, as well as a small subset of the *RXTE* data reported here. Although data gaps prevented them from making a firm conclusion regarding n because of the possibility of glitches, their tentative estimate (made assuming neither glitches nor substantial timing noise) $n = 1.86 \pm 0.08$, inconsistent with our result. There are two plausible explanations for this discrepancy. The first is that significant timing noise and/or glitches cannot be definitively excluded in the 6-yr gap between successive *ASCA* observations. The second is that the coordinate used to barycentre these data was ultimately found to be off by $\sim 7''$. The earlier study used coordinates

derived from *ASCA* data with a 20″ position uncertainty, prior to the availability of the new measurement provided by the *Chandra X-ray Observatory* used herein.

Our measured $n = 2.65 \pm 0.01$ is significantly less than 3, as is the case for all established values of n, which are shown in Table 5.2. There are several ideas for the nature of the deviation from the prediction of simple magnetic dipole braking. A time-varying magnetic moment could produce an observed n less than the true $n_0 = 3$ (Blandford, 1994). A varying B-field can in principle be verified with a measurement of the third frequency derivative, $\ddot{\nu}$, which may or may not ultimately be possible for this source, depending on the number and stregth of the glitches it experiences, as well as on the strength of its timing noise. At present, $\ddot{\nu}$ has been measured for only two pulsars, both of which are consistent with a constant B (Lyne et al., 1993; Livingstone et al., 2005b). Another suggested explanation for $n < 3$ is that a fallback disk forms from supernova material and modulates the spin-down of young pulsars via a propeller torque. Spin-down via a combination of magnetic dipole radiation and propeller torque results in $2 < n < 3$ (e.g. Alpar et al., 2001). However, this requires that the disk material does not suppress the pulsed emision during the propeller phse, which is difficult to achieve (Menou et al. 2001). Angular momentum loss due to a stellar wind would result in $n = 1$ (Michel & Tucker, 1969). Thus spin-down due to some combination of relativistic pulsar winds associated with young neutron stars and observed indirectly as pulsar wind nebulae (e.g. Roberts et al., 2003), and magnetic dipole spin-down may result in measured values of $n < 3$ (e.g. Harding et al., 1999).

Melatos (1997) presented an intriguing solution to the $n < 3$ problem. He postulated that the radius pertinent to dipole radiation is not the physical neutron star radius, but a "vacuum radius," associated with the location closest to the neutron star where field-aligned flow breaks down. Since this radius can be significantly larger than the neutron-star radius, the system can no longer be treated as a point dipole and $n = 3$ is not necessarily true. This model provides a prediction for n, given three observables: ν, $\dot{\nu}$, and α, the angle between the spin and magnetic axis. This model predicts that $2 < n < 3$ and that n approaches 3 as pulsar ages. Currently, there is no

Table 5.2: Timing parameters for pulsars with measured n

Name	$\boldsymbol{n}^a$	$\boldsymbol{\nu}$	$\boldsymbol{\dot{\nu}}$	$\boldsymbol{\tau_c}^b/\boldsymbol{\tau}^c$	$\boldsymbol{B}^d$	$\boldsymbol{\dot{E}}^e$	**Refs**
			$(\mathbf{10^{-11}})$		$(\mathbf{10^{12}})$	$(\mathbf{10^{36}})$	
		$(\mathbf{s^{-1}})$	$(\mathbf{s^{-2}})$	**(kyr)**	**(G)**	$(\mathbf{erg\,s^{-1}})$	
J1846−0258	2.65(1)	3.07	−6.68	0.73/0.88	49	8.1	1
B0531+21	2.51(1)	30.2	−38.6	1.24/1.64	3.8	460	2
B1509−58	2.839(3)	6.63	−6.76	1.55/1.69	15	18	3
J1119−6127	2.91(5)	2.45	−2.42	1.61/1.68	41	2.3	4
B0540−69	2.140(9)	19.8	−18.8	1.67/2.94	5.1	150	5
B0833−45[g]	1.4(2)	11.2	−1.57	11.3/57	3.4	6.9	6

[a]Uncertainties on n are in the last digit.

[b]Characteristic age is given by $\tau_c = \nu/2\dot{\nu}$, as in Eq. 1.16.

[c]Inferred upper limit timing age given n, $\tau = \nu/(n-1)\dot{\nu}$, assuming $\nu_0 >> \nu$, as in Eq. 1.17.

[d]Dipole magnetic field estimated by $B_{\rm dipole} = 3.2 \times 10^{19}(-\dot{\nu}/\nu^3)\,{\rm G}$, as in Eq. 1.11.

[e]Spin-down luminosity, $\dot{E} \equiv 4\pi^2 I \nu \dot{\nu}$, as in Eq. 1.8.

References (1) This work, (2) Lyne et al. (1993), (3) Livingstone et al. (2005b), (4) Camilo et al. (2000), (5) Livingstone et al. (2005a) (6) Lyne et al. (1996).

[g]Braking index for the Vela pulsar was not determined from a standard timing analysis due to the large glitches experienced by this object. Instead, measurements of $\dot{\nu}$ were obtained from assumed "points of stability" 100 days after each glitch (see Lyne et al., 1996, for details).

measurement of α for PSR J1846−0258. However, for the model to be consistent with our measured n within 3σ, α must lie between 8.1° and 9.6°. This is small but not unreasonable given the broad pulse profile for this source. Future radio polarimetric observations could in principle constrain α, though at present, no radio detection of this source has been reported (Kaspi et al., 1996; Archibald et al., 2008).

The measurement of n for PSR J1846−0258 brings the total number of measured braking indices to six, shown in Table 5.2, along with ν, $\dot{\nu}$, τ, τ_c, $B_{\rm dipole}$, and $\dot{E}$ for each object. Comparing this new value to the other four measurements obtained via typical timing methods (i.e. excluding the Vela pulsar whose n was measured using a different method, due to the glitches), we find no correlation between n and any of the other parameters. If the Vela pulsar is included in the analysis, there is a slight correlation between n and characteristic age. However, there is a relatively large scatter among the n values for the five younger pulsars, suggesting the Vela pulsar's value could also be just an extremum of the scatter, or that this value of n remains contaminated by large glitches.

The large scatter in the observed values of n could be intrinsic to the individual pulsar, for instance, there may exist a relationship between n and α or B, as suggested by Melatos (1997). One way to test this possibility would be to obtain more precise measurements of α for the youngest pulsars, e.g. via polarimetric observations. This, however, may prove difficult given that young radio pulsars tend to show very flat position angle swings (e.g. Crawford et al., 2001; Johnston et al., 2005). Alternatively, the scatter could be the result of a physical process outside the neutron star that is affecting the pulsar spin down, such as a supernova fallback disk as suggeted by Menou et al. (2001). There is some evidence for a fallbback disk surrounding a single neutron star, the AXP 4U 0142+61, however, there there is no indication that the disk and the neutron star are interacting (Wang et al., 2006).

PSR J1846−0258 is in an emerging class of high magnetic field rotation-powered pulsars (e.g. Camilo et al., 2000; Pivovaroff et al., 2000; Kaspi & McLaughlin, 2005; McLaughlin et al., 2003). The existence of these sources raises the question of why

they appear to be powered by rotation instead of by their large magnetic fields, as are the magnetars. The magnetar model proposed by Thompson et al. (2002) provides a prediction for the X-ray luminosity of a neutron star with a magnetic field of $\sim 10^{14}\,\mathrm{G}$ given a measurement of n. In the model, the neutron-star magnetosphere suffers a large scale "twist" of the north magnetic hemisphere with respect to the southern hemisphere, and resulting magnetospheric currents both scatter thermal surface photons and themselves heat the surface upon impact. Both effects result in the observed X-ray emission from magnetars. The model predicts a one-to-one relationship between twist angle, ϕ_{N-S}, and n, as well as L_X. In the case of PSR J1846−0258, if the above model were applicable, the measurement of $n = 2.65 \pm 0.01$ would imply a twist angle of $\phi \simeq 1.2\,\mathrm{rad}$, which would predict an X-ray luminosity of $L_X \simeq 9 \times 10^{34}\,\mathrm{erg\,s^{-1}}$. The observed luminosity in the 0.5 – 10 keV energy band is less than this prediction, e.g. for a distance range of 6 – 10 kpc, $L_X \simeq 2 - 5 \times 10^{34}\,\mathrm{erg\,s^{-1}}$.

In addition, since the observed X-ray flux can be easily accounted for by the spin-down luminosity of the pulsar, PSR J1846−0258 is clearly not an "anomalous" X-ray pulsar. Moreover, the pulsar's X-ray spectrum is much harder than that of any anomalous X-ray pulsar below ∼10 keV and inconsistent with what is predicted from the magnetar model. Indeed the spectrum is much more in line with those seen from rotation-powered pulsars (Gotthelf, 2003). More theoretical work needs to be done to explain the difference between the magnetars and the rotation-powered pulsars having inferred magnetar-strength fields.

Looking ahead Seven years of X-ray timing of PSR J1846−0258 revealed that it has many properties in common with other young and energetic rotation-powered pulsars. Notably, a measurable braking index $n < 3$ and occasional, small glitches. In this respect, PSR J1846−0258 is very much like the Crab pulsar. However, the pulsar also possesses an inferred magnetic field in excess of the Quantum-critical field (see Eq. 1.26), and lacks radio pulsations. These properties suggest a connnection with the magnetars, but during seven years of X-ray monitoring, PSR J1846−0258 did

not display any of the hallmarks of magnetar behaviour: either an X-ray luminosity larger than its spin-down luminosity, or radiative variability in the X-ray band.

6
Outburst Timing Behaviour of PSR J1846−0258

This Chapter is based primarily on the article "Timing Behavior of the Magnetically Active Rotation-Powered Pulsar in the Supernova Remnant Kesteven 75" (Livingstone et al., 2010a).

6.1 Introduction

As of 2006 May, PSR J1846−0258 was believed to be simply a high-magnetic field rotation-powered pulsar, with radio pulsations that do not cross our line of sight. However, on 2006 May 31, the source experienced a series of X-ray bursts and a sudden increase in X-ray flux. Both of these behaviours had never before been seen from a rotation-powered pulsar, but are common among magnetars, strongly suggesting magnetic activity in PSR J1846−0258 (Gavriil et al., 2008). The source also showed contemporaneous variations in its spectrum and surrounding nebula (Gavriil et al., 2008; Kumar & Safi-Harb, 2008; Ng et al., 2008).

The five bursts from PSR J1846−0258 were short (<0.1 s), with no detectable emission lines, preferentially occurred at pulse maximum and had peak luminosities greater than the Eddington luminosity (for isotropic emission from a $M = 1.4M_{\odot}$ neutron star; Gavriil et al., 2008). These bursts are essentially indistinguishable from X-ray bursts from AXPs and SGRs.

The observed flux flare is also typical magnetar behaviour, observed in many cases, and believed to arise from a twisted magnetosphere and the resulting magnetospheric currents that induce enhanced thermal emission and resonant upscattering of photons (Thompson et al., 2002; Beloborodov & Thompson, 2007). Flux enhancements are

also interpreted as a sudden release of energy in the crust, followed by a thermal afterglow.

Observations of PSR J1846−0258 with *Chandra X-ray Observatory* in 2000 and a serendipitous observation during the 2006 event show that the total flux increased by a factor of ~ 5.5 in the 2 – 10 keV energy range, but increased by a factor of ~ 17 in the 0.5 – 2 keV energy range, implying that the source spectrum softened significantly during outburst, tranforming the spectrum of PSR J1846−0258 into one reminiscent of the AXPs in quiescence (Gavriil et al., 2008).

Prior to this episode from PSR J1846−0258, no X-ray bursts nor flux flares have been detected from any RPP, making PSR J1846−0258 a unique transition object between rotation-powered pulsars and magnetars. The X-ray luminosity of PSR J1846−0258 can be accounted for entirely by the spin-down power of the pulsar, however, the observed X-ray bursts and flux flare are phenomena only seen thus far from magnetars (Gavriil et al., 2008).

In this paper, we discuss the timing behaviour of PSR J1846−0258 prior to, during, and following the period of magnetic activity observed in 2006 May-July. We show that a large glitch occurred contemporaneous with the X-ray bursts and onset of the flux flare, accompanied by an unusual increase in the timing noise of the pulsar. We show that the glitch recovery is very unusual for a RPP but is reminiscent of timing behaviour observed from magnetars and is further evidence of magnetic activity in PSR J1846−0258.

6.2 Observations and Data analysis

The data analyzed in this Chapter span 8.9 years from 2000 January 31 – 2008 December 10 (MJD 51574 – 54810). Data from 2000 January 31 – 2006 May 24 (MJD 51574 – 53879) were previously described in Chapter 5. Analysis of data spanning 2006 May 31 – 2008 December 10 (MJD 53578 – 54810) is presented here. Typically, two to three PCUs were operational during an observation. As in the previous Chapter, we used the first xenon layer of each operational PCU and extracted

events in the 2 – 20 keV energy range.

The known ephemeris (see Chapter 5) was used to fold each time series with 16 phase bins and resulting profiles were cross-correlated with a high signal-to-noise profile. The cross-correlation process used to create TOAs assumes that the pulse profile is stable (see Section 3.7); indeed, we found no evidence for profile variability that could bias TOA measurement, as shown in Figure 6.1, and confirmed by Kuiper & Hermsen (2009). The figure shows average profiles from before, after, and throughout the outburst and unusual timing behaviour. A single TOA was determined for each observation (as previously described) and then fitted to a timing model with `TEMPO`. After phase-connecting the data, we merged observations occurring on a single day and used the ephemeris to re-fold the data in order to obtain more precise TOAs. This process produced 199 TOAs with a typical uncertainty ∼9 ms (∼2.7% of the pulse period).

6.3 Timing Analysis and Results

Phase-coherent timing is a powerful method for obtaining accurate pulsar parameters, but can only be used when timing noise and glitches are relatively small (e.g. Livingstone et al., 2005a). Phase-coherent timing for PSR J1846−0258 spanning MJD 51574 – 53879 is discussed in Chapter 5. Phase coherence was lost with the observation occurring on 2006 May 31 (MJD 53886) which contained 4 X-ray bursts and a pulse flux increase (Gavriil et al., 2008). For the following 32 observations spanning 192 days, no unambiguous phase coherent timing solution was possible. Instead, we performed periodograms to determine the pulse frequency. Uncertainties were determined from a Monte Carlo simulation, where noise was added to simulated sinusoidal pulses and the frequency for each trial was determined in the same way as for the real data (the same process was used here as for the periodogram analysis of *ASCA* data detailed in Chapter 5). Phase coherence was once again obtained starting MJD 54126 with closely spaced "bootstrapping" observations after the source reappeared from behind the Sun after 48 days. A single phase coherent timing solution was obtained

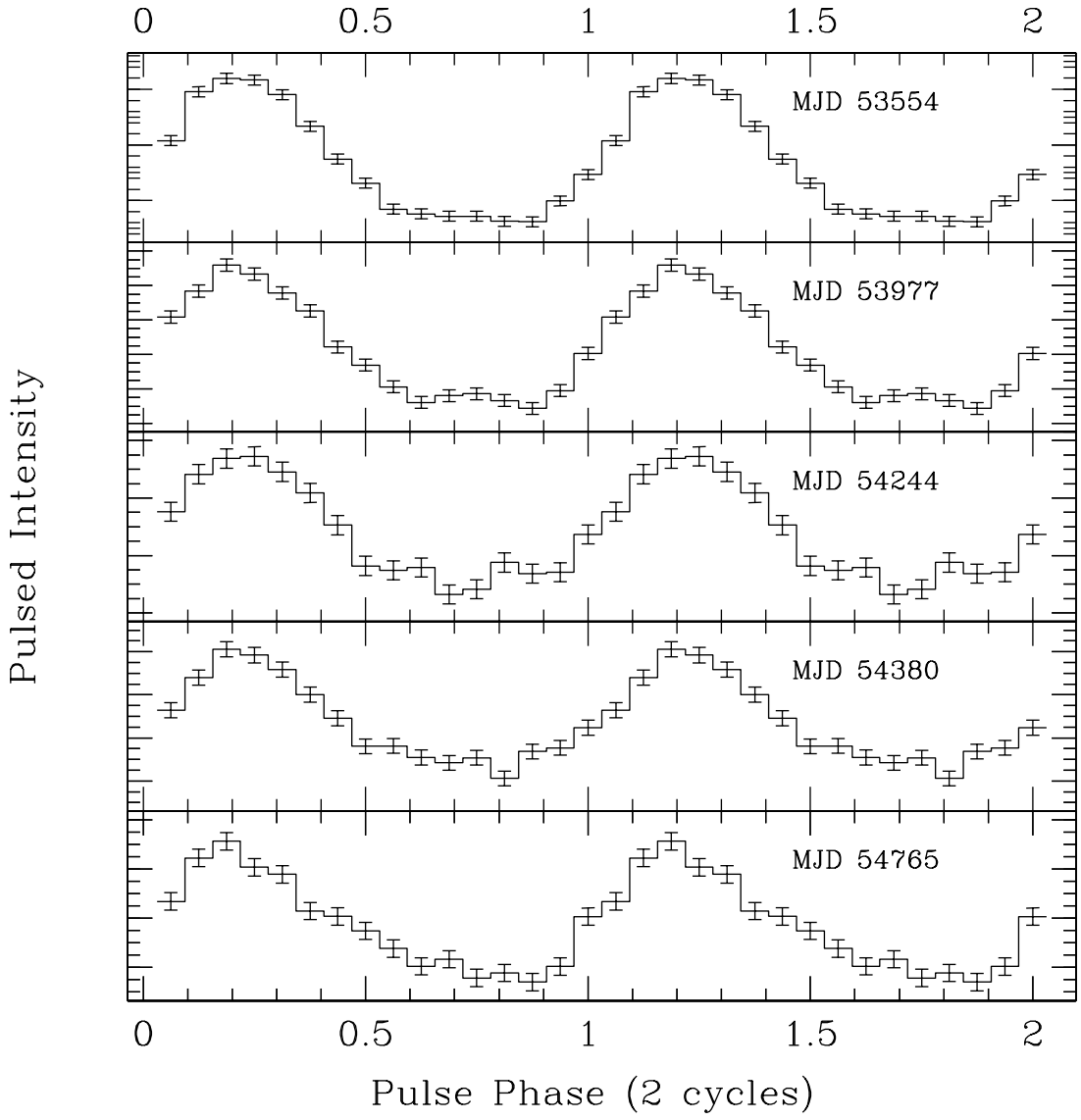

Figure 6.1: Five average 2 – 20 keV pulse profiles for PSR J1846−0258. Each profile is based on a single phase-coherent subset of data, except for the profile made from un-connected periodogram measurements of ν after the burst. For each profile, the centre date of observations is listed in the top right hand corner. The top panel shows the added profile for a phase-coherent timing solution spanning MJD 53228 – 53879, with ν, $\dot{\nu}$, and $\ddot{\nu}$ fitted. The profile includes 29 observations with a total exposure time of 223 ks. The second panel shows the summed profile for 9 observations after the X-ray bursts and flux flare spanning MJD 53949 – 54005 with an exposure time of 44.3 ks. The third panel shows the profile for a phase-coherent timing solution of 8 observations with ν and $\dot{\nu}$ fitted spanning MJD 54215 – 54265, near the unusual variations in $\dot{\nu}$. The total exposure time is 38.9 ks. The fourth panel shows the average pulse profile near the end of the glitch recovery, using a coherent timing solution of 9 observations with ν and $\dot{\nu}$ fitted, spanning MJD 54363 – 54397. The exposure time is 40.2 ks. The bottom profile shows the average pulse profile after the glitch had recovered using a coherent timing solution of 12 observations, spanning MJD 54726 – 54805. The exposure time is 59.0 ks.

spanning MJD 54126 – 54810. This timing solution is severely contaminated by long-term glitch recovery and timing noise, so the fitted parameters for the global solution are of limited value.

To analyze the long-term rotational behaviour of the pulsar, we created short phase-coherent timing solutions from 2000 until the onset of bursts, and from 2007 and 2008. Each timing solution included only ν and $\dot{\nu}$, and included as much data as possible while requiring the reduced χ^2 value of the fit to be $\sim$1. This resulted in 11 measurements of ν and $\dot{\nu}$ pre-glitch and 11 measurements post-glitch. In order to better utilize the available data in the post-glitch period, we created short overlapping timing solutions, each of which uses approximately half the data from two of the above described short data subsets, and has the same fitted parameters and χ^2 requirements. This can be useful because the short coherent timing solutions result in parameter fits that are dominated by the end points, which can be problematic when ν is varying rapidly from glitch recovery as in this case, or when timing noise is a significant effect. This produces an additional 9 post-glitch measurements of ν and $\dot{\nu}$. Coherent frequency measurements (crosses), overlapping frequency measurements (filled circles) and frequency measurements obtained via periodograms (open circles), are plotted in the top panel of Figure 6.2, with the pre-burst ν, $\dot{\nu}$, and $\ddot{\nu}$ removed. The middle panel of Figure 6.2 shows measurements of $\dot{\nu}$ from the short coherent timing solutions as crosses, with the overlapping $\dot{\nu}$ measurements in filled circles. In addition, open circles show three measurements of $\dot{\nu}$ that are each calculated from weighted least-squares fits to nine periodogram measurements of ν.

A frequency increase is apparent in the frequency residual plot (top panel and inset, Figure 6.2), indicating that a glitch occurred (also noted by Kuiper & Hermsen, 2009). Two measurements of ν are larger than the pre-glitch predicted value. We calculated the average $\Delta\nu = (5.5 \pm 2.3) \times 10^{-6}$ at MJD 53890 (4 – 11 days after the glitch occurred). The initial value of $\Delta\nu$ at the time of the glitch was presumably larger than this value, as indicated by the exponential fit to the data discussed below.

We fitted the measured frequencies of PSR J1846−0258 (fitting only 3 pre-glitch ν

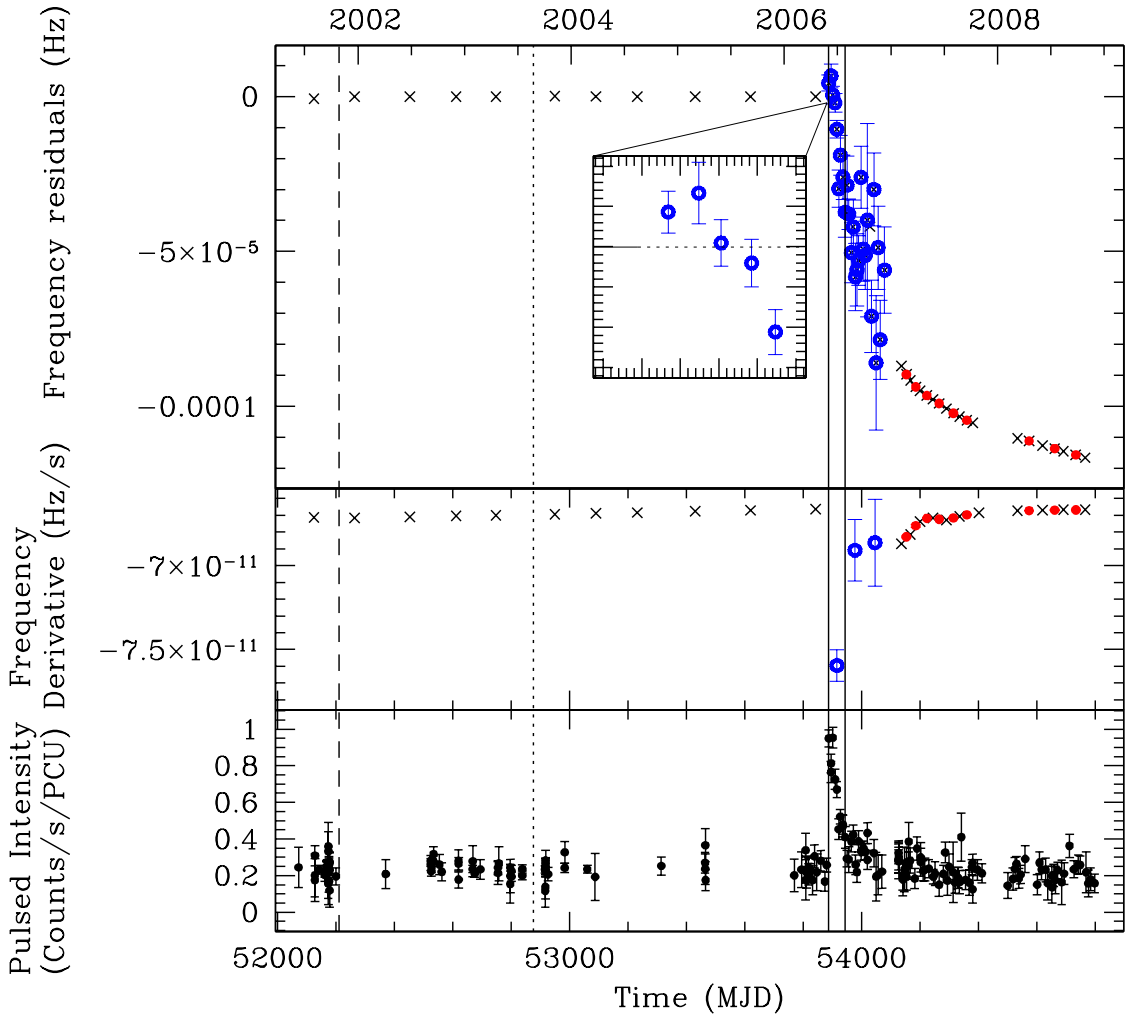

Figure 6.2: Timing and pulsed flux evolution of PSR J1846−0258 over 9 years. Top panel: Frequency measurements with pre-glitch ν, $\dot{\nu}$, and $\ddot{\nu}$ removed from all points for clarity. Black crosses are produced from short phase-coherent measurements of ν and $\dot{\nu}$, while filled red circles are produced similarly but from overlapping segments of data. Uncertainties are smaller than the points and are excluded for clarity. Open blue circles are periodogram measurements of ν. Middle panel: Frequency derivative ($\dot{\nu}$) measurements. Crosses are produced from short phase-coherent measurements of ν and $\dot{\nu}$, while filled red circles are from overlapping segments of data, but are otherwise produced in the same manner. See Section 6.3 for details. Open blue circles are from weighted least-squares fits of periodogram ν measurements. Bottom panel: Pulsed intensity measurements in the 2 – 20 keV energy band, as described in Section 6.4. The only significant flux increase is coincident with 4 X-ray bursts observed on MJD 53886. All panels: The dashed line represents the epoch of a small Crab-like glitch near MJD 52210, while the dotted line represents the epoch of a candidate glitch between MJDs 52837 and 52915 (as in Chapter 5). The two solid lines show the epochs where bursts were detected (Gavriil et al., 2008).

values) with an exponential recovery glitch model (Eq. 1.29), the results of which are shown in Figure 6.3. The top panel of the Figure shows frequency measurements with the pre-glitch ephemeris (ν, $\dot{\nu}$ and $\ddot{\nu}$) removed (as in Figure 6.2), while the bottom panel shows residuals from the glitch fit. The uncertainties from the periodogram measurements of ν are $2-3$ orders of magnitude larger than those from short coherent fits to the data and thus contribute minimally to the overall χ^2 value. Thus the glitch residuals (bottom panel, Figure 6.3) are shown to highlight the deviation from the fit of the coherent frequencies, which dominate the χ^2. Significant deviations from the fit can be seen during the period of glitch recovery, giving rise to a large reduced χ^2 value of ~ 267 for 45 degrees of freedom for the best fit (bottom panel, Figure 6.3).

Given the poor fit, the formal uncertainties underestimate the true values. To determine more reasonable uncertainties on the glitch parameters, we multiplied the uncertainties on the coherent ν measurements by a factor until the reduced χ^2 of the fit was ~ 1. We applied a multiplicative factor only to the phase coherent ν measurements because these uncertainties were $\sim 2-3$ orders of magnitude smaller than those from periodogram ν measurements, determined in a different way, and the contribution to χ^2 was mainly from the coherent ν values. Quoted uncertainties on the glitch parameters are from $\Delta\chi^2 = 1$ contours from the fit with multiplied uncertainties. The fitted value of the initial fractional frequency increase is $\Delta\nu/\nu = 4.0(1.3) \times 10^{-6}$, very large for such a young pulsar, where a typical value is $\Delta\nu/\nu \sim 10^{-8}$. More remarkable yet, however, is the amount by which the frequency recovers. We find $Q = 8.7(2.5)$, corresponding to a net decrease in frequency of $\Delta\nu_p = 9.52(9) \times 10^{-5}$ Hz. All fitted glitch parameters are given in Table 6.1.

While the deviation from the exponential fit is very significant for several months (bottom panel, Figure 6.3) the overall evolution after the glitch is dominated by the exponential recovery: the deviation from the fit is $\sim$2 orders of magnitude smaller than the overall post-glitch decrease in ν. The deviation from exponential recovery may well have been larger in the period just following the glitch, however, the large uncertainties on the periodogram measurements of ν (i.e. $\delta\nu \sim 10^{-6}$ Hz) prevent any

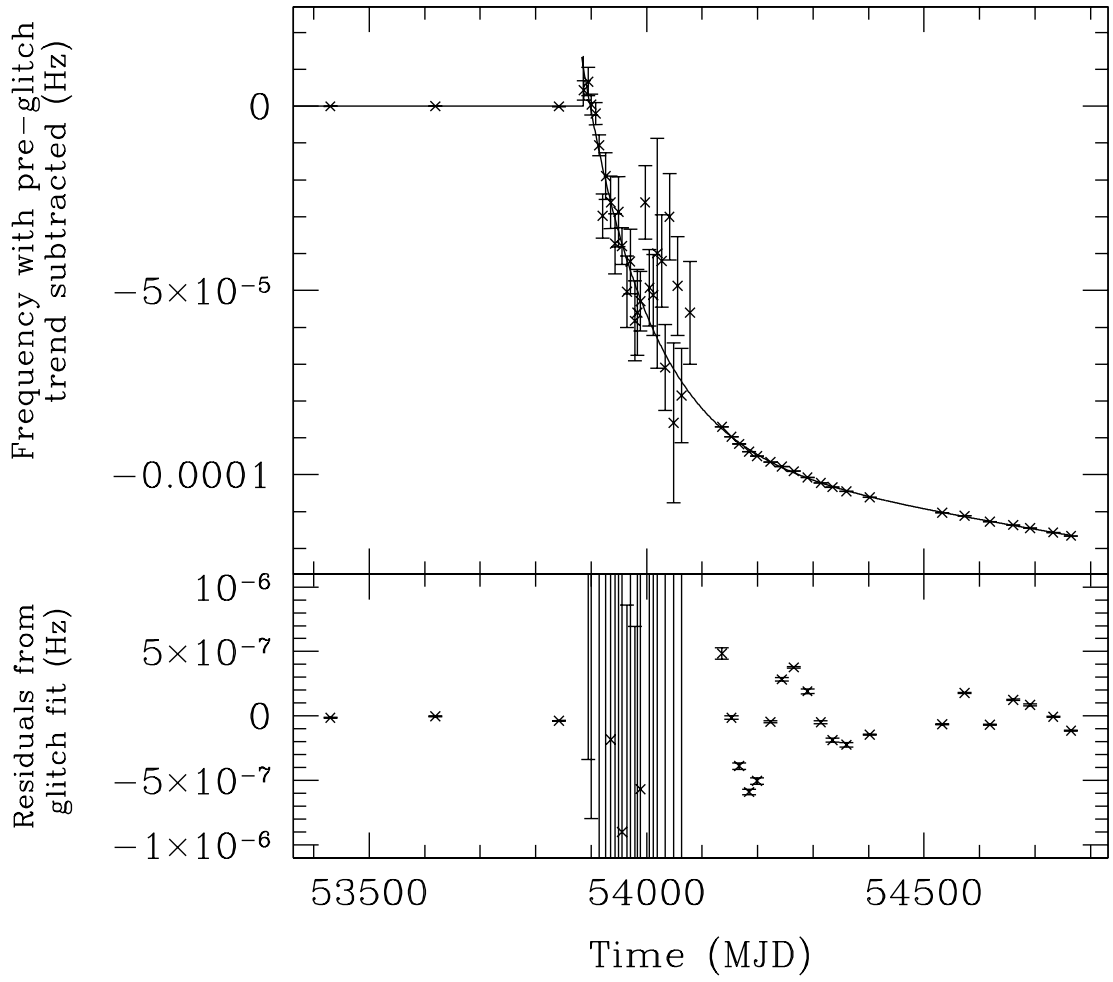

Figure 6.3: Top panel: Frequency measurements of PSR J1846−0258 (points) and the fitted exponential recovery glitch model (solid line). Pre-glitch ν, $\dot{\nu}$, and $\ddot{\nu}$ have been removed from all frequency measurements. Bottom panel: Residuals from the fit with the formal, un-multiplied uncertainties. The best fit has a ${\chi^2}_\nu$ of ~ 267 for 45 degrees of freedom. Significant variation from the fitted exponential is clear, however, the exponential recovery dominates the change in ν by ~ 2 orders of magnitude over the remaining systematic variations in ν. Given the large χ^2, we increased the uncertainties on the phase-coherent ν measurements until ${\chi^2}_\nu \sim 1$, and report uncertainties on the fitted model from the $\Delta\chi^2 = 1$ contours. All fitted parameters are given in Table 6.1.

Table 6.1: Glitch parameters for PSR J1846−0258

Parameter	**Value**
Epoch (Modified Julian Day)	53883.0(3.0)
$\Delta\nu/\nu$	$4.0(1.3) \times 10^{-6}$
$\Delta\dot{\nu}/\dot{\nu}$	0.0041(2)
τ_d (days)	127(5)
Q	8.7(2.5)
$\Delta\nu_p$	$-9.52(9) \times 10^{-5}$
$\Delta\nu_d$	$10.8(4) \times 10^{-5}$

Figures in parentheses are uncertainties in the last digits quoted and are the estimated 1σ uncertainties from the fitted exponential glitch recovery model using $\Delta\chi^2 = 1$ contours. The model is fitted to data with uncertainties on coherent measurements that are increased by a factor until ${\chi^2}_\nu \sim 1$ (see Section 6.3 for details).

firm conclusion. However, since the corresponding pulse TOAs cannot be unambiguously phase-connected, it is likely that large variations in ν and $\dot{\nu}$ occurred during the 240-day period between the glitch epoch and when we regained phase-coherence. It is also possible that a second, smaller glitch ($\Delta\nu/\nu < 10^{-7}$) occurred during this period. The observed deviation from the exponential recovery decreases as the glitch recovers. Thus, in the closing months of 2008, the pulsar was rotating regularly again, similar to its pre-glitch, pre-outburst behaviour.

Figure 6.4 shows post-glitch phase-coherent measurements of $\dot{\nu}$ (a subset of the $\dot{\nu}$ measurements shown in the middle panel of Figure 6.2). The pre-glitch measurements are excluded here for clarity. The solid line is the derivative of the glitch model fitted to the ν measurements, clearly showing that there is significant deviation from the model. The overall effect of the glitch recovery on $\dot{\nu}$ is clear, however, from MJD 54100 – 54300, the $\dot{\nu}$ measurements deviate from the exponential recovery by $\sim 0.15\%$. The effect of this anomalous change in $\dot{\nu}$ is not directly evident in the measurements of ν (which are dominated by the exponential recovery) but does help explain why the exponential glitch fit is not a satisfactory description of the data,

and is clear in the residuals of the glitch fit in the bottom panel of Figure 6.2.

6.4 Bursts and Pulsed Flux

The glitch during PSR J1846−0258's outburst was accompanied by a major pulsed flux enhancement (Gavriil et al., 2008). In order to quantify the radiative properties of the source during the glitch recovery, we extracted its pulsed flux using all available *RXTE* observations. First, we generated separate event lists for each PCU in FITS[1] format using the standard `FTOOLS`[2]. We then filtered our event lists such that we only preserved photons in the 2 – 20 keV band, from the first xenon layer, as for the timing analysis. The photon arrival times were then barycentered using the source position (Table 2.3) and the JPL DE200 solar system ephemeris. We folded the filtered barycentered photon arrival times using the ephemeris determined in our phase-coherent timing analysis with 16 phase bins. Using the folded profiles, we calculated the RMS pulsed flux in each PCU using the Fourier method described by Woods et al. (2004) keeping only the contribution from the 1st harmonic given the source's roughly sinusoidal profile. Because not all the observations were pointed at PSR J1846−0258 (see Table 2.1), we corrected for the reduced efficiency in each PCU due to the offset pointing using the collimator response of each PCU and the instrument attitude files. Finally, we averaged the pulsed flux in each PCU weighted by the fractional exposure of each PCU. We excluded the contribution from PCU 0 because of the loss of its propane layer which resulted in a significant change in sensitivity and background for this PCU, as well as the numerous detector breakdown events. Our pulsed flux time series is presented in the bottom panel of Figure 6.2. The event lists for each PCU created for the pulsed flux analysis were binned into 31.25 ms lightcurves and were searched for bursts using the burst search algorithm introduced in Gavriil et al. (2002). No additional bursts were found other than the five reported in Gavriil et al. (2008).

[1] http://fits.gsfc.nasa.gov

[2] http://heasarc.gsfc.nasa.gov/docs/software/ftools/

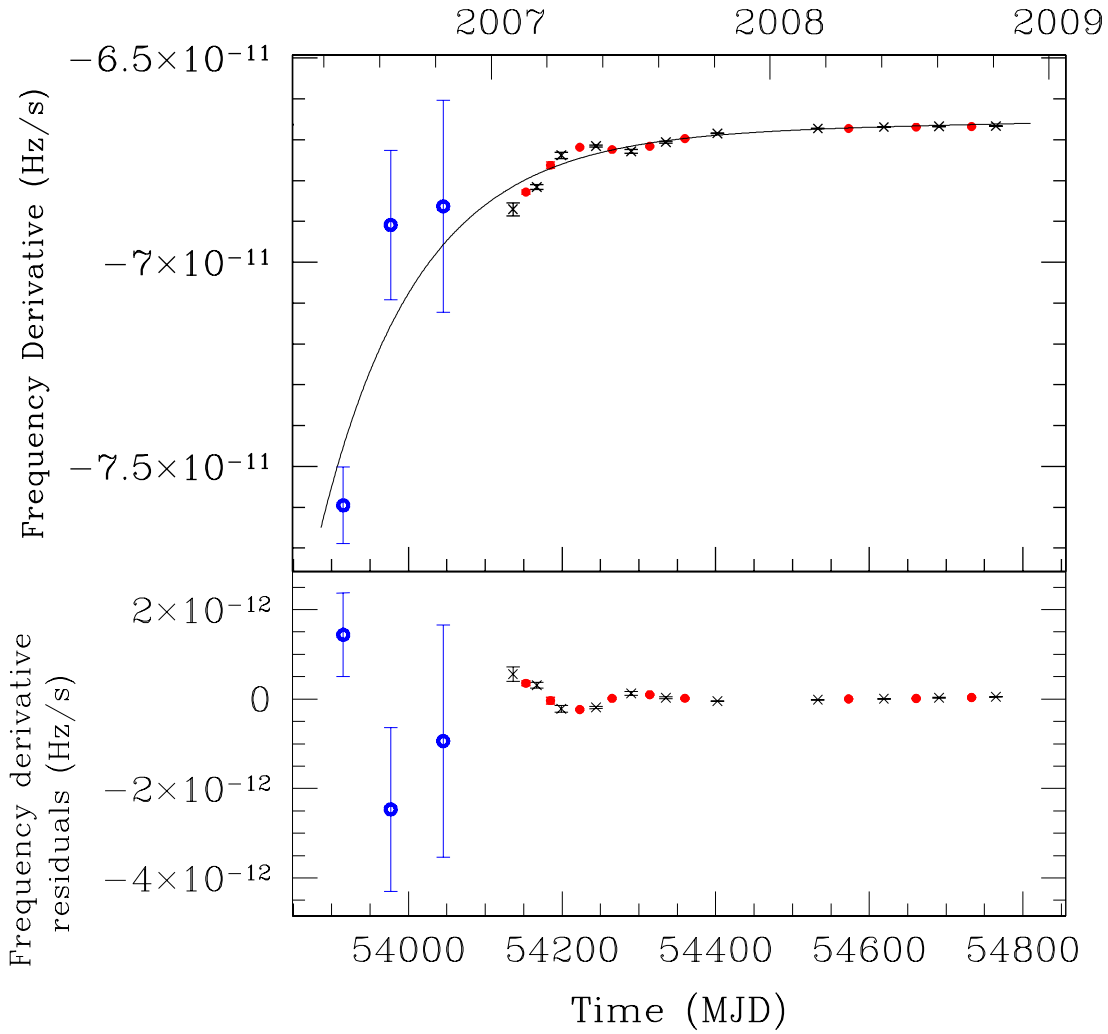

Figure 6.4: Top panel: Post-burst $\dot{\nu}$ measurements of PSR J1846−0258. Black crosses are produced from short phase-coherent measurements of ν and $\dot{\nu}$, while filled red circles are from overlapping segments of data, but are otherwise produced in the same manner. Open blue circles are from weighted least-squares fit to periodogram measurements of ν. See Section 6.3 for details. Note the significant deviation from a simple exponential glitch recovery evident in the coherent $\dot{\nu}$ measurements in the interval MJD 54100 – 54300. The solid line is the derivative of the exponential recovery model fitted to the frequency data. Bottom panel: Residuals of the $\dot{\nu}$ measurements and derivative of the exponential glitch recovery model.

We checked for a correlation between torque and pulsed flux by plotting the pulsed flux against the spin frequency derivative in log-log space, shown in Figure 6.5. All measurements of $\dot{\nu}$ before and after the glitch and bursts are shown, including three measurements of $\dot{\nu}$ obtained from weighted least-squares fits to ν measurements obtained from periodograms. These three $\dot{\nu}$ measurements have uncertainties $2-3$ orders of magnitude larger than those for $\dot{\nu}$ measurements from coherent timing.

The plot shows a possible correlation between flux and torque when both parameters are extreme. Fitting a power law to the data gives a power law index of ∼8. However, this value is constrained by a single measurement of $\dot{\nu}$ when the flux, and timing noise, are both very large. Excluding this point, no significant correlation between flux and $\dot{\nu}$ is observed.

The observed variations in $\dot{\nu}$ immediately following the glitch are at the $\sim 15\%$ level, while during the later phase connected period are at the $\sim 3\%$ level (Figure 6.4). Correspondingly small fluctuations in pulsed flux are not detectable in these data.

6.5 Discussion

6.5.1 Glitch properties

Four X-ray bursts in PSR J1846−0258 coincided with the onset of a flux flare on 2006 May 31 (MJD 53886). The pulsed flux decayed over ∼2 months and reached quiescence around the time of the fifth burst on 2006 July 27 (MJD 53943; Gavriil et al., 2008). Significant spectral changes also occurred (Gavriil et al., 2008; Kumar & Safi-Harb, 2008; Kuiper & Hermsen, 2009) and flux enhancement up to 300 keV was observed (Kuiper & Hermsen, 2009). Contemporaneous with the sudden change in the X-ray emission from PSR J1846−0258, we observed a large glitch with an initial frequency increase of $\Delta\nu = 1.24(41) \times 10^{-5}$ Hz. The glitch decayed over 127(5) days, with a recovery fraction of $Q = 8.7(2.5)$, resulting in a net decrease of the pulse frequency of $\Delta\nu = -9.52(9) \times 10^{-5}$ Hz. Furthermore, the timing behaviour during the period of recovery is not well modeled by a simple exponential function and measurements of $\dot{\nu}$ in particular are suggestive of a high level of timing noise for

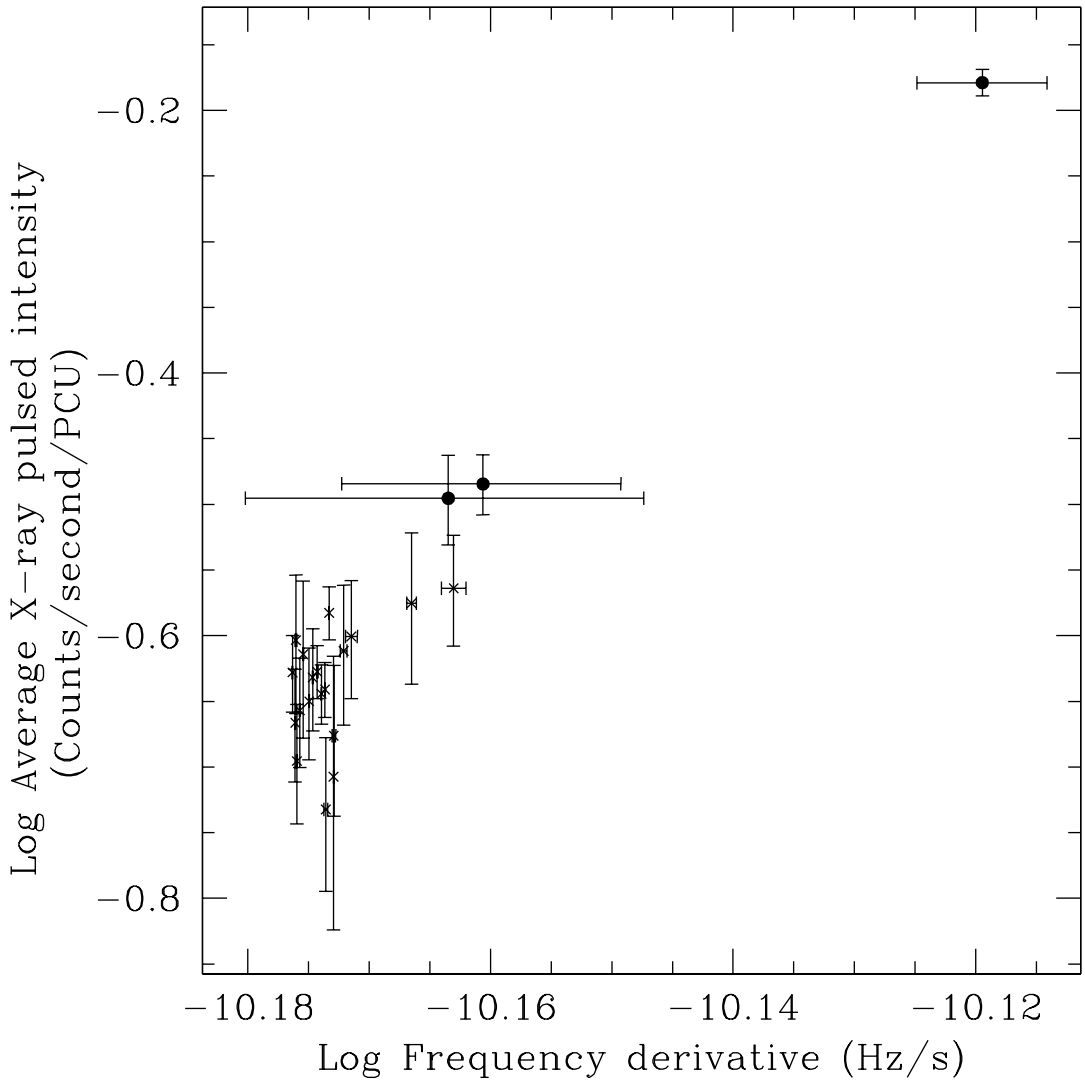

Figure 6.5: Observed relationship between pulsed flux and the spin-down rate of PSR J1846−0258. The measurements of $\dot{\nu}$ from phase-coherent timing solutions before and after the outburst are shown as crosses. The three $\dot{\nu}$ measurements made from least squares fits to periodogram measurements of ν are shown as filled circles. The best-fit power-law index to all data is ~ 8, however, the correlation is constrained by a single measurement of $\dot{\nu}$, made when the timing noise was extremely large. Excluding this single point results in no significant correlation. See Section 6.4 for details.

several hundred days following the glitch.

This glitch and subsequent recovery reinforces that PSR J1846−0258 underwent a period of magnetic activity in 2006. This glitch is entirely different from the previous glitch in this source, which was radiatively silent, small in magnitude ($\Delta\nu/\nu = 2.5(2) \times 10^{-9}$), dominated by a change in $\dot{\nu}$ ($\Delta\dot{\nu}/\dot{\nu} = 9.3(1) \times 10^{-4}$), and had no measurable recovery (Chapter 5). This small glitch is similar to those observed in the Crab pulsar (e.g. Wong et al., 2001) and other very young rotation-powered pulsars such as PSR B0540−69 (Livingstone et al., 2005a). It is unusual to have two such disparate initial $\Delta\nu$ magnitudes in the same source, particularly in such a young pulsar, though this has been seen in some older pulsars such as PSR B1737−30, which has glitch magnitudes spanning four orders of magnitude (Lyne et al., 2000; Janssen & Stappers, 2006). In fact, the glitch reported here is the largest glitch ever observed in any of the pulsars with characteristic ages less than $\sim 2\,\mathrm{kyr}$ (the Crab pulsar, B0540−69, B1509−59, and J1119−6127), none of which have experienced glitches with fractional magnitudes larger than $\Delta\nu/\nu \sim 10^{-8}$.

The glitch reported here has a recovery fraction of $Q = 8.7 \pm 2.5$. The measured value of $Q > 1$ implies that the net frequency change after the glitch recovery is negative, $\Delta\nu_p = -9.52(9) \times 10^{-5}$, as shown in Figure 6.2. A similar effect was recently observed in the AXP 4U 0142+61, though with much smaller magnitude of $Q = 1.07 \pm 0.02$ (Gavriil et al., 2009).

The negative change in ν resulting from the over-recovery of the PSR J1846−0258 glitch is similar in magnitude to the unresolved timing event seen in the magnetar SGR 1900+14 in the months before the giant flare in 1998 (Woods et al., 1999). In that case, an enhanced spin-down of the magnetar was observed over ∼3 months. Closely spaced timing observations around the time of the timing event were not available, so no glitch could be resolved, if indeed one occurred. Thompson et al. (2000) attribute the observed behaviour in SGR 1900+14 to one of two possibilities. The first is an increase in the magnitude of $\dot{\nu}$ by a factor of ~ 2.3, persisting for $\sim 80\,\mathrm{days}$. The second is that a negative glitch, that is, a sudden spin-down occurred,

with magnitude $\Delta\nu/\nu \simeq 1 \times 10^{-4}$. However, a timing event similar to that observed in PSR J1846−0258 could also describe the data. It is curious, however, that such similar fractional changes in ν should occur in two sources that experienced such disparate radiative changes, with the energy output from SGR 1900+14 being several orders of magnitude larger than from PSR J1846−0258.

AXP 1E 2259+586 experienced a glitch contemporaneous with 80 X-ray bursts, a flux flare and pulse profile changes in 2002 (Kaspi et al., 2003; Woods et al., 2004). Neither this glitch nor the large PSR J1846−0258 glitch can be described with a single exponential decay model. The addition of an exponential growth component better describes the 1E 2259+586 glitch, however, the addition of a similar component for the PSR J1846−0258 glitch does not provide a significant improvement to the fit. Interestingly, the flux enhancement observed in 1E 2259+586 lasted much longer ($>$ 2 yr; Zhu et al., 2008) than the glitch recovery time scale ($\tau_d \sim 16$ days), whereas the reverse is true for PSR J1846−0258, with $\tau_d = 127$ days and a flux decay timescale of 55.5 ± 5.7 days (Gavriil et al., 2008). The 1E 2259+586 event can also be distinguished from the PSR J1846−0258 glitch in that its recovery fraction is much smaller, with $Q \simeq 0.19$. In 2001, the AXP 1RXS J170849.0−400910 also experienced a glitch with recovery that was not well described by a simple exponential, and not improved with the addition of a second exponential term (Kaspi & Gavriil, 2003; Dall'Osso et al., 2003; Dib et al., 2008a). Woods et al. (2004) argued that it is unlikely that 1RXS J170849.0−400910 experienced bursts or a pulsed flux flare associated with this glitch because a flux flare would have had to decay on a time scale less than the glitch decay time scale. However, this is exactly the behaviour observed from PSR J1846−0258, albeit with a much longer time scale. Long-term spectral changes and flux variations have been claimed in 1RXS J170849.0−400910 (Rea et al., 2005; Campana et al., 2007; Israel et al., 2007b).

An interesting characteristic of some AXP glitches is a period of enhanced spin-down immediately following the glitch, as observed in 1E 2259+586, 1E 1841−045, and 1RXS J170849.0−400910 (Kaspi & Gavriil, 2003; Dib et al., 2008a).

The spin-down rate immediately after a glitch can be determined by taking one derivative of Equation 1.29 and setting $t = t_g$,

$$\dot{\nu} = \dot{\nu}_{\rm pre-glitch} - \Delta\dot{\nu} - \Delta\nu_d/\tau_d. \tag{6.1}$$

The additional instantaneous spin-down at the glitch epoch owing to the exponential recovery corresponds to the last term in the above equation, $\dot{\nu}_{\rm inst} = -\Delta\nu_d/\tau_d$. For the 1E 2259+586 glitch, $\dot{\nu}_{\rm inst} = (8.2 \pm 0.6)\dot{\nu}$, while a typical value for a RPP is $\sim 0.005\dot{\nu}$ (see Peralta, 2006, and references contained therein). For PSR J1846−0258 the instantaneous spin-down is $\dot{\nu}_{\rm inst} = 0.15\dot{\nu}$, larger than for any other RPP glitch, but not as large as those measured for some AXPs. However, an enhanced spin-down is not observed in every AXP glitch, nor in the first confirmed PSR J1846−0258 glitch.

In the post-glitch era for PSR J1846−0258, there is evidence for a ∼200-day interval where $\dot{\nu}$ deviates significantly from an exponential glitch recovery, and it is possible that further significant deviation occurred during the 240-day period comprising unconnected data and a gap in observations following the glitch. Perhaps $\dot{\nu}$ is varying in a stochastic fashion similar to that observed in the AXP 1E 1048.1−5937 (Gavriil & Kaspi, 2004; Dib et al., 2009). In this AXP, a ∼year-long period of rapid $\dot{\nu}$ variations followed a large pulsed flux flare and a possible glitch in 2002. Another glitch in 2007 coincided with the onset of a pulsed-flux flare, again followed by stochastic variations in $\dot{\nu}$. Another similarity between these sources is that the flux enhancement decayed away long before the timing variations subsided. Alternatively, perhaps the variations are more simply attributed to timing noise, as is seen in many young RPPs. The behaviour remains unusual however, since this is qualitatively very different from the mild timing noise observed in PSR J1846−0258 prior to magnetic activity, and such a large change in timing noise behaviour is unprecedented among RPPs.

A simple estimate of the transfer of rotational kinetic energy at the time of the glitch can be obtained by treating the star as a solid rotating body. Assuming the canonical neutron star moment of inertia of $I = 10^{45}\,{\rm g\,cm^2}$, the energy deposited in the

solid crust at the time of the glitch owing to the increase in ν is $\Delta E \simeq (2\pi)^2 I \nu \Delta\nu \sim 2\times10^{42}$ erg. However, it is well established that neutron stars are comprised of at least two components, a solid crust coupled to the core and a loosely coupled superfluid component in the crust. Taking the two-component model into account but not making any further assumptions about the nature of the two components, we can calculate the energy transferred between the components at the time of the glitch. The first constraint is that angular momentum is conserved, that is,

$$I_C \Delta\nu = I_{SF} \Delta\nu_{SF}, \tag{6.2}$$

where $\Delta\nu$ is the observed increase in spin-frequency, and $\Delta\nu_{SF}$ is the unknown change in spin-frequency of the superfluid, and I_C and I_{SF} are the moment of inertia of the solid crust and core, and superfluid, respectively. An estimate of the energy contained in the glitch can then be calculated as

$$E_g = \Delta E_C - \Delta E_{SF} = (2\pi)^2 I_C \Delta\nu(\nu - \nu_{SF}). \tag{6.3}$$

The frequency lag between the crust and superfluid can be estimated from the glitch decay time, τ_d, as

$$\nu_{lag} = \nu_{SF} - \nu \ \simeq \frac{\tau_d \nu}{\tau_c}, \tag{6.4}$$

where τ_c is the characteristic age of the pulsar (Shapiro & Teukolsky, 1983). For PSR J1846−0258, the frequency lag is $\nu_{SF} - \nu \ \sim 0.0013$ Hz, giving a glitch energy of $\sim 7\times10^{39}$ erg for the measured glitch parameters (see Table 6.1). If the measured glitch decay timescale, τ_d, in this case is dominated by processes external to the neutron star (as discussed in Section 6.5.2), any other glitch decay timescale would occur on a shorter timescale than the one observed, so this estimate of the frequency lag and thus glitch energy can be considered an upper limit.

For a distance to the pulsar of 6 kpc (Leahy & Tian, 2008), the energy estimated to have been released in the bursts and flux flare, assuming isotropic emission, is $(3.8 - 4.8) \times 10^{41} (d/6 \text{ kpc})^2$ erg (2 – 60 keV). A new estimate of the distance to the pulsar of ∼10 kpc (Su et al., 2009) implies a large amount of energy contained

in the radiative outburst of $(1.1 - 1.3) \times 10^{42} (d/10\ \mathrm{kpc})^2\,\mathrm{erg}$ (2 – 60 keV). For either distance, the energy contained in the radiative outburst is several orders of magnitude larger than that contained in the glitch. This is similar to the bursts and glitch from 1E 2259+586, for which the energy contained in the glitch was ∼2 orders of magnitude less than the energy contained in the bursts and flux flare (Woods et al., 2004). This is suggestive that the glitch alone is not responsible for the radiative outburst, in contrast to the argument put forward by Kuiper & Hermsen (2009). Moreover, there is no evidence in this event (or in any other similar AXP event) that the glitch preceded the radiative event. This could be tested only by sensitive continuous X-ray monitoring of this and other similar sources.

6.5.2 Physical models for "magnetic glitches"

Rotation-powered pulsar glitches are thought to arise from differential rotation in the neutron star, where the crust contains superfluid neutrons rotating more rapidly than the surrounding matter (e.g. Alpar et al., 1984; Alpar & Pines, 1993, and discussed in Chapter 1). Magnetar glitches may instead be triggered by strong internal magnetic fields as the crust is deformed, either plastically or cracked violently (Thompson & Duncan, 1996). This idea is supported by the large number of glitches now observed to occur at approximately the same epoch as magnetically powered radiative events, such as bursts and flares (e.g. Kaspi et al., 2003; Dib et al., 2009; Israel et al., 2007a).

The physics underlying glitches with $Q > 1$ is unclear. The classical glitch model of vortex unpinning in the superfluid crust of the neutron star does not readily produce such dramatic glitch recoveries. One possibility is that some parts of the superfluid are in fact rotating more slowly than the crust. Then the initial ν increase would be from a transfer of angular momentum from a more rapidly rotating region of the superfluid to the crust, which is then followed by a transfer of angular momentum from the crust to the more sluggish region of the superfluid. This is the explanation put forward by Thompson et al. (2000) as a possible explanation of the net spin-down event in SGR 1900+14. They argue that regions of slowly rotating superfluid can occur in magnetars because vortex motion is dominated by advection across the

neutron star surface by the deforming crust and that gradual plastic deformation of the neutron star crust will cause the superfluid to rotate more slowly than the crust. However, it is not clear whether such behaviour is expected in a neutron star with a magnetic field of $\sim 5 \times 10^{13}$ G, spinning relatively rapidly compared to the magnetars ($\sim$10 times faster).

That the recovery of the PSR J1846−0258 glitch so far overshoots the initial frequency increase is suggestive of an external torque following the glitch. Previous evidence for an external torque includes the large fraction of I implied to have been decoupled in the core of the pulsar (and thus a large fraction of I) decouples temporarily from the crust (Kaspi & Gavriil, 2003; Woods et al., 2004). In PSR J1846−0258, however, the post-glitch relaxation amplitude is much greater than the initial glitch amplitude, offering support for the idea that the post-glitch spin-down behaviour results from an external source.

One possibility is that a magnetic field twist responsible for the X-ray bursts and flux enhancement also affects the spin-down of the pulsar. In this case the observed recovery is driven by the propagation of magnetic field untwisting (similar to a shock wave) through the magnetosphere. During this process, the spin-down of the star may increase because the effective magnetic field has increased. When the "shock" reaches the light cylinder, which can take place on few month time scales, the spin-down should return to its pre-burst value (Beloborodov, 2009). This theory also allows for non-monotonic behaviour in the spin-down after an event, as observed in both AXP 1E 1048.1−5937 (Gavriil & Kaspi, 2004; Dib et al., 2009) and PSR J1846−0258. This model also predicts a delay between flux variations and the onset of timing variability, as was observed in 1E 1048.1−5937, though not observed in PSR J1846−0258. However, as in the model of variably rotating superfluid, it is not immediately clear how the more rapid rotation and smaller magnetic field of PSR J1846−0258 compared with magnetars affect the relevance of this model. In particular, the smaller light cylinder radii of PSR J1846−0258 compared to the AXPs should result in different shock propagation times.

Alternatively, it has been proposed that fallback disks from the supernova explosion creating the neutron star could be interacting with magnetars and be responsible for some of the observed emission (e.g. Chatterjee et al., 2000; Alpar, 2001). In this case, the initial X-ray bursts could irradiate a fossil disk commencing a period of disk activity. The interaction between the neutron star and a disk could cause the enhanced spin-down, which would decay as the disk cooled. However, in the framework of this model, it is difficult to understand how accretion causing variations in the spin-down rate could continue for so much longer (∼1 year) than the pulsed-flux enhancement (∼2 months). A correlation between pulsed flux and torque would be expected in a disk model, as hinted at in Figure 6.5, though cannot be confirmed given that the correlation between the two parameters is based primarily on a single data point.

6.5.3 Magnetar and high-B rotation-powered pulsar properties

Another RPP, PSR J1119−6127, has very similar spin properties to those of PSR J1846−0258. Its P, $\dot{E}$, and τ_c are all similar, and notably, it has a similarly large magnetic field of $B = 4.1 \times 10^{13}$ G (Camilo et al., 2000). This pulsar has shown only hints of unusual X-ray emission. No magnetospheric X-ray pulsations have been detected, but thermal pulsations with a $\sim 75\%$ pulsed fraction and a large surface temperature are detected (Gonzalez et al., 2005). No direct evidence of magnetic activity (i.e. bursts or flux enhancements) is present in this pulsar. Given the similarities between PSR J1119−6127 and PSR J1846−0258, both sources, as well as other high B-field RPPs are currently being monitored with *RXTE* for similar magnetic activity.

PSR J1846−0258 may be related to the transient AXPs (TAXPs). PSR J1846−0258 appears to be a typical RPP $\geq 95\%$ of the time, with brief periods of magnetic activity occurring approximately once a decade. The transient AXP XTE J1810−197 increased in brightness by a factor of ∼100 and was subsequently visible for several years as a pulsed X-ray source (Ibrahim et al., 2004; Halpern & Gotthelf, 2005). Another transient AXP, 1E 1547−5408 was detected as a pulsed radio source after

an X-ray outburst in which the flux increased by at least a factor of 16 (Camilo et al., 2007b). Interestingly, both XTE J1810−197 and 1E 1547−5408, two *bona fide* transient AXPs, are the only two magnetars with detected radio pulsations. By contrast, no radio pulsations have been detected from PSR J1846−0258 despite extensive searches both before and after the magnetic activity (Kaspi et al., 1996; Archibald et al., 2008).

6.6 Conclusions

In *RXTE* observations of PSR J1846−0258, we have observed a large glitch with an unusual quasi-exponential over-recovery of ν and substantial timing noise contemporaneous with X-ray bursts and a flux increase. These observations strengthen the tie between magnetic activity in neutron stars and unusual glitch activity, as has been previously noted (e.g. Dib et al., 2008b). A glitch with recovery fraction $Q > 1$ has never before been observed from a rotation-powered pulsar and is not compatible with the standard model of pulsar glitches. The unusually large glitch recovery reported here for PSR J1846−0258, as well as the radiative changes occurring contemporaneously with the PSR J1846−0258 glitch and several AXP glitches, together provide the best evidence that there are physical differences between typical RPP glitches and some glitches observed in magnetars.

7
Persistent Changes to the Timing Properties of PSR J1846−0258

This Chapter contains major excerpts of a paper submitted to the *Astrophysical Journal*. The manuscript describes timing observations of PSR J1846−0258 after the recovery of the large glitch described in Chapter 6, and a 2009 *Chandra X-ray Observatory* observation of the pulsar and its pulsar wind nebula, analyzed by Dr. C.-Y. Ng. The analysis and discussion of the *Chandra* observation is not included here, thus in the text of this Chapter, we make reference to the *Chandra* results by citing "Livingstone et al. (2010b)".

7.1 Introduction

As we have shown in the previous Chapters, PSR J1846−0258 exhibits properties common to those of RPPs the majority of the time, and is one of the few with a measured braking index, $n = 2.65 \pm 0.01$ (Chapter 5). But the pulsar is also remarkable for having exhibited distinctly magnetar-like behaviour in 2006 May-June, when it showed several X-ray bursts, an X-ray flux increase (Gavriil et al., 2008), a sizable rotational glitch with remarkable "overshoot" recovery (Chapter 6), as well as spectral changes (Kumar & Safi-Harb, 2008; Gavriil et al., 2008; Ng et al., 2008). This pulsar, a clear RPP/magnetar transition object, presents a unique opportunity to explore the long-term relationship between magnetic activity and neutron star spin-down.

Bursts of X-rays and variable X-ray flux, as observed in most magnetars and PSR J1846−0258, are proposed to originate from small- or large-scale reorganizations of the magnetic field (e.g. Thompson et al., 2002). As the magnetic field is intimately

connected with the temporal evolution of pulsars, comparing timing behaviour before and after an episode of magnetic activity in a neutron star could provide important insight into the physics of neutron star magnetospheres. More specifically, magnetars typically experience a significant level of "timing noise" (in some cases preventing phase-coherent timing, e.g. Gavriil & Kaspi, 2004), and in several cases, large glitches (Dib et al., 2008a, and references therein). Together, these factors have prevented the measurement of n for every known magnetar, despite their young ages ($\tau_c \sim 1 - 100$ kyr)[1].

By contrast, prior to outburst, PSR J1846−0258 rotated relatively steadily. Between its discovery in 1999 (Gotthelf et al., 2000) and the outburst in 2006, it experienced a level of timing noise typical of young RPPs. Prior to the outburst and large glitch in 2006 (Chapter 6 and Kuiper & Hermsen, 2009), one small glitch ($\Delta\nu/\nu \sim 2.5 \times 10^{-9}$ near MJD 52210) and one small candidate glitch ($\Delta\nu/\nu < 5 \times 10^{-8}$ near MJD 52910) had been observed. The pre-outburst n measurement for PSR J1846−0258, made with regular monitoring observations with the *Rossi X-ray Timing Explorer* (*RXTE*), was enabled by its then relatively steady rotation (Chapter 5).

Also available from regular *RXTE* monitoring is the pulsed flux of PSR J1846−0258. As reported by Gavriil et al. (2008), the pulsed flux had returned to its quiescent value roughly two months after the 2006 May outburst and no further flux variations have been observed (see Chapter 6). However, because *RXTE* is a non-focusing X-ray telescope, no information about the total flux or the phase-averaged spectrum are available from these data. To measure these quantities and to confirm the *RXTE* results, a focusing X-ray instrument such as the *Chandra X-ray Observatory* is required.

Indeed *Chandra* observations of the pulsar and PWN revealed flux and spectral changes at the time of the 2006 outburst (Gavriil et al., 2008; Kumar & Safi-Harb, 2008; Ng et al., 2008). The pulsar's total flux rose considerably, but equally as in-

[1]See http://www.physics.mcgill.ca/∼pulsar/magnetar/main.html for a catalog of known magnetars.

teresting was its change in spectrum. The quiescent spectrum of PSR J1846−0258 is much like that of other young, high spin-down luminosity RPPs: a simple power law. *Chandra* observations showed that while in outburst, the spectrum softened significantly such that it became reminiscent of those observed from Anomalous X-ray Pulsars (AXPs), namely, well described by a power law with an additional thermal component. In addition, the superior angular resolution of *Chandra* allowed detailed observations of the PWN, which appeared to have changed between 2000 and immediately post-outburst. The effect of magnetar-like outbursts on PWNe is an open question, as none of the *bona fide* magnetars power nebulae. Kumar & Safi-Harb (2008) suggested a causal relation between the possible PWN changes suggested by the 2006 observations and this or past magnetar-like outbursts of the pulsar and Kargaltsev & Pavlov (2008) suggested that the PWN was over-luminous compared to those of other young pulsars, perhaps owing to previous, unseen magnetar outbursts. However, a revised distance estimate of $\sim$6 kpc (Leahy & Tian, 2008), rather than the previously claimed 19 kpc (Becker & Helfand, 1984), reduces the implied nebular X-ray efficiency to $\eta = L_{PWN}/\dot{E} \simeq 0.02$. While this is still large, it is similar to that observed from the Crab, hence need not be powered by previous outbursts. Thus, the long-term effect, if any, of the 2006 outburst on the PWN could help clarify this point.

In this Chapter, we report on 2.2-yr of *RXTE* timing observations of PSR J1846−0258 in the post-magnetic activity, post-glitch recovery period. We perform phase-coherent and partially phase-coherent timing analyses after the 2006 glitch had largely recovered, and we report a post-burst measurement of $n = 2.16 \pm 0.13$, smaller than the pre-outburst value at the 3.8σ level. We also quantify the increase of the timing noise observed over the bursting episode and discuss the implications of these observations.

7.2 Observations

In this Chapter we report primarily on observations of PSR J1846−0258 taken with *RXTE* between 2008 January 27 and 2010 April 22 (MJD 54492 – 55308). The data were reduced and analyzed in the same manner as previously described in Chapters 5 and 6. Data are spaced relatively regularly (observations every 6 – 10 days, with two $\sim$ 6 week breaks each year corresponding to a Solar constraint). All observations are pointed directly at PSR J1846−0258 (see Table 2.1). The data analyzed in this Chapter comprise 100 TOAs spanning 2.2 years.

7.3 Timing Analysis

7.3.1 Phase-coherent timing analysis

In order to make a significant measurement of a deterministic value of $\ddot{\nu}$ and thus n, we restricted our phase-coherent timing analysis to MJD 54492 – 55308 (2008 January 27 – 2010 April 22), because earlier observations are highly contaminated by glitch recovery and timing noise, as discussed in Chapter 6.

We obtained a single phase-coherent timing solution (with no phase ambiguities) fitting only ν and $\dot{\nu}$ for the 100 TOAs during this time period, shown in the top panel of Figure 7.1. The residuals show a very significant phase contribution from a second frequency derivative (i.e. $\sim$15 phase turns over $\sim$2 years). We therefore added $\ddot{\nu}$ to our phase-coherent fit, and the resulting residuals are shown in the middle panel of the figure. The fitted $\ddot{\nu}$ corresponds to a braking index of $n = 1.888 \pm 0.002$. As visible in the middle panel of Figure 7.1, significant timing noise remains in the data; the timing residuals are not Gaussian distributed. As a result, the formal 1σ uncertainty on n from this global phase-coherent fit underestimates the true uncertainty. Spin parameters from this fit are given in Table 7.1.

We fitted higher order frequency derivatives to "whiten" the phase residuals, a common procedure to lessen the contaminating effect of timing noise on fitted parameters (e.g. Kaspi et al., 1994). Fitting 12 frequency derivatives (the maximum possible given current machine precision) removes the majority of the timing noise,

Table 7.1: Timing parameters for PSR J1846−0258 spanning MJD 54492–55308.

Phase-coherent timing analysis	
Date range (Modified Julian Day)	54492.089 – 55287.847
Date range (Years)	2008 Jan 27 – 2010 Apr 22
Number of TOAs	100
Epoch (Year)	2009 Mar 1
Epoch (MJD)	54834.0
ν (Hz)	3.0621185489(4)
$\dot{\nu}$ (10^{-11} s^{-2})	−6.664350(2)
$\ddot{\nu}$ (10^{-21} s^{-3})	2.739(3)
Number of derivatives fitted	2
RMS residuals (ms)	63.5
Partially phase-coherent timing analysis	
$\ddot{\nu}$ (10^{-21} s^{-3})	3.13(19)
Braking index (n)	2.16(13)

Quoted uncertainties are the formal 1σ uncertainties as repored by `TEMPO` for the fully phase-coherent timing analysis. Details about the uncertainty on $\ddot{\nu}$ and n for the partially coherent timing solution are from a bootstrap analysis, as explained in the text.

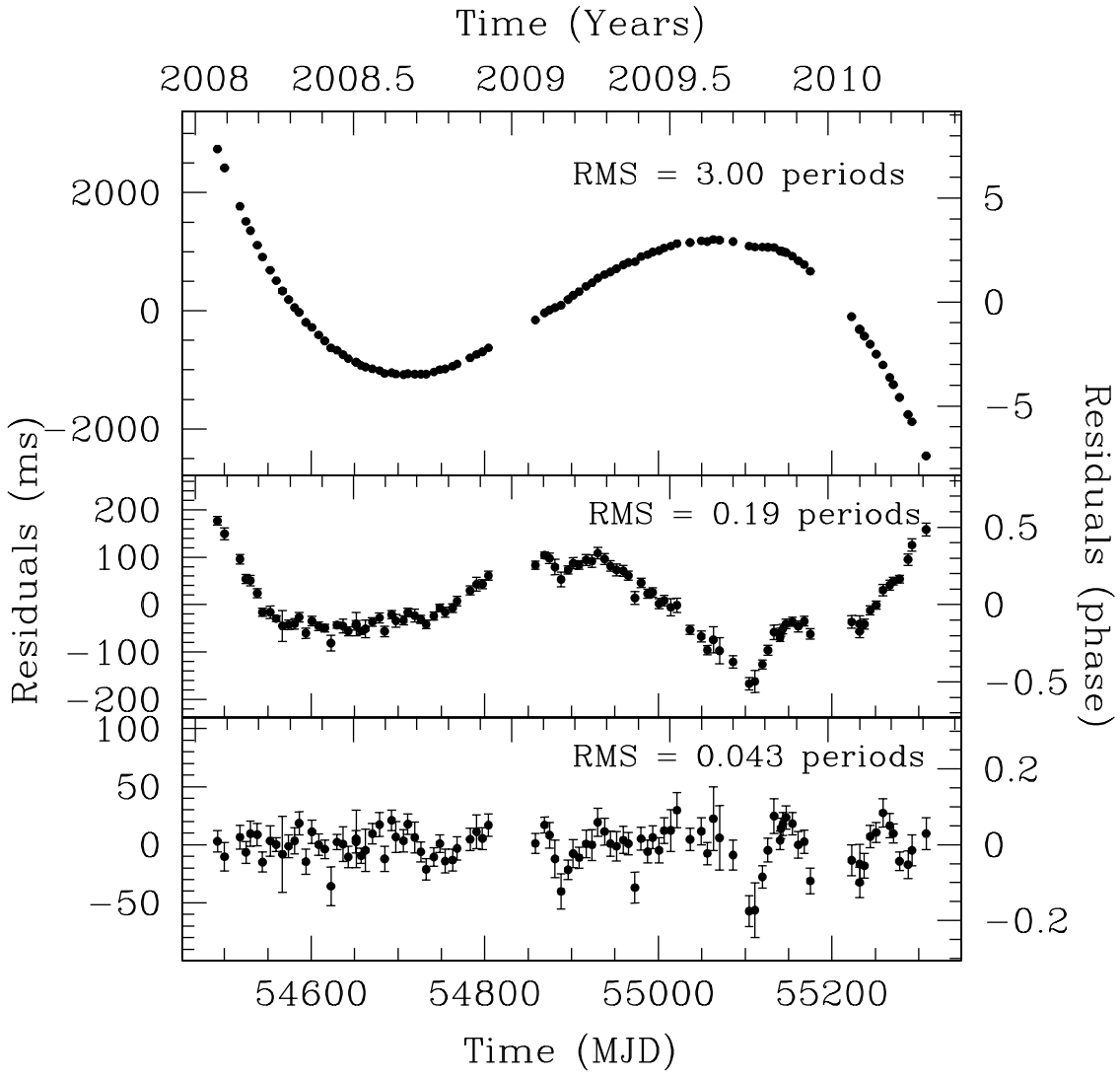

Figure 7.1: Timing residuals of PSR J1846−0258 spanning MJDs 54492 – 55308. The top panel shows residuals with ν and $\dot{\nu}$ fitted. The middle panel shows residuals with ν, $\dot{\nu}$ and $\ddot{\nu}$ fitted while the bottom panel shows residuals with 12 frequency derivatives fitted.

Table 7.2: Variation of n with number of fitted derivatives

Derivatives fitted	**Braking Index n**	χ^2_ν
2	1.888(2)	39.71
3	2.010(3)	6.12
4	1.980(8)	6.00
5	2.05(1)	5.48
6	2.08(2)	5.50
7	2.51(4)	3.51
8	2.60(4)	3.26
9	2.95(7)	2.93
10	2.91(7)	2.73
11	2.1(1)	2.12
12	2.1(1)	2.14

The number of degrees of freedom for two fitted derivatives is 96. Uncertainties are the formal 1σ uncertainties returned by `TEMPO` for the timing solution spanning MJD 54492 – 55308.

though does not render the phase residuals entirely Gaussian, as shown in the bottom panel of Figure 7.1. In addition, the resulting ${\chi^2}_\nu$ for a timing solution with 12 frequency derivatives fitted is 2.14 for 86 degrees of freedom. Table 7.2 shows the variation of n as derivatives are fitted, as well as ${\chi^2}_\nu$. The value of n varies between $n = 1.89 - 2.95$ as higher order derivatives are fitted, without converging to a single value, rendering the true value of n ambiguous from this analysis. Nevertheless, the range of measured n values from this analysis is relatively narrow: the timing noise has increased and clearly contaminates, but does not completely dominate $\ddot{\nu}$. In cases where a parameter is dominated by a noise process, it can be several orders of magnitude larger and often of the wrong sign (e.g. Hobbs et al., 2010), neither of which are seen here. In cases where timing noise contaminates a measurement of a deterministic parameter but may not dominate, using a partially coherent timing analyis can be useful to find the true value.

7.3.2 Partially coherent timing analysis

To mitigate the effects of timing noise, we performed a partially coherent timing analysis. We created 48 short phase-coherent timing solutions for the entire data span, MJDs 51574–55308. For each short timing solution, we fit only ν and $\dot{\nu}$. The time span included in each subset was determined from the requirement that the reduced χ^2 of the fit was $\sim$1, and that no red noise-like structure was visible in the data. Figure 7.2 shows the resulting $\dot{\nu}$ measurements spanning 2000 – 2010. This analysis excludes observations taken between 2006 May 31 and 2007 January 27, when glitch recovery and timing noise prevented a coherent timing solution. Red crosses include data that overlap the data included in the black points by $\sim 1/2$ to improve coverage, which is of particular importance while the timing noise level is very high. Sparse data sampling, especially near the beginning of the data span, prevents overlapping timing solutions during some epochs. From 2000 – 2006 May, $\dot{\nu}$ increased very regularly, excepting the small glitch in 2001. The steady increase in $\dot{\nu}$ corresponds to a braking index of $n = 2.65 \pm 0.01$, as measured from a phase-coherent analysis of these data (see Chapter 5). The large glitch and the increase in timing noise (Chapter 6) had largely recovered by the beginning of 2008, as shown in Figure 7.2.

To obtain a post-burst measurement of n, we ignored all timing data prior to MJD 54492, where the aforementioned glitch recovery and timing noise dominate. We performed a weighted least-squares fit to 16 $\dot{\nu}$ measurements spanning MJDs 54492 – 55308. Given the large scatter in the post-burst $\dot{\nu}$ measurements, and the known effects of timing noise on these data, it is likely that the formal uncertainties significantly underestimate the true uncertainties. Thus, to better estimate the uncertainty on $\ddot{\nu}$, we employed a bootstrap error analysis, helpful when formal uncertainties may underestimate the true uncertainties (Efron, 1979), and previously used for this same purpose in Livingstone et al. (2005a,b). This results in $\ddot{\nu} = 3.13(19) \times 10^{-21}\,\mathrm{s}^{-3}$, corresponding to $n = 2.16 \pm 0.13$, where the uncertainty from the bootstrap estimate is larger than the formal uncertainty by a factor of $\sim$2.4. This new measurement of

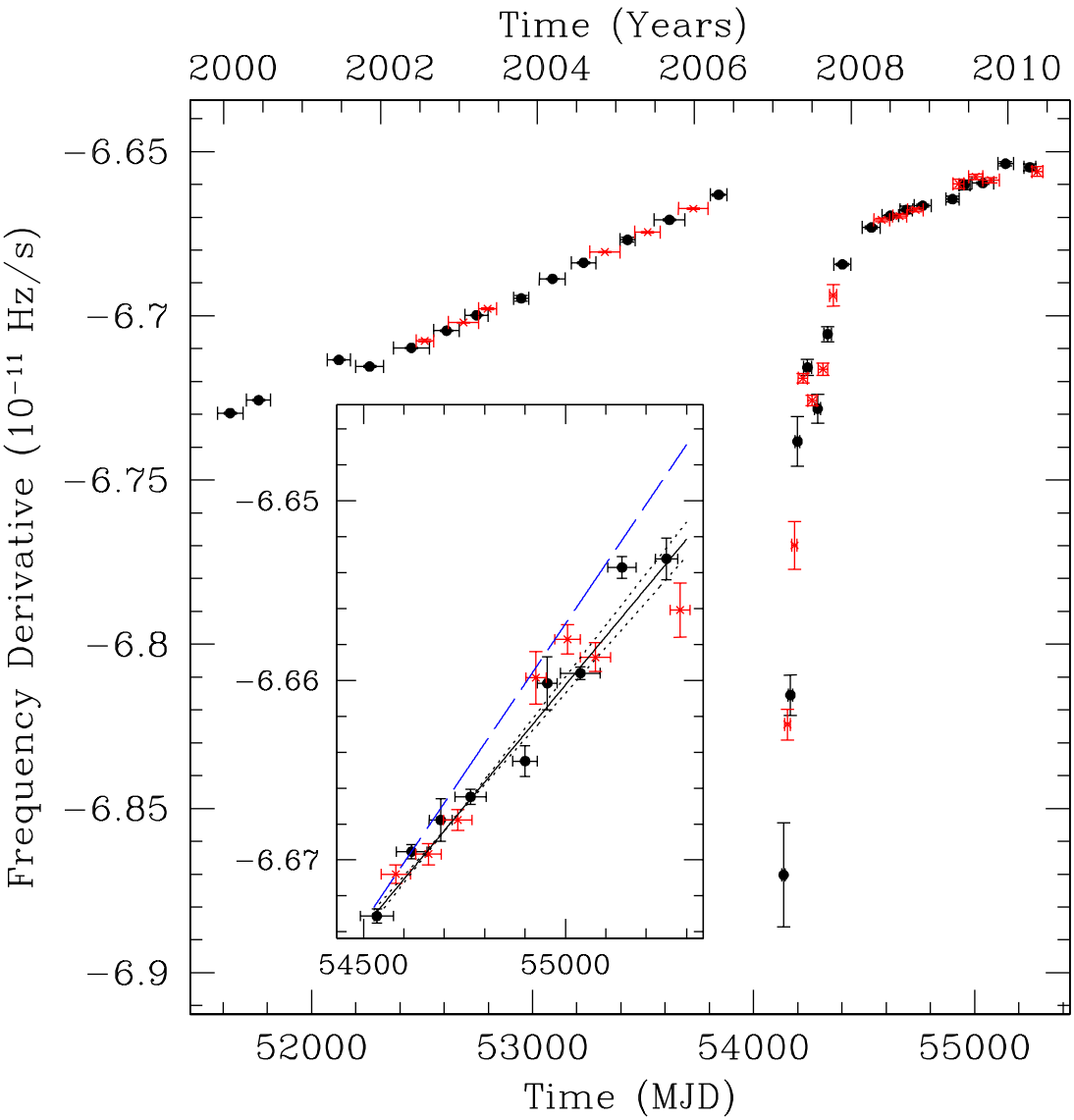

Figure 7.2: Evolution of the frequency derivative of PSR J1846−0258 over ∼10 years of *RXTE* timing observations. Red crosses represent data sets which overlap by ∼ 1/2 the measurements represented by filled circles (black in the online version). The inset shows measurements of $\dot{\nu}$ from MJDs 54492 – 55308, with the best-fit slope shown as a solid line and the $\pm 1\sigma$ uncertainties (from the bootstrap analysis which better account for the increase in timing noise) shown as dotted lines. The slope corresponding to the pre-outburst n is shown as a blue dashed line, where uncertanties are roughly an order of magnitude smaller than those post-outburst and are not visible on the figure.

n is smaller than the pre-outburst value of $n = 2.65 \pm 0.01$ at the 3.8σ level (or 9.1σ if only the formal uncertainties are considered). Thus, the braking index decreased by $\Delta n = -0.49 \pm 0.13$, following the period of magnetar-like activity in 2006. This is the first observed significant measurement of a change of a braking index.

To further confirm a change in n, we performed an identical partially coherent timing analysis on the pre-outburst measurements of $\dot{\nu}$. Because of the small glitch and candidate glitch, the data were separated into three large subsets. The first subset (prior to the small glitch near MJD 52210), contains only three measurements of $\dot{\nu}$, resulting in $n = 2.63 \pm 0.04$ (where uncertainties for this measurement are the formal uncertainties because a bootstrap error analysis can not be performed with no additional degrees of freedom). The second subset lies between the small glitch and a 78-day gap in the data (containing a candidate glitch). In this data subset, we performed a weighted least squares fit and bootstrap error analysis on 7 measurements of $\dot{\nu}$. This resulted in $n = 2.61 \pm 0.07$. We repeated this analysis for the 8 measurements of $\dot{\nu}$ prior to the magnetar-like outburst, resulting in $n = 2.68 \pm 0.03$. The three values of n are in agreement with each other and the value obtained from a fully phase-coherent timing analysis ($n = 2.65 \pm 0.01$). Each measured n pre-outburst is systematically larger than n obtained post-outburst. Note that the uncertainties on the two measurements of n from partially coherent analyses (with bootstrap uncertainties) to pre-outburst data are smaller than the uncertainty for the post-outburst value of n, despite similar data spans fitted in each case. This is indicative of an increase in the timing noise post-outburst. This is discussed further below.

A complicating factor in timing some magnetically active neutron stars is that pulse profile changes often accompany radiative changes and/or glitches (e.g. Kaspi et al., 2003). This can affect measured timing parameters and must therefore be quantified. It has previously been reported that no significant changes in the pulse profile were detected during the outburst (see Chapter 6 and Kuiper & Hermsen, 2009). We further verified that the pulse profile in the ∼2-year period immediately

prior to the outburst is not statistically different from the summed profile from the ∼2-yr of data used to measure n, shown in Figure 7.3.

We performed a second partially coherent timing analysis, this time with each data subset having ν, $\dot{\nu}$, and $\ddot{\nu}$ fitted. The same conditions of ${\chi^2}_\nu \sim 1$ and Gaussian-distributed residuals, were applied to determine the length of each subset, and once again, the period between 2006 May 31 and 2007 January 27 was excluded owing to the lack of a coherent timing solution. Six values of $\ddot{\nu}$ were obtained before the outburst, while nine values of $\ddot{\nu}$ were obtained after the outburst, shown in Figure 7.4. The measurements of $\ddot{\nu}$ before the outburst indicate the regular rotation of the pulsar during this period, while the single value of $\ddot{\nu}$ above the average (visible in the inset) occurs directly after the candidate glitch near MJD 52910, providing the best evidence for a glitch during this period. As visible in the Figure, the value of $\ddot{\nu}$ changed dramatically immediately after the outburst, to a maximum of ∼200 times the quiescent value, as well as varying in sign, indicating a dramatic increase in timing noise during the period of glitch recovery. The magnitude of $\ddot{\nu}$ decays as the glitch recovers during 2007. The inset of Figure 7.4 shows the variation of $\ddot{\nu}$ on a smaller scale. While the effects of glitch recovery and timing noise have subsided substantially by 2008, the post-outburst variation of $\ddot{\nu}$ remains larger than its pre-outburst behaviour, as is visible in the Figure.

7.3.3 Timing noise

Qualitatively, the timing noise in the 2.2-year period used to obtain the post-burst measurement of n is larger than that observed prior to the outburst, though much smaller than in the initial aftermath of the outburst, when no phase-coherent timing solution was possible. One measure of the change in timing noise can be found by comparing the RMS residuals from MJDs 54492 – 55308 with those in a similar time span from before the outburst. Fitting ν, $\dot{\nu}$, and $\ddot{\nu}$ phase-coherently to the 2.2-yr segment of data spanning MJD 53086 – 53879, just before the outburst, results in a timing solution with RMS residuals of 11.4 ms, (0.035 periods), a factor of ∼5.5 smaller than the RMS residuals from MJDs 54492 – 55308, of 63.6 ms (0.19 periods).

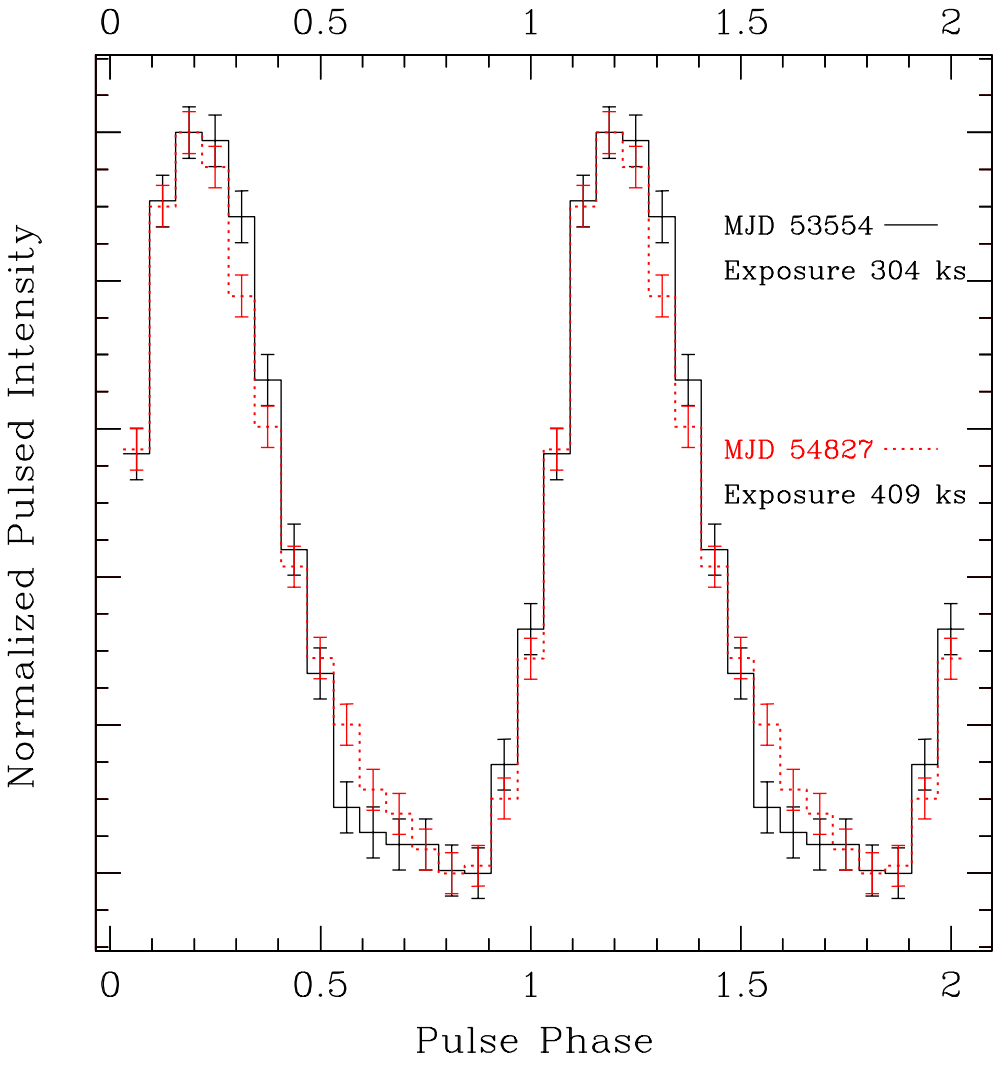

Figure 7.3: Pulse profile of PSR J1846−0258 for two sections of data of ∼2 yr. Two cycles are shown for clarity. The solid black line shows the pulse profile before the outburst in 2006 May. The dotted red line shows the summed pulse profile for 2008 January – 2010 April. Subtracting the two profiles results in residuals with $\chi^2{}_\nu \sim 1.3$, where the probability of this $\chi^2{}_\nu$ or higher occurring by chance is 19%. Thus the two profiles are statistically identical.

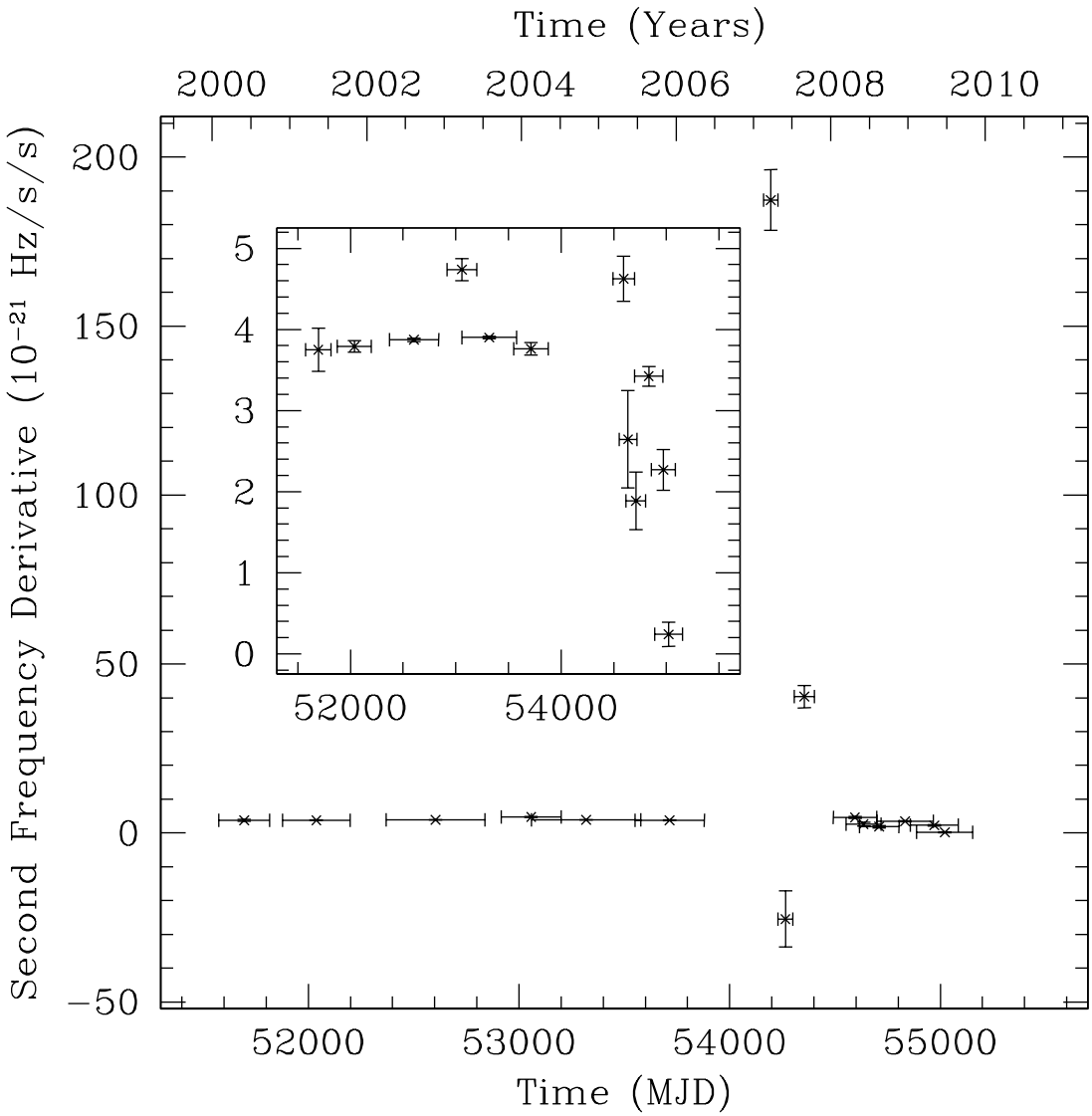

Figure 7.4: Second derivative measurements for PSR J1846−0258. Measurements of the second frequency derivative from 2000 – 2009. The three measurements occurring after the glitch and outburst are 1-2 orders of magnitude larger than the subsequent measurements and vary in sign, indicating that they are severely contaminated by glitch recovery and/or timing noise. The variation in $\ddot{\nu}$ during the period from 2008 to 2010 is larger than in the pre-outburst era, and the mean value is systematically smaller. The one value of $\ddot{\nu}$ pre-burst that is significantly larger than the average is directly after the candidate glitch near MJD 52910, and is the best evidence that a glitch actually occurred at that epoch.

This shows that the timing noise post-burst is significantly larger than before the magnetar-like outburst. This is reflected in the new measurement of n by the increased uncertainty compared to that on the pre-outburst value of n for similar measurement baselines.

Another measure of the increase in timing noise is the time span that can be included in each partially coherent measurement of $\dot{\nu}$ shown Figure 7.2. When the pulsar is less noisy, more data can be included in each short timing solution while satisfying the conditions that ${\chi^2}_\nu \sim 1$ and that no red noise-like structure remain in the data. The pulse profile and pulsed flux are steady, important because variability in either could cause changes in TOA uncertainties, and thus affect the time span for each $\dot{\nu}$ measurement. From 2000 until 2006 May, on average, each measurement of $\dot{\nu}$ was obtained with data spanning 111 ± 26 days, while in 2007 (when glitch recovery was still a significant effect), each measurement of $\dot{\nu}$ spanned an average of 33 ± 20 days. From 2008 – 2010, the average time span for each measurement was 68 ± 16 days. Thus, nearly four years post-outburst, the pulsar remains noisier than prior to the outburst.

A well known measure of timing noise is the Δ_8 parameter, defined as the contribution to the rotational phase of the pulsar from a measurement of $\ddot{\nu}$ over a period of 10^8 seconds assuming that $\ddot{\nu}$ is entirely dominated by timing noise (Arzoumanian et al., 1994). However, this parameter is of limited value for a pulsar where $\ddot{\nu}$ is dominated by secular spin-down, where most of the phase contribution from $\ddot{\nu}$ is due to magnetic braking or another deterministic spin-down mechanism. To quantify the change in timing noise observed in PSR J1846−0258, we define a similar parameter which quantifies the contribution to the rotational phase from the measurement of the third frequency derivative, $\dddot{\nu}$, over a time span of $\sim 2.5 \times 10^7$ s. The time span is optimized for this particular pulsar, as it is the approximate amount of time required to obtain a significant measurement of $\dddot{\nu}$, while allowing several measurements to be made. Thus, in analogy with the Δ_8 parameter we define:

$$\Delta_{\dddot{\nu}} \equiv \log\left(\frac{1}{24}\frac{\mid \dddot{\nu} \mid (2.5 \times 10^7)^4}{\nu}\right). \tag{7.1}$$

We measured the $\Delta_{\ddot{\nu}}$ parameter for each $\sim 2.5 \times 10^7$ s segment of data where a phase-coherent timing solution was available, and show the results in Figure 7.5. The value of $\Delta_{\ddot{\nu}}$ increases dramatically after the 2006 outburst, after which it decays, but by 2010 has not returned the pre-outburst quiescent level.

7.4 Discussion

We have observed a decrease in the braking index from $n = 2.65 \pm 0.01$ to $n = 2.16 \pm 0.13$, corresponding to $\Delta n = -0.49 \pm 0.13$, or a decrease of $18 \pm 5\%$. The change in n was accompanied by an increase in the timing noise in the pulsar, which remains larger than the pre-outburst level, nearly four years after the glitch and outburst on 2006 May 31. Previous long-term observations of n in young pulsars have shown that they are remarkably steady. In PSR B1509−58, timing observations over 21 years show that n varies by only $\sim 1.5\%$ (Livingstone et al., 2005b), while the Crab pulsar exhibits variations on the order of 5% (Lyne et al., 1993).

There are two possible ways to interpret the measurement of $\Delta n = -0.49 \pm 0.13$. The first is that the true n decreased by a significant amount after the 2006 outburst. The second possible interpretation is that the increase in timing noise is causing an apparent decrease in n. We discuss each of these interpretations next.

If the true value of the braking index changed permanently at the time of the magnetar-like outburst, what could be the physical cause of such an effect? From the spin-down law derived assuming magnetic dipole braking, (e.g. Ostriker & Gunn, 1969),

$$\dot{\nu} = \frac{-8\pi^2}{3} \frac{B^2 R^6 \sin^2\alpha}{I c^3} \nu^3, \tag{7.2}$$

we can infer that $d^2I/dt^2 > 0$, $d\alpha/dt > 0$ or $dB/dt > 0$ will cause a measured value of $n < 3$[1].

[1]Note the different dependence for I which arises from the time derivative of the rotational kinetic energy: $dE/dt = I\Omega d\Omega/dt + dI/dt\Omega^2/2$. Because I is typically assumed to be constant, the second term is neglected in the simple form of the spin-down model, but must be included to find the dependence of n with a changing I.

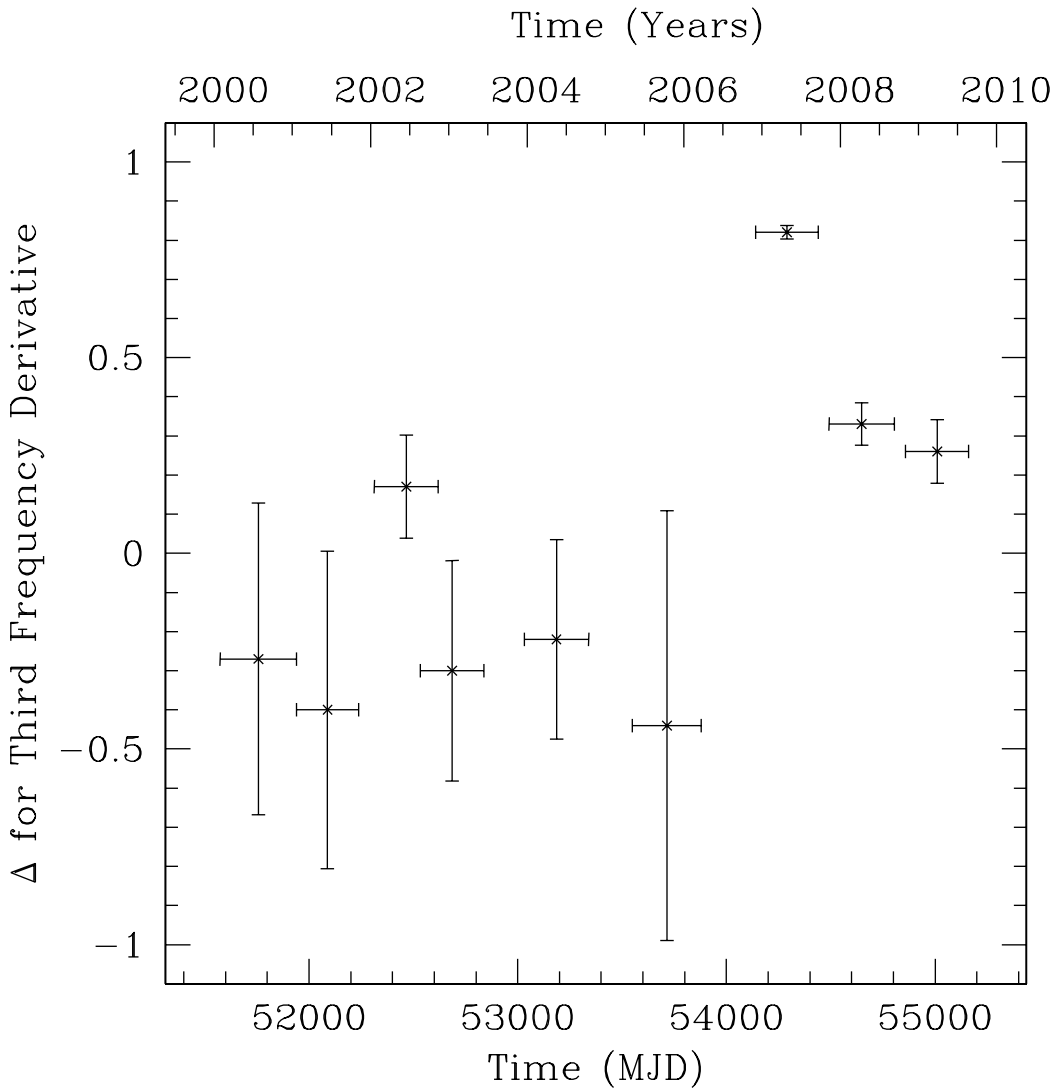

Figure 7.5: A quantification of the timing noise in PSR J1846−0258 over 10 yr. Each point is a measurement of the $\Delta_{\dddot{\nu}}$ parameter for approximately 2.5×10^7 s. This provides an estimate of the amount of timing noise observed in the pulsar, and shows a dramatic increase after the large glitch observed in 2006.

While it is hard to imagine a physical situation causing an accelerated growth or decay in I, varying values of α or B have been considered in the literature. Counter-alignment of the magnetic field (i.e. an increasing α) results in $n < 3$, even if $\Delta n = 0$. A sudden increase in the rate of change of α would produce $\Delta n < 0$. However, this is difficult to invoke for the observations of PSR J1846−0258 because the pulse profile shows no variation over the relevant time period (e.g. Figure 7.3). A small change in α could still be possible if our line of sight is crossing the centre of the pulsar beam, as a large change in the pulse profile may not be required from a small change in field orientation. However, this is hard to reconcile with the lack of detected radio pulsations from the source (Archibald et al., 2008), which is typically interpreted as our line-of-sight missing the magnetic pole, from where the radio emission is thought to originate, and crossing only the wider X-ray beam.

An increase in the magnitude of B, without a change in the orientation of the field could also cause a decrease in n (Blandford & Romani, 1988; Blandford et al., 1983). Making all the assumptions of perfect dipole spin-down but allowing $dB/dt > 0$, a braking index of $n = 2.65$ implies a time scale of growth for the magnetic field of $\sim$8000 yr, while $n = 2.16$ shortens the growth timescale to $\sim$3500 yr. The possibility of magnetic field growth is intriguing given the magnetic activity observed prior to the change in n. Bhattacharya & Soni (2007) suggest that magnetar-strength fields emerge over a period of time, as shielding currents dissipate. If the effective B is currently in such a period of growth, the smaller value of n could result (Lyne, 2004).

The standard spin-down law (Eq. 7.2, and see also §1.3) is a major idealization even for a rotation-powered pulsar; for magnetars, the picture is almost certainly much more complicated. According to one version of the magnetar model, there is a one-to-one relationship between n and the large-scale twist angle between the north and south hemispheres of magnetic field, $\Delta\phi_{\mathrm{N-S}}$ (Thompson et al., 2002). Here, a decrease in n would imply an increase in the twist angle. A braking index of $n = 2.65$ corresponds to a twist angle of $\Delta\phi \simeq 1$ rad, while $n = 2.16$ implies a twist angle of $\Delta\phi \simeq 2$ rad. If the magnetic field remains approximately constant before and after the

outburst, such an increase in the twist angle should be accompanied by an increase in the X-ray luminosity of $\sim 50\%$, whereas no persistent increase in in L_X is observed in PSR J1846−0258 as evidenced by the consistent flux value measured with *Chandra* in 2000 and 2009 (Livingstone et al., 2010b). Further, while the above model assumes a global magnetic field twist, Beloborodov (2009) argues that such global self-similar twists do not present a viable explanation for magnetar behavior. He suggests instead that magnetospheric currents are confined to narrow regions on the most extended field lines, which are not responsible for the bulk of magnetar X-ray emission. If this picture is correct, the spin-down of the star can vary without accompanying changes in X-ray luminosity. In addition this model predicts that an increase in spin-down torque (though not necessarily monotonic) should occur sometime after a radiative event, and should eventually return to the pre-outburst torque value. Qualitatively, this seems to present an explanation of the observed timing variability in PSR J1846−0258, however, it provides no quantitative prediction for n.

A variable n provides an unambiguous test of the theory of spin down presented by Melatos (1997). He posits that the radius relevant to neutron star spin down is not the point-like neutron star radius, but a somewhat larger 'vacuum radius" where field aligned flow breaks down. This radius is large enough that the system can no longer be treated as a point dipole, resulting in modifications to the standard spin-down predictions. In the context of this model, a measurement of ν, $\dot{\nu}$, and α uniquely predicts n. While there is no estimate of α for PSR J1846−0258, given that there are now two measurements of n the theory can be tested. Given the observed change in n, and assuming that α is stable over the magnetar-like outburst, this theory predicts that the magnetic field should have increased by a factor of $\sim$6. This is not observed, however, as the magnetic field estimate has increased by just 0.3% compared with the pre-outburst value, in contradiction to this theory. Alternatively, if α were allowed to change at the time of the event, Melatos (1997) predicts that the angle between the spin and magnetic axes changed from $\sim 9^\circ$ to $\sim 4^\circ$. Unfortunately, this possibility cannot currently be tested as there is no instrument available that can determine this

angle.

Another possible explanation put forth for a static measurement of $n < 3$ is that magnetic field lines are deformed due to plasma in the magnetosphere (Blandford & Romani, 1988). A sudden increase in the amount of plasma in the magnetosphere of PSR J1846−0258, perhaps injected at the time of the magnetar-like outburst, could cause n to decrease. Along with the six measurements of $n < 3$ (Lyne et al., 1993, 1996; Camilo et al., 2000; Livingstone et al., 2005a,b, and Chapter 5), the best evidence for a plasma-filled magnetosphere affecting pulsar spin-down is found from the "intermittent" radio pulsar, PSR B1931+24, which has dramatic, quasi-periodic changes in $\dot{\nu}$ correlated with radio pulsations which turn on and off (Kramer et al., 2006). Harding et al. (1999) propose that spin down can arise from a combination of magnetic dipole radiation and wind losses. An increase in losses from the wind relative to dipole radiation will manifest as a smaller value of n. The spin-down formula given by Harding et al. (1999) implies a braking index of

$$n = 3 - \frac{2\nu}{\dot{\nu}} \frac{{L_p}^{1/2} B R^3}{2I\sqrt{6c^3}}, \tag{7.3}$$

where L_p is the kinematic luminosity of the wing, which can be estimated with a measurement of n:

$$L_p = \left(\frac{3-n}{2}\right)^2 \left(\frac{\dot{\nu}}{\nu} \frac{2I\sqrt{6c^3}}{Br^3}\right)^2. \tag{7.4}$$

For PSR J1846−0258, a change in n from 2.65 to 2.16 corresponds to an increase in the persistent particle luminosity from $L_p \sim 1 \times 10^{36}\,\mathrm{erg\,s^{-1}}$ to $L_p \simeq 6 \times 10^{36}\,\mathrm{erg\,s^{-1}}$. Because the outflowing particles travel near the speed of light, the additional particles would populate the PWN and be observable as a factor of ∼6 increase in the PWN flux in the 2009 *Chandra* observation as compared to the observation in 2000. However, no such flux increase is detected (Livingstone et al., in preparation). The lack of a PWN flux increase seems to refute the idea that an increase in wind losses is responsible for $\Delta n < 0$, however, a more rigorous derivation of the relationship between wind losses and spin down may provide further insight into this issue.

Interestingly, a change in the plasma conditions in the magnetosphere might also affect magnetospheric torques affecting the pulsar rotation, thus could possibly ex-

plain an increase in timing noise observed in PSR J1846−0258 (e.g. Cheng, 1987). As shown in Lyne et al. (2010), timing noise in some pulsars can be traced to magnetospheric fluctuations. For these radio-loud rotation-powered pulsars, there is a correlation between torque variations and pulse shape changes. While no radio pulsations have been detected from PSR J1846−0258 (Archibald et al., 2008), there is no evidence for profile variability in the X-ray band (see Fig. 7.3).

Contopoulos & Spitkovsky (2006) note that if the co-rotation radius of the magnetosphere, $r_{\text{co-rot}}$, is less than the light cylinder radius owing to imperfect reconnection within the magnetosphere, $1 \leq n \leq 3$ will result. If the co-rotation radius decreased at the time of the magnetar-like outburst from magnetic field lines opening, n would also decrease. They parametrize the relationship between $r_{\text{co-rot}}$ and n as

$$r_{\text{co-rot}} = R_{LC} \left(\frac{\nu}{\nu_0} \right)^{\frac{3-n}{2}} . \tag{7.5}$$

If the initial spin-period of PSR J1846−0258 was $P_0 = 10\,\text{ms}$, the implied co-rotation radius prior to outburst was $r_{\text{co-rot}} = 0.54 R_{LC}$ when $n = 2.65 \pm 0.01$, and would have decreased to $0.23 R_{LC}$ post-outburst when $n = 2.16 \pm 0.13$. Changes to the extent of the co-rotation region of the magnetosphere might be visible as changes in the pulse profile, however, no such changes have been observed from PSR J1846−0258. In the context of this model, however, it is impossible to rule out changes to the extent of the magnetosphere as no independent estimate of the initial spin period is available. Taking $P_0 = 10\,\text{ms}$, as an upper limit to the true P_0 gives an upper limit on the decrease in the co-rotation radius in the context of this model, since a slower birth period implies a smaller change in $r_{\text{co-rot}}$ for two values of n.

The second possible interpretation of the observation of $\Delta n < 0$ is that the true n is constant but the increased timing noise is of such a level that the true value of n is currently masked. The increase in timing noise could arise as a result of changes to the superfluid interior brought on by the unusual 2006 glitch, or changes in the magnetosphere after the outburst. Though a bootstrap error analysis was employed in order to better account for the effect of the increase in timing noise, a definitive test is not possible. Continued timing observations may be able to solve this issue, if the

timing noise level continues to decrease and the new braking index remains steady. However, it is also possible that the increased level of timing noise and the decreased braking index are connected, for example, via an increase in the magnetospheric plasma density. In that case, if the pre-outburst conditions are eventually reobtained, both the timing noise and braking index should relax to their pre-outburst values, rendering a temporary value of $n < 2.65$ ambiguous in nature.

Fluctuations in pinned superfluid in the pulsar interior is one of the possible causes of timing noise (e.g. Alpar et al., 1986). Thus, one possible explanation for the increase in timing noise is that significant changes were imparted to the neutron star interior at the time of the 2006 glitch and outburst. The glitch was followed by an unusual overshoot recovery ($Q \simeq 8.7$ on a timescale of $\tau_d \sim$127 days) and a permanent increase in the magnitude of $\dot{\nu}$ (with fractional magnitude $\Delta\dot{\nu}/\dot{\nu} \simeq 0.0041$; Chapter 6). This recovery is thus far unique and the origin and long-term consequences of such behavior is not well understood. By contrast, the permanent change in $\dot{\nu}$ following the glitch is not unusual when compared to those measured after other glitches. In addition, we note that the change in $\dot{\nu}$ is not responsible for the observed decrease in n. Because the fractional increase in $\dot{\nu}$ is three orders of magnitude smaller than the fractional change in $\ddot{\nu}$, it is the later effect that dominates the change in n.

In addition to the detected glitch recovery and permanent increase in $\dot{\nu}$, non-monotonic variations in $\dot{\nu}$ were observed in the aftermath of the glitch. While glitch recovery and discrete jumps in $\dot{\nu}$ are both well established phenomena, to our knowledge, no other rotation-powered pulsar has experienced similar changes in timing noise. However, variable spin-down torque (separate from glitch recovery) has been observed in several magnetars. For example, the AXP 1E 1048.1−5937 twice experienced approximately year-long periods of rapid $\dot{\nu}$ variations, i.e. sudden, but temporary increases in timing noise (Gavriil & Kaspi, 2004; Dib et al., 2009). Thus the observed change in timing noise in PSR J1846−0258 can be interpreted as yet another example of magnetar-like properties from this rotation-powered pulsar, even if the phenomenon is currently unexplained.

7.5 Conclusions

The observed change in n after the magnetar-like outburst in PSR J1846−0258, if shown to be steady via ongoing timing observations, has important implications for the physics of neutron star spin-down. A decrease in n could have several origins, and a detailed theoretical framework is necessary for interpreting this observation.

Most theoretical descriptions of a changing braking index require an accompanying persistent change in radiative behaviour of the pulsar. However, we observe no pulse profile variability or persistent flux enhancement. An increase in particle wind losses relative to dipole losses does not provide a good description $\Delta n < 0$ for PSR J1846−0258 because of the lack of a persistent increase in PWN luminosity (Harding et al., 1999). However, variability in magnetospheric plasma remains a promising avenue for future consideration, especially considering the recent report of variable spin-down correlated with radio pulse shape for several pulsars (Lyne et al., 2010). While no variability in X-ray pulse shape is detected in PSR J1846−0258, short time scale variability could be averaged in our X-ray observations which are typically 1.5 – 2 hr-long.

The timing noise in PSR J1846−0258 is observed to be of a higher level than prior to the outburst. That is, even four years after the glitch and magnetic activity, the pulsar is rotating less regularly than in its pre-outburst quiescent state. It is interesting to note, however, that the current timing noise in PSR J1846−0258 would not be unusual if observed in any young pulsar. Rather, it is the sudden change in the level of timing noise in PSR J1846−0258 that is noteworthy. Since the timing noise is simply of a higher level and not otherwise different from that observed in other pulsars, the phenomenon cannot be used as a diagnostic of previous, unseen magnetic activity in other pulsars.

The observed decrease in n and increase in timing noise reported here may or may not be permanent. Regular monitoring observations beyond the *RXTE* era may help to answer this question, as well as to search for future magnetar-like X-ray outbursts and glitches from PSR J1846−0258.

8 Conclusions

8.1 Introduction

This Chapter provides a summary of the results presented for PSR J0205+6449 (Chapter 4) and PSR J1846−0258 (Chapters 5, 6, and 7). The results are discussed in a wider context and suggestions for future research are considered.

8.2 PSR J0205+6449: Summary and Conclusions

PSR J0205+6449 has long been associated with the historical supernova of 1181 (Clark & Stephenson, 1977), though evidence is mounting – including our observation of two large glitches (summarized in Table 8.1) – that this association is spurious and the pulsar is closer to 5 – 10 kyr old. Along with significant timing noise, these glitches prevented a measurement of the braking index for this pulsar. We showed that the pulsar is detectable up to 40 keV, one of very few pulsars detected as a hard X-ray pulsar. An interesting property of this pulsar is that is has a very strict upper limit on its surface temperature, $kT < 88$ eV, which provides a strong constraint on neutron star cooling models (Slane et al., 2004) and may ultimately be connected to the glitch properties of the pulsar (see also §8.5.2).

The phase delay between the radio and X-ray pulse for PSR J0205+6449, $\phi = 0.10 \pm 0.01$ is consistent with the delay between the radio and γ-ray pulse as measured with *Fermi* (Abdo et al., 2009b). The phase relationship between radio and high-energy pulses as a function of energy is an important clue to help differentiate between different models of pulsar emission (e.g. Romani & Yadigaroglu, 1995; Baring, 2004). Although the number of γ-ray pulsars is growing rapidly owing to recent advances made with *Fermi* (Abdo et al., 2010b), there remains a paucity of pulsars that have

Table 8.1: Summary of glitch parameters for PSR J0205+6449

Glitch Epoch (MJD)	$\Delta\nu/\nu$ (10^{-6})	$\Delta\dot{\nu}/\dot{\nu}_{\rm perm}$ (10^{-3})	Q	τ_d (days)
52538−52571	0.34(0.11)	5(1)	–	–
52777−53062	5.4(1.8)	−4.6(1)	0.7(0.1)	285(5)

been detected as both magnetospheric X-ray and γ-ray sources. To date, only 8 pulsars have both radio-to-X-ray and radio-to-γ-ray phase offsets measured: the Crab pulsar, the Vela pulsar, B1706−44, B1509−58, J2229+6114, the millisecond pulsars B1821−24 and J0218+4232, and PSR J0205+6449 (Table 4.2 and references therein). In all cases but two, J0218+4232 and J2229+6114, the X-ray and γ-ray phase offsets are in agreement within 3σ, though there is also some disagreement about the radio-to-γ-ray phase offset for the young pulsar PSR B1509−58 (Kuiper et al., 1999; Pellizzoni & et al., 2009) and the millisecond pulsar B1821−24 (Rots et al., 1998; Rutledge et al., 2004).

Ongoing radio monitoring of PSR J0205+6449 with the Jodrell Bank Observatory consists of closely spaced observations (every 2 – 3 days), which are necessary to maintain a phase-coherent timing solution in the presence of significant timing noise, and to provide more stringent constraints on future glitches from the source. A phase-coherent timing solution spanning future PSR J0205+6449 glitches will place better constraints on glitch parameters, including possible instances of $\Delta\nu/\nu < 0$. Future multi-wavelength observations could also verify that the phase relationship between the radio and high-energy pulses does not vary with time and that changes in the dispersion measure are not affecting the implied phase offsets.

The timing noise in PSR J0205+6449 is such that it prevents a measurement of n despite its young age and rapid spin-down rate. Timing noise has long been thought to arise from a stochastic torque component in the pulsar interior (e.g. Alpar et al., 1986). Recently, Lyne et al. (2010) showed that for several pulsars, timing noise is instead related to magnetospheric variations. In these sources, variations in the

spin-down rate (i.e. torque) are correlated to pulse shape changes. Fluctuations in plasma density can account for both pulse shape and torque variability, although the underlying cause of the magnetospheric fluctuations is not well understood, nor is the quasi-periodic nature of the variability. Given the possibly quasi-periodic form of the timing residuals of PSR J0205+6449 (e.g. Fig. 4.5), sensitive observations of the pulse profile could possibly show a similar effect. However, because this pulsar is such a weak pulsed radio and X-ray source, this is a difficult proposition. In addition, glitches have thus far limited the available span of data for showing a significant correlation between changes in pulse profile and spin-down rate.

8.3 PSR J1846−0258: Summary and Conclusions

Prior to the work presented here, PSR J1846−0258 was a recently discovered pulsar with several interesting properties, but about which not very much was known. The characteristic age estimate was the smallest (728 yr), and the spin-down inferred dipole magnetic field was among the largest of all rotation-powered pulsars (5×10^{13} G; Gotthelf et al., 2000). The pulsar had not been detected as a radio pulsar (Kaspi et al., 1996) and while unusual, other young radio-quiet pulsars were known (e.g. PSR J1811−1925; Kaspi et al., 2001b).

Our long-term monitoring of PSR J1846−0258 with the *Rossi X-ray Timing Explorer* enabled the first measurement of the braking index for this pulsar of $n = 2.65 \pm 0.01$ (Chapter 5). Of more than 1800 known pulsars[1], PSR J1846−0258 is only the sixth with a measurement of n. This new measurement lies within the range of previously measured values of $1.4 \leq n \leq 2.91$ (Lyne et al., 1993; Livingstone et al., 2005a,b; Camilo et al., 2000; Lyne et al., 1996).

We observed a small glitch with no detectable relaxation (see Table 8.2 for a summary of glitch parameters for PSR J1846−0258). This glitch was very similar to those observed from other very young pulsars, e.g. the lone glitch observed from the $\sim$ 1700 yr-old pulsar B0540−69, which has detected radio pulsations and a normal

[1]ATNF pulsar database www.atnf.csiro.au/research/pulsar/psrcat/

Table 8.2: Summary of Glitch parameters for PSR J1846−0258

Glitch Epoch (MJD)	$\Delta\nu/\nu$ (10^{-6})	$\Delta\dot{\nu}/\dot{\nu}_{\rm perm}$ (10^{-3})	Q	τ_d (days)	Radiative behaviour
52210	0.0025(2)	0.93(1)	–	–	No
52910-cand	< 0.05	–	–	–	?
53879	4.0(1.3)	4.1(2)	8.7(2.5)	127(5)	Yes

Summary of glitches observed from PSR J1846−0258.

magnetic field strength of $B = 5 \times 10^{12}$ G (Livingstone et al., 2005a). There is some evidence that a second small glitch occurred in PSR J1846−0258 during a gap in the data due to a solar constraint.

PSR J1846−0258 is one of the high magnetic field rotation-powered pulsars: pulsars with inferred dipole fields similar in strength to those of the magnetars, but without the hallmarks of magnetic field decay (see also §1.7). In all the high-B RPPs, the X-ray luminosity is a small fraction of the spin-down luminosity, in contrast to what is observed from magnetars. From its discovery, PSR J1846−0258 was set apart from the other high-B RPPs. PSR J1846−0258 has both the largest $\dot{E}$ and smallest τ_c of the high-B RPPs. Its magnetospheric X-ray luminosity is 1 – 3 orders of magnitude larger than those of any other members of the class (though still a small fraction of $\dot{E}$), and it has the hardest X-ray spectrum (Olausen et al., 2010, and references therein). In addition, PSR J1846−0258 is the only known radio-quiet high-B RPP. By contrast, the majority of magnetars are radio-quiet. The differences between PSR J1846−0258 and PSR J1119−6127 are particularly worth noting. These two sources have very similar spin parameters (P, $\dot{E}$, B, and τ_c, see Table 1.2) and both have measured n. In contrast to PSR J1846−0258, PSR J1119−6127 is radio-loud and has an X-ray luminosity two orders of magnitude smaller than PSR J1846−0258. The similarity in $\dot{E}$ and disparity in L_X mean that PSR J1119−6127 is an order of magnitude less efficient at converting its spin-down luminosity into X-rays than is PSR J1846−0258. While PSR J1846−0258 is dominated by magnetospheric X-ray emission and no detectable thermal component (e.g. Helfand et al., 2003), PSR J1119−6127 is primarily

visible as an X-ray source from its thermally cooling surface below ∼2 keV (Gonzalez et al., 2005; Safi-Harb & Kumar, 2008).

In May 2006, PSR J1846−0258 transformed suddenly into an apparently new type of object that bridges the gap between rotation-powered pulsars and magnetars. A series of X-ray bursts and an increase in the pulsed flux were observed with *RXTE*, while the spectrum softened such that it was reminiscent of those observed from AXPs (Gavriil et al., 2008; Kumar & Safi-Harb, 2008; Kuiper & Hermsen, 2009). To date, it is the only rotation-powered pulsar that has exhibited a magnetar-like radiative outburst. We report that a glitch three orders of magnitude larger than the previous glitch occurred contemporaneously with the outburst. The glitch was followed by a large over-recovery of the initial spin-up event, such that there was a net decrease of the spin frequency almost an order of magnitude greater than the spin-up event (see Table 8.2). Such a glitch over-recovery is unprecedented among rotation-powered pulsars, and is discussed further in §8.5.

Four years after the magnetar-like outburst in PSR J1846−0258, and after the glitch had recovered, the timing noise in PSR J1846−0258 has not returned to the pre-burst level. The timing noise in the pulsar increased dramatically at the time of the glitch and outburst and decayed significantly over the next two years. However, between 2008 and 2010, the timing noise remained larger than prior to the outburst and did not experience any further decay. Such behaviour is unprecedented among rotation-powered pulsars and points toward a further connection between PSR J1846−0258 and the magnetars.

Though the timing noise level remained higher than pre-outburst, it had decayed enough that the braking index was once again measurable between 2008 and 2010. We measured a braking index of 2.16 ± 0.13, $18 \pm 5\%$ smaller than the pre-outburst value of 2.65 ± 0.01. This is the first measurement of n for any pulsar after an episode of magnetic activity, as well as the first measurment of a significant change of a pulsar braking index.

PSR J1846−0258 continues to be monitored weekly with *RXTE*. Each observa-

tion is tested against previous timing observations to search for glitches, pulsed flux variations, and X-ray bursts. This monitoring program will continue for as long as *RXTE* is active. After the demise of *RXTE*, monitoring of the pulsar could continue with the X-ray telescope *Swift*. The future timing behaviour of this fascinating young pulsar may hold further clues to the connections between pulsars and magnetars. It remains to be seen if the pulsar will entirely return to its quiescent state or if it has permanently transformed. Ongoing timing observations will further constrain n and the timing noise properties, as well as possible evolution of either property. Observations of future glitches and/or radiative outbursts will help constrain the recurrence rate of such events.

8.4 Pulsar Spin Down: Braking Indices

8.4.1 Physical models for non-dipolar spin down

The measurement of pulsar braking indices provides a window into the physics governing pulsar spin down. What conclusions can be reached from the fact that $1 < n < 3$ in all known cases? First, it indicates that gravitational radiation ($n = 5$) is not a dominant source of pulsar spin-down (Ferrari & Ruffini, 1969). This would not be expected, except perhaps in the first moments of the life of a pulsar, if it is born spinning very rapidly and is initially non-spherical (Manchester & Taylor, 1977; Ferrari & Ruffini, 1969). In fact, less than 2% of the spin-down power for the Crab pulsar could be from gravitational radiation based on a search for gravitational waves with LIGO (Abbott et al., 2010). The measurements of $n < 3$ also indicate that higher-multipole magnetic radiation (implying $n = 5$ or higher) are not important sources of torque in rotating neutron star systems. That $1 < n < 3$ in all known cases likely indicates that the true spin-down of pulsars is a modified form of magnetic dipole radiation (Manchester & Taylor, 1977). It is known that pulsars do not rotate in vacuo but rather have plasma-filled magnetospheres, as first described by Goldreich & Julian (1969) and summarized in §1.5.1. The best observational evidence of magnetospheric plasma and its connection to braking torque is the "intermittent" radio pulsar whose

pulsed radio emission exhibits a binary division between "on" and "off," which is correlated with changes to its spin-down rate (Kramer et al., 2006).

Another possible modification of the standard spin-down model is a torque arising from an interaction with a fallback disk, which also gives $n < 3$ (Menou et al., 2001). For radio pulsations to be present, matter cannot fall into the magnetosphere, but must be ejected, leading to "propeller" mode accretion. Infrared observations of two AXPs can be explained with a fallback disk, but in both cases there is no evidence of interaction between the disk and neutron star (Wang et al., 2006; Kaplan et al., 2009). Moreover, no measurement of n is available for either AXP.

It may be interesting that of the six measurements of n, the three pulsars with $B > 10^{13}\,\mathrm{G}$ also have the three largest values of n (see Table 5.2). However, there is no evidence for a linear correlation between n and B. A possible explanation for $n < 3$ is that the magnetic fields of these pulsars are currently experiencing growth (Blandford & Romani, 1988). In this case, the smaller the value of n, the more rapid the field growth. In this context, the tendency of larger n in pulsars with larger B is potentially interesting. If the magnetic fields of "normal" field strength pulsars are rapidly growing and perhaps even transforming into magnetars (e.g. Lyne, 2004; Esposito et al., 2010) and the larger field pulsars are experiencing a lesser amount of field growth, but are still moving towards the magnetar regime, then which sources are the progenitors of the bulk of the normal pulsar population? Because the magnetars are highly variable and may lay in quiescent states for long periods, it is possible that the magnetar birthrate could be as much as $\sim 50\%$ percent of that of normal pulsars (Muno et al., 2008). Even so, it would be unusual for all the young pulsars with measured braking indices to be magnetar progenitors, and none to be progenitors of normal pulsars. It seems unlikely, then, that field growth is the whole solution to the $n < 3$ problem. Alternatively, field growth could occur during a very short phase of pulsar evolution, not persisting for sufficient time to significantly affect the B-field. The pulsars for which n has been measured are all very young, thus if $n < 3$ were only true for a short phase of pulsar evolution, this would not have been detected. In

fact, there is some evidence via population studies that $n = 3$ is a good description of the braking torque for the majority of pulsars, though this is far from certain (Faucher-Giguère & Kaspi, 2006; Contopoulos & Spitkovsky, 2006).

Prior to the availability of the results presented in Chapter 7, none of the six measured braking indices showed any evidence for significant variability. A variable braking index indicates a significant deviation from magnetic dipole spin-down, and a further deviation from any of the models put forward to explain $n < 3$.

8.4.2 Implications of a variable braking index

The observation of a decrease in the braking index for PSR J1846−0258 presents serious challenges to our understanding of normal pulsar spin down. That the change in n is not accompanied by any observable persistent change in the radiative properties of the pulsar is especially interesting, as discussed in §7.4. That the 2009 X-ray luminosity of the pulsar is consistent with that measured in quiescence in 2000 (Livingstone et al., 2010b) argues against a global magnetic field twist as being responsible for the change in spin-down behaviour (Thompson et al., 2002). Similarly, a relatively simple model for spin-down due to a combination of dipole and wind losses explains $\Delta n < 0$ with a significant increase in the luminosity of particles and thus in the pulsar wind nebula, which is not observed in PSR J1846−0258.

If the magnetar-like outburst in PSR J1846−0258 was accompanied by a significant flux of particles away from the surface, some previously closed field lines could have been blown open in the process. This would have the effect of changing the co-rotation radius of the pulsar, which in turn, should imply a smaller braking index that would persist after the particle flux had decayed. This could provide an explanation of the observation of $\Delta n < 0$ for PSR J1846−0258 (Contopoulos & Spitkovsky, 2006), though the details of the co-rotation radius before and after the outburst are related to the rate of magnetospheric reconnection, which may also be affected by the outburst (Contopoulos, 2007).

If $n < 3$ or $\Delta n < 0$ indicates that B or α are currently experiencing growth, a measurement of the second braking index, m (Eq. 1.14), would provide a verification of

the functional form of growth (Blandford, 1994). This parameter, which can be calculated with a measurement of $\ddot{\nu}$, has only been determined for two pulsars (Lyne et al., 1993; Livingstone et al., 2005b), and will only be measurable for PSR J1846−0258 if the level of timing noise decreases. A change in n is not predicted by most models of pulsar spin down and suggests new avenues of theoretical work.

8.5 Challenges to Standard Glitch Models

In this thesis, we have presented four new glitches in two young pulsars, summarized in Tables 8.1 and 8.2. There now exists a wide range of glitch properties in various types of neutron stars. Together with all known glitch observations, the unusual glitch properties presented here present challenges to standard glitch models, as summarized in this section.

8.5.1 "Magnetic" glitches

The large glitch and outburst in PSR J1846−0258 were contemporaneous, suggesting that the two are related, perhaps with one event acting as a trigger. Because glitches in rotation-powered pulsars may require a trigger (see, e.g. Link & Epstein, 1996), it stands to reason that whatever causes violent, energetic X-ray bursts could also trigger a release of superfluid vortices and thus a glitch. However, that both the initial spin-up magnitude and overshoot recovery were so unusual for PSR J1846−0258 suggests that the connection between the two events may be deeper. It is possible that this event, along with several AXP events (e.g. Kaspi et al., 2003; Dib et al., 2008a; Gavriil et al., 2009) may be significantly different in origin than normal glitches and are instead, in some sense, "magnetic" glitches.

It is tempting to try to link several unusual behaviours seen in the large PSR J1846−0258 glitch and in some magnetar glitches: over-recovery, radiative changes, and "enhanced" spin-down (see Eq. 6.1) following a spin-up glitch. Both confirmed glitches with $Q > 1$, in PSR J1846−0258 and in the AXP 4U 0142+61 (where the glitch over-recovered by a few percent; Gavriil et al., 2009), were accompanied by

radiative changes. However, glitches with normal recovery values (i.e. $Q < 1$) have accompanied other radiative events in magnetars (e.g. $Q = 0.19$ for 1E 2259+586; Kaspi et al., 2003).

Enhanced spin-down, where the value of $\dot{\nu}$ measured immediately after the glitch is significantly larger than the pre-glitch value owing to glitch recovery (§6.5), has been observed in AXP glitches with and without detected accompanying radiative changes (e.g. Dib et al., 2008a). The spin-down enhancement following these glitches is qualitatively similar to what is observed in any normal glitch recovery, but much different in magnitude, e.g. for 1E 2259+586, $\dot{\nu}_{\rm inst} = (8.2 \pm 0.6)\dot{\nu}$ (Kaspi et al., 2003) while a typical rotation-powered pulsar value is $\sim 0.005\dot{\nu}$ (see Peralta, 2006, and references therein). It is not understood why this difference is observed, and it may imply that for cases such as 1E 2259+586, that either a core glitch – where the core is briefly decoupled from the crust (Kaspi et al., 2003), or that an external source of torque (e.g. from wind losses Harding et al., 1999) is present in "magnetic" glitches.

8.5.2 Glitch activity and neutron star temperature

There is a well established relationship between the glitch activity parameter, A_g (Eq. 1.30) and characteristic age (or τ_c; McKenna & Lyne, 1990). In general, pulsars with $\tau_c < 5\,\mathrm{kyr}$, presumably with the highest internal temperatures, have glitches that are small and infrequent (i.e. A_g is small). Glitch frequency and size are usually largest for pulsars with $\tau_c \sim 5 - 10\,\mathrm{yr}$ and then slowly decay as τ_c increases and the neutron star cools (Lyne et al., 2000). McKenna & Lyne (1990) suggested that this is due to the relationship between the vortex creep rate and the internal temperature of the neutron star. If the large internal temperatures allow superfluid vortices to rearrange plastically, rather than via cracking, fewer and smaller glitches will result (Link & Epstein, 1996). As the star cools, the vortices become more rigid, resulting in the large glitches observed in the Vela pulsar. In the context of the glitches reported in this thesis, along with observations of large glitches in some AXPs, one can pose the question: does this theory continue to provide an adequate description of the observations?

PSR J1846−0258 should have one of the highest internal temperatures among neutron stars. Along with being one of the youngest pulsars, it has undergone at least one episode of reheating (i.e. the 2006 outburst). Thus, if the above theory were valid, a large glitch should not have occurred in PSR J1846−0258. The AXPs that have experienced large glitches also have high measured surface temperatures (Kaspi et al., 2003; Dib et al., 2008a), again seeming to contradict the connection between glitch size and internal temperature. While a large spin-up is in itself unusual in a pulsar as young as PSR J1846−0258, the large glitches experienced by the AXPs are similar in fractional magnitude when compared to those in RPPs of similar characteristic age (Peralta, 2006, and references therein). However, RPPs aged $10 - 100\,\mathrm{kyr}$ are systematically colder than the AXPs (e.g. Kaspi et al., 2006, and references therein). Perhaps, however, these glitches are better explained in the context of "magnetic glitches," as discussed in §8.5.1.

A connection between glitch size and neutron star temperature could have implications for the glitches observed from PSR J0205+6449. An independent confirmation that PSR J0205+6449 was born in the historical SN of 1181 would imply that the observed glitches (see Table 8.1) are larger than expected for an 829 yr-old pulsar, while not related to any magnetic activity in the neutron star. In this case, one might think that the large glitches are related to its cold temperature (Slane et al., 2004).

While glitches are common occurrences in young RPPs and magnetars, the third type of young neutron star, the CCOs, have not yet been observed to glitch. Three CCOs have been timed phase-coherently for the past 3 – 8 years (Pavlov et al., 2002; Halpern et al., 2007; Gotthelf & Halpern, 2009a). These objects have large surface temperatures, in the range $kT = 0.25 - 0.6\,\mathrm{keV}$ (Kaspi et al., 2006, and references therein), and thus glitches, or lack thereof could help clarify the connection between surface temperature and glitch size and frequency. Thus far, the CCOs are unlike other young pulsars in that they have very little timing noise, but knowing whether or not they glitch would be very illuminating.

8.5.3 *Variable spin-up magnitude in young pulsars*

As previously observed in older pulsars such as PSR B1737−30 ($\tau_c = 20\,\mathrm{kyr}$; Janssen & Stappers, 2006; Zou et al., 2008), spin-up amplitudes spanning several orders of magnitude have now been observed in a very young pulsar: that the two glitches in PSR J1846−0258 had such different spin-up amplitudes is in itself a challenge to most glitch theories.

According to Alpar et al. (1996), the youngest pulsars should have only small glitches, with fractional magnitudes in the range of $\Delta\nu/\nu \sim 10^{-9} - 10^{-8}$. In this picture, large glitches result from inhomogeneities in the vortex distribution which are built over several thousand years as a result of small glitches (see §1.8.2). A large glitch in a pulsar less than 1 kyr-old presents a clear challenge to this picture, or suggests that the glitch size is affected by events involved in the outburst.

8.5.4 *Net torque decrease following a glitch*

A glitch followed by a decrease in the magnitude of $\dot{\nu}$, as observed in PSR J0205+6449 and in the Rotating Radio Transient PSR J1819−1458 (Lyne et al., 2009), in contrast to the increase in magnitude seen in other cases, must also be allowed by a successful theory of glitches.

These observations could suggest a decrease in the net torque acting on the pulsar following a glitch. The torque could decrease either by a reduction in the magnetic moment (i.e. a decrease of B or α, via the spin-down law given in Eq. 1.7). Alternatively, a sudden change in $\dot{\nu}$ can be explained in the context of the superfluid interior of the neutron star. An explanation for the more typically observed $\Delta\dot{\nu}/\dot{\nu} > 0$ is that glitches create areas of low-vortex density, which effectively uncouples certain regions from the bulk rotation of the star (effectively lowering I). If this process were reversed after some glitches, that is, previously uncoupled regions of superfluid were re-coupled to the star (effectively increasing I), an observation of $\Delta\dot{\nu}/\dot{\nu} < 0$ would result, although how this opposite situation might arise has not been thoroughly studied. Another possible explanation for $\Delta\dot{\nu}/\dot{\nu} < 0$, as suggested by Lyne et al.

(2009) is that the effective magnetic field decreased by $\sim 1\%$ for PSR J1819−1458, or by $\sim 0.2\%$ for PSR J0205+6449, at the time of their respective glitches. Although magnetic field decay is described in the magnetar model (e.g. Thompson & Duncan, 1996), a permanent increase in $\dot{\nu}$ is not seen in magnetar glitches. In addition, possible reasons for field decay in a pulsar such as PSR J0205+6449 with a low magnetic field of 3.6×10^{12} G are not considered in the magnetar model, and in fact, Goldreich & Reisenegger (1992) argue that such a low field should not experience decay.

8.5.5 *Variability in glitch recovery*

Current theories describing pulsar glitches do not provide a satisfactory description of all the glitch recovery behaviours now observed. A successful theory must explain: an overshoot recovery, significant deviation from an exponential recovery, enhanced spin-down, and variable decay time, τ_d, and recovery fraction, Q.

Both the two-component model and the standard vortex creep model (as described in §1.8.2) require that the glitch recovery timescale, τ_d, which is directly related to coupling between the superfluid and solid components of the crust, is constant from glitch to glitch in a single pulsar. One possible way to circumvent the requirement of constant τ_d in the vortex creep model is from the fact that the coupling via vortex creep is strongly temperature dependent (Link et al., 1992). A sudden deposition of heat in the crust could result in weaker coupling between the lattice and superfluid, leading to a longer relaxation time. Effectively, this would increase the equilibrium frequency lag between the two components – the crust will spin down at an increased rate for longer in order to reach the new, larger equilibrium frequency lag. This could account for an over-recovery of a glitch if the heat deposition were of sufficient magnitude (Bennett Link, private communication). This is particularly interesting in the context of the large PSR J1846−0258 glitch occurring along with radiative activity, where the flux increase makes a crustal heat deposition very likely. This is not a comprehensive theory, however, and does not address why over-recovery does not regularly follow radiatively loud magnetar glitches.

Further, any measurement of $Q = 0$ following a glitch, that is, a glitch with no

recovery, as observed in the first PSR J1846−0258 glitch as well as in many other glitches, is difficult to understand within either the two-component or vortex creep model. If you perturb a system with two coupled components, some recovery towards equilibrium should be seen in every case.

8.6 Young Neutron Stars

There is now a wide range of observed behaviour in the three known types of young neutron stars. The "normal" Crab-like pulsars, such as PSR J0205+6449, have large spin-down luminosities, power pulsar wind nebulae and are typically observable as radio, X-ray, and γ-ray pulsars. These are, like the large majority of known pulsars, powered by their rotational kinetic energy.

The magnetars exhibit occasional bursts of X-rays, variable flux and spectra, and typically have X-ray luminosities far in excess of their spin-down luminosities. All these behaviours are thought to arise from their super-critical magnetic fields (Thompson & Duncan, 1996). PSR J1846−0258 is now identified as a transition object between rotation-powered pulsars and magnetars.

Finally, the central compact objects either do not pulse or exhibit only thermal X-ray pulsations (de Luca, 2008). No evidence for magnetospheric emission has been detected, that is, they do not power pulsar wind nebulae or radio or γ-ray pulsations.

The three types of young neutron stars show an astonishing array of behaviour, given that the observed population of older isolated pulsars is comparitively uniform. Many questions remain to be solved about pulsars in general, and the youngest pulsars in particular. Pulsar timing has been a useful tool for over 40 years to provide insight into these objects: their temporal evolution, their interiors, and their magnetospheres. Pulsar timing will continue to play a key role in the development of a coherent global theory of pulsars.

8.7 Concluding Remarks

This thesis was written during what is likely to be the last year of operation for *RXTE*. When it is de-orbited, a great gulf will open in the area of astrophysical X-ray timing studies. *RXTE* has been of huge benefit to the field of neutron stars over its lifetime. In contrast to many telescopes where many of the interesting results have arrived soon after launch, owing to the highly variable nature of the X-ray sky and the telescope's ability to capitalize on this property, *RXTE* has continued to produce valuable new results well into its later years. After its demise, some of the work currently being performed with *RXTE* can be done with other instruments. Notably, the *Swift* X-ray Telescope can monitor some of the neutron stars that pulse only in the X-ray band, such as PSR J1846−0258 and the AXPs. *AstroSAT* is an Indian multi-instrument satellite housing a PCA-like instrument which is set to be launched in 2011. However, neither instrument will devote as much time to the study of neutron stars as has *RXTE*. An opportunity exists for a new X-ray timing telescope to make significant discoveries about the nature of the violently variable X-ray sky.

Bibliography

Abbott, B. P., Abbott, R., Acernese, F., & et al. 2010, ApJ, 713, 671

Abdo, A. A., Ackermann, M., Ajello, M., & et al. 2009a, Science, 325, 840

—. 2009b, ApJL, 699, L102

—. 2009c, ApJ, 706, 1331

—. 2009d, ApJ, 700, 1059

—. 2010a, ApJ, 708, 1254

—. 2010b, ApJS, 187, 460

Abdo, A. A., Ackermann, M., Atwood, W. B., & et al. 2008, Science, 322, 1218

—. 2009e, ApJL, 695, L72

—. 2009f, ApJ, 696, 1084

—. 2009g, ApJ, 699, 1171

Alpar, M. A. 2001, ApJ, 554, 1245

Alpar, M. A., Anderson, P. W., Pines, D., & Shaham, J. 1981, ApJ, 249, L29

—. 1984, ApJ, 276, 325

Alpar, M. A., Ankay, A., & Yazgan, E. 2001, ApJL, 557, L61

Alpar, M. A., Chau, H. F., Cheng, K. S., & Pines, D. 1993, ApJ, 409, 345

—. 1994, ApJ, 427, L29

—. 1996, ApJ, 459, 706

Alpar, M. A., Cheng, K. S., & Pines, D. 1989, ApJ, 346, 823

Alpar, M. A., Nandkumar, R., & Pines, D. 1986, ApJ, 311, 197

Alpar, M. A. & Pines, D. 1993, in Isolated Pulsars, ed. R. E. K. A. van Riper & C. Ho (Cambridge University Press), 17

Anderson, P. W. & Itoh, N. 1975, Nature, 256, 25

Archibald, A. M., Kaspi, V. M., Livingstone, M. A., & McLaughlin, M. A. 2008, ApJ, 688, 550

Arzoumanian, Z., Nice, D. J., Taylor, J. H., & Thorsett, S. E. 1994, ApJ, 422, 671

Auriere, M., Silvester, J., Wade, G. A., Bagnulo, S., Donati, J., Johnson, N., Landstreet, J. D., Ligneres, F., Lueftinger, T., Mouillet, D., Paletou, F., Petit, P., & Strasser, S. 2003, A Peculiar Newsletter, vol. 39, 39

Baade, W. & Zwicky, F. 1934a, Phys. Rev., 45, 138

—. 1934b, Phys. Rev., 46, 76

Backer, D. C., Dexter, M. R., Zepka, A., D., N., Wertheimer, D. J., Ray, P. S., & Foster, R. S. 1997, PASP, 109, 61

Backer, D. C., Hama, S., Van Hook, S., & Foster, R. S. 1993, ApJ, 404, 636

Bai, X. & Spitkovsky, A. 2010, ApJ, 715, 1282

Baring, M. G. 2004, Advances in Space Research, 33, 552

Baring, M. G. & Harding, A. K. 1998, ApJ, 507, L55

Baym, G., Pethick, C., & Pines, D. 1969, Nature, 224, 673

Baym, G. & Pines, D. 1971, Ann. Phys. (U.S.A.), 66, 816

Becker, R. H. & Helfand, D. J. 1984, ApJ, 283, 154

Becker, W. & Aschenbach, B. 2002, in Neutron Stars, Pulsars, and Supernova Remnants, ed. W. Becker, H. Lesch, & J. Trümper, 64

Becker, W., Jessner, A., Kramer, M., Testa, V., & Howaldt, C. 2005, ApJ, 633, 367

Becker, W., Kramer, M., Jessner, A., Taam, R. E., Jia, J. J., Cheng, K. S., Mignani, R., Pellizzoni, A., de Luca, A., Słowikowska, A., & Caraveo, P. A. 2006, ApJ, 645, 1421

Beloborodov, A. M. 2009, ApJ, 703, 1044

Beloborodov, A. M. & Thompson, C. 2007, ApJ, 657, 967

Bhattacharya, D. & Soni, V. 2007, arXiv:0705.0592

Bietenholz, M. F. 2006, ApJ, 645, 1180

Bietenholz, M. F. & Bartel, N. 2008, MNRAS, 386, 1411

Bietenholz, M. F., Kassim, N. E., & Weiler, K. W. 2001, ApJ, 560, 772

Black, D. C. 1969, Nature, 221, 157

Blackburn, J. K. 1995, in Astronomical Society of the Pacific Conference Series, Vol. 77, Astronomical Data Analysis Software and Systems IV, ed. R. A. Shaw, H. E. Payne, & J. J. E. Hayes, 367

Blandford, R. D. 1994, MNRAS, 267, L7

Blandford, R. D., Applegate, J. H., & Hernquist, L. 1983, MNRAS, 204, 1025

Blandford, R. D. & Romani, R. W. 1988, MNRAS, 234, 57P

Blanton, E. L. & Helfand, D. J. 1996, ApJ, 470, 961

Bombaci, I. 1996, A & A, 305, 871

Boynton, P. E., Groth, E. J., Hutchinson, D. P., Nanos, G. P., Partridge, R. B., & Wilkinson, D. T. 1972, ApJ, 175, 217

Boynton, P. E., Groth, III, E. J., Partridge, R. B., & Wilkinson, D. T. 1969, ApJL, 157, L197

Bradt, H. V., Rothschild, R. E., & Swank, J. H. 1993, Astronomy and Astrophysics Supplement Series, 97, 355

Brogan, C. L., Gaensler, B. M., Gelfand, J. D., Lazendic, J. S., Lazio, T. J. W., Kassim, N. E., & McClure-Griffiths, N. M. 2005, ApJL, 629, L105

Buccheri, R., Bennett, K., Bignami, G. F., Caraveo, P. A., Bloemen, J. B. G. M., Hermsen, W., Boriakoff, V., Kanbach, G., Manchester, J. L., & Masnou, J. L. 1983, A&A, 128, 245

Buchner, S. & Flanagan, C. 2008, in American Institute of Physics Conference Series, Vol. 983, 40 Years of Pulsars: Millisecond Pulsars, Magnetars and More, ed. C. Bassa, Z. Wang, A. Cumming, & V. M. Kaspi, 145

Buchner, S. J. & Flanagan, C. 2006, in IAU Joint Discussion, Vol. 2, IAU Joint Discussion

Burgay, M., Joshi, B. C., D'Amico, N., Possenti, A., Lyne, A. G., Manchester, R. N., McLaughlin, M. A., Kramer, M., Camilo, F., & Freire, P. C. C. 2006, MNRAS, 368, 283

Burnell, S. J. B. 1977, Annals of the New York Academy of Science

Camilo, F., Cognard, I., Ransom, S. M., Halpern, J. P., Reynolds, J., Zimmerman, N., Gotthelf, E. V., Helfand, D. J., Demorest, P., Theureau, G., & Backer, D. C. 2007a, ApJ, 663, 497

Camilo, F. & Gaensler, B. M., eds. 2004, Young Neutron Stars and Their Environments, IAU Symposium 218 (San Francisco: Astronomical Society of the Pacific)

Camilo, F., Kaspi, V. M., Lyne, A. G., Manchester, R. N., Bell, J. F., D'Amico, N., McKay, N. P. F., & Crawford, F. 2000, ApJ, 541, 367

Camilo, F., Lorimer, D. R., Bhat, N. D. R., Gotthelf, E. V., Halpern, J. P., Wang, Q. D., Lu, F. J., & Mirabal, N. 2002a, ApJ, 574, L71

Camilo, F., Manchester, R. N., Gaensler, B. M., Lorimer, D. L., & Sarkissian, J. 2002b, ApJ, 567, L71

Camilo, F., Ransom, S., Halpern, J., Reynolds, J., Helfand, D., Zimmerman, N., & Sarkissian, J. 2006a, Nature, 442, 892

Camilo, F., Ransom, S. M., Gaensler, B. M., & Lorimer, D. R. 2009a, ApJL, 700, L34

Camilo, F., Ransom, S. M., Gaensler, B. M., Slane, P. O., Lorimer, D. R., Reynolds, J., Manchester, R. N., & Murray, S. S. 2006b, ApJ, 637, 456

Camilo, F., Ransom, S. M., Halpern, J. P., & Reynolds, J. 2007b, ApJ, 666, L93

Camilo, F., Ray, P. S., Ransom, S. M., Burgay, M., J., ., Kerr, M., Gotthelf, E. V., Halpern, J. P., Reynolds, J., Romani, R. W., Demorest, P., Johnston, S., van Straten, W., Saz Parkinson, P. M., Ziegler, M., Dormody, M., Thompson, D. J., Smith, D. A., Harding, A. K., Abdo, A. A., Crawford, F., Freire, P. C. C., Keith, M., Kramer, M., Roberts, M. S. E., Weltevrede, P., & Wood, K. S. 2009b, ApJ, 705, 1

Camilo, F., Stairs, I. H., Lorimer, D. R., Backer, D. C., Ransom, S. M., Klein, B., Wielebinski, R., Kramer, M., McLaughlin, M. A., Arzoumanian, Z., & Müller, P. 2002c, ApJ, 571, L41

Campana, S., Rea, N., Israel, G. L., Turolla, R., & Zane, S. 2007, A & A, 463, 1047

Carroll, B. W. & Ostlie, D. A. 2007, An Introduction to Modern Astrophysics, Second Edition (San Francisco: Addison Wesley)

Chadwick, J. 1932, Nature, 129, 312

Chakrabarty, D., Pivovaroff, M. J., Hernquist, L. E., Heyl, J. S., & Narayan, R. 2001, ApJ, 548, 800

Champion, D. J., Ransom, S. M., Lazarus, P., Camilo, F., Bassa, C., Kaspi, V. M., Nice, D. J., Freire, P. C. C., Stairs, I. H., van Leeuwen, J., Stappers, B. W., Cordes, J. M., Hessels, J. W. T., Lorimer, D. R., Arzoumanian, Z., Backer, D. C., Bhat, N. D. R., Chatterjee, S., Cognard, I., Deneva, J. S., Faucher-Giguère, C., Gaensler, B. M., Han, J., Jenet, F. A., Kasian, L., Kondratiev, V. I., Kramer, M., Lazio, J., McLaughlin, M. A., Venkataraman, A., & Vlemmings, W. 2008, Science, 320, 1309

Chatterjee, P., Hernquist, L., & Narayan, R. 2000, ApJ, 534, 373

Chatterjee, S., Gaensler, B. M., Melatos, A., Brisken, W. F., & Stappers, B. W. 2007, ApJ, 670, 1301

Cheng, K. S. 1987, ApJ, 321, 799

Cheng, K. S., Ho, C., & Ruderman, M. 1986a, ApJ, 300, 500

—. 1986b, ApJ, 300, 522

Cheng, K. S., Ruderman, M., & Zhang, L. 2000, ApJ, 537, 964

Chevalier, R. A. 1998, Mem. della Soc. Ast. It., 69, 977

Clark, D. H. & Stephenson, F. R. 1977, The Historical Supernovae (Oxford: Pergamon Press)

Cline, T. L., Desai, U. D., Pizzichini, G., Teegarden, B. J., Evans, W. D., Klebesadel, R. W., Laros, J. G., Hurley, K., Niel, M., Vedrenne, G., Estoolin, I. V., Kouznetsov, A. V. an Zenchenko, V. M., Hovestadt, D., & Gloeckler, G. 1980, ApJ, 237, L1

Cognard, I. & Backer, D. C. 2004, ApJ, 612, L125

Contopoulos, I. 2005, A & A, 442, 579

—. 2007, A & A, 466, 301

Contopoulos, I., Kazanas, D., & Fendt, C. 1999, ApJ, 511, 351

Contopoulos, I. & Spitkovsky, A. 2006, ApJ, 643, 1139

Cordes, J. M. & Downs, G. S. 1985, ApJS, 59, 343

Cordes, J. M. & Greenstein, G. 1981, ApJ, 245, 1060

Cordes, J. M. & Lazio, T. J. W. 2002, astro-ph/0207156

Crawford, F., Manchester, R. N., & Kaspi, V. M. 2001, AJ, 122, 2001

Cusumano, G., Hermsen, W., Kramer, M., Kuiper, L., Löhmer, O., Massaro, E., Mineo, T., Nicastro, L., & Stappers, B. W. 2004, Nuclear Physics B Proceedings Supplements, 132, 596

D'Alessandro, F., McCulloch, P. M., Hamilton, P. A., & Deshpande, A. A. 1995, MNRAS, 277, 1033

Dall'Osso, S., Israel, G. L., Stella, L., Possenti, A., & Perozzi, E. 2003, ApJ, 599, 485

Daugherty, J. K. & Harding, A. K. 1982, ApJ, 252, 337

—. 1996, ApJ, 458, 278

de Jager, O. C., Raubenheimer, B. C., & Swanepoel, J. W. H. 1989, A & A, 221, 180

de Luca, A. 2008, in American Institute of Physics Conference Series, Vol. 983, 40 Years of Pulsars: Millisecond Pulsars, Magnetars and More, ed. C. Bassa, Z. Wang, A. Cumming, & V. M. Kaspi, 311

De Luca, A., Caraveo, P. A., Mereghetti, S., Negroni, M., & Bignami, G. F. 2005, ApJ, 623, 1051

De Luca, A., Mereghetti, S., Caraveo, P. A., Moroni, M., Mignani, R. P., & Bignami, G. F. 2004, A&A, 418, 625

Deeter, J. 1984, ApJ, 281, 482

Deneva, J. S., Cordes, J. M., & Lazio, T. J. W. 2009, ApJL, 702, L177

Dib, R., Kaspi, V. M., & Gavriil, F. P. 2007, ApJ, 666, 1152

—. 2008a, ApJ, 673, 1044

—. 2008b, ApJ, 673, 1044

—. 2009, ApJ, 702, 614

Dodson, R. G., McCulloch, P. M., & Lewis, D. R. 2002, ApJL, 564, L85

Duncan, R. C. & Thompson, C. 1992, ApJ, 392, L9

Dyks, J. & Rudak, B. 2003, ApJ, 598, 1201

Efron, B. 1979, The Annals of Statistics, 7, 1

Esposito, P., Israel, G. L., Turolla, R., Tiengo, A., Götz, D., de Luca, A., Mignani, R. P., Zane, S., Rea, N., Testa, V., Caraveo, P. A., Chaty, S., Mattana, F., Mereghetti, S., Pellizzoni, A., & Romano, P. 2010, MNRAS, 498

Fahlman, G. G. & Gregory, P. C. 1981, Nature, 293, 202

Faucher-Giguère, C.-A. & Kaspi, V. M. 2006, ApJ, 643, 332

Feroci, M., Frontera, F., Costa, E., Amati, L., Rapisarda, M., & Orlandini, M. 1999, ApJL, 515, L9

Feroci, M., Hurley, K., Duncan, R. C., & Thompson, C. 2001, ApJ, 549, 1021

Ferrari, A. & Ruffini, R. 1969, ApJL, 158, L71+

Fesen, R., Rudie, G., Hurford, A., & Soto, A. 2008, ApJS, 174, 379

Fesen, R. A. 1983, ApJ, 270, L53

Foster, R. S., Ray, P. S., Lundgren, S. C., Backer, D. C., Dexter, M. R., & Zepka, A. 1996, in Pulsars: Problems and Progress, IAU Colloquium 160, ed. S. Johnston, M. A. Walker, & M. Bailes (San Francisco: Astronomical Society of the Pacific), 25

Frail, D. A., Goss, W. M., & Whiteoak, J. B. Z. 1994, ApJ, 437, 781

Frank, J., Kind, A. R., & Raine, D. J. 1992, Accretion Power in Astrophysics (Cambridge: Cambridge University Press)

Göğüş, E., Kouveliotou, C., Woods, P. M., Finger, M. H., & van der Klis, M. 2002, ApJ, 577, 929

Gaensler, B. M., Arons, J., Kaspi, V. M., Pivovaroff, M. J., Kawai, N., & Tamura, K. 2002, ApJ, 569, 878

Gavriil, F. P., Dib, R., & Kaspi, V. M. 2009, ApJ, submitted (arXiv:0905.1256)

Gavriil, F. P., Gonzalez, M. E., Gotthelf, E. V., Kaspi, V. M., Livingstone, M. A., & Woods, P. M. 2008, Science, 319, 1802

Gavriil, F. P. & Kaspi, V. M. 2002, ApJ, 567, 1067

—. 2004, ApJ, 609, L67

Gavriil, F. P., Kaspi, V. M., & Woods, P. M. 2002, Nature, 419, 142

Ghosh, P. 2007, Rotation and Accretion Powered Pulsars (New Jersey: World Scientific)

Giaconni, R., Gursky, H., Kellogg, E., Schreier, E., & Tananbaum, H. 1971, ApJ, 167, L67

Glasser, C. A., Odell, C. E., & Seufert, S. E. 1994, IEEE Transactions on Nuclear Science, 41, 1343

Gold, T. 1968, Nature, 218, 731

Goldreich, P. & Julian, W. H. 1969, ApJ, 157, 869

Goldreich, P. & Reisenegger, A. 1992, ApJ, 395, 250

Gonzalez, M. E., Kaspi, V. M., Camilo, F., Gaensler, B. M., & Pivovaroff, M. J. 2005, ApJ, 630, 489

Gotthelf, E. V. 2003, ApJ, 591, 361

Gotthelf, E. V., Gavriil, F. P., Kaspi, V. M., Vasisht, G., & Chakrabarty, D. 2002a, ApJ, 564, L31

Gotthelf, E. V. & Halpern, J. P. 2007, ApJ, 664, L35

—. 2008, ApJ, 681, 515

—. 2009a, ApJ, 695, L35

—. 2009b, ApJL, 700, L158

Gotthelf, E. V., Halpern, J. P., & Dodson, R. 2002b, ApJ, 567, L125

Gotthelf, E. V., Halpern, J. P., & Seward, F. D. 2005, ApJ, 627, 390

Gotthelf, E. V., Vasisht, G., Boylan-Kolchin, M., & Torii, K. 2000, ApJL, 542, L37

Green, D. A. & Gull, S. F. 1982, Nature, 299, 606

Greenstein, G. 1979, BAAS, 11, 426

Groth, E. J. 1975, ApJS, 29, 453

Gunn, J. E. & Ostriker, J. P. 1969, Nature, 221, 454

Gupta, Y., Mitra, D., Green, D. A., & Acharyya, A. 2005, Current Science, 89, 853

Güver, T., Özel, F., Cabrera-Lavers, A., & Wroblewski, P. 2010a, ApJ, 712, 964

Güver, T., Wroblewski, P., Camarota, L., & Ozel, F. 2010b, arXiv:1002.3825

Haberl, F. 2007, Astrophys. Space Sci., 181

Haberl, F., Motch, C., Zavlin, V. E., Reinsch, K., Gänsicke, B. T., Cropper, M., Schwope, A. D., Turolla, R., & Zane, S. 2004, A & A, 424, 635

Haensel, P., Zdunik, J. L., & Douchin, F. 2002, A & A, 385, 301

Halpern, J. P., Camilo, F., Giuliani, A., Gotthelf, E. V., McLaughlin, M. A., Mukherjee, R., Pellizzoni, A., Ransom, S. M., Roberts, M. S. E., & Tavani, M. 2008, ApJL, 688, L33

Halpern, J. P., Camilo, F., Gotthelf, E. V., Helfand, D. J., Kramer, M., Lyne, A. G., Leighly, K. M., & Eracleous, M. 2001, ApJ, 552, L125

Halpern, J. P. & Gotthelf, E. V. 2005, ApJ, 618, 874

—. 2010a, ApJ, 709, 436

—. 2010b, ApJ, 710, 941

Halpern, J. P., Gotthelf, E. V., Camilo, F., & Seward, F. D. 2007, ApJ, 665, 1304

Hambaryan, V., Hasinger, G., Schwope, A. D., & Schulz, N. S. 2002, A&A, 381, 98

Hamilton, P. A., McCulloch, P. M., Manchester, R. N., Ables, J. G., & Komesaroff, M. M. 1977, Nature, 265, 224

Harding, A. 2009, Astrophys. Space Sci., 357, 521

Harding, A. K., Contopoulos, I., & Kazanas, D. 1999, ApJ, 525, L125

Harding, A. K., Muslimov, A. G., & Zhang, B. 2002a, ApJ, 576, 366

Harding, A. K., Strickman, M. S., Gwinn, C., Dodson, R., Moffet, D., & McCulloch, P. 2002b, ApJ, 576, 376

Helfand, D. J. & Becker, R. H. 1987, ApJ, 314, 203

Helfand, D. J., Collins, B. F., & Gotthelf, E. V. 2003, 582, 783

Hermsen, W., Kuiper, L., Schönfelder, V., Strong, A. W., Bennett, K., Much, R., McConnell, M., Ryan, J., & Carramiñana, A. 1997, in ESA Special Publication, Vol. 382, The Transparent Universe, ed. C. Winkler, T. J.-L. Courvoisier, & P. Durouchoux, 287

Hessels, J. W. T., Ransom, S. M., Stairs, I. H., Freire, P. C. C., Kaspi, V. M., & Camilo, F. 2006, Science, 311, 1901

Hester, J. J., Mori, K., Burrows, D., Gallagher, J. S., Graham, J. R., Halverson, M., Kader, A., Michel, F. C., & Scowen, P. 2002, ApJ, 577, L49

Hewish, A., Bell, S. J., Pilkington, J. D. H., Scott, P. F., & Collins, R. A. 1968, Nature, 217, 709

Ho, W. C. G. & Heinke, C. O. 2009, Nature, 462, 71

Hobbs, G. 2002, PhD thesis, University of Manchester

Hobbs, G., Faulkner, A., Stairs, I. H., Camilo, F., Manchester, R. N., Lyne, A. G., Kramer, M., D'Amico, N., Kaspi, V. M., Possenti, A., McLaughlin, M. A., Lorimer, D. R., Burgay, M., Joshi, B. C., & Crawford, F. 2004, MNRAS, 352, 1439

Hobbs, G., Lyne, A. G., Joshi, B. C., Kramer, M., Stairs, I. H., Camilo, F., Manchester, R. N., D'Amico, N., Possenti, A., & Kaspi, V. M. 2002, MNRAS, 333, L7

Hobbs, G., Lyne, A. G., & Kramer, M. 2010, MNRAS, 402, 1027

Hobbs, G., Lyne, A. G., Kramer, M., Martin, C. E., & Jordan, C. 2004, MNRAS, 353, 1311

Hurley, K., Boggs, S. E., Smith, D. M., Duncan, R. C., Lin, R., Zoglauer, A., Krucker, S., Hurford, G., Hudson, H., Wigger, C., Hajdas, W., Thompson, C., Mitrofanov, I., Sanin, A., Boynton, W., Fellows, C., von Kienlin, A., Lichti, G., Rau, A., & Cline, T. 2005, Nature, 434, 1098

Hurley, K., Cline, T., Mazets, E., Barthelmy, S., Butterworth, P., Marshall, F., Palmer, D., Aptekar, R., Golenetskii, S., Ill'lnskii, V., Frederiks, D., McTiernan, J., Gold, R., & Trombka, T. 1999, Nature, 397, 41

Hurley, K., Li, P., Kouveliotou, C., Murakami, T., Ando, M., Strohmayer, T., van Paradijs, J., Vrba, F., Luginbuhl, C., Yoshida, A., & Smith, I. 1999, ApJ, 510, L111

Ibrahim, A. I., Markwardt, C. B., Swank, J. H., Ransom, S., Roberts, M., Kaspi, V., Woods, P. M., Safi-Harb, S., Balman, S., Parke, W. C., Kouveliotou, C., Hurley, K., & Cline, T. 2004, ApJ, 609, L21

Ibrahim, A. I., Strohmayer, T. E., Woods, P. M., Kouveliotou, C., Thompson, C., Duncan, R. C., Dieters, S., Swank, J. H., van Paradijs, J., & Finger, M. 2001, apj, 558, 237

Israel, G. L., Campana, S., Dall'Osso, S., Muno, M. P., Cummings, J., Perna, R., & Stella, L. 2007a, ApJ, 664, 448

Israel, G. L., Götz, D., Zane, S., Dall'Osso, S., Rea, N., & Stella, L. 2007b, A & A, 476, L9

Israel, G. L., Rea, N., Mangano, V., Testa, V., Perna, R., Hummel, W., Mignani, R., Ageorges, N., Curto, G. L., Marco, O., Angelini, L., Campana, S., Covino, S., Marconi, G., Mereghetti, S., & Stella, L. 2004, ApJ, 603, L97

Jackson, J. D. 1975, Classical Electrodynamics, 2nd Edition (New York: Wiley)

Jahoda, K., Markwardt, C. B., Radeva, Y., Rots, A. H., Stark, M. J., Swank, J. H., Strohmayer, T. E., & Zhang, W. 2006, ApJS, 163, 401

Janssen, G. H. & Stappers, B. W. 2006, A & A, 457, 611

Janssen, G. H., Stappers, B. W., Kramer, M., Nice, D. J., Jessner, A., Cognard, I., & Purver, M. B. 2008, A & A, 490, 753

Jewell, P. R. & Prestage, R. M. 2004, in Society of Photo-Optical Instrumentation Engineers (SPIE) Conference Series, Vol. 5489, Society of Photo-Optical Instrumentation Engineers (SPIE) Conference Series, ed. J. M. Oschmann Jr., 312–323

Johnston, S., Hobbs, G., Vigeland, S., Kramer, M., Weisberg, J. M., & Lyne, A. G. 2005, MNRAS, 364, 1397

Johnston, S., Lyne, A. G., Manchester, R. N., Kniffen, D. A., D'Amico, N., Lim, J., & Ashworth, M. 1992, MNRAS, 255, 401

Johnston, S., Walker, M. A., & Bailes, M., eds. 1996, Pulsars: Problems and Progress, IAU Colloquium 160 (San Francisco: Astronomical Society of the Pacific)

Kaplan, D. L., Chakrabarty, D., Wang, Z., & Wachter, S. 2009, ApJ, 700, 149

Kaplan, D. L. & van Kerkwijk, M. H. 2005, ApJ, 635, L65

Kargaltsev, O. & Pavlov, G. G. 2008, in American Institute of Physics Conference Series, Vol. 983, 40 Years of Pulsars: Millisecond Pulsars, Magnetars and More, ed. C. Bassa, Z. Wang, A. Cumming, & V. M. Kaspi, 171–185

Kaspi, V. M. 2007, Astrophys. Space Sci., 308, 1

Kaspi, V. M., Chakrabarty, D., & Steinberger, J. 1999, ApJ, 525, L33

Kaspi, V. M., Crawford, F., Manchester, R. N., Lyne, A. G., Camilo, F., D'Amico, N., & Gaensler, B. M. 1998, ApJ, 503, L161

Kaspi, V. M. & Gavriil, F. P. 2003, ApJ, 596, L71

Kaspi, V. M., Gavriil, F. P., Chakrabarty, D., Lackey, J. R., & Muno, M. P. 2001a, ApJ, 558, 253

Kaspi, V. M., Gavriil, F. P., Woods, P. M., Jensen, J. B., Roberts, M. S. E., & Chakrabarty, D. 2003, ApJ, 588, L93

Kaspi, V. M., Lackey, J. R., & Chakrabarty, D. 2000, ApJ, 537, L31

Kaspi, V. M., Manchester, R. N., Johnston, S., Lyne, A. G., & D'Amico, N. 1996, AJ, 111, 2028

Kaspi, V. M., Manchester, R. N., Siegman, B., Johnston, S., & Lyne, A. G. 1994, ApJ, 422, L83

Kaspi, V. M. & McLaughlin, M. A. 2005, ApJL, 618, L41

Kaspi, V. M., Roberts, M. S. E., & Harding, A. K. 2006, in Compact Stellar X-ray Sources, ed. W. H. G. Lewin & M. van der Klis (UK: Cambridge University Press)

Kaspi, V. M., Roberts, M. S. E., Vasisht, G., Gotthelf, E. V., Pivovaroff, M., & Kawai, N. 2001b, ApJ, 560, 371

Kirshner, R. P., Morse, J. A., Winkler, P. F., & Blair, W. P. 1989, ApJ, 342, 260

Kouveliotou, C., Dieters, S., Strohmayer, T., van Paradijs, J., Fishman, G. J., Meegan, C. A., Hurley, K., Kommers, J., Smith, I., Frail, D., & Murakami, T. 1998, Nature, 393, 235

Kouveliotou, C., Eichler, D., Woods, P. M., Lyubarsky, Y., Patel, S. K., Göğüş, E., van der Klis, M., Tennant, A., Wachter, S., & Hurley, K. 2003, ApJ, 596, L79

Kouveliotou, C., Strohmayer, T., Hurley, K., Van Paradijs, J., Finger, M. H., Dieters, S., Woods, P., Thompson, C., & Duncan, R. C. 1999, ApJ, 510, L115

Koyama, K., Hoshi, R., & Nagase, F. 1987, PASJ, 39, 801

Kramer, M., Lyne, A. G., Hobbs, G., Löhmer, O., Carr, P., Jordan, C., & Wolszczan, A. 2003, ApJ, 593, L31

Kramer, M., Lyne, A. G., O'Brien, J. T., Jordan, C. A., & Lorimer, D. R. 2006, Science, 312, 549

Kramer, M., Stairs, I. H., Manchester, R. N., McLaughlin, M. A., Lyne, A. G., Ferdman, R. D., Burgay, M., Lorimer, D. R., Possenti, A., D'Amico, N., Sarkissian,

J. M., Hobbs, G. B., Reynolds, J. E., Freire, P. C. C., & Camilo, F. 2006, Science, 314, 97

Kuiper, L. & Hermsen, W. 2009, A & A, 501, 1031

Kuiper, L., Hermsen, W., den Hartog, P., & Collmar, W. 2006, ApJ, 645, 556

Kuiper, L., Hermsen, W., Krijger, J. M., Bennett, K., Carramiñana, A., Schönfelder, V., Bailes, M., & Manchester, R. N. 1999, A&A, 351, 119

Kuiper, L., Hermsen, W., & Stappers, B. 2004, 33, 507

Kulkarni, S. R., Kaplan, D. L., Marshall, H. L., Frail, D. A., Murakami, T., & Yonetoku, D. 2003, ApJ, 585, 948

Kumar, H. S. & Safi-Harb, S. 2008, ApJL, 678, L43

Lamb, R. C., Fox, D. W., Macomb, D. J., & Prince, T. A. 2002, ApJ, 574, L29

Landau, L. & Lifshitz, E. M. 1987, Fluid Mechanics (Oxford: Butterworth-heinemann)

Large, M. I., Vaughan, A. E., & Mills, B. Y. 1968, Nature, 220, 340

Lattimer, J. H. & Prakash, M. 2004, Science, 304, 536

Leahy, D. A., Elsner, R. F., & Weisskopf, M. C. 1983, ApJ, 272, 256

Leahy, D. A. & Tian, W. W. 2008, A & A, 480, L25

Levine, A. M., Bradt, H., Cui, W., Jernigan, J. G., Morgan, E. H., Remillard, R., Shirey, R. E., & Smith, D. A. 1996, ApJL, 469, L33+

Link, B., Epstein, R., & Baym, G. 1992, ApJ, 390, L21

Link, B. & Epstein, R. I. 1996, ApJ, 457, 844

—. 1997, ApJL, 478, L91

Link, B., Epstein, R. I., & Baym, G. 1993, ApJ, 403, 285

Link, B. K. & Epstein, R. I. 1991, ApJ, 373, 592

Livingstone, M. A., Kaspi, V. M., & Gavriil, F. P. 2005a, ApJ, 633, 1095

—. 2010a, ApJ, 710, 1710

Livingstone, M. A., Kaspi, V. M., Gavriil, F. P., & Manchester, R. N. 2005b, ApJ, 619, 1046

Livingstone, M. A., Kaspi, V. M., Gotthelf, E. V., & Kuiper, L. 2006, ApJ, 647, 1286

Livingstone, M. A., Ng, C., Kaspi, V. M., Gavriil, F. P., & Gotthelf, E. V. 2010b, ApJ, Submitted (arXiv:1007.2829)

Livingstone, M. A., Ransom, S. M., Camilo, F., Kaspi, V. M., Lyne, A. G., Kramer, M., & Stairs, I. H. 2009, ApJ, 706, 1163

Lorimer, D. R., Faulkner, A. J., Lyne, A. G., Manchester, R. N., Kramer, M., McLaughlin, M. A., Hobbs, G., Possenti, A., Stairs, I. H., Camilo, F., Burgay, M., D'Amico, N., Corongiu, A., & Crawford, F. 2006, MNRAS, 372, 777

Lorimer, D. R. & Kramer, M. 2005, Handbook of Pulsar Astronomy (Cambridge, UK: Cambridge University Press)

Lyne, A., Hobbs, G., Kramer, M., Stairs, I., & Stappers, B. 2010, Science, 329, 408

Lyne, A. G. 1996, in Pulsars: Problems and Progress, IAU Colloquium 160, ed. S. Johnston, M. A. Walker, & M. Bailes (San Francisco: Astronomical Society of the Pacific), 73–81

Lyne, A. G. 2004, in Young Neutron Stars and Their Environments, IAU Symposium 218, ed. F. Camilo & B. M. Gaensler (San Francisco: Astronomical Society of the Pacific), 257–260

Lyne, A. G., McLaughlin, M. A., Keane, E. F., Kramer, M., Espinoza, C. M., Stappers, B. W., Palliyaguru, N. T., & Miller, J. 2009, MNRAS, 400, 1439

Lyne, A. G., Pritchard, R. S., Graham-Smith, F., & Camilo, F. 1996, Nature, 381, 497

Lyne, A. G., Pritchard, R. S., & Shemar, S. L. 1995, Journal of Astrophysics and Astronomy, 16, 179

Lyne, A. G., Pritchard, R. S., & Smith, F. G. 1993, MNRAS, 265, 1003

Lyne, A. G., Shemar, S. L., & Graham-Smith, F. 2000, MNRAS, 315, 534

Lyne, A. G. & Smith, F. G. 2005, Pulsar Astronomy, 3rd ed. (Cambridge: Cambridge University Press)

Lyne, A. G., Smith, F. G., & Pritchard, R. S. 1992, Nature, 359, 706

Macy, Jr., W. W. 1974, ApJ, 190, 153

Manchester, R. N. 2004, Science, 304, 542

Manchester, R. N., Fan, G., Lyne, A. G., Kaspi, V. M., & Crawford, F. 2006, ApJ, 649, 235

Manchester, R. N., Hobbs, G. B., Teoh, A., & Hobbs, M. 2005, AJ, 129, 1993

Manchester, R. N., Lyne, A. G., Camilo, F., Bell, J. F., Kaspi, V. M., D'Amico, N., McKay, N. P. F., Crawford, F., Stairs, I. H., Possenti, A., Morris, D. J., & Sheppard, D. C. 2001, MNRAS, 328, 17

Manchester, R. N., Lyne, A. G., D'Amico, N., Bailes, M., Johnston, S., Lorimer, D. R., Harrison, P. A., Nicastro, L., & Bell, J. F. 1996, MNRAS, 279, 1235

Manchester, R. N. & Peterson, B. A. 1989, ApJ, 342, L23

Manchester, R. N. & Taylor, J. H. 1977, Pulsars (San Francisco: Freeman)

Marshall, F. E., Gotthelf, E. V., Middleditch, J., Wang, Q. D., & Zhang, W. 2004, ApJ, 603, 682

Marshall, F. E., Gotthelf, E. V., Zhang, W., Middleditch, J., & Wang, Q. D. 1998, ApJ, 499, L179

Mazets, E. P., Cline, T. L., Aptekar', R. L., Butterworth, P. S., Frederiks, D. D., Golenetskii, S. V., Il'Inskii, V. N., & Pal'Shin, V. D. 1999, Astronomy Letters, 25, 635

Mazets, E. P., Golenetskii, S. V., Ilinskii, V. N., Apetkar, R. L., & Guryan, Y. A. 1979, Nature, 282, 587

McGarry, M. B., Gaensler, B. M., Ransom, S. M., Kaspi, V. M., & Veljkovik, S. 2005, ApJL, 627, L137

McKenna, J. & Lyne, A. G. 1990, Nature, 343, 349

McLaughlin, M. A., Cordes, J. M., Deshpande, A. A., Gaensler, B. M., Hankins, T. H., Kaspi, V. M., & Kern, J. S. 2001, ApJ, 547, L41

McLaughlin, M. A., Lyne, A. G., Keane, E. F., Kramer, M., Miller, J. J., Lorimer, D. R., Manchester, R. N., Camilo, F., & Stairs, I. H. 2009, MNRAS, 400, 1431

McLaughlin, M. A., Lyne, A. G., Lorimer, D. R., Kramer, M., Faulkner, A. J., Manchester, R. N., Cordes, J. M., Camilo, F., Possenti, A., Stairs, I. H., Hobbs, G., D'Amico, N., Burgay, M., & O'Brien, J. T. 2006, Nature, 439, 817

McLaughlin, M. A., Stairs, I. H., Kaspi, V. M., Lorimer, D. R., Kramer, M., Lyne, A. G., Manchester, R. N., Camilo, F., Hobbs, G., Possenti, A., D'Amico, N., & Faulkner, A. J. 2003, ApJ, 591, L135

Melatos, A. 1997, MNRAS, 288, 1049

Melatos, A. & Peralta, C. 2007, ApJL, 662, L99

Menou, K., Perna, R., & Hernquist, L. 2001, ApJ, 559, 1032

Mereghetti, S., Bandiera, R., Bocchino, F., & Israel, G. L. 2002, ApJ, 574, 873

Mereghetti, S., Tiengo, A., Esposito, P., Götz, D., Stella, L., Israel, G. L., Rea, N., Feroci, M., Turolla, R., & Zane, S. 2005, ApJ, 628, 938

Mereghetti, S., Tiengo, A., Stella, L., Israel, G. L., Rea, N., Zane, S., & Oosterbroek, T. 2004, ApJ, 608, 427

Mestel, L., Panagi, P., & Shibata, S. 1999, MNRAS, 309, 388

Meszaros, P. 1992, High-Energy Radiation from Magnetized Neutron Stars (Chicago: University of Chicago Press)

Michel, F. C. & Tucker, W. H. 1969, Nature, 223, 277

Mignani, R. P. 2009, Advances in Space Research, accepted (arXiv:0912.2931)

Moffett, D. A. and Hankins, T. H. 1996, ApJ, 468, 779

Mori, K. & Hailey, C. J. 2006, ApJ, 648, 1139

Morris, D. J., Hobbs, G., Lyne, A. G., Stairs, I. H., Camilo, F., Manchester, R. N., Possenti, A., Bell, J. F., Kaspi, V. M., Amico, N. D., McKay, N. P. F., Crawford, F., & Kramer, M. 2002, MNRAS, 335, 275

Muno, M. P. 2007, in American Institute of Physics Conference Series, Vol. 924, The Multicolored Landscape of Compact Objects and Their Explosive Origins, ed. T. di Salvo, G. L. Israel, L. Piersant, L. Burderi, G. Matt, A. Tornambe, & M. T. Menna, 166–173

Muno, M. P., Gaensler, B. M., Nechita, A., Miller, J. M., & Slane, P. O. 2008, ApJ, 680, 639

Murray, S. S., Slane, P. O., Seward, F. D., Ransom, S. M., & Gaensler, B. M. 2002, ApJ, 568, 226

Nagase, F., Deeter, J., Lewis, W., Dotani, T., Makino, F., & Mitsuda, K. 1990, ApJ, 351, L13

Nather, R. E., Warner, B., & Macfarlane, M. 1969, Nature, 221, 527

Ng, C.-Y., Romani, R. W., Brisken, W. F., Chatterjee, S., & Kramer, M. 2007, ApJ, 654, 487

Ng, C.-Y., Slane, P. O., Gaensler, B. M., & Hughes, J. P. 2008, ApJ, 686, 508

Ohashi, T., Ebisawa, K., Fukazawa, Y., Hiyoshi, K., Horii, M., Ikebe, Y., Ikeda, H., Inoue, H., Ishida, M., Ishisaki, Y., Ishizuka, T., Kamijo, S., Kaneda, H., Kohmura, Y., Makishima, K., Mihara, T., Tashiro, M., Murakami, T., Shoumura, R., Tanaka, Y., Ueda, Y., Taguchi, K., Tsuru, T., & Takeshima, T. 1996, PASJ, 48, 157

Olausen, S. A., Kaspi, V. M., Lyne, A. G., & Kramer, M. 2010, ApJ, Submitted (arXiv:1007.1196)

Ostriker, J. P. & Gunn, J. E. 1969, ApJ, 157, 1395

Özel, F., Psaltis, D., & Kaspi, V. M. 2001, ApJ, 563, 255

Pacini, F. 1967, Nature, 216, 567

—. 1968, Nature, 219, 145

Page, D., Geppert, U., & Weber, F. 2006, Nuclear Physics A, 777, 497

Palmer, D. M., Barthelmy, S., Gehrels, N., Kippen, R. M., Cayton, T., Kouveliotou, C., Eichler, D., Wijers, R. A. M. J., Woods, P. M., Granot, J., Lyubarsky, Y. E., Ramirez-Ruiz, E., Barbier, L., Chester, M., Cummings, J., Fenimore, E. E., Finger, M. H., Gaensler, B. M., Hullinger, D., Krimm, H., Markwardt, C. B., Nousek, J. A., Parsons, A., Patel, S., Sakamoto, T., Sato, G., Suzuki, M., & Tueller, J. 2005, Nature, 434, 1107

Pavlov, G. G., Sanwal, D., & Teter, M. A. 2004, in IAU Symposium, Vol. 218, Young Neutron Stars and Their Environments, ed. F. Camilo & B. M. Gaensler, 239

Pavlov, G. G., Zavlin, V. E., & Sanwal, D. 2002, in Neutron Stars, Pulsars, and Supernova Remnants, ed. W. Becker, H. Lesch, & J. Trümper (Garching: Max-Plank-Institut für Extraterrestrische Physik), 273, astro-ph/0206024

Pavlov, G. G., Zavlin, V. E., Sanwal, D., & Trümper, J. 2002, ApJ, 569, L95

Pellizzoni, A. & et al. 2009, ApJL, 695, L115

Pellizzoni, A., Pilia, M., Possenti, A., & et al. 2009, ApJ, 691, 1618

Peralta, C. 2006, Ph.D. Thesis, University of Melbourne

Peralta, C., Melatos, A., Giacobello, M., & Ooi, A. 2006, ApJ, 651, 1079

Pethick, C. J. & Ravenhall, D. G. 1991, in Neutron Stars: Theory and Observation, ed. J. Ventura & D. Pines (Dordrecht: Kluwer), 3–20

Pines, D. & Alpar, M. A. 1985, Nature, 316, 27

Pivovaroff, M., Kaspi, V. M., & Camilo, F. 2000, ApJ, 535, 379

Prestage, R. M., Constantikes, K. T., Hunter, T. R., King, L. J., Lacasse, R. J., Lockman, F. J., & Norrod, R. D. 2009, IEEE Proceedings, 97, 1382

Radhakrishnan, V. & Manchester, R. N. 1969, Nature, 222, 228

Radhakrishnan, V. & Srinivasan, G. 1982, Curr. Sci., 51, 1096

Ramanamurthy, P. V., Bertsch, D. L., Dingus, B. L., Espositio, J. A., Fierro, J. M., Fichtel, C. E., Etienne, A., Fichtel, C. E., Friedlander, D. P., Hunter, S. D., Kanbach, G., Kniffen, D. A., Lin, Y. C., Lyne, A. G., Mattox, J. R., Mayer-Hasselwander, H. A., Merck, M., Michelson, P. F., von Montigny, C., Mukherjee, R., Nolan, P. L., & Thompson, D. J. 1995, ApJ, 447, L109

Ransom, S., Camilo, F., Kaspi, V., Slane, P., Gaensler, B., Gotthelf, E., & Murray, S. 2004, in AIP Conf. Proc. 714: X-ray Timing 2003: Rossi and Beyond, ed. P. Kaaret, F. K. Lamb, & J. H. Swank, 350–356

Ransom, S. M. 2001, PhD thesis, Harvard University

Rea, N., Oosterbroek, T., Zane, S., Turolla, R., Méndez, M., Israel, G. L., Stella, L., & Haberl, F. 2005, MNRAS, 361, 710

Roberts, M., Ransom, S., Gavriil, F., Kaspi, V., P., Ibrahim, A., Markwardt, C., & Swank, J. 2004, in American Institute of Physics Conference Series, Vol. 714, X-ray Timing 2003: Rossi and Beyond, ed. P. Kaaret, F. K. Lamb, & J. H. Swank, 306–308

Roberts, M. S. E., Romani, R. W., & Johnston, S. 2001, ApJ, 561, L187

Roberts, M. S. E., Tam, C. R., Kaspi, V. M., Lyutikov, M., Vasisht, G., Pivovaroff, M., Gotthelf, E. V., & Kawai, N. 2003, ApJ, 588, 992

Roger, R. S., Milne, D. K., Kesteven, M. J., Wellington, K. J., & Haynes, R. F. 1988, ApJ, 332, 940

Romani, R. W. 1996, ApJ, 470, 469

Romani, R. W. & Yadigaroglu, I.-A. 1995, ApJ, 438, 314

Rothschild, R. E., Blanco, P. R., Gruber, D. E., Heindl, W. A., MacDonald, D. R., Marsden, D. C., Pelling, M. R., Wayne, L. R., & Hink, P. L. 1998, ApJ, 496, 538

Rothschild, R. E., Kulkarni, S. R., & Lingenfelter, R. E. 1994, Nature, 368, 432

Rots, A. H., Jahoda, K., & Lyne, A. G. 2004, ApJL, 605, L129

Rots, A. H., Jahoda, K., Macomb, D. J., Kawai, N., Saito, Y., Kaspi, V. M., Lyne, A. G., Manchester, R. N., Backer, D. C., Somer, A. L., Marsden, D., & Rothschild, R. E. 1998, ApJ, 501, 749

Ruderman, M. 1969, Nature, 223, 597

Ruderman, M. A. & Sutherland, P. G. 1975, ApJ, 196, 51

Rutledge, R. E., Bildsten, L., Brown, E. F., Pavlov, G. G., & Zavlin, V. E. 2002, ApJ, 577, 346

Rutledge, R. E., Fox, D. W., Kulkarni, S. R., Jacoby, B. A., Cognard, I., Backer, D. C., & Murray, S. S. 2004, ApJ, 613, 522

Safi-Harb, S. & Kumar, H. S. 2008, ApJ, 684, 532

Saito, Y. 1998, PhD thesis, University of Tokyo

Sakurai, J. J. 1994, Modern Quantum Mechanics (Revised Edition) (New York: Addison Wesley)

Sanwal, D., Pavlov, G. G., Zavlin, V. E., & Teter, M. A. 2002, ApJ, 574, L61

Scott, D., Finger, M., & Wilson, C. 2003, MNRAS, 344, 412

Serlemitsos, P. J., Joalota, L., Soong, Y., Kunieda, H., Taw ara, Y., Tsusaka, Y., Suzuki, H., Yamazaki, Y., Yoshioka, H., Fur uzawa, A., Yamashita, K., Awaki, H., Itoh, M., Ogasaka, Y., Honda, H., & Uchibori, Y. 1995, PASJ, 47, 105

Seward, F. D., Charles, P. A., & Smale, A. P. 1986, ApJ, 305, 814

Seward, F. D., Harnden, F. R., & Helfand, D. J. 1984, ApJ, 287, L19

Seward, F. D. & Harnden Jr., F. R. 1982, ApJ, 256, L45

Shapiro, S. L. & Teukolsky, S. A. 1983, Black Holes, White Dwarfs and Neutron Stars. The Physics of Compact Objects (New York: Wiley–Interscience)

Shemar, S. L. & Lyne, A. G. 1996, MNRAS, 282, 677

Shibazaki, N., Murakami, T., Shaham, J., & Nomoto, K. 1989, Nature, 342, 656

Sigurdsson, S., Richer, H. B., Hansen, B. M., Stairs, I. H., & Thorsett, S. E. 2003, Science, 301, 193

Slane, P., Helfand, D. J., van der Swaluw, E., & Murray, S. S. 2004, ApJ, 616, 403

Slane, P. O., Helfand, D. J., & Murray, S. S. 2002, ApJ, 571, L45

Snodgrass, H. B. & Ulrich, R. K. 1990, ApJ, 351, 309

Sonobe, T., Murakami, T., Kulkarni, S. R., Aoki, T., & Yoshida, A. 1994, ApJ, 436, L23

Spitkovsky, A. 2004, in Young Neutron Stars and Their Environments, IAU Symposium 218, ed. F. Camilo & B. M. Gaensler (San Francisco: Astronomical Society of the Pacific), 357–364

Spitkovsky, A. 2006, ApJL, 648, L51

Spitkovsky, A. 2008, in American Institute of Physics Conference Series, Vol. 983, 40 Years of Pulsars: Millisecond Pulsars, Magnetars and More, ed. C. Bassa, Z. Wang, A. Cumming, & V. M. Kaspi, 20–28

Spruit, H. C. 2008, in American Institute of Physics Conference Series, Vol. 983, 40 Years of Pulsars: Millisecond Pulsars, Magnetars and More, ed. C. Bassa, Z. Wang, A. Cumming, & V. M. Kaspi, 391–398

Staelin, D. H. & Reifenstein, III, E. C. 1968, Science, 162, 1481

Standish, E. M. 1982, A&A, 114, 297

Stephenson, F. R. 1971, Q. J. R. Astron, 12, 10

Stephenson, F. R. & Green, D. A. 2002, Historical supernovae and their remnants (Oxford: Oxford University Press)

Su, Y., Chen, Y., Yang, J., Koo, B.-C., Zhou, X., Jeong, I.-G., & Zhang, C.-G. 2009, ApJ, 694, 376

Sugizaki, M., Nagase, F., Torii, K. I., Kinugasa, K., Asanuma, T., Matsuzaki, K., Koyama, K., & Yamauchi, S. 1997, PASJ, 49, L25

Sun, M., Seward, F. D., Smith, R. K., & Slane, P. O. 2004, ApJ, 605, 742

Tam, C. & Roberts, M. S. E. 2003, ApJL, 598, L27

Tanaka, Y., Inoue, H., & Holt, S. S. 1994, PASJ, 46, L37

Tauris, T. M. & Manchester, R. N. 1998, MNRAS, 298, 625

Taylor, J. H. 1992, Philos. Trans. Roy. Soc. London A, 341, 117

Thompson, C. & Blaes, O. 1998, Phys. Rev. D, 57, 3219

Thompson, C. & Duncan, R. C. 1993, ApJ, 408, 194

Thompson, C. & Duncan, R. C. 1995, MNRAS, 275, 255

Thompson, C. & Duncan, R. C. 1996, ApJ, 473, 322

—. 2001, ApJ, 561, 980

Thompson, C., Duncan, R. C., Woods, P. M., Kouveliotou, C., Finger, M. H., & van Paradijs, J. 2000, ApJ, 543, 340

Thompson, C., Lyutikov, M., & Kulkarni, S. R. 2002, ApJ, 574, 332

Thompson, D. J., Bailes, M., Bertsch, D. L., Cordes, J., D'Amico, N., Esposito, J. A., Finley, J., Hartman, R. C., Hermsen, W., Kanbach, G., Kaspi, V. M., Kniffen, D. A., Kuiper, L., Lin, Y. C., Manchester, R., Matz, S. M., Mayer-Hasselwander, H. A., Michelson, P. F., Nolan, P. L., Ogelman, H., Pohl, M., Ramanamurthy, P. V., Sreekumar, P., Reimer, O., Taylor, J. H., & Ulmer, M. 1999, ApJ, 516, 297

Tian, W. W. & Leahy, D. A. 2008, ApJ, 677, 292

Timokhin, A. N. 2006, MNRAS, 368, 1055

Torii, K., Tsunemi, H., Dotani, T., & Mitsuda, K. 1997, ApJ, 489, L145

Torii, K., Tsunemi, H., Dotani, T., Mitsuda, K., Kawai, N., Kinugasa, K., Saito, Y., & Shibata, S. 1999, ApJ, 523, L69

Urama, J. O., Link, B., & Weisberg, J. M. 2006, MNRAS, 370, L76

Urama, J. O. & Okeke, P. N. 1999, MNRAS, 310, 313

van den Heuvel, E. P. J. & Habets, G. M. H. J. 1984, Nature, 309, 598

van Kerkwijk, M. H. & Kaplan, D. L. 2008, ApJL, 673, L163

Vasisht, G. & Gotthelf, E. V. 1997, ApJ, 486, L129

Vasisht, G., Gotthelf, E. V., Torii, K., & Gaensler, B. M. 2000, ApJ, 542, L49

Wang, N., Manchester, R. N., Pace, R., Bailes, M., Kaspi, V. M., Stappers, B. W., & Lyne, A. G. 2000, MNRAS, 317, 843

Wang, Z., Chakrabarty, D., & Kaplan, D. L. 2006, Nature, 440, 772

Winkler, P. F., Tuttle, J. H., Kirshner, R. P., & Irwin, M. J. 1988, in IAU Colloq. 101: Supernova Remnants and the Interstellar Medium, ed. R. S. Roger & T. L. Landecker, 65

Wolszczan, A., Cordes, J. M., & Dewey, R. J. 1991, ApJL, 372, L99

Wolszczan, A. & Frail, D. A. 1992, Nature, 355, 145

Wong, T., Backer, D. C., & Lyne, A. 2001, ApJ, 548, 447

Woods, P. M. 2008, in American Institute of Physics Conference Series, Vol. 983, 40 Years of Pulsars: Millisecond Pulsars, Magnetars and More, ed. C. Bassa, Z. Wang, A. Cumming, & V. M. Kaspi, 227–233

Woods, P. M., Kaspi, V. M., Thompson, C., Gavriil, F. P., Marshall, H. L., Chakrabarty, D., Flanagan, K., Heyl, J., & Hernquist, L. 2004, ApJ, 605, 378

Woods, P. M., Kouveliotou, C., Finger, M. H., Göğüş, E., Wilson, C. A., Patel, S. K., Hurley, K., & Swank, J. H. 2007, ApJ, 654, 470

Woods, P. M., Kouveliotou, C., Göğüş, E., Finger, M. H., Swank, J., Markwardt, C. B., Hurley, K., & van der Klis, M. 2002, ApJ, 576, 381

Woods, P. M., Kouveliotou, C., Göğüş, E., Finger, M. H., Swank, J., Smith, D. A., Hurley, K., & Thompson, C. 2001, ApJ, 552, 748

Woods, P. M., Kouveliotou, C., van Paradijs, J., Finger, M. H., & Thompson, C. 1999, ApJ, 518, L103

Woods, P. M., Kouveliotou, C., van Paradijs, J., Finger, M. H., Thompson, C., Duncan, R. C., Hurley, K., Strohmayer, T., Swank, J., & Murakami, T. 1999, ApJ, 524, L55

Woods, P. M. & Thompson, C. 2006, in Compact Stellar X-ray Sources, ed. W. H. G. Lewin & M. van der Klis (UK: Cambridge University Press)

Woosley, S. E. & Weaver, T. A. 1986, Ann. Rev. Astr. Ap., 24, 205

Yakovlev, D. G., Kaminker, A. D., Haensel, P., & Gnedin, O. Y. 2002, A&A, 389, L24

Yuan, J. P., Wang, N., Manchester, R. N., & Liu, Z. Y. 2010, MNRAS, 137

Zavlin, V. E. & Pavlov, G. G. 2002, in Neutron Stars, Pulsars, and Supernova Remnants, ed. W. Becker, H. Lesch, & J. Trümper, 263

Zavlin, V. E. & Pavlov, G. G. 2004, ApJ, 616, 452

Zavlin, V. E., Pavlov, G. G., Sanwal, D., Manchester, R. N., Trümper, J., Halpern, J. P., & Becker, W. 2002, ApJ, 569, 894

Zavlin, V. E., Pavlov, G. G., Sanwal, D., & Trümper, J. 2000, ApJ, 540, L25

Zhang, B. & Harding, A. K. 2000, ApJ, 535, L51

Zhang, B., Harding, A. K., & Muslimov, A. G. 2000, ApJ, 531, L135

Zhu, W., Kaspi, V. M., Dib, R., Woods, P. M., Gavriil, F. P., & Archibald, A. M. 2008, ApJ, 686, 520

Zhu, W., Kaspi, V. M., Gonzalez, M. E., & Lyne, A. G. 2009, ApJ, 704, 1321

Zou, W. Z., Wang, N., Manchester, R. N., Urama, J. O., Hobbs, G., Liu, Z. Y., & Yuan, J. P. 2008, MNRAS, 384, 1063